Synthesis and Photophysical Properties of New Di- and Mononuclear Phosphorescent Iridium(III) Complexes

DANIEL GWYN CONGRAVE

Synthesis and Photophysical Properties of New Di- and Mononuclear Phosphorescent Iridium(III) Complexes

Daniel Gwyn Congrave

Ustinov College

Department of Chemistry

Durham University

A thesis submitted for the degree of Doctor of Philosophy at Durham University

January 2018

Abstract

Cyclometallated Ir(III) complexes have attracted significant attention as luminescent materials due to a range of favourable properties, such as their high photoluminescence quantum yields, microsecond phosphorescence lifetimes, thermal stability, robust electrochemistry and synthetic versatility, which has enabled their emission to be tuned across the visible spectrum from the near-UV to the near-IR. They have been applied to various applications, such as in bioimaging, sensing, photocatalysis, and as sensitisers for singlet oxygen and as emitters in organic light emitting devices (OLEDs).

While mononuclear Ir(III) complexes have been extensively studied, dinuclear derivatives have received less attention. This is likely related to their high molecular weights, which limits their application to solution-processed rather than vacuum-processed OLEDs. Historically, diiridium complexes have also been noted to exhibit poorer luminescence efficiency than their mononuclear analogues. Nevertheless, a number recent of studies have indicated that correctly designed dimers can indeed be highly emissive and interest in dinuclear Ir(III) complexes has increased. They are particularly interesting as they introduce a bridging ligand, which can be used to modify the electronic communication between the Ir centers as well as the various photophysical and physical properties of the complex.

In this thesis a range of new diiridium complexes bridged by hydrazide (N^O) chelates will be discussed. In Chapter 2 further structural variation of the peripheral cyclometallating and bridging ligands of the prototypical complex **34** is explored through complexes **35–38**. Results indicated that functionalisation of either the bridging or peripheral ligands can facilitate colour tuning, and the matrix dependent photophysical properties of **37** and **38** were explained. Intramolecular π–π interactions were also observed between the peripheral and bridging ligands of the complexes. In Chapter 3, such interactions were enhanced through fluorination of aryl moieties on the bridging ligands, and were utilised to modify the photophysical properties of diiridium complexes (complexes **62**–**66**). The first examples of sky-blue emitting diiridium complexes are also presented (complexes **68**–**70**). In Chapter 4 the series was extended through the application of topical bulky 1,2-diarylimidazole cyclometallating ligands, leading to the first example of sky-blue aggregation-induced phosphorescent emission (AIPE) from a diiridium complex. Inspired by the findings in Chapter 3, in Chapter 5 mononuclear Ir(III) diasteromers featuring chiral oxazoline ancillary ligands were investigated as a platform for a deeper fundamental study into the effect of intramolecular π–π interactions on the photophysical properties of Ir(III) phosphors.

Statement of copyright

Declaration

The work in this thesis was carried out in the Department of Chemistry at Durham University between October 2014 and December 2017. All the work was carried out by the author unless otherwise stated and has not previously been submitted for a degree at this or any other University.

Publications

Portions of the literature review and original research conducted in preparation of this thesis have been published in the following articles:

Chapter 1: "Recent advances in luminescent dinuclear iridium(III) complexes and their application in organic electroluminescent devices" G. Li, D. G. Congrave, D. Zhu, Z. Su and M. R. Bryce, *Polyhedron*, **2018**, 140, 146–157. *Invited review in special issue "Molecules for devices: the inorganic chemistry behind modern technologies".*

Chapter 2: "Synthesis, diastereomer separation, and optoelectronic and structural properties of dinuclear cyclometalated iridium(III) complexes with bridging diarylhydrazide ligands" D. G. Congrave, Y-T. Hsu, A. S. Batsanov, A. Beeby and M. R. Bryce, *Organometallics*, 2017, **36**, 981–993.

Chapter 3: "Sky-blue emitting bridged diiridium complexes: beneficial effects of intramolecular π–π stacking" D. G. Congrave, Y-T. Hsu, A. S. Batsanov, A. Beeby, M. R. Bryce, *Dalton Trans.,* 2018. *Accepted,* DOI: 10.1039/c7dt04201a.

Acknowledgements

Funding from the EPSRC Doctoral Training Grant is acknowledged.

I would like to thank my supervisor, Prof. Martin Bryce, for his support and guidance during all stages of this project. Particularly, I'd like to thank him for giving me the freedom to explore my own research ideas. I would also like to acknowledge all past and present members of the Bryce group for providing a productive and relaxed work environment. Dr Gilles Yzambart, Dr Markus Gantenbein and Dr Jonathan Ward are thanked for useful discussion throughout the project and making my time in Durham so enjoyable. Some special thanks are required for Dr Helen Benjamin and Dr Iain Wright, who were especially helpful (and patient!) during the first year of this project. I'd also like to thank the members of LOMOX (Dr Luke Judd and Dr Matt Aldred) for the good times that we've had during my PhD.

Prof. Andy Beeby is acknowledged for useful discussion related to his photophysical expertise. He is also acknowledged for use of his equipment, particularly for invaluable assistance in obtaining variable temperature photoluminescence data. Some special thanks go to Dr Yu-Ting (Helen) Hsu for spending many laborious hours obtaining much of the photophysical data presented in this thesis, and for training me to conduct photophysical measurements.

Dr Andrei Batsanov is acknowledged for tirelessly solving all X-ray crystal structures presented within this thesis, from single crystals that were often of questionable quality. His contribution cannot be understated.

Dr Mark Fox is thanked for training me to carry out the computational work presented in this thesis, and for his constant and indispensable help troubleshooting any issues that I encountered.

Many thanks go to the analytical staff for their expertise and for providing services that run so smoothly that they are all too easy to take for granted. Particularly, I would like to thank Dr Alan Kenwright and Dr Juan Aguilar Malavia for their NMR expertise, and Dr Aileen Congreve for her help with the departmental spectroscopy equipment.

Finally, I'd like to thank my parents, family and friends for their support and patience during my studies. Thanks in particular go to Steph for coping with my Chemistry obsession and to my North Wales and Bangor friends for the good times we've had, even if we only meet up once a year: Rob, Sarah, Lauren, Dave, Mel, Peter, Charles, Gavin, Aron and Jack.

Table of Contents

List of abbreviations

$\Delta G^{\ddagger}$	Free energy of activation
$\Delta H^{\ddagger}$	Enthalpy of activation
$\Delta S^{\ddagger}$	Entropy of activation
Φ_{PL}	Photoluminescence quantum yield
N_{A}	Number of photons absorbed
N_{A}	Number of photons absorbed
T_{coal}	Coalescence temperature
k_{nr}	Non-radiative rate constant
k_{r}	Radiative rate constant
k_{coal}	Exchange rate at coalescence point
N_{A}	Number of photons absorbed
N_{E}	Number of photons emitted
$[Ir(COD)\mu–Cl]_2$	Bis(1,5-cyclooctadiene)diiridium(I) dichloride
$[Ir(dfppy)_2\mu–Cl]_2$	Tetrakis(2-(2,4-difluorophenyl)pyridine-*C*^{2},*N*')(μ-dichloro)diiridium
$[Ir(mesppy)_2\mu\text{-}Cl]_2$	Tetrakis(2-phenyl-4-(2,4,6-trimethylphenyl)-pyridine-*C*^{2},*N*')(μ-dichloro)diiridium
$[Ir(ppy)_2\mu–Cl]_2$	Tetrakis(2-phenylpyridine-*C*^{2},*N*')(μ-dichloro)diiridium
$[Ir(ppy)_2phen]^+$	1,10-Phenanthroline-bis(2-phenylpyridine)iridium(III)
$[Ru(bpy)_3]^{2+}$	Ruthenium(II)-tris(bipyridine)
2-MeTHF	2-Methyltetrahydrofuran
A	Absorption
abs	Absorption
acac	Acetylacetanoate
AIPE	Aggregation-inducted phosphorescent emission
ap. t	Apparent triplet
ASAP	Atmospheric solids analysis probe
B3LYP	Becke, 3-parameter, Lee-Yang-Parr
bs	Broad singlet
Bu	Butyl
c	Concentration (for Beer-Lambert law)
CB	Chlorobenzene
CBP	4,4'-Bis(*N*-carbazolyl)-1,1'-biphenyl
CCD	Charge-coupled device
CIE_{xy}	Commission Internationale d'Éclairage coordinates
COSY	Homonuclear correlation spectroscopy
CT	Charge transfer
CV	Cyclic voltammetry
d	Doublet
DABCO	1,4-Diazabicyclo[2.2.2]octane
DCM	Methylene chloride (dichloromethane)
DCTB	*trans*-2-[3-(4-*tert*-Butylphenyl)-2-methyl-2-propenylidene]malononitrile
dd	Doublet of doublets

ddd	Doublet of doublet of doublets
dfppy	2,4-Difluorophenylpyridine
DFT	Density functional theory
DMF	*N*,*N*-Dimethylformamide
DMSO	Dimethylsulfoxide
DPV	Differential pulse voltammetry
E_g	Bandgap
EL	Electroluminescence
em	Emission
$E^{ox(n)}$	Oxidation potential for nth oxidation
EQE	External quantum efficiency
ESI	Electrospray ionisation
E_T	Triplet energy
Et	Ethyl
Et_2O	Diethyl ether
EtOAc	Ethyl acetate
EtOH	Ethanol
f	Oscillator strength
fac	Facial isomer
fac-Ir(pmb)$_3$	*fac*-Iridium(III) tris(1-phenyl-3-methylbenzimidazolin-2-ylidene-C,C2')
fac-Ir(pmp)$_3$	*fac*-Iridium(III) tris(1-phenyl-3-methylpyridimidazolin-2-ylidene-C,C2')
fac-Ir(ppy)$_3$	*fac*-Iridium(III)-tris(2-phenylpyridine)
fac-Ir(ppz)$_3$	*fac*-Iridium(III)-tris(*N*-phenylpyrazole)
Fc*	Decamethylferrocene
FcH	Ferrocene
FcH^+	Ferrocenium
FMO	Frontier molecular orbital
FWHM	Full width at half maximum
GCMS	Gas chromatography coupled mass spectrometry
HMBC	Heteronuclear multiple-bond correlation spectroscopy
HOMO	Highest occupied molecular orbital
HRMS	High resolution mass spectrometry
HSQC	Heteronuclear single-quantum correlation spectroscopy
hv_A	Absorbed photon
hv_E	Emitted photon
ILCT	Interligand charge transfer state
IQE	Internal quantum efficiency
Ir(btp)$_2$acac	Bis(2-(2'-benzothienyl)-pyridinato-N,C3')iridium(III)(acetylacetonate)
Ir(ppy)$_2$acac	Acetylacetanoate-bis(2-phenylpyridine)iridium(III)
Ir(ppy)$_2$vacac	Allyl acetoacetate-bis(2-phenylpyridine)iridium(III)
ISC	Intersystem crossing
$K_2OsO_2(OH)_4$	Potassium osmate (VI) dihydrate
$K_3Fe(CN)_6$	Potassium ferricyanide

K_BT	Ambient energy ($K_BT \times N_A$ = 2.279 kJmol^{-1})
l	Path length (for Beer-Lambert law)
L	Ligand
LANL2DZ	Los Alamos national laboratory two double zeta
LC	Ligand-centred state
LEEC	Light-emitting electrochemical cell
LMCT	Ligand-to-metal charge transfer state
LUMO	Lowest unoccupied molecular orbital
M	Metal
MALDI	Matrix-assisted laser desorption/ ionisation
MC	Metal-centred state
Me	Methyl
MeCN	Acetonitrile
MeOH	Methanol
mer	Meridional isomer
meso	Meso isomer
MLCT	Metal-to-ligand charge transfer state
MO	Molecular orbital
MS	Mass spectrometry
N_A	Avagadro's number (6.02×10^{23})
n-Bu_4NPF_6	Tetra-*n*-butylammonium hexafluorophosphate
n-Buli	*n*-Butyllithium
NEt_3	Triethylamine
NH_4OAc	Ammonium acetate
NHC	*N*-Heterocyclic carbene
NMR	Nuclear magnetic resonance
NOESY	Nuclear Overhauser effect spectroscopy
OLED	Organic light-emitting diode
PBD	2-(4-*tert*-Butylphenyl)-5-(4-biphenylyl)-1,3,4-oxadiazole
$Pd(OAc)_2$	Palladium(II) acetate
$Pd(PPh_3)_4$	Tetrakis(triphenylphosphine)palladium(0)
$Pd_2dba_3 \bullet CHCl_3$	Tris(dibenzylideneacetone)dipalladium(0)-chloroform adduct
Ph	Phenyl group
PL	Photoluminescence
PLQY/ Φ/ Φ_{PL}	Photoluminescence quantum yield
PMMA	Poly(methyl methacrylate)
PMT	Photomultiplier
PPh_3	Triphenylphosphine
ppy	2-Phenylpyridine
ppz	*N*-Phenylpyrazole
Pr	Propyl
p-TSA	*para*-Toluenesulfonic acid
Py	Pyridyl group
Pz	Pyrazolyl group
rac	Racemic
RIM	Restriction of intramolecular motion
S	singlet
S_EAr	Electrophilic aromatic substitution

S_M	Huang-Rhys factor
S_n	Singlet state
SOC	Spin-orbit coupling
T	Triplet
T_{50}	Lifetime to 50% luminance
T_{80}	Lifetimes to 80% luminance
TADF	Thermally activated delayed fluorescence
t-BuLi	*tert*-Butyllithium
TCE	1,1,2,2-Tetrachloroethane
TD-DFT	Time dependent density functional theory
tert-BuOH	*tert*-Butanol
THF	Tetrahydrofuran
TLC	Thin layer chromatography
TMS	Tetramethylsilane
T_n	Triplet state
TOF	Time of flight
v'_n	S_1 or T_1 vibrational state
vacac	Allyl acetoacetate
v_n	Ground vibrational state
δ−	Partial positive charge
δ+	Partial negative charge
ΔE	Energy difference
$\Delta E_{1/2}$	Difference in half wave potential
ΔE^{ox}	Difference in oxidation potential
Δ_O	Crystal field splitting parameter
ΔS	Difference/ change in spin
ΔST	Exchange energy (singlet-triplet energy gap)
Δ-TRISPHAT	Δ-Tetrabutylammonium phosphorus(V) tris(tetrachlorocatecholate)
ΔΔG	Stacking free energy
ε	Extinction coefficient (for Beer-Lambert law)
ε	Extinction coefficient
λ_{max}	Maximum wavelength
σ_{meta}	*meta* Hammett substitution constant
σ_{para}	*para* Hammett substitution constant
R	Gas constant
T	Temperature
$\delta v_{r.t.}$	Difference in frequency at room temperature
δv	Difference in frequency
η	Refractive index
τ	Excited state lifetime

Chapter 1: Introduction

Since the first reports on the luminescence of classic phosphorescent transition metal complexes such as $[Ru(bpy)_3]^{2+}$ and *fac*-$Ir(ppy)_3$ (Figure 1.1) in 1959[1] and 1985[2], respectively, research into photoactive transition metal complexes has expanded quickly.[3–8]

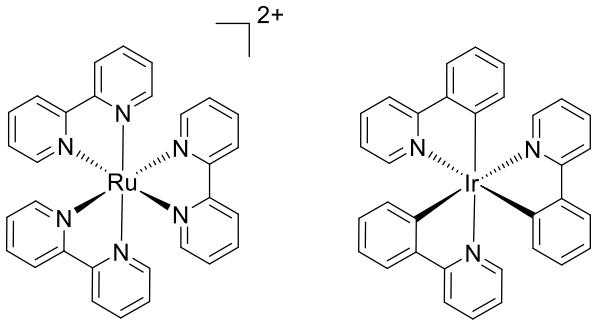

$[Ru(bpy)_3]^{2+}$ **fac-$Ir(ppy)_3$**

Figure 1.1: Molecular structures of some archetypal transition metal phosphors.

This work has been motivated by a diverse range of applications, for example as phosphors for organic light-emitting devices (OLEDs) and light-emitting electrochemical cells (LEECs),[9–11] as photocatalysts,[12] singlet oxygen sensitisers in therapeutics,[13] probes in bioimaging[14] and dyes in dye-sensitised solar cells.[15] Transition metal complexes with conjugated ligands present many beneficial properties, such as excited states of mixed character (e.g. metal-ligand and ligand-ligand etc.),[16–18] the variable oxidation states of the metal core and the opportunity for modular synthesis.[19] The addition of a bridging ligand and a second metal centre to form a bimetallic complex adds even greater potential for structural variation and an extra dimension to modulate the photophysical properties of the complexes.[20] At the heart of these properties is the phenomenon of luminescence. As our understanding of structure-property relationships has improved, monometallic Ir(III)-based systems have demonstrated colour-tunability across the whole visible spectrum while maintaining high luminescence efficiency, due to judicious molecular design.[21–23] Building on this stable foundation, research into dinuclear Ir(III) complexes (diiridium complexes) is an expanding field. This review will cover the fundamentals of luminescence in Ir(III) complexes, leading on to recent advances in the development of luminescent dinuclear Ir(III) systems.

Luminescence

Luminescence is the emission of light from a substance due to radiative relaxation of an electronically excited state.[24] The process of luminescence may be more rigorously defined based

on the mechanism of excitation, for example: chemiluminescence – the emission of light as the result of a chemical reaction; mechanoluminescence – the emission of light as the result of mechanical action on a solid; and thermoluminescence – the re-emission of absorbed energy when a substance is heated. Two particularly interesting categories of luminescence with regards to luminescent Ir(III) complexes are photoluminescence (PL) and electroluminescence (EL).

PL results from excitation of a molecule due to the absorption of photons. This phenomenon has been long-recognised; for example the first report of photoluminescence from quinine (Figure 1.2) was reported by Sir John Fredrich William Hershel in 1845.[25]

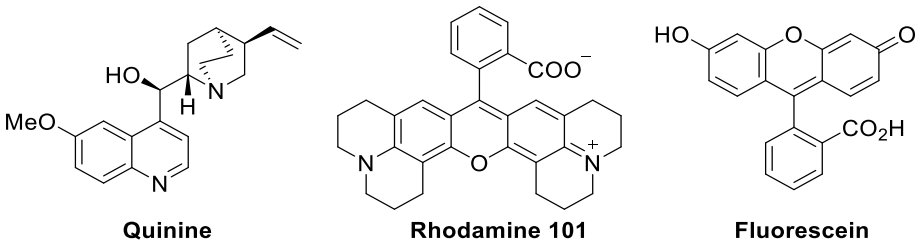

Figure 1.2: Molecular structures of some classic organic fluorophores.

After photoexcitation, there are several different fates which can befall an excited state. Generally, a molecule will lose energy to its surroundings via vibrations and rotations, known as non-radiative decay. However, if non-radiative decay is sufficiently slow, the molecule can dissipate excess energy via radiative decay – the emission of a photon via fluorescence or phosphorescence. These processes are well represented by a Jablonski diagram[26,27]. A Jablonski diagram is featured in Figure 1.3 and typical rates for the entailed processes are listed in Table 1.1.[28–31]

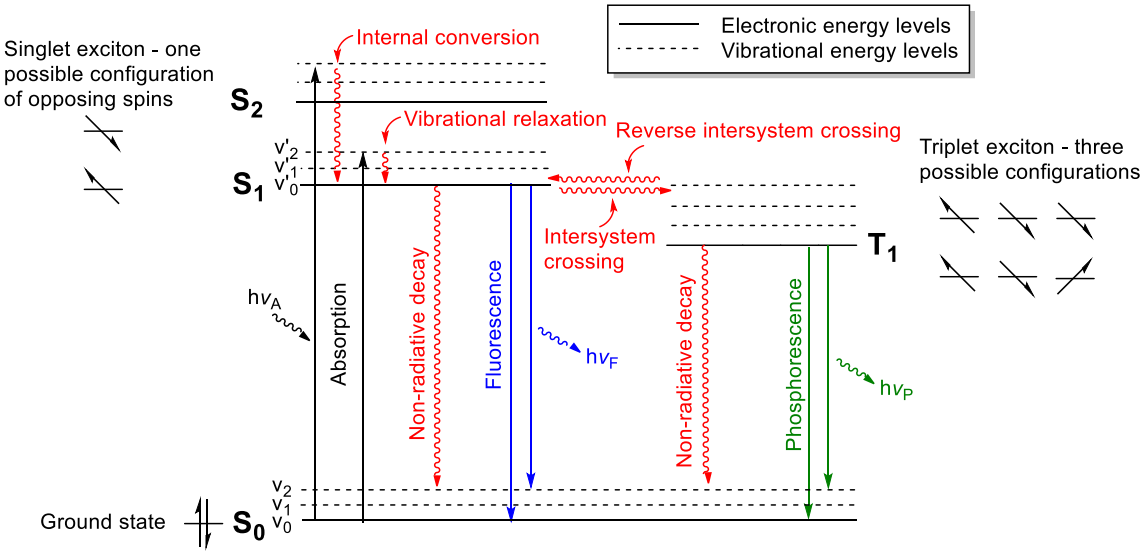

Figure 1.3: One form of a Jablonski diagram.

Table 1.1 Approximate rates of radiative and non-radiative processes.

Process	Rate (s^{-1})
Absorption	10^{15}
Internal conversion and vibrational relaxation	10^{11}–10^{14}
Fluorescence	10^{7}–10^{9}
Intersystem crossing	Variable (0.1 – > 10^{13})
Phosphorescence	< 10^{3}–10^{6}
Non-radiative decay	10^{7}–10^{9}

The singlet ground, the first and second electronic states are denoted by S_0, S_1 and S_2, respectively. The first triplet excited state is labelled T_1. Electronic states converge with increasing energy and for a typical aromatic molecule ΔE (S_0, S_1) lies in the UV-visible energy range (c*a.* 200–750 nm/ 13–50 × 10^3 cm^{-1}/ 1.7–6.2 eV). Each electronic state features a ladder of vibrational energy levels (denoted as v_n for S_0 and v'_n for S_1). These states also converge with increasing energy and their energy spacing corresponds to the infrared (typically *ca.* 2.5−25 × 10^3 nm/ 400−4000 cm^{-1}/ 50–500 meV for the mid-infrared). Rotational energy levels, which diverge with increasing energy and have energy spacing corresponding to the microwave region of the electromagnetic spectrum are also present, but omitted from Figure 1.3 for clarity. Radiative transitions are drawn as vertical straight arrows as a consequence of the Born-Oppenheimer approximation,[24] whereas non-radiative transitions are drawn as wavy lines.

Upon photoexcitation from S_0 a singlet excited state (e.g. S_1 or S_2) is generated due to the spin selection rule ($\Delta S = 0$). The nature of the most probable transition is proportional to the square of the overlap integral of the ground and excited state vibrational wavefunctions (Franck-Condon principle). Regardless of the intially formed state, it will usually undergo fast internal conversion/ vibrational relaxation to S_1, v'_0 before any appreciable emission may occur (Kasha's rule).[28]

Fluorescence is a spin-allowed radiative decay process (e.g. $S_1 \rightarrow S_0$) and so is relatively fast with lifetimes on the nanosecond timescale. Analogous to absorption, the most probable transition is again related to vibrational wavefunction overlap. Potential energy well diagrams and corresponding idealised absorption and emission spectra for two different classes of fluorescent molecule are shown in Figure 1.4; where a) is a fluorophore with very similar ground and excited state geometries (dominant $v_0 \leftrightarrow v'_0$ transitions) and b) is an example where the excited state geometry is displaced relative to the ground state. As the most probable absorption and emission

transitions are effectively the same in example a), it features a very small Stokes shift ($\Delta\lambda_{max}$ abs/ em).[32,33]

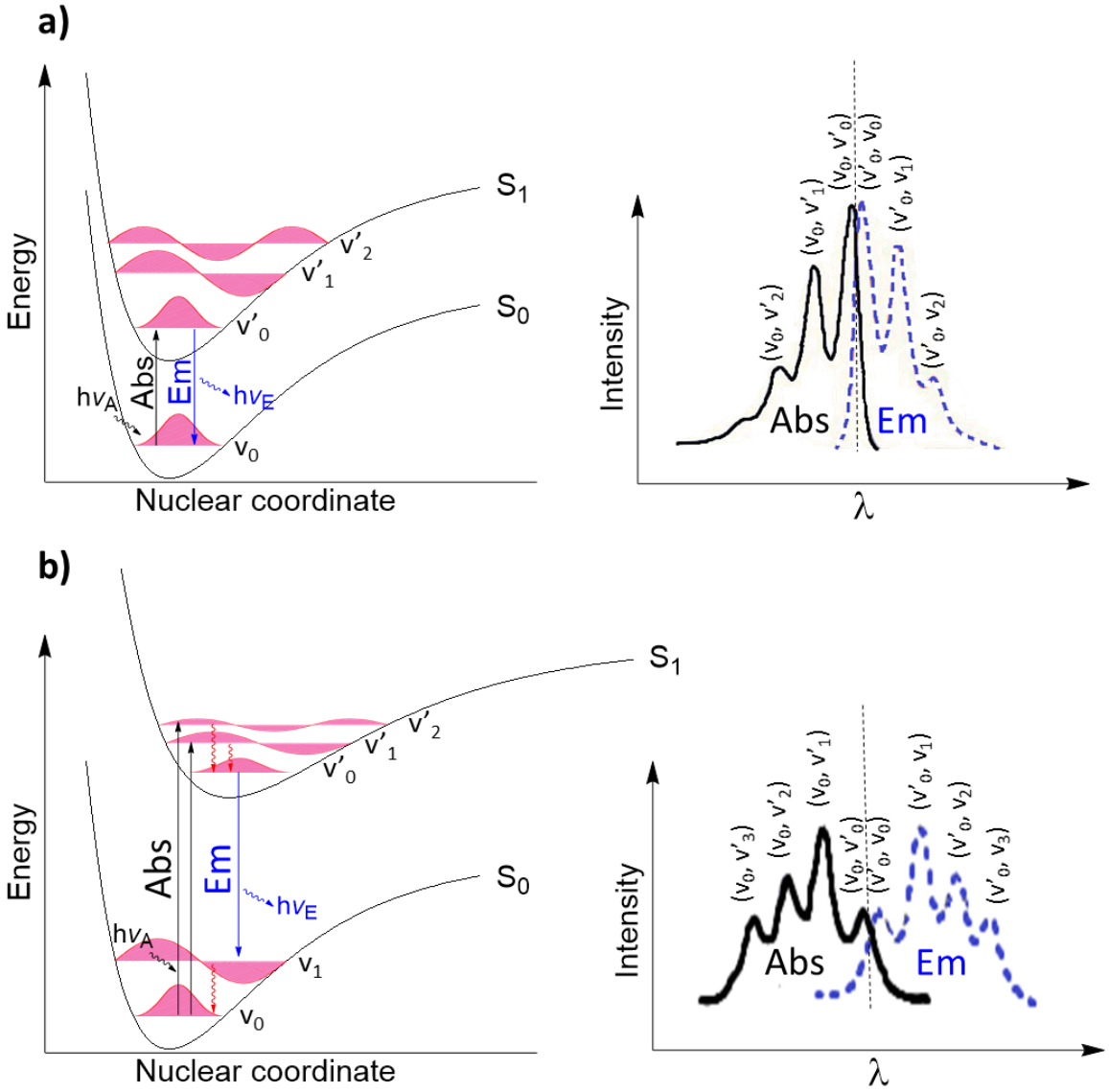

Figure 1.4: Potential energy well diagrams with corresponding idealised absorption and emission spectra. Straight (–, –) and wavy (~~) lines correspond to radiative and non-radiative processes, respectively. Vibrational wavefunctions are drawn in pink.

When a molecule has been promoted to an excited singlet state, it can change spin multiplicity and undergo intersystem crossing (ISC) to the triplet manifold. This process is formally spin-forbidden ($\Delta S \neq 0$) and so for purely organic molecules often has a negligible influence on the singlet excited state lifetime. However, incorporating a heavy atom such as a halogen or a transition metal can relax the spin selection rule due to a strong spin-orbit coupling (SOC) effect and promote ISC. For example, the intersystem crossing rate of *fac*-Ir(ppy)$_3$ (Figure 1.1) has been experimentally

observed to be on the order of 10^{13} s^{-1}.[29] This is significantly faster than fluorescence and non-radiative decay and so the T_1 state is formed with unitary efficiency.

Emission from triplet states is also spin forbidden ($\Delta S \neq 0$) and is known as phosphorescence. Similarly to ISC, phosphoresence can be exceptionally slow for purely organic molecules with rates as low as 0.1 s^{-1}. However, perturbing selection rules through the incorporation of a heavy metal, such as Ir or Pt, can increase the rate of phosphorescence to obtain lifetimes on the order of microseconds.[18,34]

Quantum efficiency

In the context of photoluminescence, the efficiency of emission from an excited state can be quantified through the photoluminescence quantum yield (PLQY, Φ_{PL}). Provided that the emissive state is formed with unitary efficiency upon excitation,[35,*] it is simply the ratio of photons emitted (N_{E}) to photons absorbed (N_{A}). It also corresponds to the ratio of the rate constants for radiative (k_{r}) and non-radiative (k_{nr}) decay stated in Equation 1.1. The excited state lifetime (τ) is also defined in Equation 1.2.

$$\Phi_{PL} = \frac{N_{\mathrm{E}}}{N_{\mathrm{A}}} = \frac{k_{\mathrm{r}}}{k_{\mathrm{r}} + k_{\mathrm{nr}}} \tag{1.1}$$

$$\tau = \frac{1}{k_{\mathrm{r}} + k_{\mathrm{nr}}} \tag{1.2}$$

For PL, upon excitation the initially populated state (the Franck-Condon state) is singlet in nature due to the Pauli exclusion principle and spin selection rule. Therefore, Φ_{PL} values of unity (100%) are possible via either fluorescence or phosphorescence (after ISC) according to the Jablonski diagram above (Figure 1.3). The case is notably different for EL – luminescence from a molecule excited by applying an electrical bias. Excited states are formed via charge recombination i.e. the electrons involved in the excited state were not bound in the same molecule before exciton formation, and so a statistical distribution of spin states is obtained (Figure 1.5).[31] The internal quantum efficiency (IQE) (the EL equivalent of Φ_{PL}) is therefore limited to 25% for traditional fluorescent molecules,[34] as in 75% of instances non-emissive triplet states are directly generated, for which reverse intersystem crossing (Figure 1.3) is improbable due to a large exchange energy (ΔST).[36] However, phosphorescent heavy metal complexes are particularly appealing for EL – the

[*] In the context of phosphorescence 'unitary efficiency' is a particularly significant statement. The rate of ISC to the emissive triplet state must be orders of magnitude faster than fluorescence and non-radiative decay to S_0 from the singlet state. This is commonly the case for heavy metal phosphors (e.g. Ir and Pt complexes).

75% directly generated triplets are emissive, as are the remaining 25% singlets after prompt ISC, leading to a maximum possible IQE of 100% via electrophosphorescence.[18]

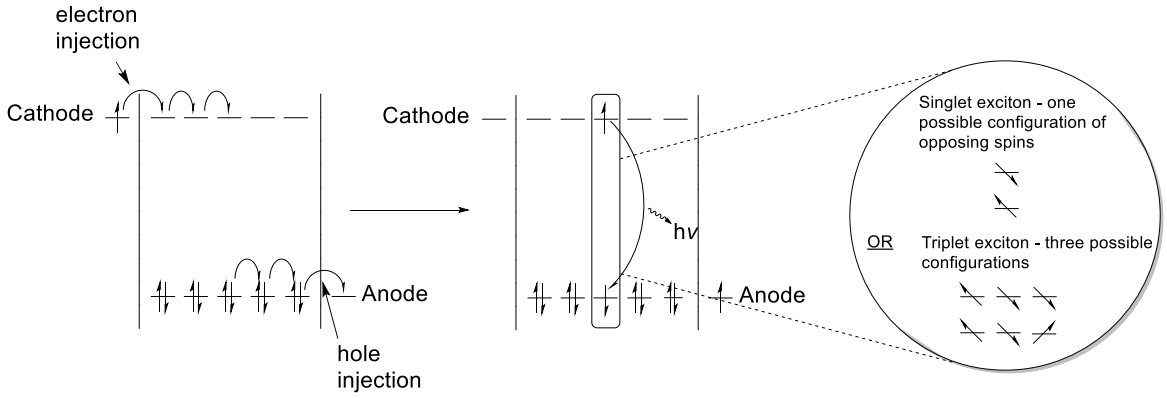

Figure 1.5: Schematic to highlight the statistical recombination of charges in electroluminescent devices.

The anatomy and stereochemistry of Ir(III) complexes

Phosphorescent complexes based on Ir(III) are popular due to a range of useful properties. Iridium has a large SOC constant which leads to efficient ISC and results in short τ due to intense phosphorescence.[7] Iridium complexes are also usually highly robust, being thermally stable while featuring reversible electrochemistry.[16] Due to the synthetic versatility of the conjugated organic ligands and strong electronic interactions between the ligands and the metal, it is also possible to tune their photophysical properties through systematic structural variations.[17,37]

Phosphorescent Ir(III) complexes are octahedral and usually incorporate chelating cyclometallating ligands, which coordinate to the metal through a carbanionic C and a neutral N atom (C^N ligands) to form a 5- or 6-membered metallocycle. The archetypal cyclometallating ligand is 2-phenylpyridine (ppy) (Figure 1.6). Such Ir(III) complexes can be divided into two basic categories: 1) homoleptic complexes which feature identical ligands (usually three monoionic C^N chelates) and 2) heteroleptic complexes which feature non-identical ligands (usually 2 identical monoionic C^N chelates and a third non-identical chelate). Homoleptic complexes can exist as two isomers, meridional (*mer*) and facial (*fac*).

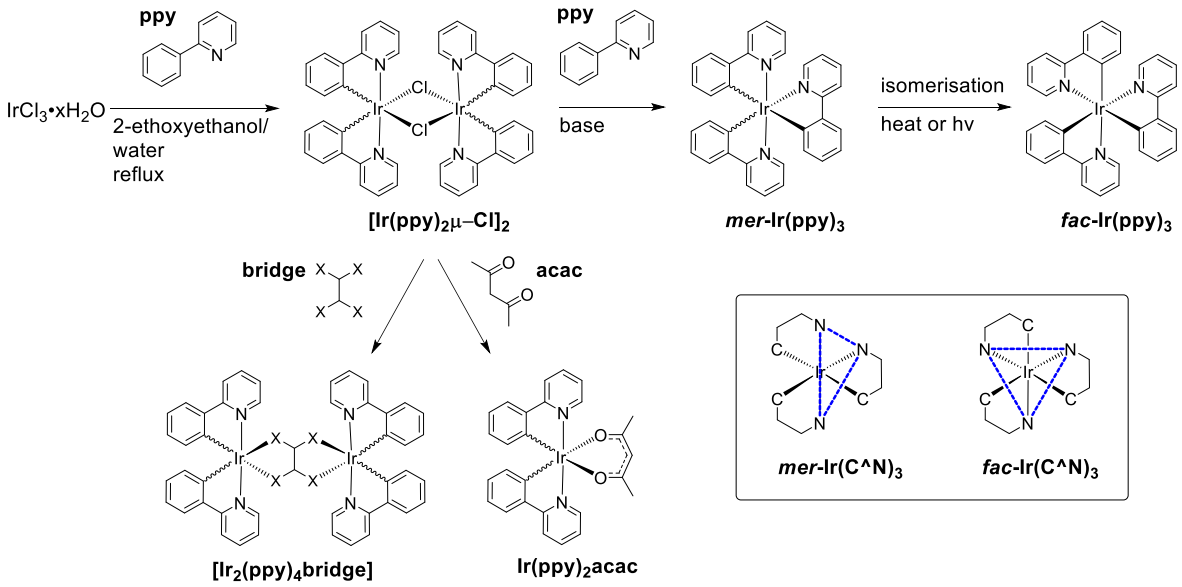

Figure 1.6: Scheme for the synthesis of homo- and heteroleptic complexes from $[Ir(ppy)_2\mu–Cl]_2$. (Inset) representations of *fac* and *mer* homoleptic complexes.

The classic synthetic scheme for obtaining *fac*-$Ir(ppy)_3$ from $IrCl_3•xH_2O$ features both homo- and heteroleptic complexes and also *fac* and *mer* isomers (Figure 1.6). Refluxing ppy with $IrCl_3•xH_2O$ in a mixture of 2-ethoxyethanol and water via Watts procedure[38] (a modification of Nonoyama's 1974 protocol[39]) yields the heteroleptic bis(μ–Cl)-bridged dimer $[Ir(ppy)_2\mu–Cl]_2$. Bis(μ–Cl) dimers exhibit distorted octahedral geometries about the Ir centers. A single isomer is obtained exclusively: this is the meridional (*mer*) isomer featuring the nitrogen atoms of the peripheral cyclometallating ligands coordinated *trans* to each other and axial with respect to the plane of the bridging chloride ligands. This is because the cyclometallating carbon atoms exert the strongest *trans* influence, whereas the bridging chloride atoms exert the weakest *trans* influence.[7] The bis(μ–Cl) dimer can be cleaved with a third ligand, such as acetylacetone (acac), or a bridging ligand to obtain a heteroleptic mono- or dinuclear iridium complex, respectively, for which the *mer* regiochemistry of the bis(μ–Cl) dimer is usually retained (e.g. $Ir(ppy)_2$acac and $[Ir_2(ppy)_4$bridge] in Figure 1.6).[7,40,41] If the third ligand is ppy the homoleptic complex *mer*-$Ir(ppy)_3$ is obtained as the kinetic product after substitution of the bridging chloride ligands. The *mer* isomer can be converted into the more thermodynamically stable facial isomer *fac*-$Ir(ppy)_3$ via thermal or photochemical means.[42,43] Due to the unfavourable *trans* disposition of Ir–C bonds in *mer* homoleptic complexes, their emission tends to be broader and red shifted compared to their *fac* analogues with lower luminescence efficiency due to larger values of k_{nr}.[42]

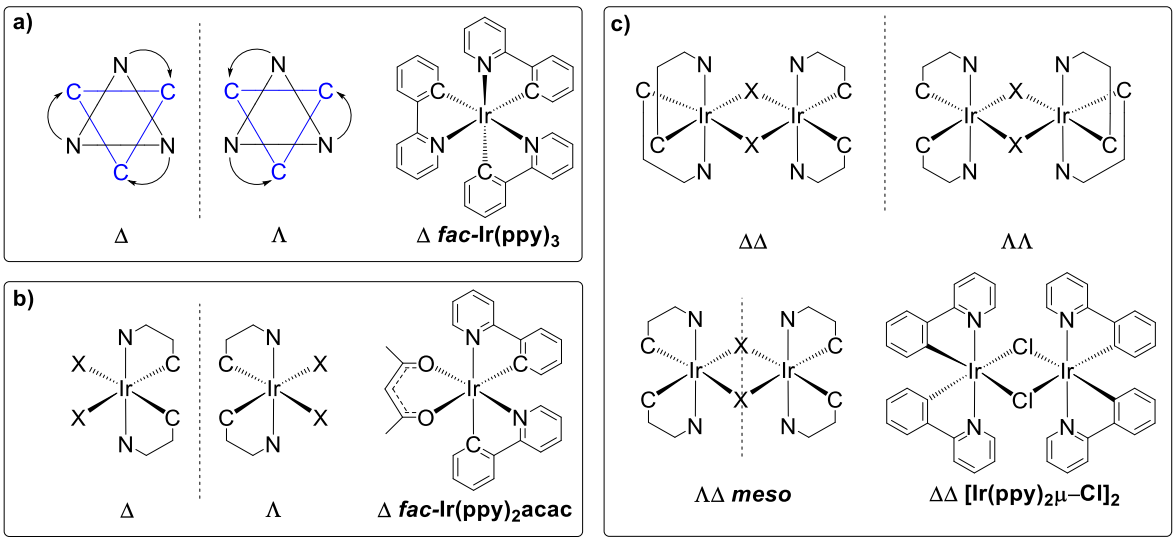

Figure 1.7: a) Representations of Δ and Λ enantiomers in a homoleptic monoiridium complex. b) Representations of Δ and Λ enantiomers in a heteroleptic monoiridium complex. c) Representations of (ΔΔ/ ΛΛ) *rac* and (ΛΔ) *meso* diastereomers in a diiridium complex. Dashed lines are mirror planes.

Octahedral centres such as those found in Ir(III) complexes are chiral when coordinated to chelating ligands. Consequently, cyclometallated monoiridium complexes are usually isolated and studied as racemic mixtures of Λ and Δ enantiomers.[44,45] This is justified considering that enantiomers display identical photophysical properties other than their rotation of plane polarised light.[46] Diiridium complexes such as those of the general formula [Ir_2(ppy)$_4$bridge] (Figure 1.6) feature two such centres. Therefore, mixtures of diastereoisomers (diastereomers) are possible. Provided that each Ir centre has the same coordination environment (as is the case for the complexes reviewed here) two diastereomers are potentially formed: a *meso* ΛΔ form featuring an internal mirror plane, and a racemic pair of enantiomers (the *rac* ΛΛ/ ΔΔ form). Mixtures of diastereomers are common for diiridium complexes featuring Ir---Ir distances greater than *ca.* 5 Å,[47–53] whereas shorter Ir---Ir distances (< 4 Å) tend to favour the *rac* form due to steric constraints.[54–66] Unlike enantiomers, diastereomers have different physical properties and so their photophysical characteristics are potentially significantly different. The Λ and Δ enantiomers of homoleptic and heteroleptic monoiridium complexes are represented in Figure 1.7, along with the *meso* ΛΔ and *rac* ΛΛ/ ΔΔ diastereomers encountered for cyclometallated diiridium complexes.

The excited states of Ir(III) complexes

Ir(III) has a d^6 configuration which commonly favours the formation of complexes of an octahedral geometry, as previously mentioned. Being a 3rd row transition metal in the +3 oxidation state Ir exhibits a large ligand field splitting[67] even when coordinated to quite weak-field ligands, and so the low-spin configuration is adopted (Figure 1.8). Consideration of both the metal orbitals and the

orbitals of conjugated ligands such as ppy leads to the molecular orbital diagram displayed in Figure 1.8. Although the orbitals span the entire molecule, they can be assigned as either mainly metal (M) or ligand (L) based. Excited states can, therefore, be described based on the different types of transition that lead to their formation.

1) Metal-centred (MC)
2) Metal-to-ligand charge transfer (MLCT)
3) Ligand-centred (LC)
4) Ligand-to-metal charge transfer (LMCT)

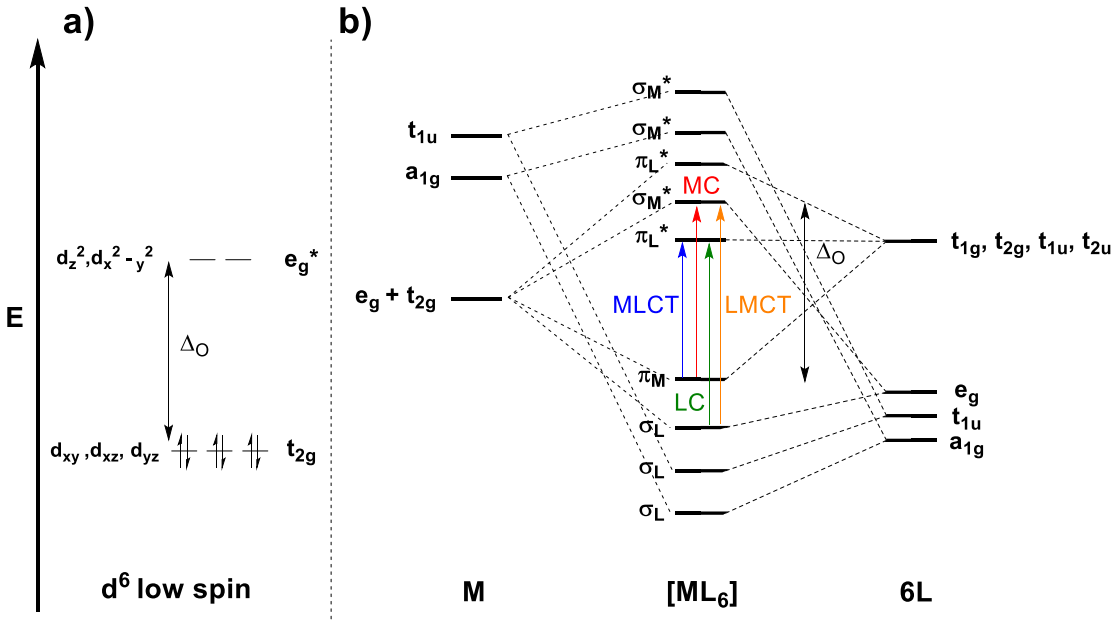

Figure 1.8: a) Low-spin configuration for a d^6 octahedrally-coordinated metal such as Ir^{3+}. b) Generalised molecular orbital diagram for an octahedral metal complex ML_6.

The lowest energy excited state for an Ir(III) complex often comprises an admixture of states with varying contributions.[17] In this part of the review the most relevant states will be discussed. Some key examples that highlight how the relative energies of such states can heavily influence the photophysical properties of the complexes will follow.

Metal-centred (MC)

MC states are formed due to transitions from metal d orbitals to metal d* orbitals. As there is no change in orbital parity, such transitions have comparatively low extinction coefficients (ε) for octahedral complexes, being formally forbidden by the Laporte selection rule. However, this can be relaxed by SOC or vibronic coupling. Population of these states involves population of orbitals that are antibonding with respect to the M–L bonds and so they are often significantly structurally

distorted compared to the ground state geometry. Therefore, they often provide efficient radiationless pathways to the ground state and tend to be non-emissive.[32] Moving down a group in the periodic table the crystal field splitting parameter (Δ_O) increases as d orbitals become more diffuse and so for 2nd and 3rd row transition metals with conjugated ligands MC states become less likely to constitute the lowest energy excited states.[68] However, the energy of MC states is still important, particularly in the design of high energy blue emitters for which they can provide efficient thermally accessible quenching pathways (Figure 1.9).[69] Therefore, an energy difference of 0.37 to 0.50 eV (> K_BT) between emitting and quenching states is important to prevent thermal population of the quenching state at room temperature.[67]

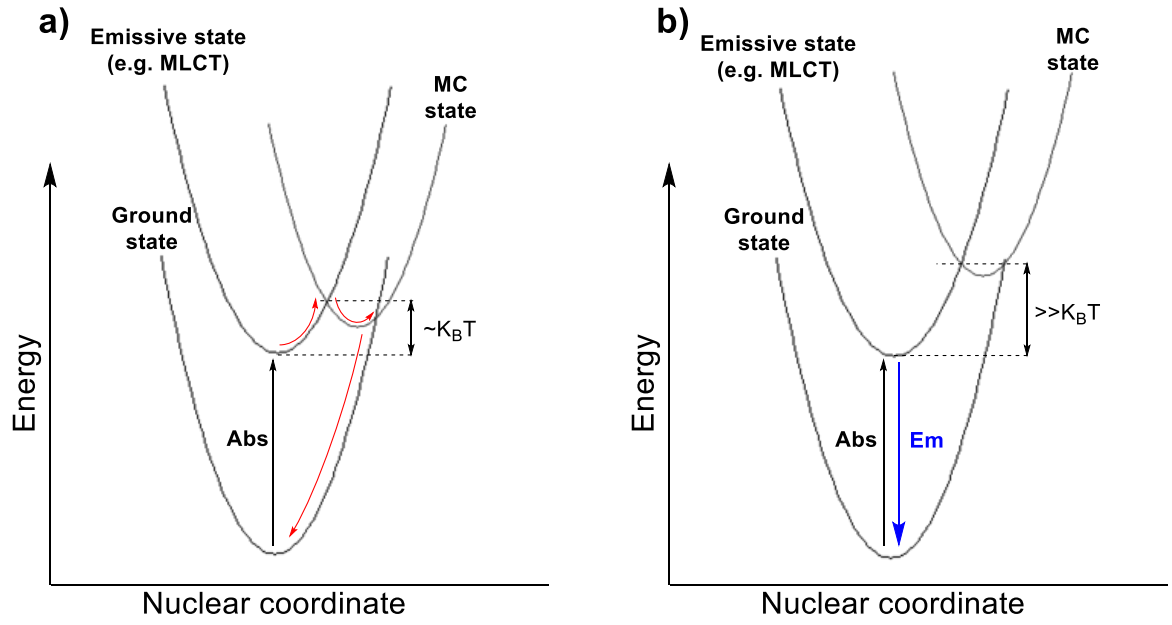

Figure 1.9: a) Harmonic oscillators for a system with a low-lying thermally accessible MC state that quenches emission b) Harmonic oscillators for a highly emissive system with a MC that is not thermally accessible at room temperature. **–** = Absorption, – = emission and – = non-radiative processes.

Metal-to-ligand charge transfer (MLCT)

MLCT states are formed due to promotion of an electron from a metal d orbital to a ligand π* orbital. The metal and ligand are transiently oxidised and reduced, respectively.[68] Due to the charge transfer (CT) nature of such transitions, their spectra are broad and featureless. As there is a change in orbital parity such transitions are formally Laporte allowed and so feature larger extinction coefficients than the d–d* transitions responsible for MC states. MLCT states feature metal character. Therefore, for heavy metals SOC can perturb selection rules making both ^{1}MLCT⟶ ^{3}MLCT and ^{3}MLCT ⟶ S_0 transitions highly probable, leading to efficient PL from such states.[18]

Ligand-centred (LC)

Ligand-centred transitions occur upon transfer of an electron between the π and π* orbitals localised on a ligand. Provided the ligand is not heavily structurally distorted upon coordination to the metal, the spectra for such transitions resemble those for the free ligand.[68] Emission from LC states tends to feature a well resolved vibronic fine structure and is sharper than emission from MLCT states. Metal contribution is absent from LC states making SOC effects weak.[68] The spin selection rule forbidding the ^{3}LC $\rightarrow$ S_0 transition is therefore hardly perturbed, resulting in lower k_r values for emission from ^{3}LC states compared to ^{3}MLCT states, which leads to longer τ and lower Φ_{PL}.[67,70] Interligand charge transfer states (ILCT) are similar to LC states. ILCT states are possible for heteroleptic complexes and constitute electron transfer between the π and π* orbitals of different ligands. As for LC transitions, weak SOC effects reduce the likelihood of the formally forbidden ^{3}ILCT $\rightarrow$ S_0 transition.[71] However, in contrast to LC states, emission from ILCT states tends to show less vibronic features due to their charge transfer character.

Ligand-to-metal charge transfer (LMCT)

LMCT transitions arise from electron transfer from a ligand π orbital to a vacant d orbital. Therefore, they are most probable for complexes with highly electron-deficient metals such as early transition metals in high oxidation states and are generally not relevant for Ir(III) complexes.[68]

Representative Ir(III) complexes

The following five monoiridium complexes have been selected to illustrate how structural features can influence the relative energies of the various excited states, leading to marked effects on their photophysical properties.

fac-Ir(ppy)$_3$

This complex emits in the green region of the spectrum with λ_{max} = 519 nm in DCM.[29] The emission originates from a state which is primarily of ^{3}MLCT character due to the higher energy of the ^{3}LC state (ppy phosphorescence λ_{max} = 460 nm).[18] Due to the strong field cyclometallating ligands the ^{3}MC state is thermally inaccessible at temperatures of up to at least 398 K.[69] As a consequence, at room temperature *fac*-Ir(ppy)$_3$ displays a relatively broad and featureless emission spectrum (Figure 1.10) with a near-unity PLQY (90 ± 5% in DCM,[29] 97 ± 3% in toluene[69], 96 ± 4% in poly(methyl methacrylate) (PMMA)[29]) and a comparatively short τ (1.6 μs in DCM, 1.4 μs in PMMA).[69]

Density functional theory (DFT) calculations (Figure 1.10) are in good agreement with the assigned MLCT character: they predict that the highest occupied molecular orbital (HOMO) is primarily

localised on the Ir centre, with significant contribution from the cyclometallating phenyl groups, while the lowest unoccupied molecular orbital (LUMO) is primarily localised on the pyridyl moieties.[42,67] This is typical for cyclometallated Ir complexes based on ppy ligands.[72–74] As the frontier molecular orbitals are spatially separated, their energies can be varied relatively independently which enables colour tuning.[75,76]

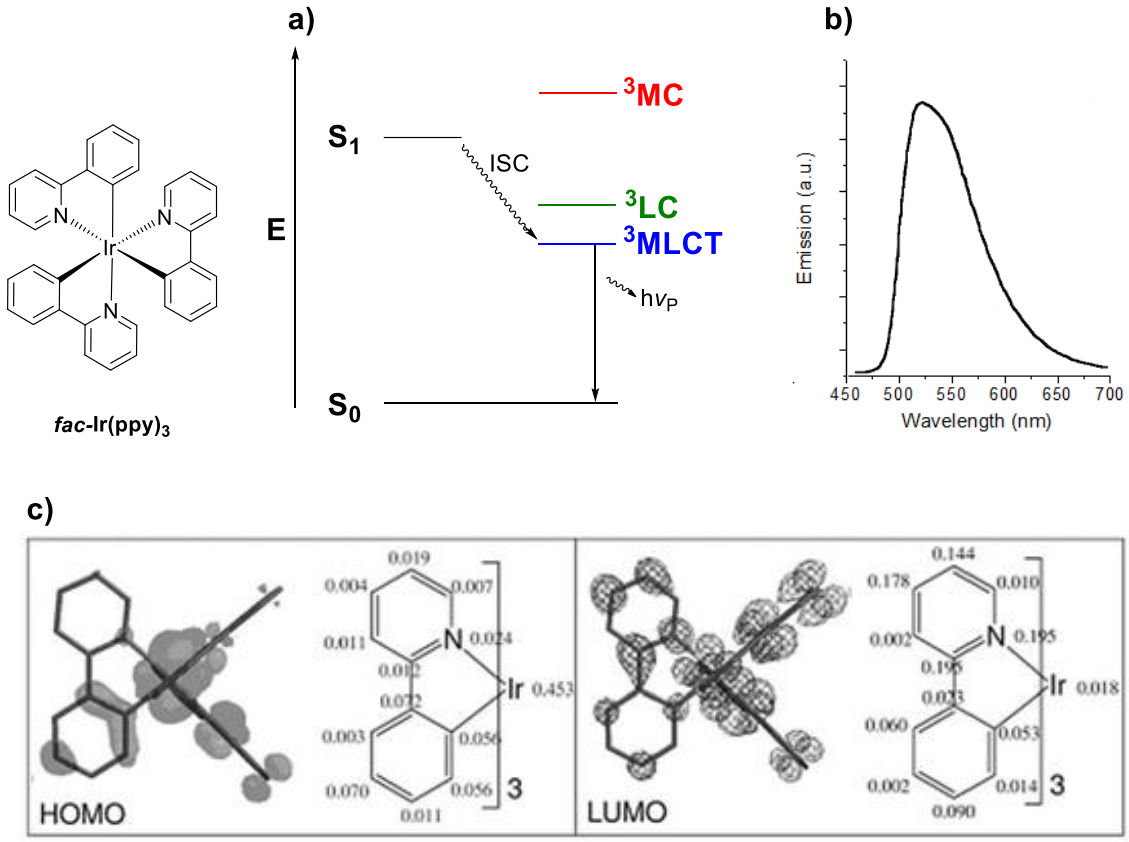

Figure 1.10: Structure of *fac*-Ir(ppy)$_3$ with a) a simplified Jablonksi diagram illustrating the nature of the lowest energy excited state, b) an emission spectrum recorded in DCM at 300 K and c) molecular orbital diagrams showing the HOMO and LUMO distribution. Figure adapted from references 29 and 67 with permission from the American Chemical Society copyright 2010 and Wiley VCH copyright 2008.

Ir(btp)$_2$acac

This heteroleptic complex is a red emitter with λ_{max} = 612 nm in 2-MeTHF.[37] Unlike *fac*-Ir(ppy)$_3$, for Ir(btp)$_2$acac the HOMO is primarily localised on the highly conjugated and electron rich benzothiophene units[18] and consequently the lowest energy excited state is primarily of ^{3}LC character (Figure 1.11). Due to this lower metal character in the excited state, the emission of Ir(btp)$_2$acac has more defined vibronic character and the complex has a lower ambient temperature PLQY (26 ± 20% in 2-MeTHF[77]) and longer τ (5.8 µs in 2-MeTHF).[37]

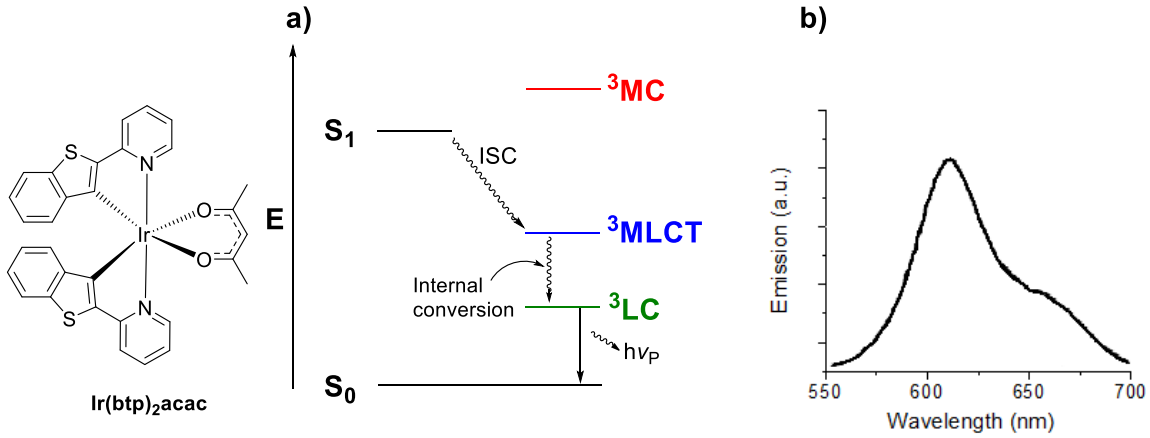

Figure 1.11: Structure of $Ir(btp)_2acac$ with a) a simplified Jablonksi diagram illustrating the nature of the lowest energy excited state and b) an emission spectrum recorded in 2-MeTHF at room temperature. Figure adapted from reference 37 with permission from the American Chemical Society copyright 2001.

FIrpic

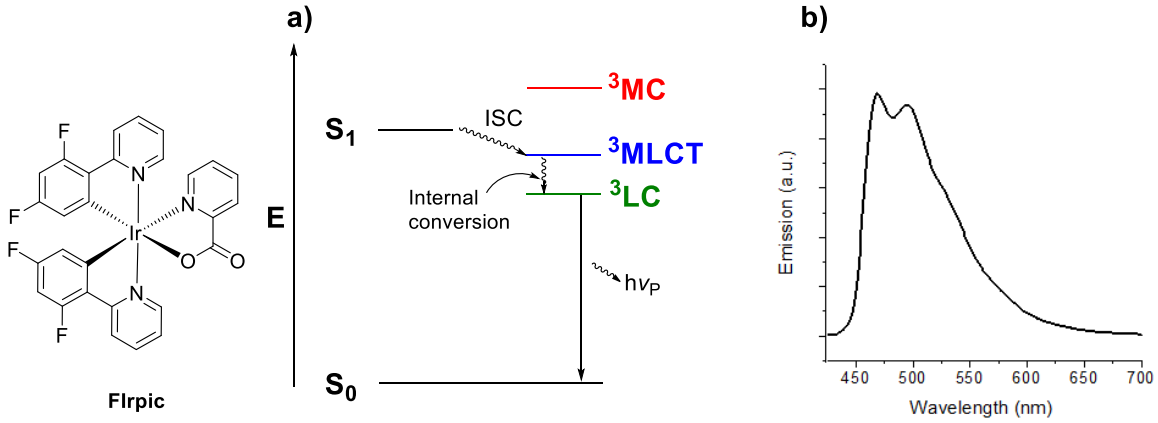

Figure 1.12: Structure of FIrpic with a) a simplified Jablonksi diagram illustrating the nature of the lowest energy excited state and b) an emission spectrum recorded in DCM at room temperature.[†]

FIrpic is the archetypal sky-blue phosphor, with λ_{max} = 468 nm in DCM.[72] In a similar manner to $Ir(btp)_2acac$ it features a lowest energy excited state with a greater ^{3}LC contribution than *fac*-$Ir(ppy)_3$. However, in the case of FIrpic this occurs because fluorination of the ppy cyclometallating ligands (dfppy) and the incorporation of the electron deficient picolinate ancillary ligand destabilises the ^{3}MLCT state, blue shifting the emission while increasing ^{3}LC character (Figure 1.12).[18] FIrpic therefore displays an emission spectrum with a well resolved vibronic progression. The PLQYs at ambient temperature are high (83 ± 10% in DCM, 84 ± 10% in THF, 89 ± 10% in PMMA), while the reported τ values are marginally longer than for *fac*-$Ir(ppy)_3$ (1.9 µs in DCM, 1.8 µs in THF,

[†] This spectrum was measured at Durham University chemistry department by Dr Yu-Ting Hsu.

1.7 µs in PMMA).[78] This is due to the lower ^{3}MLCT character of the excited state and so lower k_r ($5.2 \times 10^5\ s^{-1}$ for FIrpic vs. $6.9 \times 10^5\ s^{-1}$ for *fac*-Ir(ppy)$_3$, both in PMMA).[29,78]

fac-Ir(ppz)$_3$

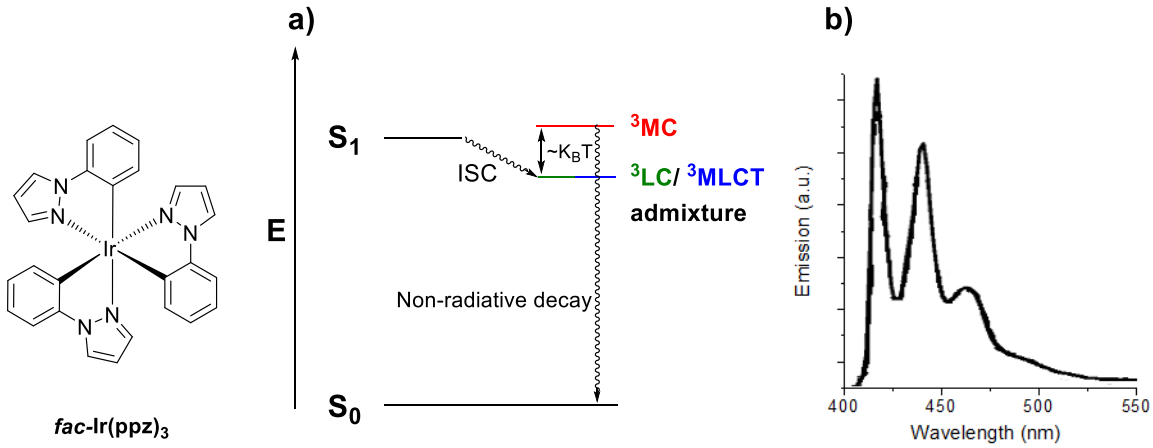

Figure 1.13: Structure of *fac*-Ir(ppz)$_3$ with a) a simplified Jablonksi diagram illustrating the nature of the lowest energy excited state and b) an emission spectrum recorded in 2-MeTHF at 77 K. Figure adapted from reference 42 with permission from the American Chemical Society copyright 2003.

Fac-Ir(ppz)$_3$ is an analogue of *fac*-Ir(ppy)$_3$ for which the LUMO-bearing pyridyl moieties are replaced by more electron rich pyrazole (ppz) ligands.[42] This has the effect of heavily destabilising the emissive ^{3}LC/ ^{3}MLCT state into the deep blue. However, the energy of the ^{3}MC state remains largely unperturbed as its energy is dependent on the coordination environment of the ligand (i.e. C^N: for both ppz and ppy). This synthetic modification therefore narrows the ^{3}MC/ ^{3}MLCT–^{3}LC energy gap to the point where the ^{3}MC state is thermally accessible at ambient temperature, which results in a non-emissive complex (Figures 1.9 and 1.13). However, at 77 K the ^{3}MC state is inaccessible and the complex is emissive in 2-MeTHF with a deep blue/ near UV λ_{max} of 414 nm and τ of 14 µs.[42]

Fac-Ir(pmp)$_3$

Fac-Ir(pmp)$_3$ is a state-of-the-art deep blue phosphor with a room temperature λ_{max} = 418 nm in 2-MeTHF.[21] The cyclometallated carbene C^C: chelate exerts a stronger ligand field splitting than C^N: chelates such as ppz, destabilising the ^{3}MC state so that it is no longer thermally accessible (Figures 1.9 and 1.14). The choice of a pyridoimidazole N-heterocyclic carbene (NHC) is important as it stabilises the LUMO and ensures that the emission is in the deep blue rather than the UV (which is observed for the benzimidazole analogue *fac*-Ir(pmb)$_3$).[69,73] At 295 K *fac*-Ir(pmp)$_3$ has a PLQY of 76 ± 5% in 2-MeTHF and a τ of 1.2 ± 0.1 µs. Due to the high ligand field strength, the corresponding

mer isomer is also highly emissive, which is uncommon in Ir complexes due to unfavourable *trans* Ir–C cyclometallated bonds.[42]

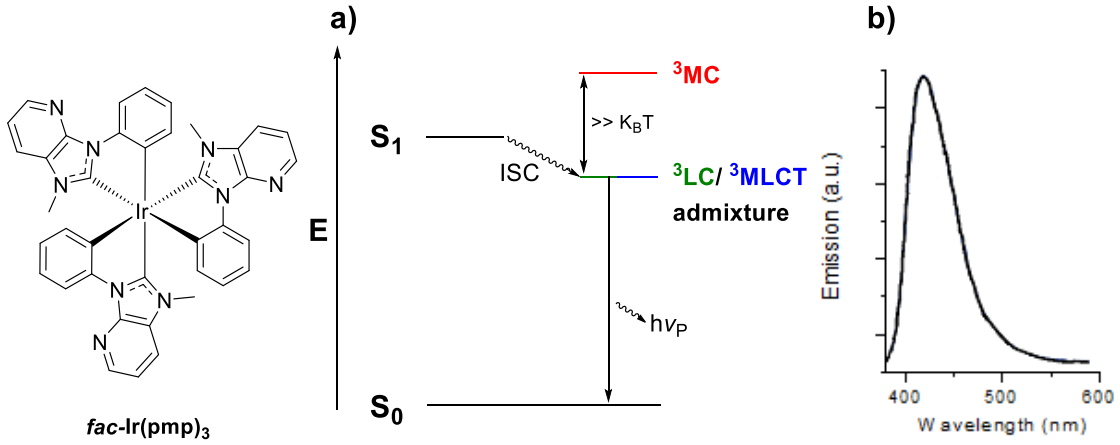

Figure 1.14: Structure of *fac*-Ir(pmp)$_3$ with a) a simplified Jablonksi diagram illustrating the nature of the lowest energy excited state and b) an emission spectrum recorded in 2-MeTHF at 295 K. Figure adapted from reference 21 with permission from Springer Nature copyright 2016.

Dinuclear Ir(III) complexes

The study of mononuclear Ir(III) complexes has gathered a large amount of attention since the early 2000s, with thousands of articles being published as highlighted in Figure 1.15. This has been heavily driven by display and lighting applications, particularly OLEDs.[11] A wide range of structural variation has been explored and complexes with high luminescent efficiencies have been reported across the visible spectrum from blue to red.[21–23] However, the field appears to have saturated and the number of publications per year is declining, perhaps due to persistent problems such as the difficulty in obtaining stable blue phosphorescent OLEDs,[79] and the development of new competing technologies such as thermally activated delayed fluorescence (TADF).[80]

In contrast, dinuclear Ir(III) systems have received comparatively little attention (Figure 1.15). This is likely related to 1) the fact that their molecular weights are too high to allow application in vacuum processed OLEDs, necessitating solution processing, and 2) the historical observation that diiridium complexes display poorer photophysical properties than their mononuclear analogues. However, recent work indicates that poor luminescence efficiencies in diiridium complexes are more a consequence of historically poor molecular design than an intrinsic property. The incorporation of a bridging ligand and a second Ir centre adds an extra dimension to the design of heavy metal phosphors. In addition to the clear opportunity to explore new structural chemistry involving the bridging ligand,[81] diiridium complexes present some prospective advantageous properties, such as an increased SOC effect due to the presence of two metal centres and easier access to efficient red/near-Ir emitters due to increased conjugation through rigid bridging

units.[49,82–84] Therefore, as a greater number of bridging motifs have been investigated and their structure-property relationships have been elucidated, research into luminescent diiridium systems has expanded. In this section an overview of recent progress in luminescent diiridium complexes is presented, categorised by the different bridging units that have been explored.

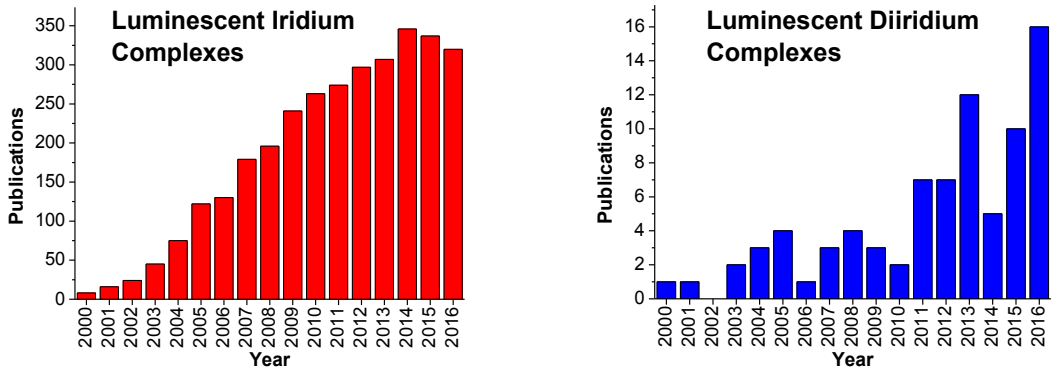

Figure 1.15: Histograms to show the number of Web of Science hits for (left) "iridium and luminescent/ phosphorescent" and (right) "diiridium/ dinuclear iridium and luminescent/ phosphorescent" for the years 2000–2016. Search date 30/10/2017.

Bis(μ–Cl) and bis(μ–NCO)-type bridges

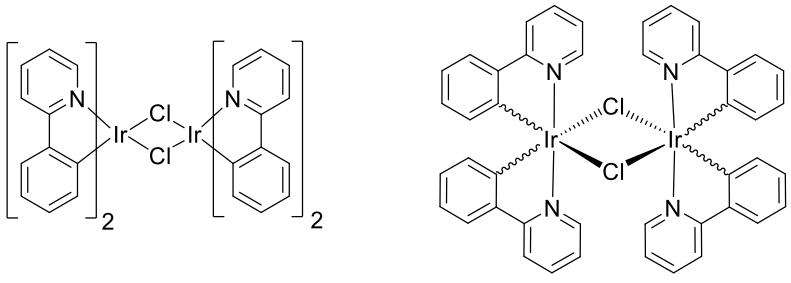

$[Ir(ppy)_2\mu–Cl]_2$

Figure 1.16: Two- and three-dimensional representations of the molecular structure of $[Ir(ppy)_2\mu–Cl]_2$.

Bis(μ–Cl) dimers such as the archetype $[Ir(ppy)_2\mu–Cl]_2$ (Figure 1.16) are the simplest and most commonly encountered cyclometallated diiridium complexes. They were first reported by Nonoyama[39] and are typically synthesised from the appropriate cyclometallating ligand and $IrCl_3•xH_2O$ by Watts' modified procedure.[38] The mechanism of Ir–C bond formation can be described as electrophilic aromatic substitution with respect to the aryl group, or dissociative ligand exchange with respect to the 18 e^- $IrCl_3•xH_2O$ complex.[85] They can also be synthesised via the 16 e^- Ir(I) precursor $[Ir(COD)\mu–Cl]_2$. In this case the Ir–C bond is formed through oxidative addition[85] which allows faster reaction times and softer reaction conditions,[40] making this route more suitable

for obtaining complexes with heavily functionalised ligands.[14,86,87] Due to steric considerations, for bis(μ–Cl) dimers only the *rac* diastereomer is generated, which minimises clash between ligands on the adjacent Ir atoms.[20,81]

$[Ir(ppy)_2\mu–Cl]_2$ is weakly emissive in room temperature DCM solution with a λ_{max} = 520 nm and PLQY = 0.1%.[66] Such a low quantum yield is typical of most bis(μ–Cl) dimers. This is due to their high k_{nr} values (e.g. for $[Ir(ppy)_2Cl]_2$ k_{nr} = 8 × 10^6 s^{-1}) and their comparatively low k_r values, (e.g. for $[Ir(ppy)_2Cl]_2$ k_r = 0.4 × 10^5 s^{-1}).[66] Such poor photophysical properties are likely a consequence of the weak ligand field strength of the bridging chloride ligands (which enhances k_{nr}).[20] Calculations also often predict high HOMO contributions from the bridging chloride ligands,[66] which is expected to decrease the MLCT character of the excited state (decreasing k_r).

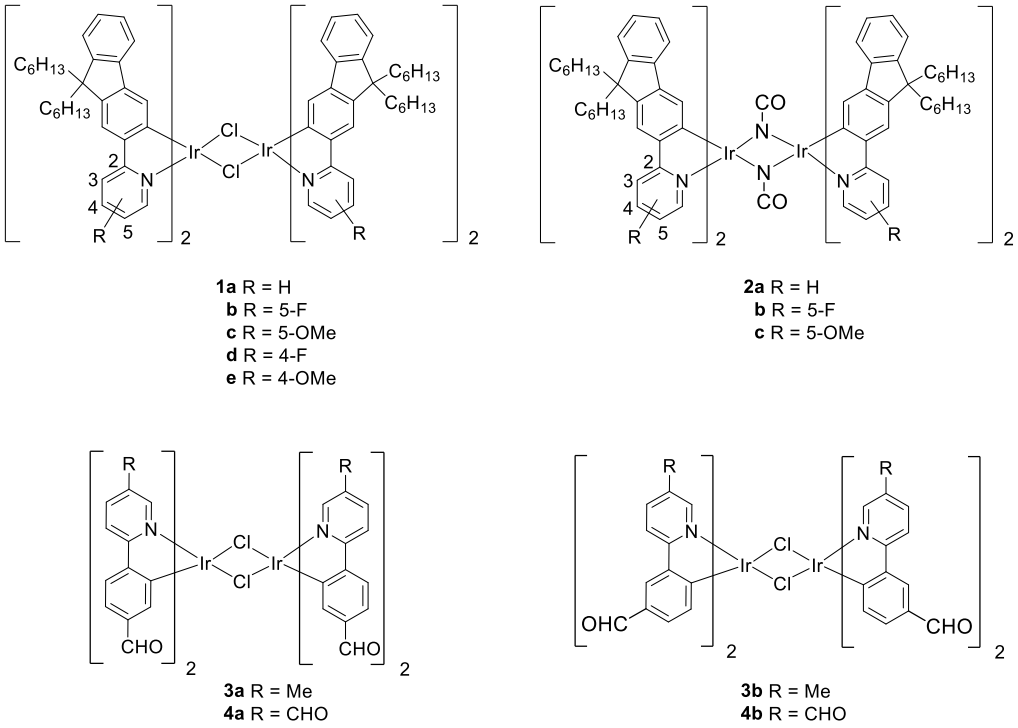

Figure 1.17: Molecular structures of bis(μ–Cl) and bis(μ-NCO)-bridged complexes.

However, there are some notable exceptions (Figure 1.17). Orange-emitting (λ_{max} *ca.* 545 nm) bis(μ–Cl) (**1a**–**e**) and bis(μ-NCO) (**2a–c**) dimers have been reported with modest PLQYs (21–43%) comparable to those of analogous homoleptic *fac* complexes (PLQYs of 30–43%).[55,56] The orange emission is afforded by the increased conjugation length of the 2-fluorenylpyridine ligands. The atypical PLQYs are likely related to: (i) increased molecular rigidity, evident from small Stokes shifts (e.g. 0.03 eV for **1a** and **2a** vs. 0.16 eV for $[Ir(ppy)_2\mu–Cl]_2$), (ii) decreased quenching via MC states due to the red shifted emission, and (iii) the negligible bridge HOMO character predicted by DFT,[56] which is a consequence of the red shift through HOMO stabilisation. Furthermore, the emission

spectra of both **1a** and **2a** display distinct vibronic progressions with shoulders at *ca.* 590 nm. This is indicative of substantial ^{3}LC character, as expected upon shifting towards the red.[18]

The introduction of formyl groups was also found to increase the quantum yields of bis(μ–Cl) systems (**3** and **4**) by Zysman-Colman et al.[66] The highest PLQYs were reported for **4a** (15.7% in DCM, 14.7% in CBP/PBD) and **4b** (0.9% in DCM, 35.6% in CBP/PBD) which feature the largest number of formyl groups. Their improved emission efficiencies, as well as being related to the red shift in emission, were suggested to originate from rigidifying hydrogen bonding interactions featuring the formyl substituents. In conclusion, it appears that the most productive design tactics for increasing the luminescence efficiency of bis(μ–Cl) and bis(μ-NCO) dimers are to engineer complexes with lower k_{nr} through red shifting emission (to lower MC character) and incorporating cyclometallating ligands which rigidify them.

N^N-type bridges

Bridges which coordinate via N^N chelates are isoelectronic with 2,2'-bipyridine, a classic neutral ligand that is commonly encountered in coordination chemistry.[1] A diverse range of charged diiridium(III) complexes bridged by N^N coordinating bridges have been reported, many of which are highlighted in Figure 1.18.

In 2003, Plummer and De Cola et al. reported red emitting cationic dinuclear iridium(III) complexes incorporating 2,2'-bipyridine chelates joined by oligo-*p*-phenylene linkers as the bridging units (**5** and **6**).[88] The complexes were synthesized via on-complex Suzuki couplings and no diastereomer separation was mentioned. The highest solution PLQY of 17.5% was reported for complex **6** (in acetonitrile), which features the longer linker. Time resolved transient spectroscopy indicates that the excited states are localized primarily on the bridge with high ^{3}LC character, as expected from the highly conjugated nature of the bridging units. In a follow-up study, an OLED incorporating **6** was prepared, which demonstrated a low external quantum efficiency (EQE)[‡] of 0.1%.[89]

Auffrant et al. reported the diiridium complex **7**, for which all stereoisomers were separated via resolution with the chiral anion Δ-tris(tetrachloro-1,2-benzenediolato)phosphate(V) (Δ-TRISPHAT).[46] No significant differences were observed in the steady state photophysical data for the stereoisomers, which emit in the red with λ_{max} = 654 nm and a PLQY of *ca.* 0.6%. X-ray crystal structure data indicates that flexibility of the bridging ligand may provide a non-radiative pathway responsible for such weak luminescence.

[‡] EQE (External quantum efficiency) = $\frac{Number\ of\ photons\ emitted\ by\ an\ OLED\ device}{Number\ of\ electrons\ injected\ into\ an\ OLED\ device}$

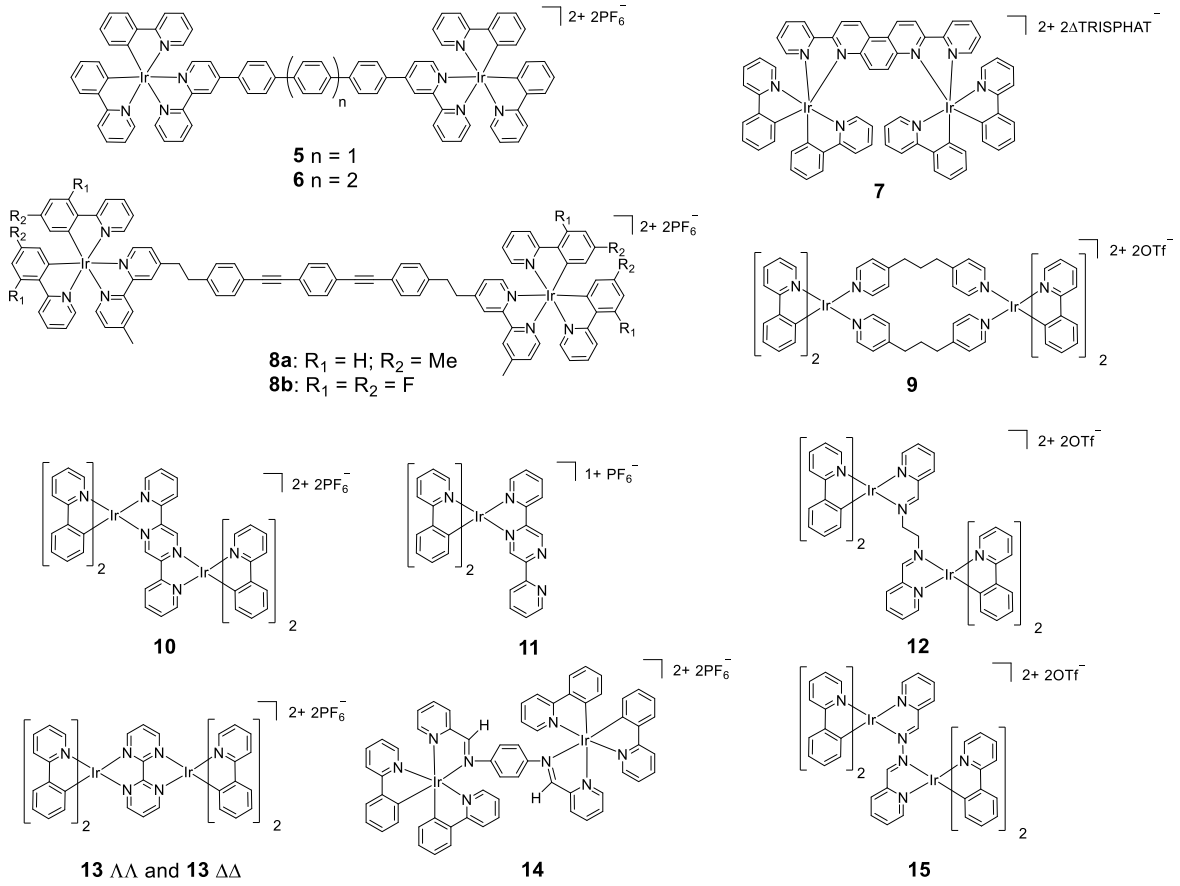

Figure 1.18: Molecular structures of charged complexes featuring N^N ligands.

Complexes **8a** and **8b** feature oligo(phenyleneethylene)-functionalised bridges that break conjugation between their iridium centres. They emit in acetonitrile with λ_{max} = 588 and 521 nm, and low PLQYs of 0.9 and 0.7%, respectively, due to notably low radiative rates (k_r *ca.* 1 × 10^4 s^{-1}). The data is rationalised by time dependent density functional theory (TD-DFT), which predicts the lowest energy excited state to be primarily of ^{3}LC character on the bridging unit, with minimal metal character.

Chandrasekhar and co-workers have studied numerous diiridium complexes featuring both non-conjugated (**9** and **12**) and conjugated (**15**) N^N bridging ligands.[47,90] No separation of diastereomers was mentioned. Complex **9** is luminescent with λ_{max} = 510 nm (shoulder at 480 nm) and a PLQY of 48% (in acetonitrile). Its emission spectrum features resolved vibronic features, indicative of high ^{3}LC character. No Ir---Ir coupling is observed in electrochemistry due to the non-conjugated bridge and the large distance between the metal centres. Complex **15** is also highly luminescent (PLQY = 51%), while its emission is red shifted to λ_{max} = 521 nm due to the presence of conjugation between the Ir centres. Broad and featureless emission was suggested to originate from an admixed ^{3}MLCT/ ^{3}ILCT excited state, as indicated by DFT calculations. Coupling is also seen between the two Ir centres in cyclic voltammetry (CV) with the anodic peak splitting (ΔE^{ox}) of 190

mV. Interestingly, and in contrast to **9**, the non-conjugated complex **12** displays a comparatively low solution PLQY of 12%, which may tentatively be related to bridge flexibility.

Zysman-Colman et al. investigated a complex bridged by a 2,5-dipyridylpyrazine ligand (**10**) alongside its mononuclear analogue (**11**).[47] The diiridium complex **10** was studied as a diastereomeric mixture, for which computational and electronic studies indicated electronic communication between the metal centres. Complex **10** is non-emissive at room temperature, in contrast to **11** which displays weak red emission with λ_{max} = 710 nm and a PLQY of = 0.9 ± 0.15% (in acetonitrile). Coordination of the second Ir atom in **10** makes the bridge a stronger electron acceptor. This reduces the reduction potential by 0.5 V, shifting the emission energy deeper into the red and quenching room temperature PL in accordance with the band gap law.[§] However, **10** is emissive at 77 K in 2-MeTHF with λ_{max} = 715 nm. The authors attributed this to reduction in non-radiative decay due to i) lower thermal energy and ii) a rigidochromic shift of emission to higher energies (compared to room temperature).

The enantiomerically pure diiridium complexes **10** ΛΛ and **10** ΔΔ, bridged by a 2,2'-bipyrimidine ligand, were recently reported by Ye et al.[91] They were prepared from enantiopure bis(μ–Cl) dimers which were obtained utilising *L*- or *D*-proline ligands as chiral auxiliaries. The methodology gives the ΛΛ and ΔΔ isomers in 99% diastereomeric excess (de). As bis(μ–Cl) dimers exist exclusively as chiral diastereomers, the achiral *meso* form was not obtained. No in-depth photophysical study was reported. This study highlights a useful procedure for synthesising diiridium complexes while avoiding the formation of diastereomeric mixtures. The strategy can also be further extended to the synthesis of larger enantiopure multimetallic Ir(III) systems.[92,93]

The Schiff base complex **11** is structurally similar to **12** and features a highly flexible N^N bridging ligand that renders it non-emissive in solution.[94] In a neat film, the non-radiative decay pathway facilitated by bridge motion is shut off, resulting in red emission (λ_{max} 644 nm and PLQY = 37 ± 5%). This phenomenon was referred to as aggregation-induced phosphorescent emission (AIPE).

In summary, N^N chelating bridges have received a comparably large amount of attention. Whereas most of the complexes reviewed here are poorly luminescent, they are useful for illustrating potential pitfalls encountered in the design of diiridium systems. Complexes **5**, **6** and **8** highlight that highly conjugated bridges can lead to excited states of predominantly ^{3}LC character, which

[§] Lower energy excited states are more likely to be able to vibronically couple to the ground state, which reduces the likelihood of radiative decay.[32] Therefore, for a given system the PLQY tends to drop with emission energy which makes it a challenge to design efficient red/ near-Ir emitters.[4]

quenches emission. Complexes **7**, **12** and **14** indicate that highly flexible bridges should be avoided if high solution PLQYs are to be targeted.

π-Bonded bridges

Lalinde et al. recently investigated a series of complexes bridged by alkynyl ligands (**16a–e**) (Figure 1.19).[95] For the majority of the analogues only the *rac* diastereomer was observed, although a mixture was observed for **16e**, which features $SiMe_3$ groups. The stability of the complexes was noted to be particularly poor, with them being unstable in solution (DCM, $CHCl_3$ and acetone), particularly in chlorinated solvents. CV studies indicate a degree of electronic communication between the Ir centres, with half wave oxidation potential differences ($\Delta E_{1/2}^{ox}$) of 260–410 mV, in agreement with DFT which predicts significant HOMO localisation on the bridging ligands. All the analogues are poorly emissive with λ_{max} in the range of 505–545 nm and a maximum PLQY of 2.4%. This was rationalised based on the dynamic behaviour of the complexes in solution, as indicated by variable temperature NMR studies.

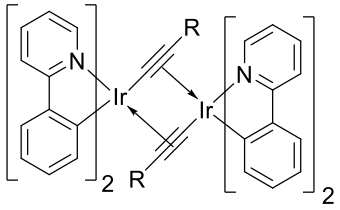

16a R = 4-tol
b R = 4-C_6H_4OMe
c R = 1-Np
d R = *t*-Bu
e R = $SiMe_3$

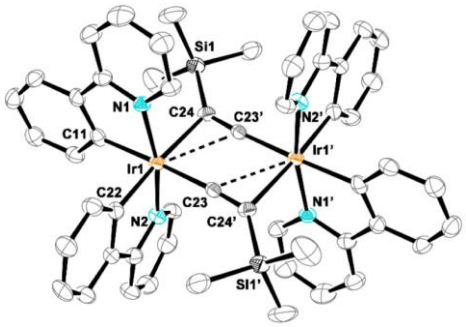

16e

Figure 1.19: (Left) molecular structures of complexes bridged by alkynyl ligands. (Right) X-ray crystal structure of complex *meso* **16e**. Figure adapted from reference 95 with permission from the American Chemical Society copyright 2015.

NHC bridges

Bielawski and co-workers studied complex **17** bridged by an NHC benzobis(imidazolylidene) unit, which was compared to its mononuclear analogue **18** (Figure 1.20).[50] The dinuclear complex was studied as a 1:1 mixture of diastereomers. **17** and **18** each emit at λ_{max} = 497 nm with identical emission profiles and similar PLQYs of 11 and 19%, respectively. These photophysical properties suggest that the two Ir centres in **17** behave independently, with the $Ir(ppy)_2$ fragments being solely responsible for emission. This is also corroborated by electrochemical data (Figure 1.20), which indicates negligible electronic coupling between Ir centres. The relatively weak luminescence of the

complexes is likely related to the *mer* configuration and the resulting *trans* Ir–C cyclometallated bonds.

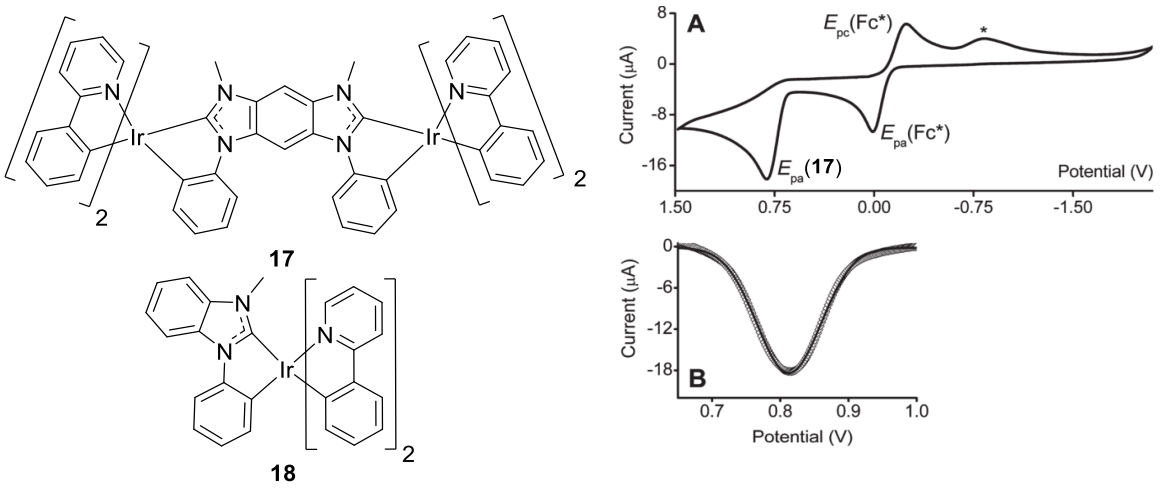

Figure 1.20: (Left) molecular structures of NHC complexes. (Right) cyclic voltammogram (A) and differential pulse voltammogram (B) for complex **17** in DCM with 0.1 M *n*-NBu_4•PF_6, both referenced vs. decamethylferrocene (Fc*). * = Reduction event, cathodic current is positive. Figure adapted from reference 50 with permission from the American Chemical Society copyright 2009.

C^N-type bridges

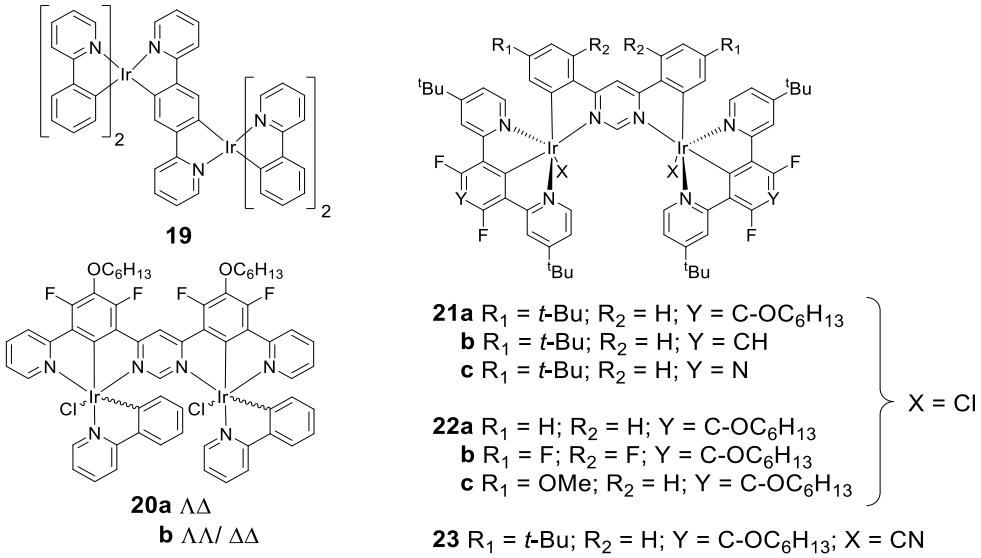

Figure 1.21: Molecular structures of C^N-bridged diiridium complexes.

Tsuboyama et al. investigated complex **19**, which features a doubly cyclometallated bis(pyridyl)benzene bridging ligand (Figure 1.21).[96] The *rac* complex was studied (after isolation in 3% yield following vigorous purification). It is a weak red emitter with λ_{max} = 665 nm, a PLQY of 4% and τ = 2.0 μs (in 2-MeTHF). This is due to the low k_r of 0.2 × 10^5 s^{-1}. A weaker SOC effect compared to *fac*-Ir(ppy)$_3$ is also evident from the lower intensity of the ^{3}MLCT band in the absorption spectrum

of **19** (ε = 100 M^{-1} cm^{-1} vs. 1500 M^{-1} cm^{-1} for *fac*-Ir(ppy)$_3$). The authors suggested that this is related to an excited state that is primarily localised on the bridge (which will be mainly of ^{3}LC character). The *trans* disposition of bridge and peripheral ligand Ir–C bonds may also be responsible for the weak luminescent properties (*trans* Ir–C bonds are absent in the structures of the highly emissive diiridium complexes **20–26** which follow).[49,82–84]

Williams, Kozhevnikov and co-workers reported the diastereomers **20a** and **20b**, featuring a cyclometallated bis-terdentate bridge (Figure 1.21).[82] They were separated via column chromatography and studied individually. In DCM the complexes are red emitters (λ_{max} = 622 nm) with high PLQYs of 65 ± 20% and notably short phosphorescence lifetimes of τ = 730 / 760 ns. Comparison against a mononuclear analogue suggests that the short lifetimes are related to the presence of the second Ir centre. The authors suggested that this leads to enhanced SOC, both in an intrinsic nature due to an augmented heavy atom effect and also potentially due to the lower experimentally observed exchange energies. No theoretical calculations were reported to investigate the distribution of the frontier molecular orbitals. However, the fact that the bridge coordinates the two Ir centres in close proximity while being highly conjugated and ambipolar makes it highly probable that the bridge and both Ir atoms are heavily involved in the excited state, leading to the notably high k_r values (> 8.5 × 10^5 s^{-1}).

Table 1.2 Photophysical properties in degassed DCM for complexes **21**–**23**.

Complex	PL λ_{max} /nm	PLQY/ % (± ≤10%)	τ/ ns	k_r / 10^6 s^{-1}
21a	552, 582sh	94	440	2.14
21b	544, 576sh	100	550	1.82
21c	526, 557sh	100	590	1.69
22a	568, 599	88	570	1.54
22b	570	91	590	1.54
22c	528, 557sh	100	360	2.78
23	517, 547sh	88	590	1.49

A series of non-stereogenic diiridium complexes (**21**–**23**) incorporating tridentate peripheral cyclometallating ligands was subsequently investigated (Figure 1.21). Key photophysical data are reported in Table 1.2. The peripheral (**21a–21c**), bridging (**22a–22c**), and monodentate ancillary (**21a** vs. **23**) ligands were systematically varied, allowing colour tuning from green to yellow/orange (λ_{max} = 517–570 nm). In solution (DCM) the complexes display PLQYs as high as unity, with exceptionally short phosphorescence lifetimes (τ = 360–590 ns) because of high k_r values > 1 × 10^6 s^{-1}. Such favourable photophysical properties can be rationalised by the TD-DFT data, which predict the lowest energy excited states to be mainly ^{3}MLCT involving the bridge. Consequently, both Ir

atoms should be highly involved in the excited state, which is expected to enhance k_r. These complexes demonstrate the best photophysical performances reported to-date for diiridium complexes that emit in their colour range.

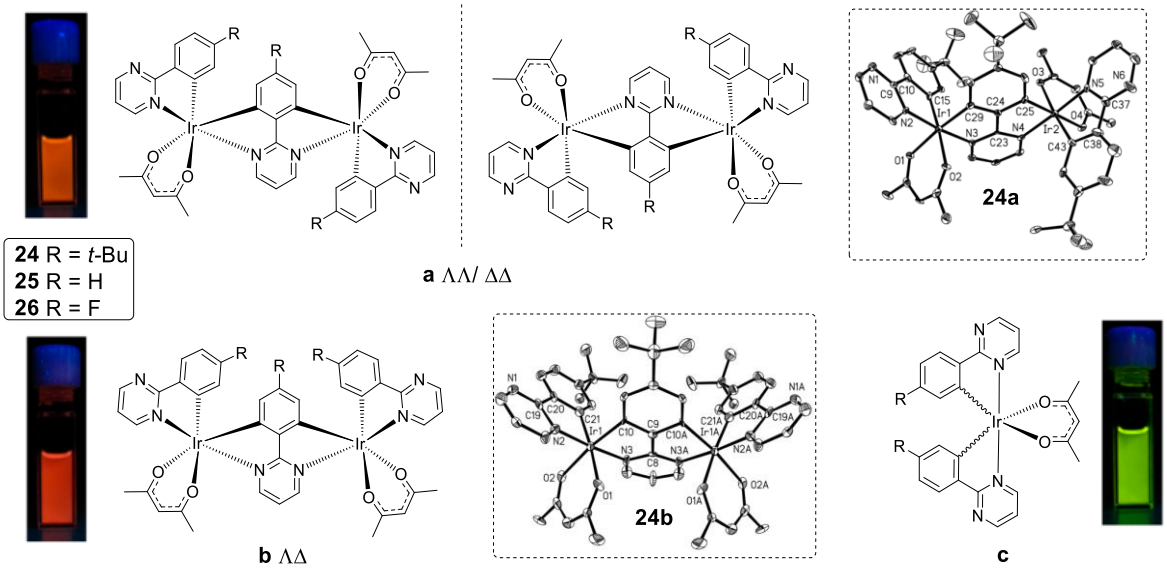

Figure 1.22: Molecular structures of complexes **24**–**26** and X-ray crystal structures of **24a** and **24b**. (Insets) emission from DCM solutions of **24a**–**c** under UV irradiation. Figure adapted from reference 49 with permission from the American Chemical Society copyright 2016.

Zhou and Wong et al. have reported a series of mono- (**24c**, **25c** and **26c**) and dinuclear (**24**–**26a** and **b**) iridium(III) complexes (Figure 1.22).[49,84] The molecular design utilizes the same cyclometallating ligand (a 2-phenylpyrimidine) as both the bridging and peripheral ligands. The diiridium complexes exhibit bright phosphorescence (PLQYs of 36–68%) at wavelengths red-shifted compared to their mononuclear analogues (λ_{max} = 580–607 nm in DCM). They also display short τ values of 180–480 ns. This is likely a consequence of high bridge contribution to the excited states of the dinuclear complexes, which is inferred from DFT calculations that suggest the excited state is mainly ^{3}MLCT involving the bridging ligand. OLEDs with a solution processed emissive layer were also fabricated from the diiridium complexes. The best OLED performance from a diiridium complex to-date was reported, with a maximum EQE of 17.9%.

In conclusion, C^N bridged complexes display advantageous photophysical properties such as high PLQYs and short τ. Within this category, an advantageous non-stereogenic design has also been presented, as has the highest performing OLED based on a dinuclear Ir complex. Consideration of the data reported by Williams and Kozhevnikov, and Zhou and Wong[49,82–84] reveals common molecular design features: rigid and ambipolar heterocyclic bridging ligands that provide a short conjugative pathway between the two iridium centres are an important feature. Such moieties should be incorporated in a manner that ensures the lowest energy excited state is of mixed ^{3}MLCT

and ^{3}LC character involving the bridging ligand. This promotes the involvement of both metal centres in the excited state, taking advantage of the second iridium atom to obtain fast sub-microsecond phosphorescence. A potential disadvantage to the systems reported so far is the incorporation of labile acac/ monodentate ancillary ligands which may reduce stability. For complexes **24**–**26**, a potential replacement is another cyclometallating ligand. However, a downside is that the most synthetically accessible isomer would probably have the *mer* configuration, which would likely reduce luminescence efficiency as reported for complex **19**.[96]

N^O and O^O-type bridges

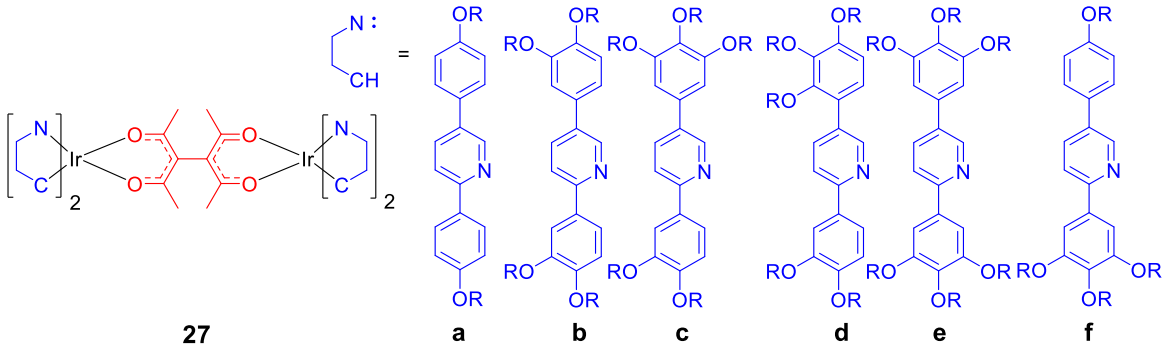

Figure 1.23: Molecular structures of complexes **27a–f**.

Bruce and co-workers reported a series of liquid crystalline diiridium complexes bridged by a 1,1,2,2-tetraacetylethane bridge (**27a–f**) (Figure 1.23).[97] The PL λ_{max} values were in the range of 541–588 nm with PLQYs of 38–58% (in DCM). It was suggested that the high efficiencies may be due to a large contribution of the ppy-based ligands to the excited state. While this helps to minimise non-radiative deactivation due to vibrational modes associated with the bridge, it also lowers the ^{3}MLCT character and lengthens τ to *ca.* 4 μs for all complexes. Mixtures of diastereomers were obtained. In some cases, they were resolved via flash chromatography, whereas in other cases they were studied as diastereomeric mixtures.

Crutchley et al. reported the crystal structure of an oxalato-bridged diiridium complex (**28**) which was inadvertently synthesised during an attempt to crystallise $Ir(ppy)_2$vacac (vacac = allyl acetoacetate) from acetone (Figure 1.24).[98] More recently Sünkel and co-workers reported an oxamidato analogue (**29**) with some photophysical characterisation (Figure 1.24).[53] A mixture of diastereomers was obtained which was not separated. However, the single crystals used for X-ray diffraction contained the *meso* isomer only, although the bonding mode of the bridge could not be unambiguously assigned. Green emission was observed with a PL λ_{max} = 523 nm and a PLQY of 60% (in DCM). The emissive state was assigned as being mainly ^{3}MLCT in nature due to the broad and featureless room temperature emission spectrum.

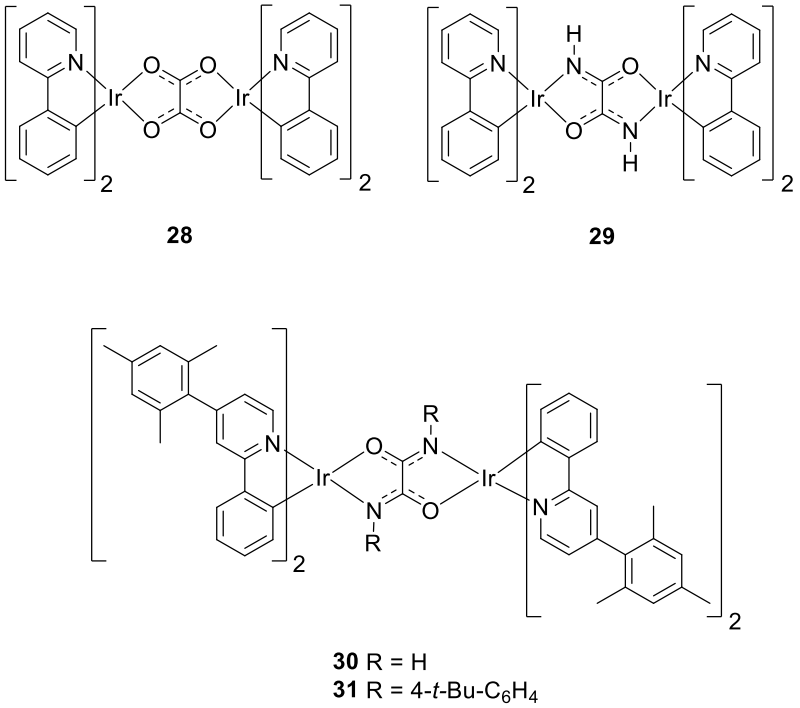

Figure 1.24: Molecular structures of complexes **28–31**.

Following these seminal studies, our group synthesised complexes **30** and **31** (Figure 1.24) and studied them as diastereomeric mixtures.[99] In solution (2-MeTHF), both of the green emitting complexes (λ_{max} **30** = 529 nm, **31** = 522 nm) are highly emissive (PLQY **30** = 73%, **31** = 63%). CV studies indicate stronger electronic communication between the Ir centres of **31** ($\Delta E_{1/2}^{ox}$ of 220 mV vs. 160 mV), which is attributed to the more conjugated bridging unit which features a larger HOMO contribution than for the bridge in **30**. OLEDs with solution processed emitter layers afforded bright green electroluminescence with luminance values as high as > 25,000 cd m^{-2}.

Some bridging ligands analogous to the popular picolinate ancillary ligand found in complexes such as FIrpic (Figure 1.12) have been reported (Figure 1.25).[48,51] Chandrasekhar et al. characterised a diiridium complex bridged by a pyrazine-3,5-dicarboxylate ligand (**32**) (Figure 1.25).[48] CV studies indicate a significant degree of electronic coupling between both iridium centres ($\Delta E_{1/2}^{ox}$ = 270 mV). The diiridium complex emits in the green region with PL λ_{max} = 500 nm and a PLQY of 38% (in DCM). The broad and featureless emission spectrum led to the assignment of the excited state as mainly ^{3}MLCT character. However, the excited state lifetime is rather long for an Ir complex with predominantly ^{3}MLCT emission (10.6 µs).[17,29,100] DFT calculations predict a 95% contribution from the bridging ligand to the LUMO (5% on the metal and 0% on pyridyl units), while the HOMO is predicted to reside on the metal and the phenyl groups of the cyclometallating ligands. It is therefore likely that there is significant ^{3}LLCT character in the emitting state, which would

rationalise the broad emission and long τ.[71] No mention was made of multiple diastereomers and crystallographic data for the *meso* isomer was presented.

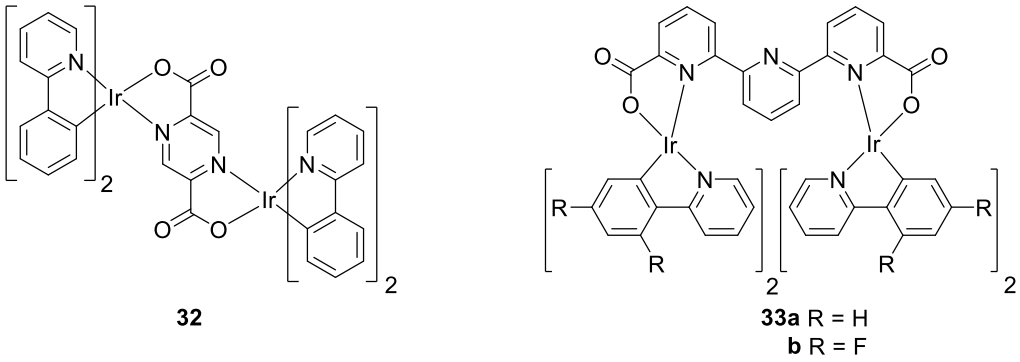

Figure 1.25: Molecular structures of complexes **32** and **33**.

Mazzanti et al. have utilised terpyridine dicarboxylate as a bridging ligand in diiridium complexes featuring both ppy and dfppy cyclometallating ligands (**33a** and **33b**) (Figure 1.25).[51] Use of the dianionic potassium salt of the bridging ligand meant that the complexes could be prepared under comparatively mild conditions (60 °C in 2-ethoxyethanol).[77,101] Only the *rac* (ΛΛ/ ΔΔ) diastereomers were detected. The complexes emit at λ_{max} values of 538 nm and 510 nm (477 nm shoulder) for **33a** and **33b**, respectively, with PLQYs of 17.7% and 4.8% (in DCM). The emissive excited states of both complexes were established to be mainly ^{3}MLCT in nature, and it was concluded that the emissive excited state of the dfppy complex (**33b**) has greater ^{3}LC contribution than that of the ppy (**33a**) analogue. This was assigned due to the smaller rigidochromic shift at 77 K (9 nm vs. 42 nm) for **33b** as well as a more well-defined vibronic fine structure in its PL spectrum.

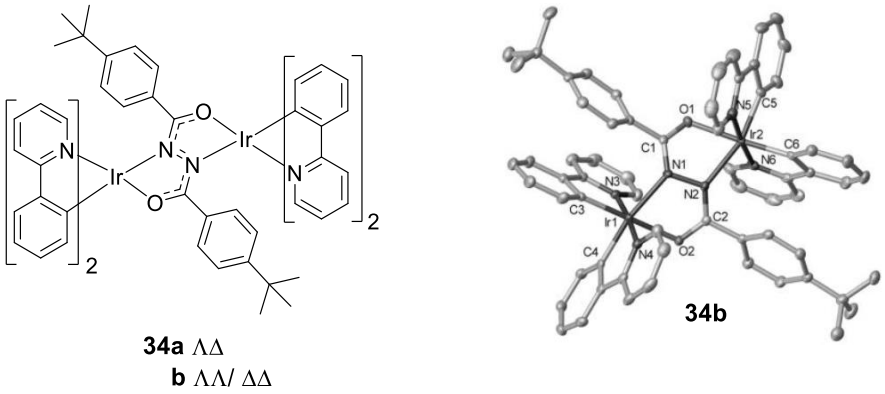

Figure 1.26: Molecular structures of the diastereomers **34a** and **34b** and X-ray crystal structure of **34b**. Figure adapted from reference 54 with permission from Wiley VCH copyright 2014.

In 2014, our group studied the cyclometallated dinuclear iridium(III) diastereomers **34a** and **34b** which are bridged by diarylhydrazide ligands (Figure 1.26). The *meso* ΛΔ/ΔΛ (**a**) and *rac* ΔΔ/ΛΛ (**b**)

diastereomers were readily separated due to their different solubilities. The PL of the complexes in solution (DCM) (λ_{max} = 521/523 nm) and in cycloolefin polymer (zeonex[**]) at room temperature, showed weak vibronic features, characteristic of an excited state with little signature of ^{3}LC character. The PLQY values in zeonex are 38% (**34a**) and 41% (**34b**). As DFT calculations predict significant HOMO localisation on the bridging units, the lowest energy excited states likely comprise of primarily ^{3}MLCT and ^{3}LLCT character. OLEDs were fabricated for both complexes with a solution processed emissive layer. The best device was based on **34b** with a peak EQE of 11%. This was superior to **34a** (EQE = 7%), which was ascribed to the better solubility of **34b**. The good performances of these complexes served as motivation for the study of the diarylhydrazide-bridged complexes investigated in this thesis (Chapters 2–4).

To summarise, N^O and O^O coordinating bridges have been incorporated into some highly emissive diiridium complexes. Complexes incorporating hydrazide and oxamide-based bridges are particularly promising as they present some of the best diiridium OLED performances to-date. These bridges offer the advantage of a very short conjugative pathway between the two iridium centres. This provides the opportunity for strong Ir---Ir electronic communication while making them promising systems for tuning emission towards the blue (Chapter 3). An intrinsic disadvantage to such systems may be the weaker Ir–bridge bonds compared to C^N type cyclometallated systems.

In conclusion, although diiridium complexes have historically afforded substandard photophysical properties compared to their mononuclear analogues, several exceptions have been reported and their structural types are diversifying. Those bridged by either N^O-type or C^N-type chelates currently constitute the most promising families. Some diiridium complexes have even been reported that demonstrate significant advantages over mononuclear complexes, such as sub-microsecond phosphorescent lifetimes. However, some disadvantages and challenges remain, particularly with respect to OLED applications. Diiridium complexes are not sufficiently volatile to be applied to vacuum-processed device architectures and so their application is restricted to solution-processed devices, which display poorer performance and lower reproducibility during fabrication. They are also less likely to afford deep blue emitters due to their more conjugated nature.

Regardless, this should not be discouraging. There are a range of other possible applications for diiridium complexes, such as in sensing and bioimaging. They are also scientifically interesting and present a versatile platform for fundamental studies to complement the standard monoiridium

[**] zeonex is a cyclic olefin polymer and serves as an optically transparent solid matrix.

complexes. Particularly, in future work the bridging ligands should offer opportunities for functionalisation with moieties that can heavily influence the physical properties of diiridium complexes while taking full advantage of their dinuclear nature.

References

1 J. P. Paris and W. W. Brandt, *J. Am. Chem. Soc.*, 1959, **81**, 5001–5002.
2 K. A. King, P. J. Spellane and R. J. Watts, *J. Am. Chem. Soc.*, 1985, **107**, 1431–1432.
3 Y. Chi and P.-T. Chou, *Chem. Soc. Rev.*, 2010, **39**, 638–655.
4 J. A. G. Williams, *Chem. Soc. Rev.*, 2009, **38**, 1783–1801.
5 C. Kaes, A. Katz and M. W. Hosseini, *Chem. Rev.*, 2000, **100**, 3553–3590.
6 R. Visbal and M. C. Gimeno, *Chem. Soc. Rev.*, 2014, **43**, 3551–3574.
7 C. Ulbricht, B. Beyer, C. Friebe, A. Winter and U. S. Schubert, *Adv. Mater.*, 2009, **21**, 4418–4441.
8 P. Chou, Y. Chi, M. Chung and C. Lin, *Coord. Chem. Rev.*, 2011, **255**, 2653–2665.
9 Y. Im, S. Y. Byun, J. H. Kim, D. R. Lee, C. S. Oh, K. S. Yook and J. Y. Lee, *Adv. Funct. Mater.*, 2017, **27**, 1603007–1603031.
10 X. Yang, G. Zhou and W.-Y. Wong, *Chem. Soc. Rev.*, 2015, **44**, 8484–8575.
11 W. C. H. Choy, W. K. Chan and Y. Yuan, *Adv Mater*, 2014, **26**, 5368–5398.
12 S. Sato, T. Morikawa, T. Kajino and O. Ishitani, *Angew. Chem. Int. Ed.*, 2013, **52**, 988–992.
13 R. Gao, D. G. Ho, B. Hernandez, M. Selke, D. Murphy, P. I. Djurovich and M. E. Thompson, *J. Am. Chem. Soc.*, 2002, **124**, 14828–14829.
14 Y. Zhou, J. Jia, W. Li, H. Fei and M. Zhou, *Chem. Commun.*, 2013, **49**, 3230–3232.
15 A. Hagfeldt, G. Boschloo, L. Sun, L. Kloo and H. Pettersson, *Chem. Rev.*, 2010, **110**, 6595–6663.
16 M. S. Lowry and S. Bernhard, *Chem. Eur. J.*, 2006, **12**, 7970–7977.
17 J. Li, P. I. Djurovich, B. D. Alleyne, M. Yousufuddin, N. N. Ho, J. C. Thomas, J. C. Peters, R. Bau and M. E. Thompson, *Inorg. Chem.*, 2005, **44**, 1713–1727.
18 M. A. Baldo, S. R. Forrest and M. E. Thompson, in *Organic Electroluminescence*, ed. Z. H. Kafafi, CRC and SPIE Press, 2005.
19 E. Baranoff, I. Jung, R. Scopelliti, E. Solari, M. Grätzel and M. K. Nazeeruddin, *Dalton Trans.*, 2011, **40**, 6860–6867.
20 J. A. G. Williams, in *Iridium(III) in Optoelectronic and Photonics Applications*, ed. E. Zysman-Colman, John Wiley & Sons, 1st edition, 2017, pp. 71–109.
21 J. Lee, H.-F. Chen, T. Batagoda, C. Coburn, P. I. Djurovich, M. E. Thompson and S. R. Forrest, *Nat. Mater.*, 2016, **15**, 92–98.
22 F. M. Hwang, H. Y. Chen, P. S. Chen, C. S. Liu, Y. Chi, C. F. Shu, F. I. Wu, P. T. Chou, S. M. Peng and G. H. Lee, *Inorg. Chem.*, 2005, **44**, 1344–1353.
23 Y.-J. Su, H.-L. Huang, C.-L. Li, C.-H. Chien, Y.-T. Tao, P.-T. Chou, S. Datta and R.-S. Liu, *Adv. Mater.*, 2003, **15**, 884–888.
24 J. Lakowicz, *Principles of Fluorescence Spectroscopy*, Springer, 3rd edition, 2006.
25 J. F. W. Herschel, *Phil Trans Roy Soc*, 1845, **135**, 143–145.
26 A. Jablonski, *Z. Phys.*, 1931, **73**, 460.
27 A. Jablonski, *Nature*, 1933, **131**, 839–840.
28 J. W. Borst and A. J. W. G. Visser, *Meas. Sci. Technol.*, 2010, **2010**, 102002–102023.
29 T. Hofbeck and H. Yersin, *Inorg. Chem.*, 2010, **49**, 9290–9299.
30 M. Seery, Light absorption and fate of excited state, https://photochemistry.wordpress.com/2009/08/24/light-absorption-and-fate-of-excited-state/, (accessed 4 October 2017).
31 H. Yersin, A. F. Rausch, R. Czerwieniec, T. Hofbeck and T. Fischer, *Coord. Chem. Rev.*, 2011, **255**, 2622–2652.
32 P. S. Wagenknecht and P. C. Ford, *Coord. Chem. Rev.*, 2011, **255**, 591–616.
33 B. J. Gierschner and J. Cornil, *Adv. Mater.*, 2007, **19**, 173–191.
34 B. Minaev, G. Baryshnikov and H. Agren, *Phys. Chem. Chem. Phys.*, 2014, **16**, 1719–1758.
35 Y. Chi and P.-T. Chou, *Chem. Soc. Rev.*, 2010, **39**, 638–655.
36 D. M. E. Freeman, A. J. Musser, J. M. Frost, H. L. Stern, A. K. Forster, K. J. Fallon, A. G.

Rapidis, F. Cacialli, I. Mcculloch, T. M. Clarke, R. H. Friend and H. Bronstein, *J. Am. Chem. Soc.*, 2017, **139**, 11073–11080.
37 S. Lamansky, P. Djurovich, D. Murphy, F. Abdel-Razzaq, H. E. Lee, C. Adachi, P. E. Burrows, S. R. Forrest and M. E. Thompson, *J. Am. Chem. Soc.*, 2001, **123**, 4304–4312.
38 S. Sprouse, K. A. King, P. J. Spellane and R. J. Watts, *J. Am. Chem. Soc.*, 1984, 6647–6653.
39 M. Nonoyama, *Bull. Chem. Soc. Jpn.*, 1974, **47**, 767–768.
40 F. Monti, M. G. I. La Placa, N. Armaroli, R. Scopelliti, M. Grätzel, M. K. Nazeeruddin and F. Kessler, *Inorg. Chem.*, 2015, **54**, 3031–3042.
41 J.-Y. Hung, Y. Chi, I.-H. Pai, Y.-C. Yu, G.-H. Lee, P.-T. Chou, K.-T. Wong, C.-C. Chen and C.-C. Wu, *Dalton Trans.*, 2009, **115**, 6472–5.
42 A. B. Tamayo, B. D. Alleyne, P. I. Djurovich, S. Lamansky, I. Tsyba, N. N. Ho, R. Bau and M. E. Thompson, *J. Am. Chem. Soc.*, 2003, **125**, 7377–7387.
43 Y. Zheng, A. S. Batsanov, R. M. Edkins, A. Beeby and M. R. Bryce, *Inorg. Chem.*, 2012, **51**, 290–297.
44 H. Oh, K.-M. Park, H. Hwang, S. Oh, J. H. Lee, J.-S. Lu, S. Wang and Y. Kang, *Organometallics*, 2013, **32**, 6427–6436.
45 E. C. Constable, C. E. Housecroft, P. Kopecky, C. J. Martin, I. A. Wright, J. A. Zampese, H. J. Bolink and A. Pertegas, *Dalton Trans.*, 2013, **42**, 8086–8103.
46 A. Auffrant, A. Barbieri, F. Barigelletti, J. Lacour, P. Mobian, J.-P. Collin, J.-P. Sauvage and B. Ventura, *Inorg. Chem.*, 2007, **46**, 6911–6919.
47 T. Hajra, J. K. Bera and V. Chandrasekhar, *Inorganica Chim. Acta*, 2011, **372**, 53–61.
48 T. Hajra, A. J. K. Bera and V. Chandrasekhar, *Aust. J. Chem.*, 2011, **64**, 561–566.
49 X. Yang, X. Xu, J. Dang, G. Zhou, C.-L. Ho and W.-Y. Wong, *Inorg. Chem.*, 2016, **55**, 1720–1727.
50 A. G. Tennyson, E. L. Rosen, M. S. Collins, V. M. Lynch and C. W. Bielawski, *Inorg. Chem.*, 2009, **48**, 6924–6933.
51 E. S. Andreiadis, D. Imbert, J. Pécaut, A. Calborean, I. Ciofini, C. Adamo, R. Demadrille and M. Mazzanti, *Inorg. Chem.*, 2011, **50**, 8197–8206.
52 L. Donato, C. E. McCusker, F. N. Castellano and E. Zysman-Colman, *Inorg. Chem.*, 2013, **52**, 8495–504.
53 M. Graf, R. Czerwieniec and K. Sünkel, *Z. Anorg. Allg. Chem.*, 2013, **639**, 1090–1094.
54 Y. Zheng, A. S. Batsanov, M. A. Fox, H. A. Al-Attar, K. Abdullah, V. Jankus, M. R. Bryce and A. P. Monkman, *Angew. Chem. Int. Ed.*, 2014, **53**, 11616–11619.
55 S. Bettington, M. Tavasli, M. R. Bryce, A. S. Batsanov, A. L. Thompson, H. A. Al Attar, F. B. Dias and A. P. Monkman, *J. Mater. Chem.*, 2006, **16**, 1046–1052.
56 A. M'hamedi, A. S. Batsanov, M. A. Fox, M. R. Bryce, K. Abdullah, H. A. Al-Attar and A. P. Monkman, *J. Mater. Chem.*, 2012, **22**, 13529–13540.
57 A. Santoro, A. M. Prokhorov, V. N. Kozhevnikov, A. C. Whitwood, B. Donnio, J. A. G. Williams and D. W. Bruce, *J. Am. Chem. Soc.*, 2011, **133**, 5248–51.
58 F. O. Garces, K. Dedeian, N. L. Keder and R. J. Watts, *Acta Cryst. C*, 1993, **49**, 1117–1120.
59 S. Bettington, A. L. Thompson, A. Beeby and A. E. Goeta, *Acta Cryst. E*, 2004, **60**, m827–m829.
60 K. A. McGee and K. R. Mann, *Inorg. Chem.*, 2007, **46**, 7800–7809.
61 A. S. Ionkin, Y. Wang, W. J. Marshall and V. A. Petrov, *J. Organomet. Chem.*, 2007, **692**, 4809–4827.
62 L. Norel, M. Rudolph, N. Vanthuyne, J. A. G. Williams, C. Lescop, C. Roussel, J. Autschbach, J. Crassous and R. Réau, *Angew. Chemie - Int. Ed.*, 2010, **49**, 99–102.
63 C. Xu, Z.-Q. Wang, X.-M. Dong, X.-Q. Hao, X.-M. Zhao, B.-M. Ji and M.-P. Song, *Inorganica Chim. Acta*, 2011, **373**, 306–310.
64 X. Yuan, S. Zhang and Y. Ding, *Inorg. Chem. Commun.*, 2012, **17**, 26–29.
65 D. L. Davies, M. P. Lowe, K. S. Ryder, K. Singh and S. Singh, *Dalton Trans.*, 2011, **40**, 1028–

1030.
66 M. Y. Wong, G. Xie, C. Tourbillon, M. Sandroni, D. B. Cordes, A. M. Z. Slawin, I. D. W. Samuel and E. Zysman-Colman, *Dalton Trans.*, 2015, **44**, 8419–8432.
67 H. Yersin, *Highly Efficient OLEDs with Phosphorescent Materials*, Wiley-VCH, Darmstadt, 2008.
68 P.-T. Chou and Y. Chi, *Chem. Eur. J.*, 2007, **13**, 380–395.
69 T. Sajoto, P. I. Djurovich, A. B. Tamayo, J. Oxgaard, W. A. Goddard and M. E. Thompson, *J. Am. Chem. Soc.*, 2009, **131**, 9813–9822.
70 G. Li, A. Wolfe, J. Brooks, Z. Zhu and J. Li, *Inorg. Chem.*, 2017, **56**, 8244–8256.
71 Y. You, J. Seo, S. H. Kim, K. S. Kim, T. K. Ahn, D. Kim and S. Y. Park, *Inorg. Chem.*, 2008, **47**, 1476–1487.
72 E. Baranoff and B. F. E. Curchod, *Dalton Trans.*, 2015, **44**, 8318–8329.
73 T. Sajoto, P. I. Djurovich, A. Tamayo, M. Yousufuddin, R. Bau, M. E. Thompson, R. J. Holmes and S. R. Forrest, *Inorg. Chem.*, 2005, **44**, 7992–8003.
74 K. Dedeian, J. Shi, N. Shepherd, E. Forsythe and D. C. Morton, *Inorg. Chem.*, 2005, **44**, 4445–4447.
75 Y. You and S. Y. Park, *Dalton Trans.*, 2009, **9226**, 1267–1282.
76 S. J. Lee, K. M. Park, K. Yang and Y. Kang, *Inorg. Chem.*, 2009, **48**, 1030–1037.
77 S. Lamansky, P. Djurovich, D. Murphy, F. Abdel-Razzaq, R. Kwong, I. Tsyba, M. Bortz, B. Mui, R. Bau and M. E. Thompson, *Inorg. Chem.*, 2001, **40**, 1704–1711.
78 A. F. Rausch, M. E. Thompson and H. Yersin, *J. Phys. Chem. A*, 2009, **113**, 5927–5932.
79 W. Song and J. Y. Lee, *Adv. Opt. Mater.*, 2017, **5**, 1600901–1600913.
80 Z. Yang, Z. Mao, Z. Xie, Y. Zhang, S. Liu, J. Zhao, J. Xu, Z. Chi and M. P. Aldred, *Chem. Soc. Rev.*, 2017, **46**, 915–1016.
81 D. G. Congrave, Y. Hsu, A. S. Batsanov, A. Beeby and M. R. Bryce, *Organometallics*, 2017, **36**, 981–993.
82 P.-H. Lanoë, C. M. Tong, R. W. Harrington, M. R. Probert, W. Clegg, J. A. G. Williams and V. N. Kozhevnikov, *Chem. Commun.*, 2014, **50**, 6831–6834.
83 R. E. Daniels, S. Culham, M. Hunter, M. C. Durrant, M. R. Probert, W. Clegg, J. A. G. Williams and V. N. Kozhevnikov, *Dalton Trans.*, 2016, **45**, 6949–6962.
84 X. Yang, Z. Feng, J. Zhao, J.-S. Dang, B. Liu, K. Zhang and G. Zhou, *ACS Appl. Mater. Interfaces*, 2016, **8**, 33874–33887.
85 J. Frey, B. F. E. Curchod, R. Scopelliti, I. Tavernelli, U. Rothlisberger, M. K. Nazeeruddin and E. Baranoff, *Dalton Trans.*, 2014, **43**, 5667–5679.
86 C.-H. Chien, S. Fujita, S. Yamoto, T. Hara, T. Yamagata, M. Watanabe and K. Mashima, *Dalton Trans.*, 2008, 916–923.
87 H. Benjamin, M. A. Fox, A. S. Batsanov, H. A. Al-Attar, C. Li, Z. Ren, A. P. Monkman and M. R. Bryce, *Dalton Trans.*, 2017, **46**, 10996–11007.
88 E. A. Plummer, W. Hofstraat and L. De Cola, *Dalton Trans.*, 2003, 2080–2084.
89 E. A. Plummer, A. van Dijken, J. W. Hofstraat, L. De Cola and K. Brunner, *Adv. Funct. Mater.*, 2005, **15**, 281–289.
90 V. Chandrasekhar, T. Hajra, J. K. Bera, S. M. W. Rahaman, N. Satumtira, O. Elbjeirami and M. A. Omary, *Inorg. Chem.*, 2012, **51**, 1319–1329.
91 S.-Y. Yao, Y.-L. Ou and B.-H. Ye, *Inorg. Chem.*, 2016, **55**, 6018–6026.
92 V. E. Pritchard, R. Martir, S. Oldknow, S. Kai, S. Hiraoka, N. J. Cookson, E. Zysman-Colman and M. J. Hardie, *Chem. Eur. J.*, 2017, **23**, 6290–6294.
93 D. R. Martir, D. Escudero, D. Jacquemin, D. B. Cordes, A. M. Z. Slawin, H. A. Fruchtl, S. L. Warriner and E. Zysman-Colman, *Chem. Eur. J.*, 2017, **23**, 14358–14366.
94 G. Li, Y. Wu, G. Shan, W. Che, D. Zhu, B. Song, L. Yan, Z. Su and M. R. Bryce, *Chem. Commun.*, 2014, **50**, 6977–6980.
95 J. Fernández-Cestau, N. Giménez, E. Lalinde, P. Montaño, M. T. Moreno and S. Sánchez,

Organometallics, 2015, **34**, 1766–1778.
96 A. Tsuboyama, T. Takiguchi, S. Okada, M. Osawa, M. Hoshino and K. Ueno, *Dalton Trans.*, 2004, 1115–1116.
97 A. M. Prokhorov, A. Santoro, J. A. G. Williams and D. W. Bruce, *Angew. Chemie Int. Ed.*, 2012, **51**, 95–98.
98 M. C. DeRosa, G. D. Enright, C. E. B. Evans and R. J. Crutchley, *Acta Crystallogr. Sect. E.-Struct Rep.*, 2005, **61**, m967–m969.
99 A. M'hamedi, M. A. Fox, A. S. Batsanov, H. A. Al-ttar, A. P. Monkman and M. R. Bryce, *J. Mater. Chem. C*, 2017, **5**, 6777–6789.
100 A. Tsuboyama, H. Iwawaki, M. Furugori, T. Mukaide, J. Kamatani, S. Igawa, T. Moriyama, S. Miura, T. Takiguchi, S. Okada, M. Hoshino and K. Ueno, *J. Am. Chem. Soc.*, 2003, **125**, 12971–12979.
101 K. Dedeian, P. I. Djurovich, F. O. Garces, G. Carlson and R. J. Watts, *Inorg. Chem.*, 1991, **30**, 1687–1688.

Chapter 2: New diarylhydrazide-bridged diiridium complexes

Introduction

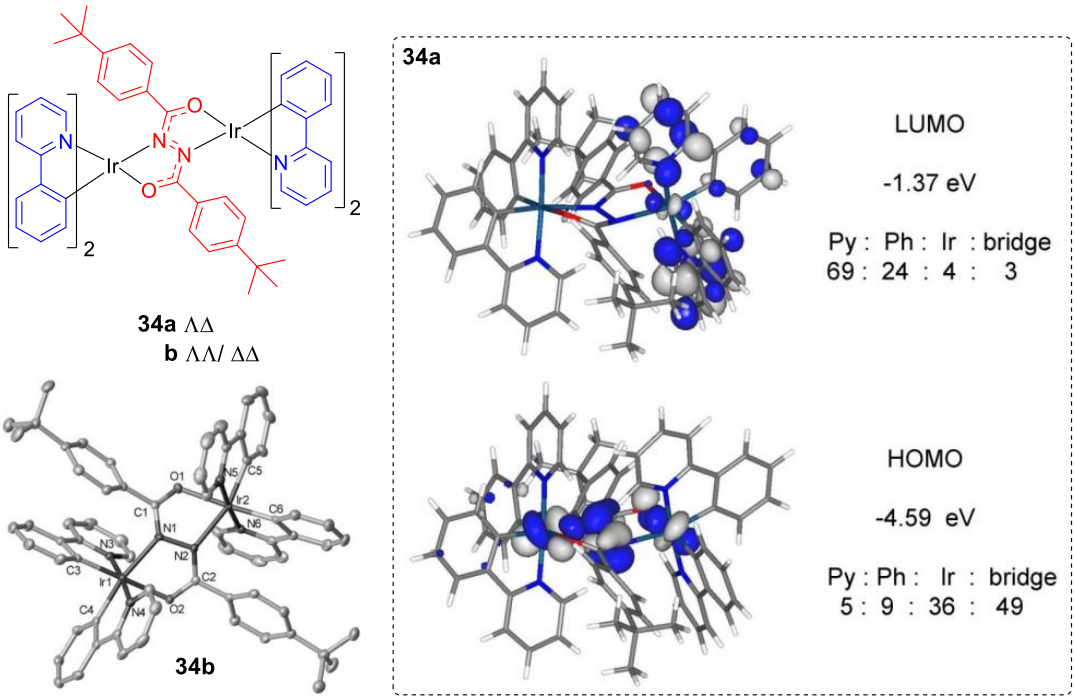

Figure 2.1: Molecular structures of the diastereomers **34a** and **34b**, X-ray crystal structure of **34b** and frontier molecular orbital plots for **34a**. The orbital contributions are percentages and the HOMO and LUMO energies were calculated at B3LYP/LANL2DZ:3–21G*. Figure adapted from reference 1 with permission from Wiley VCH copyright 2014.

In a short communication our group previously identified the diastereomers **34a** and **34b** as high performing diiridium phosphors for application in OLEDs with a solution processed emitting later.[1] The complexes exhibit some advantageous properties: facile separation of diastereomers through trituration, good PLQYs of 38% and 41% for **34a** and **34b**, respectively, and short τ of *ca.* 1.4 µs (all data for 5% w/w in zeonex). Such beneficial photophysical properties allowed the fabrication of green OLEDs with EQEs of 7% and 11% for **34a** and **34b**, respectively – record efficiencies for diiridium complexes at the time of publication. DFT calculations also predicted frontier molecular orbital (FMO) contributions from both the bridging and cyclometallating ligands as well as the metal centres. Encouraged by these results, we were prompted to further investigate this system through systematic structural variation of the bridging and cyclometallating ligands. This work is covered in this Chapter.

Results and discussion

Design and synthesis

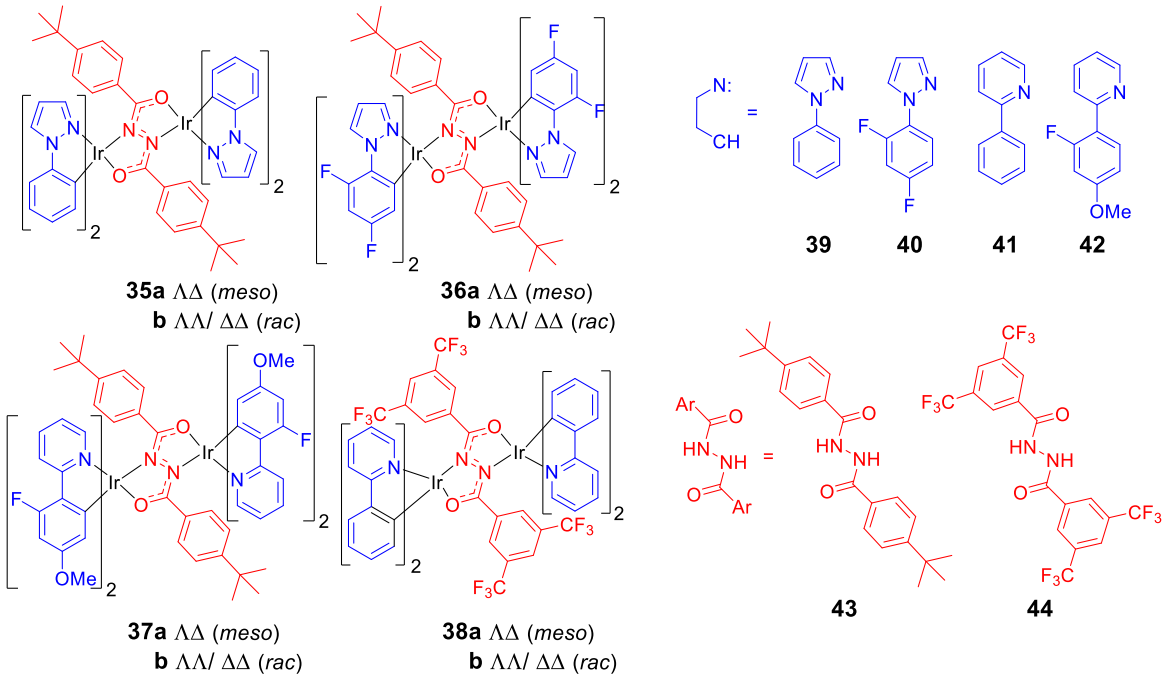

Figure 2.2: Molecular structures of the diiridium complexes and ligands studied in this chapter.

The structures of the complexes and ligands studied in this chapter are presented in Figure 2.2. Complexes **35–38** were designed based on DFT calculations on complex **34** (Figure 2.1) to investigate structure-property relationships in diarylhydrazide-bridged diiridium complexes. In complexes **35–37**, variation of the peripheral cyclometallating ligands is explored. The ppz ligands **39** and **40** were selected to blue shift the emission through destabilisation of the LUMO due to the more electron rich nature of pyrazole compared to pyridine.[2] The fluorine substituents on ligand **40** were expected to further blue shift emission through stabilisation of the HOMO, as reported for mononuclear complexes.[3,4] Although there is literature precedent for ppz-functionalised complexes being poorly/ non-emissive,[2,5,6] when this study began ppz-type cyclometallating ligands had not been applied to diiridium systems and if successful, their inclusion could provide elusive blue emission from diiridium systems. The ppy ligand **42** was selected to blue shift the emission through HOMO stabilisation. It was chosen in preference to dfppy based on studies in our group by Dr Helen Benjamin that were ongoing at the time.[7,8] Methoxy groups are known to be good alternatives to fluorine on cyclometallating ligands,[9–12] possessing similar Hammett parameters[13] while potentially avoiding the stability issues associated with Ar–F groups.[14,15]

Complex **38** was targeted to explore the effects of bridge functionalisation. As the central hydrazide core in complex **34** features high HOMO character, functionalisation of the aryl rings of bridge **44**

with electron withdrawing CF_3 groups was expected to inductively stabilise the HOMO and blue shift emission.

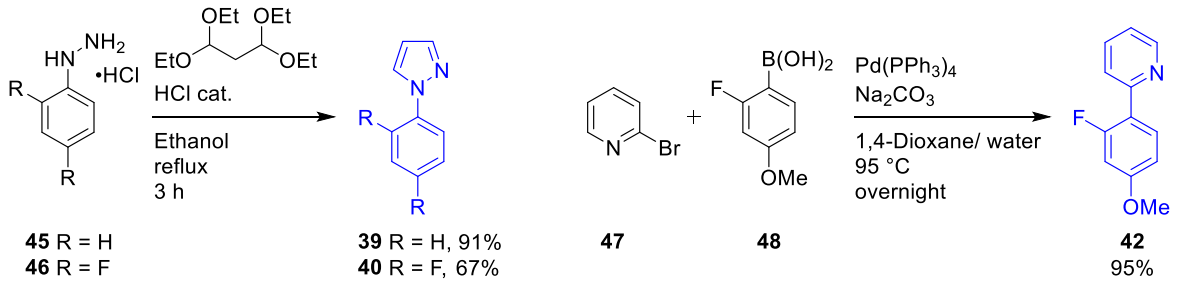

Figure 2.3: Synthetic schemes for the cyclometallating ligands **39**, **40** and **42**.

The synthetic schemes for the cyclometallating and bridging ligands studied in this chapter are presented in Figures 2.3 and 2.4, respectively. The ppz ligands **39** and **40** were synthesised according to a literature procedure.[16] Acid-catalysed condensation of the hydrochloride salts of either phenylhydrazine (**45**) or 2,4-difluorophenylhydrazine (**46**) with 1,1,3,3-tetraethoxypropane afforded **39** and **40**, respectively. Both were obtained in good yields on gram scales after a short reaction time of 3 h and purification by distillation. Ppy (**41**) (Figure 2.2) was commercially available. Ligand **42** was synthesised in near-quantitative yield through Suzuki-Miyaura coupling of 2-bromopyridine (**47**) with the corresponding boronic acid **48**.[7]

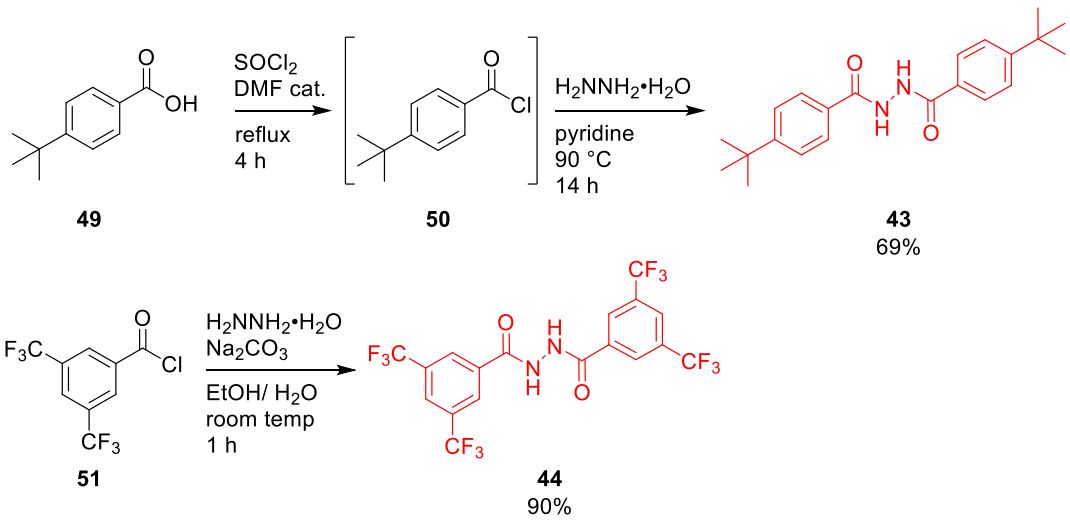

Figure 2.4: Synthetic scheme for the bridging ligands **43** and **44**.

The *tert*-butyl-functionalised bridge **43** was synthesised according to a literature procedure.[17] The benzoic acid derivative **49** was firstly heated with thionyl chloride in the presence of catalytic *N,N*-dimethylformamide (DMF) to obtain the benzoyl chloride **50** *in situ*. Subsequent treatment with hydrazine monohydrate in pyridine at 90 °C afforded **43** in 69% yield. The trifluoromethylated

bridge **44** was prepared from the commercially available benzoyl chloride **51** in a high yield of 90%. It was synthesised via a room temperature procedure utilising a EtOH/ water solvent mixture.[18] The procedure afforded an easier work-up and purification of **44** in comparison to the method used in the synthesis of **43**.

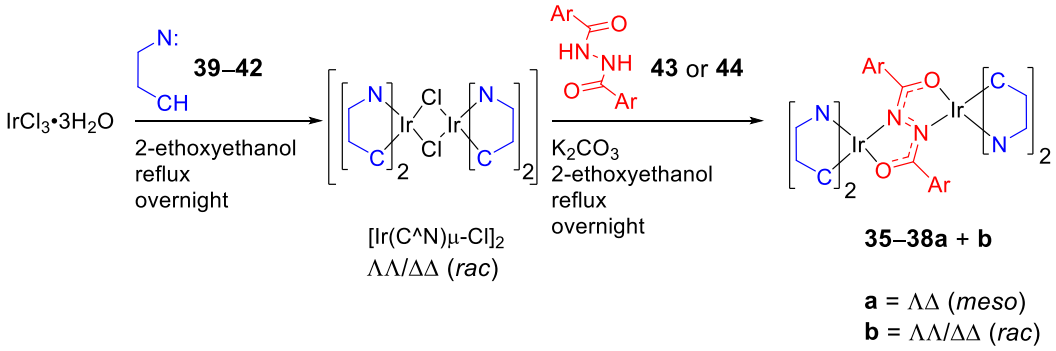

Figure 2.5: General synthetic scheme for the complexes **35–38**.

With the cyclometallating (**39–42**) and bridging (**43** and **44**) ligands in hand, the complexes **35–38** were synthesised (Figure 2.5). The cyclometallating ligands **39–42** were firstly refluxed with $IrCl_3•3H_2O$ in 2-ethoxyethanol to generate the corresponding bis(μ–Cl) dimer intermediate complexes *in situ*. The intermediate complexes were then treated with the hydrazide bridging ligands **43** or **44** in the presence of K_2CO_3 to obtain the diiridium complexes **35–38**. Mixtures of *meso* (ΛΔ **a**) and *rac* (ΛΛ/ ΔΔ **b**) diastereomers were obtained for all the complexes. From integration analysis of crude ^{1}H NMR spectra there does not appear to be any noteworthy diastereoselectivity (Figure 2.6).

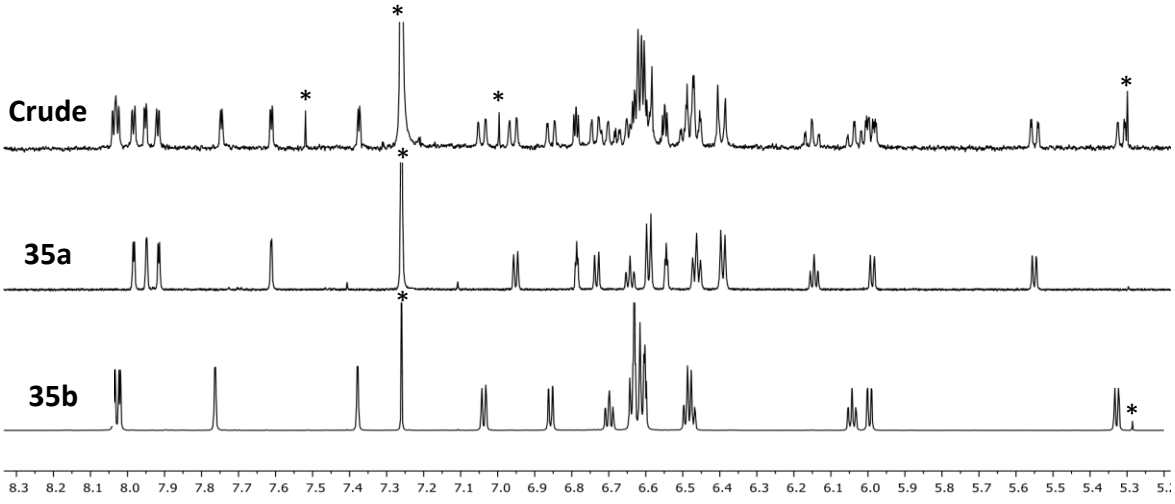

Figure 2.6: Aromatic regions of the ^{1}H NMR spectra of the resolved diastereomers **35a** and **35b** (700 MHz) and the initial crude mixture (400 MHz). Peaks marked * are due to traces of CH_2Cl_2 and also residual $CHCl_3$ in $CDCl_3$.

In all instances the diastereomers were separated and the detailed procedures are presented in the experimental section. For complexes **35**–**38** the diastereomer separation was not as straightforward as for the literature complex **34**.[1] For complexes **35**, **36** and **38**, trituration of the crude product with refluxing solvent (*n*-hexane for **35** and **36**, toluene for **38**) afforded filtrands and filtrates that were enriched with the *meso* (ΛΔ **a**) and *rac* (ΛΛ/ ΔΔ **b**) diastereomers, respectively. The enriched filtrands were then purified by a solvent wash (**38a**) or fractional recrystallisation (**35a** and **36a**) to obtain the *meso* (ΛΔ **a**) diastereomers. The *rac* (ΛΛ/ ΔΔ **b**) diastereomers were obtained through chromatographic purification of the filtrates. For complex **37** the diastereomers were resolved via flash chromatography without prior trituration. The high level of diastereomeric excess of the samples was confirmed by 700 MHz ^{1}H NMR spectroscopy. The ^{1}H NMR spectra for **35a** and **35b** after resolution are presented in Figure 2.6. Where solubility allowed, it was possible to fully assign the ^{1}H and ^{13}C environments using ^{1}H–^{1}H COSY, ^{1}H–^{1}H NOESY, ^{1}H–^{13}C HSQC and ^{1}H–^{13}C HMBC 2D NMR spectra (discussed in further detail below).

It is noteworthy that although the complexes are stable in DCM solution, they partially decompose on silica columns to form small amounts of μ-dichloro-bridged dimers when DCM is used as the chromatography eluent. Displacement of non-cyclometallated ligands to form μ-dichloro dimers in the presence of a chloride source in acidic media has been previously reported.[19] This problem was overcome by the use of K_2CO_3-saturated DCM during purification.

X-ray crystal structures[*]

Single crystals suitable for X-ray diffraction were grown for all the complexes via liquid diffusion of *n*-hexane or MeOH into their saturated or near-saturated CH_2Cl_2 solutions, or by slow evaporation of a CD_2Cl_2 solution. The X-ray crystal structures of **35**–**38** are displayed in Figure 2.7. Important geometrical parameters are listed in Table 2.1. Additional crystallographic figures are included in the Appendix (Figures A1–A3).

All structures except **36a** and **38b** contain solvent of crystallisation, which is usually disordered. Crystallisation of **36b** from a DCM/ hexane solution proceeds in two Ostwald stages: a DCM di-solvate is precipitated initially (**36b***), which then recrystallises into a mixed DCM/ hexane solvate. Similarly, crystallisation of **37a** from a DCM/ methanol solution, yields firstly a DCM tetrasolvate (**37a***) and then a methanol di-solvate with a minor substitution of methanol by DCM. In the metastable form **37a***, a large part of the complex is disordered, as suggested by the abnormally high displacement parameters of the atoms (including the Ir atoms). Complex **36b** and **38a** were studied in two different solvates, and in each instance one form contains containing two

[*] All X-ray crystal structures were solved by Dr Andrei Batsanov

symmetrically independent molecules (**36b*** and **38a***). In both cases, different crystal packing facilitates relatively minor changes in the molecular conformations and negligible differences in the bond distances.

In the crystals of all *meso* (**a**) complexes, the molecules are rigorously centrosymmetric and lie on a crystallographic inversion centre (at the midpoint of the N–N bond) which relates the two Ir centres. This is to be expected as statistics show that centrosymmetric molecules rarely crystallise in a form which does not display an inversion centre.[20] The *rac* (**b**) isomers either lie on a crystallographic twofold axis, or have no crystallographic symmetry, but the crystal is always centrosymmetric as it is racemic. In each case, both Ir atoms have distorted octahedral coordination, involving one N and one O atom of the bridge, and two C^N cyclometallating ligands arranged with their coordinating N atoms *trans* and axial, as expected.[1,21] In all *meso* (**a**) complexes the central bridging hydrazide (OCNNCO) moiety is planar. In *rac* (**b**) forms, the bridge is folded along the central CNNC dihedral so that the two OCNN planes form an angle of 10 to 30°. The Ir atoms deviate more greatly from their OCNN planes in the *meso* (**a**) forms.

In each complex, both aryl substituents of the bridging ligand (rings A) are stacked face-to-face (π–π) with a cyclometallating ligand (rings B) (Figure 2.7). The interplanar angles (Θ) of 6.6–27.2° and mean separations (*D*) of 3.26–3.66 Å between the overlapping moieties (Table 2.1) are common for arene stacking.[22] Although intramolecular π–π interactions have been studied in neutral and cationic monoiridium complexes,[23–28] at the time of this study we were unaware of any previous examples of intramolecular π–π interactions between the bridging and peripheral ligands of cyclometallated diiridium systems. Chapter 3 in this thesis focusses on manipulating such stacking interactions to influence the photophysical properties of diiridium systems.

Table 2.1: Selected geometrical parameters of diiridium complexes (bond distances in Å).

	35a	**35b**	**36a**	**36b*** [a]	**36b** [b]	**37a*** [c]	**37a** [d]	**37b**	**38a*** [e]	**38a** [f]	**38b**
Space group	$P2_1/c$	$P2_1/c$	$P\bar{1}$	$P\bar{1}$	$P2_1/n$	$P\bar{1}$	$P2_1/c$	$Pbcn$	$P\bar{1}$	$P\bar{1}$	C2/c
Mol. symmetry	C_i	--	C_i	--	--	C_i	C_i	C_2	C_i	C_i	C_2
Ir centres	ΛΔ	ΛΛ or ΔΔ	ΛΔ	ΛΛ or ΔΔ	ΛΛ or ΔΔ	ΛΔ	ΛΔ	ΛΛ or ΔΔ	ΛΔ	ΛΔ	ΛΛ or ΔΔ
Ir---Ir, Å	5.013	5.031	4.988	5.007	5.031	5.00	5.029	5.089	5.035, 5.063	5.047	5.095
Ir–C (*trans*-O)	1.992(4)	2.006(6)	2.023(5)	2.000(5)	2.007(4)		1.997(2)	1.996(3)	1.994(3)	1.990(1)	2.000(2)
Ir–C (*trans*-N)	2.004(3)	1.994(6)	2.011(5)	2.003(5)	2.008(4)		1.989(2)	1.998(3)	2.005(3)	1.997(1)	2.006(2)
Ir–N, stacked	2.011(3)	2.005(6)	2.009(5)	2.013(5)	2.015(3)		2.027(2)	2.025(3)	2.027(2)	2.028(1)	2.032(2)
Ir–N, non-stacked	2.018(3)	1.973(6)	2.014(5)	2.018(4)	2.004(3)		2.044(2)	2.032(3)	2.051(2)	2.045(1)	2.044(2)
Bridge geometry											
OCNNCO folding, °	planar	23.9	planar	13.6, 20.8	21.0	planar	planar	29.5	planar	planar	9.8
Ir displacement, Å	0.60	0.18	0.06	0.06, 0.16	0.16	0.59	0.57	0.43	0.46, 0.33	0.46	0.10
Ir–O	2.144(3)	2.116(4)	2.102(4)	2.112(4)	2.111(3)		2.154(1)	2.123(2)	2.143(2)	2.154(1)	2.144(1)
Ir–N	2.152(3)	2.156(5)	2.134(4)	2.144(4)	2.160(3)		2.155(2)	2.181(2)	2.164(2)	2.162(1)	2.174(1)
N–N	1.436(6)	1.439(7)	1.441(8)	1.444(6)	1.447(4)		1.442(3)	1.459(5)	1.444(4)	1.434(2)	1.440(3)
N–C	1.307(5)	1.324(8)	1.308(6)	1.308(6)	1.306(5)		1.315(2)	1.313(4)	1.308(3)	1.316(1)	1.313(2)
C–O	1.295(4)	1.292(8)	1.295(6)	1.286(6)	1.288(4)		1.288(2)	1.285(4)	1.283(3)	1.280(1)	1.281(2)
Intramolecular stacking (π–π)											
Θ, ° [g]	22.1	12.3, 20.3	12.2	20.6, 27.2, 16.5, 15.3	11.9, 9.4	22	12.0	15.5	7.2, 8.2	6.6	7.6
D, Å [h]	3.52	3.35, 3.57	3.26	3.64, 3.66, 3.47, 3.47	3.39, 3.42	3.54	3.40	3.40	3.43, 3.36	3.39	3.36

[a] **36b***·DCM, average of two independent molecules; [b] **36b**·2DCM·½C_6H_{14}, [c] **37a***·4DCM, major component (bond distances are unreliable due to all-molecule disorder); [d] **37a**·1.84MeOH·0.16DCM; [e] **38a***·½CD_2Cl_2, average of two independent molecules; [f] **38a**·2CD_2Cl_2; [g] interplanar angle between the cyclometallating ligand (B) and arene ring A of the bridging ligand (see **35a**, Figure 2.7); [h] distance between the cyclometallating ligand plane (B) and the centroid of ring A.

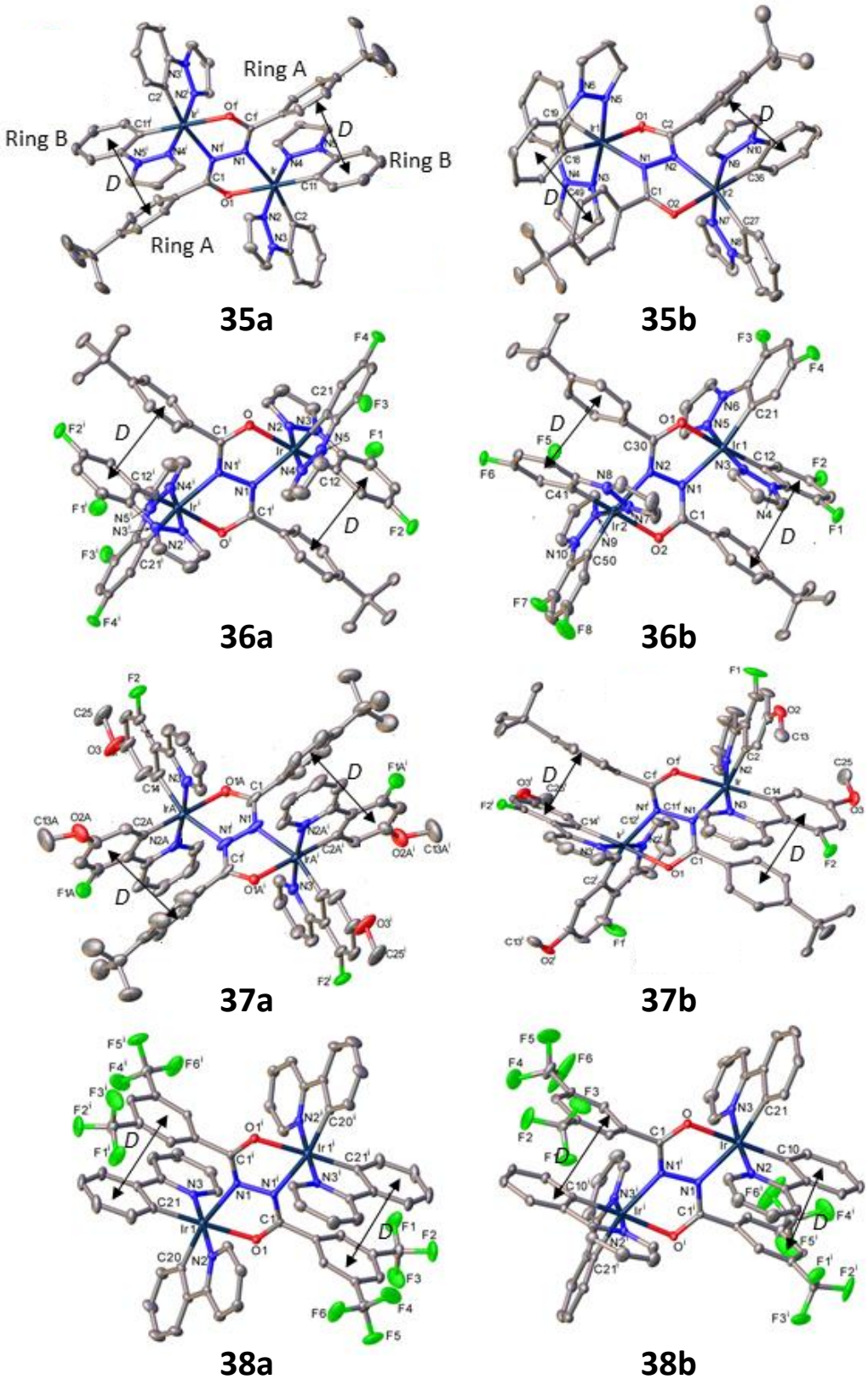

Figure 2.7: X-ray molecular structures of **35a**, **35b**, **36a**, **36b**, **37a***, **37b**, **38a** and **38b**. Thermal ellipsoids are drawn at the 50% probability level, H atoms and solvent of crystallisation are omitted for clarity. Primed atoms are generated by a crystallographic inversion centre (**35–38a**) or a twofold axis (**37b**, **38b**). Vector *D* identifies intramolecular π–π interactions (see Table 2.1).

NMR assignment

Using ^{1}H–^{1}H COSY, ^{1}H–^{13}C HSQC, ^{1}H–^{13}C HMBC and ^{1}H–^{1}H NOESY NMR experiments it is possible to fully assign the ^{1}H and ^{13}C NMR spectra of the diiridium complexes. In this section **36b** is discussed as a representative example. For the complexes studied here the *rac* diastereomers exhibit C_2 molecular symmetry and so the ligands which are interconverted by the C_2 symmetry operation are chemically equivalent. This symmetry leads to two distinct sets of cyclometallating ligand environments rather than four, which is evident in the number of environments present within the ^{1}H NMR spectra. The same effect is observed for the *meso* diastereomers due to the presence of an inversion centre and the accompanying C_i molecular symmetry.

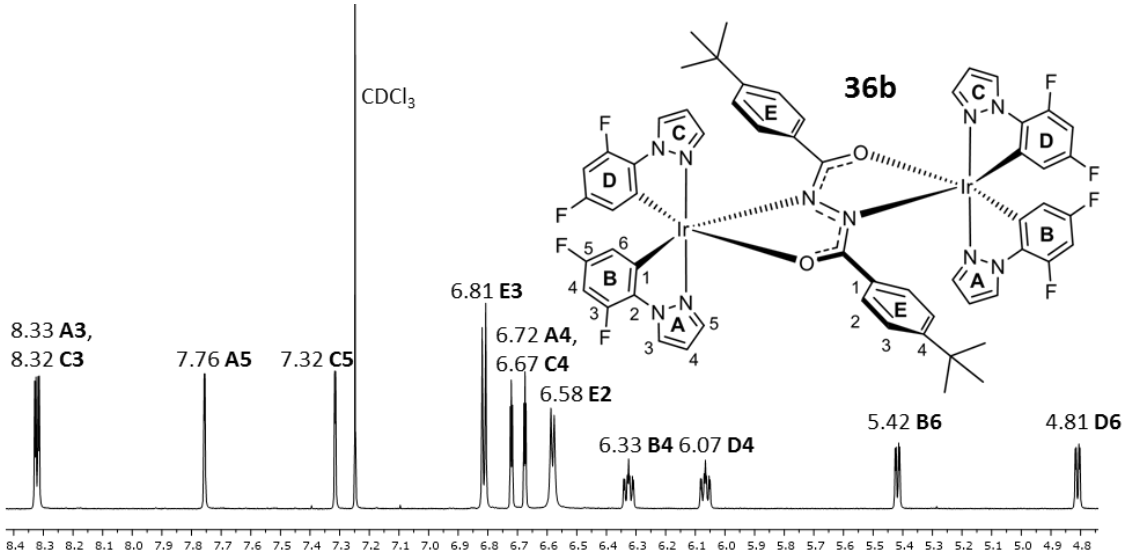

Figure 2.8: Aromatic region of the 700 MHz ^{1}H NMR spectrum of **36b** with peak assignments and molecular structure. The label '$CDCl_3$' denotes residual $CHCl_3$ in the NMR solvent.

The ^{1}H NMR spectrum for **36b** with peak assignments is presented in Figure 2.8. The aliphatic region is excluded as assignment of the bridge *tert*-butyl group is trivial. Using ^{1}H–^{1}H COSY spectroscopy (Figure 2.9) it is possible to determine which signals constitute the different pyrazole (A: 8.33, 7.76, 6.72 ppm and C: 8.32, 7.32, 6.67 ppm) and phenyl rings (B: 6.33, 5.42 ppm and D: 6.07, 4.81 ppm), although it is not possible to determine the connectivity between the rings and their orientation with respect to the bridging ligand. The phenyl signals for B4 (6.33 ppm) and D4 (6.07 ppm) are assigned due to their multiplicity (ddd). The phenyl signals corresponding to B6 (5.42 ppm) and D6 (4.81 ppm) can be assigned to due to their multiplicity (dd) and low chemical shifts. The signals at 6.81 and 6.58 are assigned to the bridge phenyl groups (E) due to the integration values and because they couple only to each other, although they cannot be differentiated using the COSY spectrum exclusively. The signals corresponding to A4 (6.72 ppm) and C4 (6.67 ppm) are assigned to the pyrazole 4 positions due to their multiplicity (dd) and coupling constants.[29] From the COSY

spectrum alone the 3 and 5 positions of the pyrazole groups (A and C) cannot be unambiguously assigned.

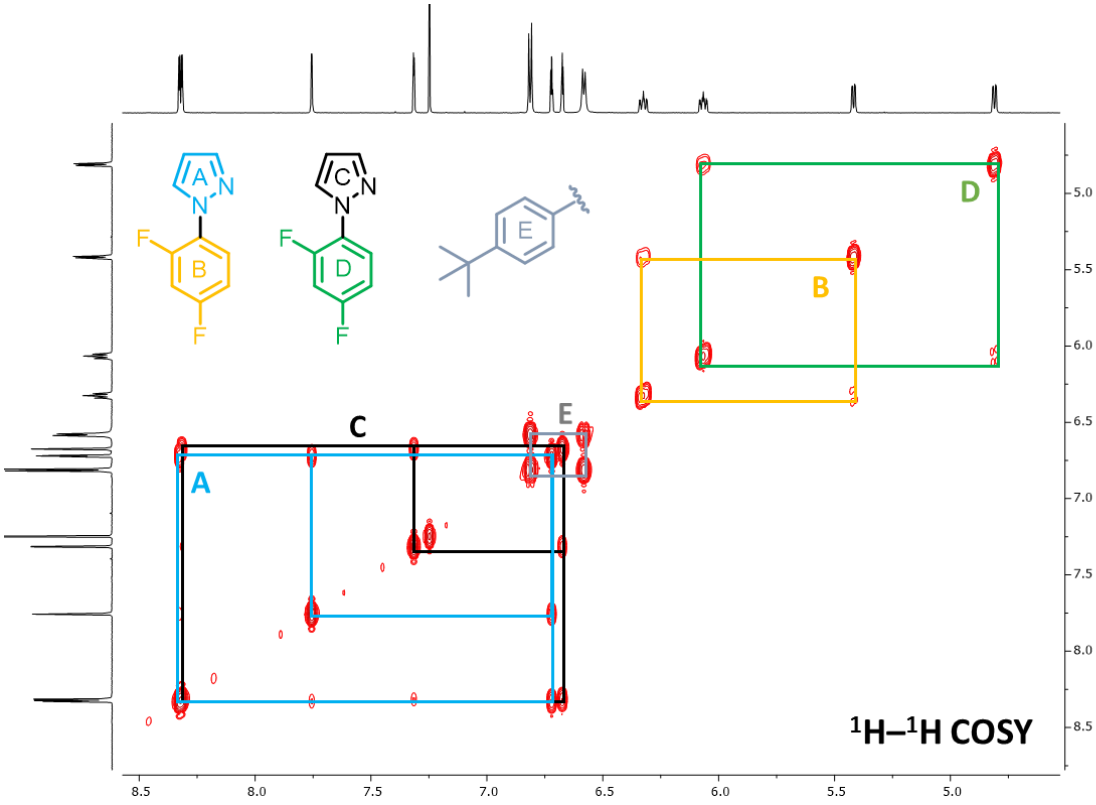

Figure 2.9: ^{1}H–^{1}H COSY NMR spectrum of **36b** with ring assignments.

^{1}H–^{1}H NOESY is useful for confirming connectivity as it shows through-space interactions (Figure 2.10). The important cross peaks are labelled, and a crystal structure fragment is included as an inset to highlight the proximity of the interacting protons.

Cross peaks are observed between the phenyl 6 positions and the pyrazole 5 positions of orthogonal cyclometallating ligands (cross peaks 1 and 2), which are in proximity in the X-ray crystal structure (inset). This makes it possible to confirm A–B and C–D connectivity. These cross peaks also enable differentiation between the 5 (A5, 7.76 and C5, 7.32 ppm) and 3 (A3, 8.33 and C3, 8.32 ppm) positions of the pyrazole groups, which is in agreement with a cross peak between A5 (7.76 ppm) and the bridge proton E2 (6.58 ppm) (cross peak 3). Cross peak 3 also enables determination of ligand orientation with respect to the plane of the bridge: ligands C–D lie parallel to the bridge and are therefore capable of intramolecular π–π stacking, whereas ligands A–B lie perpendicular to it. This is further confirmed by cross peak 4, which is observed between the *tert*-butyl proton environment (1.14 ppm) and D4 (6.07 ppm). It is also possible to distinguish between the bridge phenyl environments E2 (6.58 ppm) and E3 (6.81 ppm) due to a more intense cross peak between the *t*-butyl environment and E3 (cross peak 5).

A noteworthy feature in the ^{1}H NMR spectrum is the low chemical shift value of the D6 environment (4.81 ppm). This is likely due to its proximity to the π cloud of the bridge ring E, which shields it. This reinforces the assignment of the orientation of ring D with respect to the bridge.

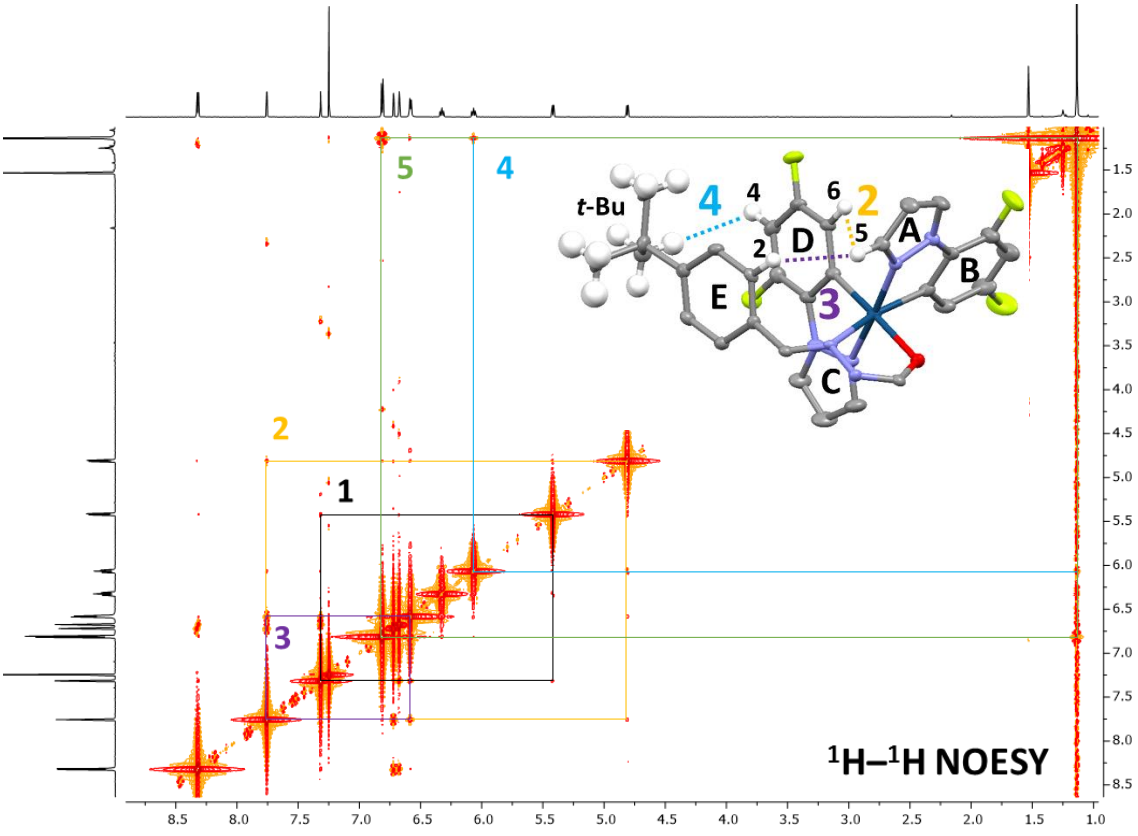

Figure 2.10: ^{1}H–^{1}H NOESY NMR spectrum of **36b** with important cross peaks highlighted. Inset is a crystal structure fragment to highlight the numbered interactions.

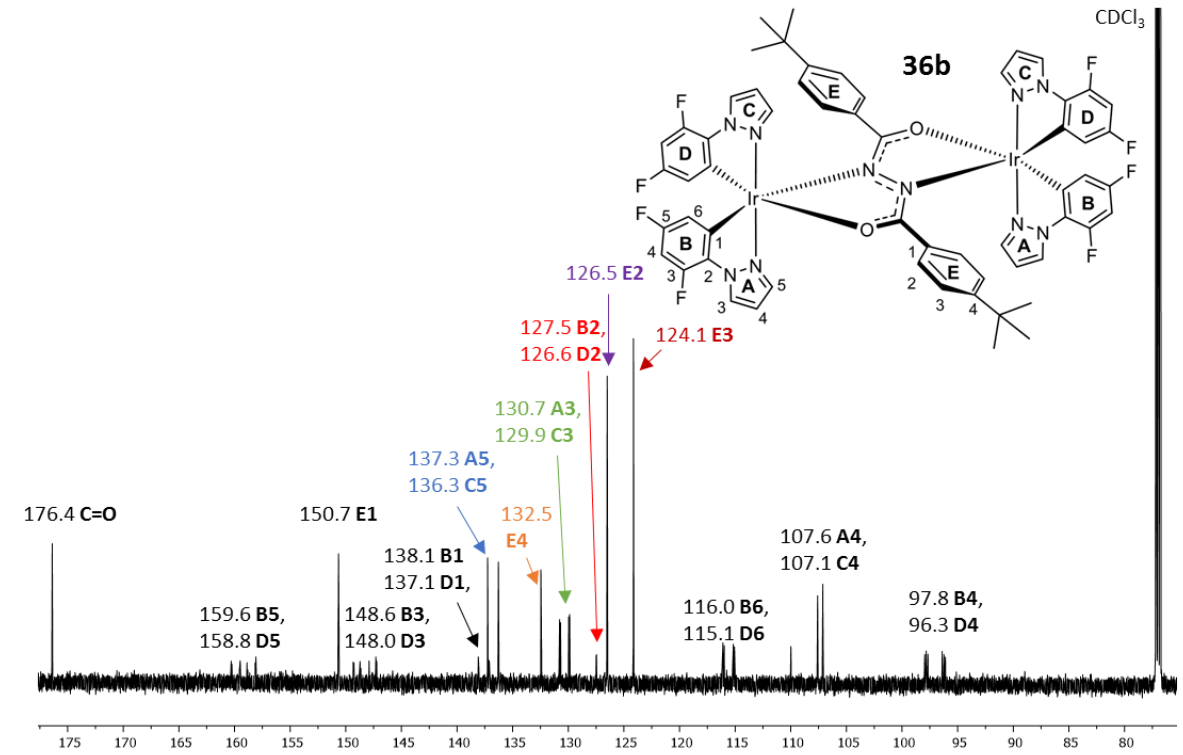

Figure 2.11: Aromatic region of the 176 MHz ^{13}C NMR spectrum of **36b** with peak assignments and molecular structure. The coloured labels are present to clarify the congested spectrum and do not correspond to any particular ring.

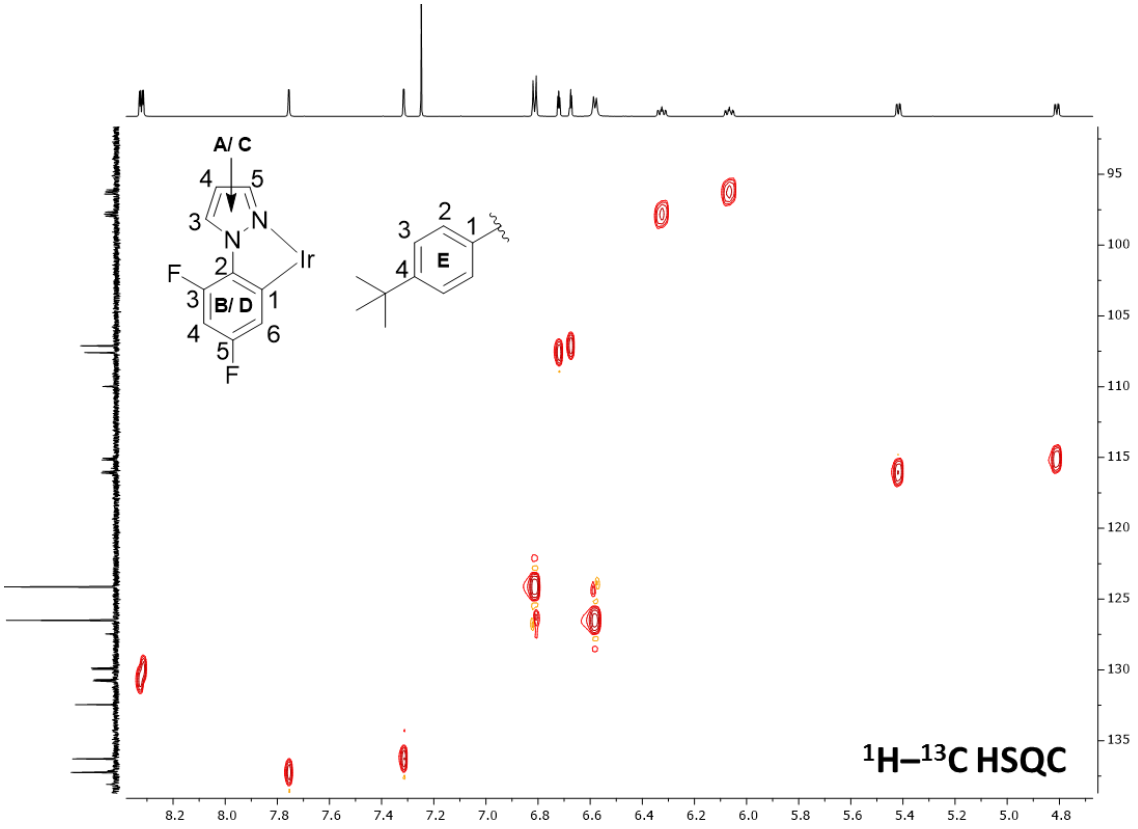

Figure 2.12: ^{1}H–^{13}C HSQC NMR spectrum of **36b** with numbering scheme for ligands.

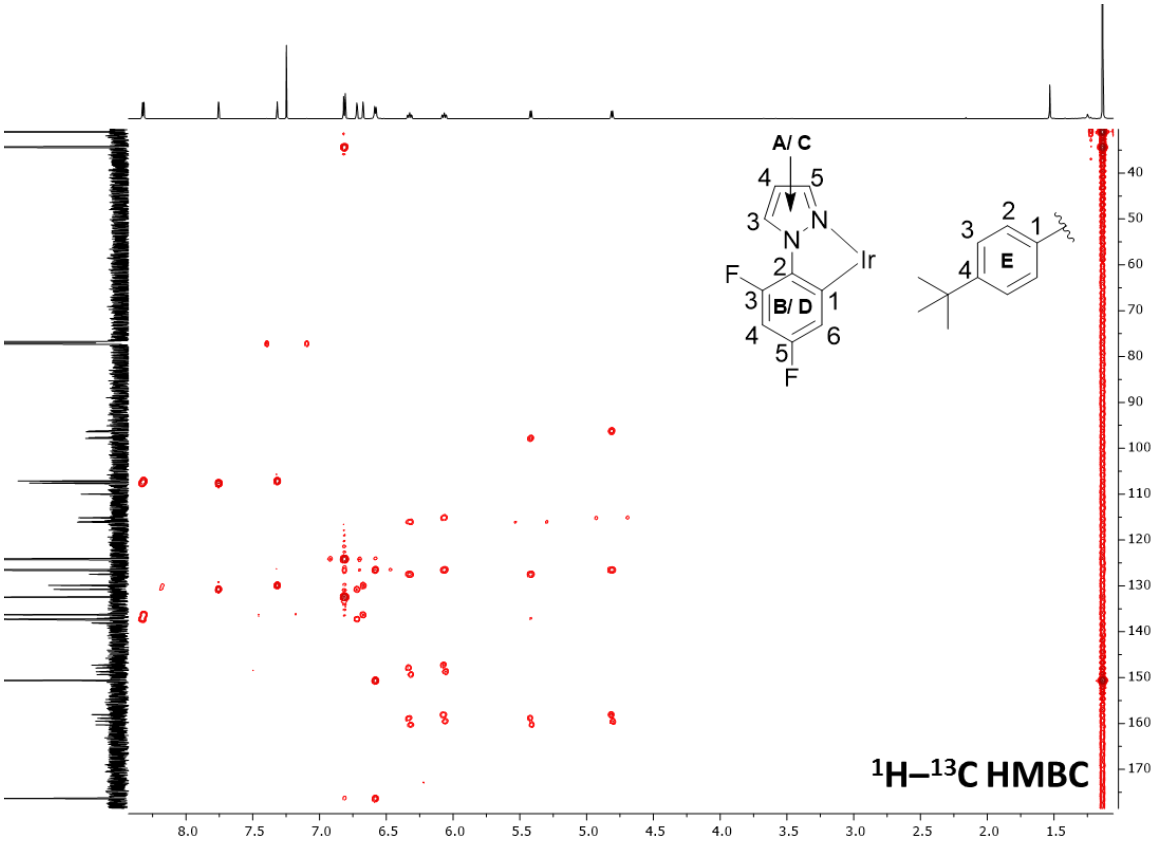

Figure 2.13: ^{1}H–^{13}C HMBC NMR spectrum of **36b** with numbering scheme for ligands.

The ^{13}C{^{1}H} NMR spectrum for **36b** with peak assignments is presented in Figure 2.11. The aliphatic region is excluded as assignment of the aliphatic ^{13}C environments is trivial. The carbon environments featuring C–H bonds (A3–5, C3–5, B4 and 6, D4 and 6, E2 and 3, *t*-Bu) can be unambiguously assigned using ^{1}H–^{13}C HSQC spectroscopy (Figure 2.12) which shows coupling between protons and their geminal carbon.

The remaining carbon environments can then be assigned from ^{1}H–^{13}C HMBC spectroscopy (Figure 2.13) which detects ^{1}H–^{13}C coupling over longer distances. The experiment used here is optimised for *meta* environments (3 bonds). $C_{C=O}$ (176.4 ppm) and E1 (150.7 ppm) are assigned due to the presence of a cross peak with E2 (6.58 ppm) and by their chemical shift values. E4 (132.5 ppm) and $C_{t\text{-Bu quart}}$ (34.3 ppm) are assigned due to cross peaks with E3 (6.81 ppm) and the *t*-butyl group (1.14 ppm), respectively. The 3 and 5 positions on the phenyl groups (B and D) are firstly assigned due to large ^1J ^{13}C–^{19}F coupling constants (*ca.* 250 Hz). They can be differentiated from inspection of cross peaks with the 4 and 6 positions – coupling is more intense to the 5 positions as they are *ortho* to both the 4 and 6 positions. The 1 and 2 positions are assigned based on cross peaks with the 4 and 6 positions, which are more intense for the 2 positions due to the *meta* optimisation.

Computational study

Electronic structure calculations were carried out on the complexes to explore the frontier orbitals and support the electrochemical and photophysical properties (discussed below). The optimised ground state S_0 geometries were first calculated for the complexes in the gas phase at the B3LYP/LANL2DZ:3–21G* level. The LANL2DZ pseudopotential was used for the iridium atoms while the 3–21G* basis set was applied to the other atoms. Therefore, the data presented here are directly comparable to previous computational studies on *fac*-Ir(ppy)$_3$ and other diiridium complexes such as **34**.[1,30,†] For the optimised geometries, the central bridge CNNC dihedral angles are generally calculated to be planar (180°) for the *meso* (**a**) isomers, while they are twisted for the *rac* (**b**) isomers and display greater variation between complexes (144–156°). This is in good agreement with the experimental X-ray diffraction data above and is ascribed to the difference in symmetry between the diastereomers: due to their centrosymmetric nature the *meso* (**a**) isomers show no folding preference, whereas the *rac* (**b**) isomers can minimise steric interactions between cyclometallating ligands on opposing Ir centres through folding.

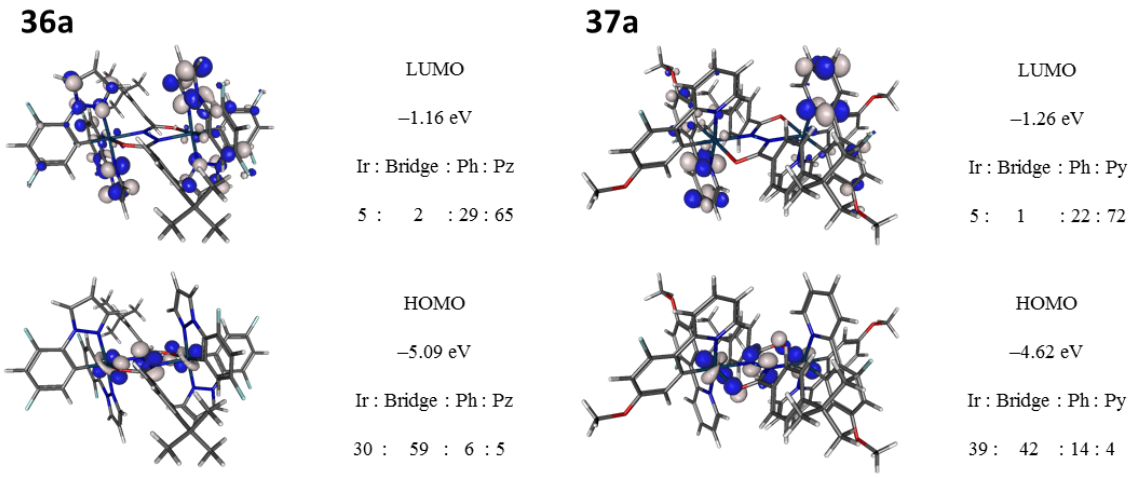

Figure 2.14: Molecular orbital compositions for **36a** and **37a**. The orbital contributions are percentages and the HOMO and LUMO energies were calculated at B3LYP/LANL2DZ:3–21G*. Bridge = bridging ligand; Ph = cyclometallating ligand phenyl groups; Py/ Pz = cyclometallating ligand heterocycles.

Molecular orbital calculations established a similar distribution of the FMOs for all the complexes. Therefore, FMO plots for complexes **36a** and **37a** are shown in Figure 2.14 as representative

[†] Previous investigation conducted by Dr Mark Fox determined that for *fac*-Ir(ppy)$_3$ and some bis(μ–Cl) dimers the 3–21G* basis set gives very similar results to the commonly employed 6–31G* while affording shorter calculation times.[30] This is particularly appealing for diiridium complexes as they are comparatively large molecules.

examples, while the data for all complexes (**35**–**38**) are summarised in Table 2.2. Additional FMO plots are included in the Appendix. (Figures A4–A9).

Table 2.2: Summary of the HOMO and LUMO compositions for the most stable minima of the complexes.

Complex	Isomer	Orbital	Ir	Bridge	Ph[a]	Py/ Pz[b]
35	**a** *meso*	LUMO	4%	1%	29%	65%
		HOMO	35%	48%	12%	4%
	b *rac*	LUMO	3%	45%	16%	36%
		HOMO	29%	61%	4%	6%
36	**a** *meso*	LUMO	5%	2%	29%	65%
		HOMO	30%	59%	6%	5%
	b *rac*	LUMO	4%	7%	28%	60%
		HOMO	30%	61%	5%	4%
37	**a** *meso*	LUMO	5%	1%	22%	72%
		HOMO	39%	42%	14%	4%
	b *rac*	LUMO	6%	1%	21%	72%
		HOMO	34%	51%	10%	5%
38	**a** *meso*	LUMO	4%	20%	20%	57%
		HOMO	46%	12%	37%	5%
	b *rac*	LUMO	4%	18%	18%	60%
		HOMO	41%	30%	23%	5%

[a]Phenyl moieties of the cyclometallating ligands [b]Pyridyl or pyrazolyl moieties of the cyclometallating ligands.

Generally, the HOMOs are primarily localised on the iridium centres, the cyclometallating phenyl moieties and the central hydrazide components of the bridging ligands (other than for **35b** where the bridge anomalously also features notable LUMO character). The LUMOs are primarily localised on the *N*-heterocycles of the cyclometallating ligands. Consequently these predictions are very similar to the FMO compositions reported for complex **34**.[1] Notably, for complexes **35** and **36** the LUMOs are still localised on the *N*-heterocycles despite the fact that they are electron rich pyrazole moieties. To the best of our knowledge these are the first heteroleptic iridium complexes for which significant LUMO localisation is predicted on the pyrazole groups of the cyclometallating ligands **39** and **40**.[5,23,31] This is indicative of the high π* energy of the bridging ligand (**43**), explained by the high heteroatom density in the central OCNNCO fragment. The bridge aryl rings do not feature FMO character for all diiridium complexes (they are ancillary). The high contribution of the bridge to the HOMO levels of all complexes (non-ancillary character) suggests that the bridging units should play

a significant role in the first oxidation potentials of the complexes as well as their excited states, and is evident in the electrochemical and photophysical data discussed below.

TD-DFT can be used to predict the absorption spectrum of a compound and gain some information about the character of excited states. Calculations were carried out in the gas phase. The calculated absorption spectrum for complex **35a** is presented as a representative example in Figure 2.15. To obtain the data for the absorption spectrum, singlet states were exclusively calculated. This helped reduce calculation times as > 150 states are required to obtain a "full" spectrum. This simplification is justified firstly because TD-DFT treats singlets and triplets as being separate (i.e. no SOC, no mixed singlet and triplet states), meaning that singlet transition energies and oscillator strengths are unperturbed by including triplet states in the calculation. Secondly, in the TD-DFT method employed here $S_0 \rightarrow T_n$ transitions have zero oscillator strength and so their inclusion has no effect on the shape of the predicted spectrum.

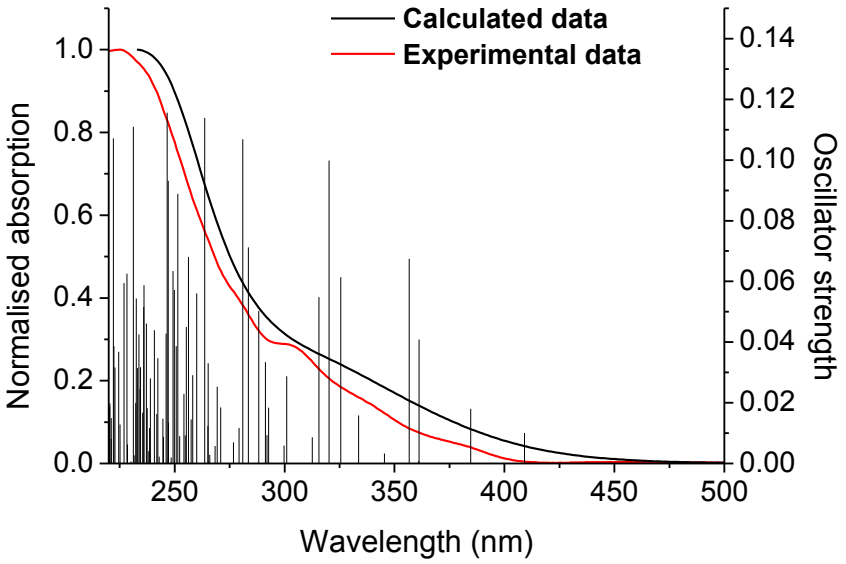

Figure 2.15: Simulated and experimental absorption spectra for complex **35a**. Experimental data were obtained in aerated MeCN.

For complex **35a** the predicted absorption spectrum is shifted to lower energy compared to the experimental data, as previously reported for other diiridium systems.[1,30,32] Otherwise, the calculated and the experimental data are in good agreement and broadly display the same spectral profiles.

The lowest energy singlet and triplet states were also investigated at the S_0 geometries. The data for the *meso* (**a**) diastereomers is presented in Table 2.3. The data for the *rac* (**b**) diastereomers are very similar. As Ir(III) complexes are phosphorescent the triplet states are of greater interest. For

complexes **37a** and **38a**, transitions to the first two triplet states ($S_0 \rightarrow T_1$ and $S_0 \rightarrow T_2$) are degenerate and involve HOMO → LUMO and HOMO → LUMO+1 transitions, respectively. This agrees with previous reports for other heteroleptic ppy Ir complexes[1,30,33] and is related to the fact that the non-equivalent pyridyl groups of the two cyclometallating ligand environments have very similar π* energies. For the same reason, the LUMO+1 orbitals for all the complexes studied here feature very similar localisations to the LUMO orbitals, residing primarily on the pyridyl moieties of the cyclometallating ligands. Therefore, the lowest energy excited states for **37** and **38** are expected to comprise an admixture of LC (on the cyclometallating ligands), MLCT (metal → cyclometallating ligand) and ILCT (bridge → cyclometallating ligand) character.

Table 2.3: Summary of the TD-DFT data for the *meso* (**a**) complexes.[a]

Transition	35a		36a		37a		38a	
	Main orbital contribution	**λ/ nm (ƒ)**	**Main orbital contribution**	**λ/ nm (ƒ)**	**Main orbital contribution**	**λ/ nm (ƒ)**	**Main orbital contribution**	**λ/ nm (ƒ)**
$S_0 \rightarrow T_1$	HOMO → LUMO+4	437	HOMO → LUMO+4	417	HOMO → LUMO	486	HOMO → LUMO	499
$S_0 \rightarrow T_2$	HOMO → LUMO	429	HOMO → LUMO	399	HOMO → LUMO+1	485	HOMO → LUMO+1	499
$S_0 \rightarrow T_3$	HOMO → LUMO+1	428	HOMO → LUMO+1	397	HOMO → LUMO+3	454	HOMO → LUMO+2	477
$S_0 \rightarrow S_1$	HOMO → LUMO	409 (0.010)	HOMO → LUMO	380 (0.010)	HOMO → LUMO	462 (0.006)	HOMO → LUMO	463 (0.000)
$S_0 \rightarrow S_2$	HOMO → LUMO+1	407 (0.000)	HOMO → LUMO+1	375 (0.000)	HOMO → LUMO+1	462 (0.000)	HOMO → LUMO+1	462 (0.020)
$S_0 \rightarrow S_3$	HOMO → LUMO+3	385 (0.018)	HOMO → LUMO+3	366 (0.000)	HOMO → LUMO+3	434 (0.020)	HOMO → LUMO+2	442 (0.014)

[a] ƒ = oscillator strength. It is only included for singlet transitions as it is zero for all triplet transitions.

This contrasts with the prediction for complexes **35a** and **36a**. In both cases the $S_0 \rightarrow T_1$ transition is primarily HOMO → LUMO+4. Slightly higher in energy (only 8 nm for **35a**) are the next two triplet transitions ($S_0 \rightarrow T_2$ and $S_0 \rightarrow T_3$) which primarily involve HOMO → LUMO and HOMO → LUMO+1, respectively. For both complexes the LUMO+4 has substantial bridge character (Figure 2.16). Therefore, for complexes **35** and **36** the lowest energy excited states are expected to also possess some character where the bridging ligand features the acceptor orbitals, i.e. LC (on the bridging ligand), MLCT (metal → bridge) and ILCT (cyclometallating ligand → bridge). This is due to the higher energy of the pyrazole π* orbitals in **35** and **36**, which makes the bridge π* orbitals more accessible. The TD-DFT data helps to explain the differing photophysical properties of **35** and **36** vs. **37** and **38** complexes (discussed below).

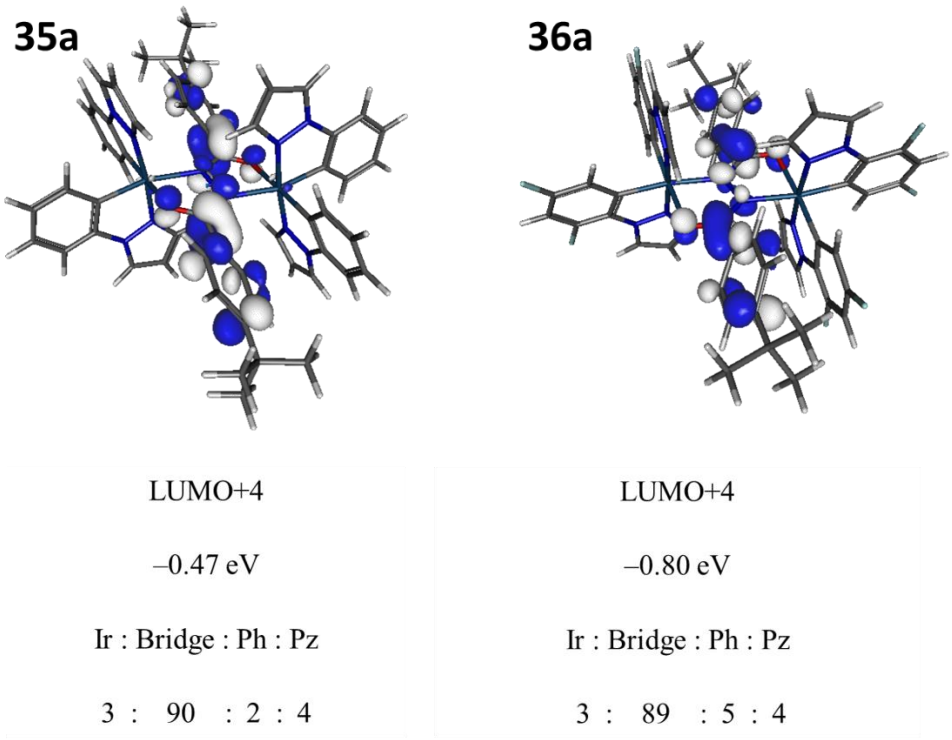

Figure 2.16: Molecular orbital plots for the LUMO+4 orbitals of **35a** and **36a**. The orbital contributions are percentages and the energies were calculated at B3LYP/LANL2DZ:3–21G*. Bridge = bridging ligand; Ph = cyclometallating ligand phenyl groups; Py/ Pz = cyclometallating ligand heterocycles.

In principle, the T_1 geometries could be optimised and then TD-DFT could be employed to predict emission energies. However, this was not carried out due to literature precedent.[30,34] For some mono- and diiridium complexes previously reported by our group, the optimised T_1 geometries are poorly modelled by open-shell DFT calculations and the calculated $S_0 \rightarrow T_1$ (absorption) transitions are more representative of the PL λ_{max} than the calculated $T_1 \rightarrow S_0$ (emission) transitions. The same will likely apply to the complexes studied here as they feature similarly small Stokes shifts to the literature examples (^{3}MLCT Abs – λ_{max} PL differences of *ca.* 20 nm – see below).

Electrochemical study

The oxidation processes for the diiridium complexes **35**–**38** were studied by CV (Figure 2.17) and the obtained data are listed in Table 2.4. All complexes display two oxidation waves ($E^{ox(1)}$ and $E^{ox(2)}$) due to the sequential oxidation of the iridium atoms (Ir^{3+}/ Ir^{4+} redox couples). The presence of two single-electron oxidations indicates electronic coupling between the two Ir centres through the bridging units (and also potential through space coupling).

The trend in the first oxidation potentials is **36** > **38** > **37** > **35**. This can be rationalised by considering the strength of the electron withdrawing substituents on the phenyl rings of the cyclometallating

ligands. Fluorination as in **36a** and **36b** lowers the HOMO more significantly than fluorination of the bridging ligand in **38a** and **38b**. This correlates with the DFT predictions (above) that the bridge phenyl moieties do not possess HOMO character, reducing the effect of the strongly withdrawing CF_3 groups on the oxidation potentials of **38a** and **38b**. As a general trend, DFT calculations overestimate the HOMO energies of the diiridium complexes compared to the experimental values. Clear reduction processes were not observed on scanning to *ca.* –2.5 V vs. FcH/FcH^+.

Table 2.4: Oxidation potentials for the Ir^{3+}/ Ir^{4+} couples (E^{ox}/ V) of complexes **35–38** referenced to $E_{1/2}$ FcH/ FcH^+ = 0.00 V. $E_{1/2}$ values are quoted for electrochemically reversible‡ oxidations.

Complex	Isomer	$E^{ox(1)}$ /V E_{pa}/ E_{pc} [$E_{1/2}$]	$E^{ox(2)}$ /V E_{pa} /E_{pc} [$E_{1/2}$]	$\Delta E_{1/2}$ /V	HOMO /eV[a]	HOMO /eV[b]	LUMO /eV[b]
35	**a** *meso*	0.29/ 0.21 [0.25]	0.78/ 0.69 [0.73]	0.48	–5.05	–4.55	–0.84
	b *rac*	0.23/ 0.15 [0.19]	0.82/ 0.73 [0.77]	0.58	–4.99	–4.52	–0.89
	a + **b** 1:1 mix	0.27/ 0.17 [0.22]	0.81/ 0.72 [0.76]	0.54	–5.02	-	-
36	**a** *meso*	0.67/ 0.57	1.11/ 0.96	0.41	–5.42	–5.09	–1.16
	b *rac*	0.55/ 0.44 [0.49]	1.08/ 0.97 [1.03]	0.54	–5.29	–5.05	–1.10
37	**a** *meso*	0.42/ 0.34 [0.38]	0.84/ 0.72	0.40	–5.18	–4.62	–1.26
	b *rac*	0.42/ 0.34 [0.38]	0.88/ 0.76	0.44	–5.18	–4.82	–1.36
38	**a** *meso*	0.57/ 0.46 [0.52]	0.82/ 0.71 [0.77]	0.25	–5.32	–5.01	–1.63
	b *rac*	0.55/ 0.46 [0.51]	0.82/ 0.71 [0.77]	0.26	–5.31	–5.04	–1.62

[a] HOMO levels calculated from CV potentials by HOMO = –4.8 + ($-E_{1/2}^{ox(1)}$), using ferrocene as the internal standard. [b] Frontier orbital energies calculated from optimised geometries at B3LYP/LANL2DZ:3–21G* level.

A noteworthy observation is that significantly different oxidation potentials are reproducibly observed for both species **35a** and **35b**, in particular for the first oxidation process ($\Delta E_{1/2}$ for $E^{ox(1)}$ = 60 mV). When a 1:1 mixture was analysed (Table 2.4) intermediary oxidation potentials were observed compared to the diastereomerically pure samples, suggesting that the observed differences are real. To try and resolve the signals corresponding to each diastereomer, differential pulse voltammetry (DPV) was employed because it has improved sensitivity compared to CV. This is because interference due to background non-Faradaic current is minimised. However, it was unsuccessful (Figure 2.18). Nevertheless, the observation of symmetrical peaks in the DPV trace

‡ Throughout this thesis "electrochemically reversible" processes are assigned based on the apparent equal magnitudes of their forward and reverse waves.

serves as further indication that the oxidation processes are reversible for **35a** and **35b**. There is also a significant difference in the oxidation potentials between the two diastereomers **36a** and **36b**. The differences in the electrochemical properties of the diastereomers can likely be ascribed to their different molecular symmetries (*meso* **a** = C_i, *rac* **b** = C_2) and the fact that diastereomers are known to commonly exhibit differing physical properties. Large differences in the CNNC dihedral angles of the bridges for the optimised geometries and crystals structures of the diastereomers (see above) also indicate that the average geometries of the diastereomers in solution may be significantly different, which could also be related to some of the observed differences in electrochemical properties between isomers. It is noteworthy that a similar difference between the oxidation potentials of diiridium diastereomers has been previously reported for a cyclometallated diiridium complex.[35]

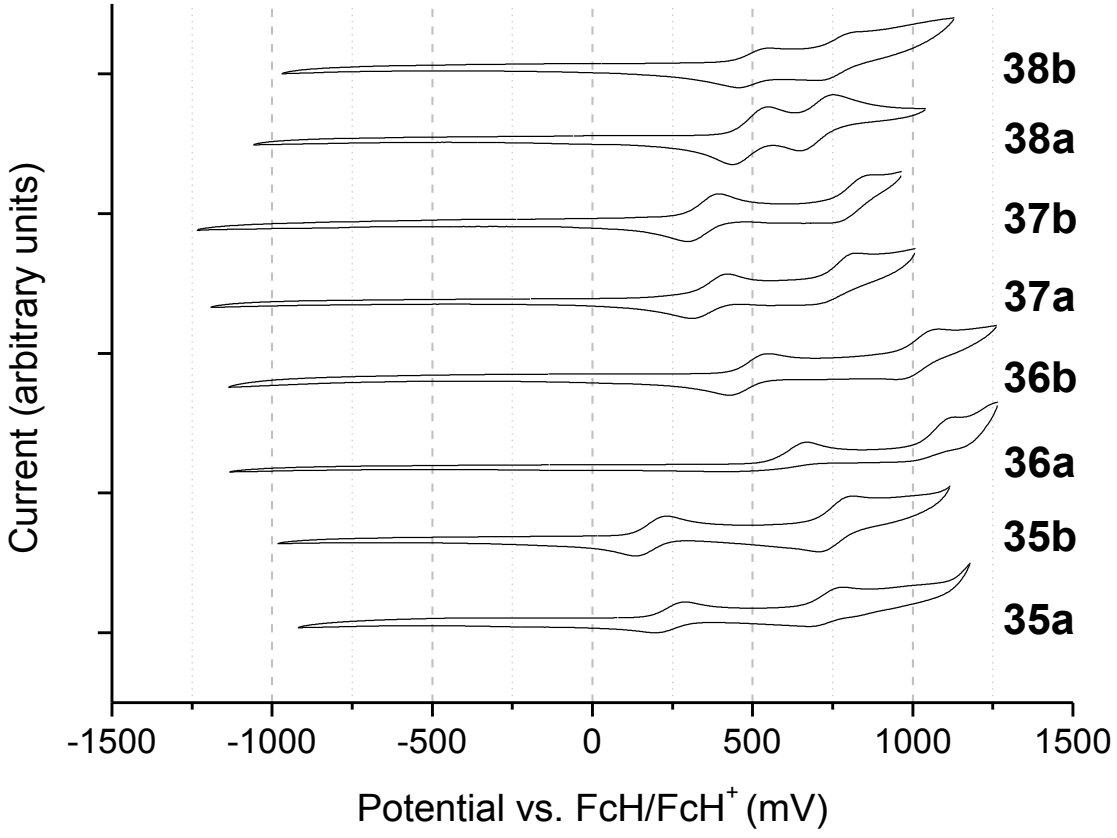

Figure 2.17: Cyclic voltammograms in 0.1 M *n*-Bu_4NPF_6/ DCM showing the oxidation processes for complexes **35**–**38**.

The peak splittings between the first and second oxidations ($\Delta E_{1/2}$) (Table 2.4) for complexes **35**–**38** vary between 250–580 mV and are ≥ 400 mV for all complexes, other than **38a** and **38b**. These are rather large for cyclometallated diiridium complexes,[30,35–39] as reported values for other bridge

systems lie between 200–350 mV, other than a 410 mV exception.[39] As $\Delta E_{1/2}$ for $[Ir(ppy)_2\mu–Cl]_2$ is 260 mV,[37] such strong coupling for **35**–**38** is not solely due to a through-space interaction (Ir---Ir distances for μ–Cl dimers are < 4 Å, whereas for the complexes studied here they are *ca.* 5 Å). These values are indicative of strong electronic coupling between the Ir atoms, in agreement with the DFT data presented above which predicts significant HOMO character on the central OCNNCO fragments of the bridging ligands. For the phenylpyridine complexes **37** and **38** the $\Delta E_{1/2}$ values are smaller than for the phenylpyrazole analogs **35** and **36**. This is in line with the lower calculated HOMO contributions from the bridges of **37** and **38** (Table 2.2). The lowest $\Delta E_{1/2}$ values (*ca.* 250 mV vs. ≥ 400 mV for all other complexes) are observed for complexes **38a** and **38b**, which can be ascribed to the functionalisation of the bridge **44** with strongly electron-withdrawing CF_3 groups which results in lower bridge HOMO contributions (Table 2.2). The electrochemical properties of the diastereomers of the phenylpyridine-functionalized complexes **37** and **38** are very similar.

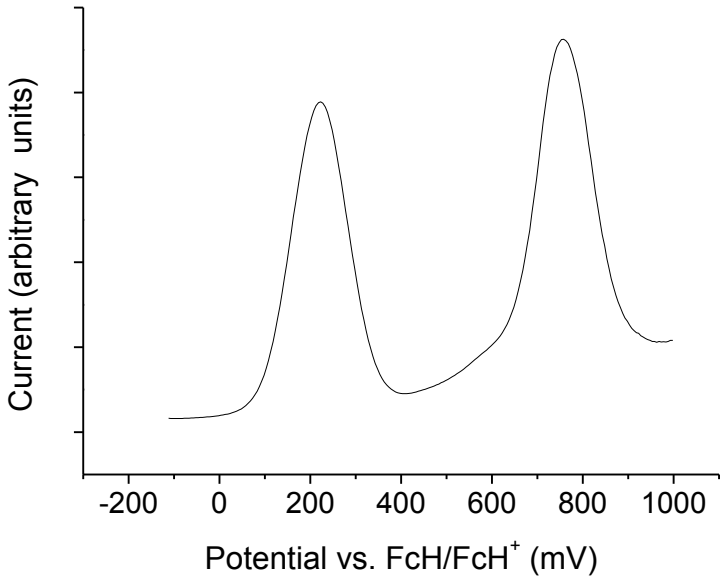

Figure 2.18: Differential pulse voltammogram recorded for a 1:1 mixture of **35a** and **35b** in 0.1 M *n*-Bu_4NPF_6/ DCM.

Photophysical properties[§]

The absorption spectra for the diiridium complexes are shown in Figure 2.19 and the data are listed in Table 2.5. For the phenylpyrazole complexes **35** and **36**, following literature precedents,[2] the bands in the 230–270 nm region are ascribed to spin-allowed ^{1}LC π–π* transitions, while the longer wavelength bands which extend to 400 nm are assigned to promotion to both ^{1}MLCT and ^{3}MLCT states (in order of increasing wavelength). The high energy absorption onsets (*ca.* 420 and 380 nm)

[§] Solution PLQYs and τ were measured by Dr Yu-ting Hsu.

indicate high triplet energies (E_T) of *ca.* 3.0 and 3.3 eV for **35** and **36**, respectively. This is consistent with the intended destabilisation of the lowest energy excited state through the incorporation of pyrazole moieties. The absorption spectra for the phenylpyridine complexes **37** and **38** are red-shifted compared to those of complexes **35** and **36** and similar assignments apply: $^1\pi$–π^* 250–350 nm, ^{1}MLCT and ^{3}MLCT 350–500 nm.[2,40]

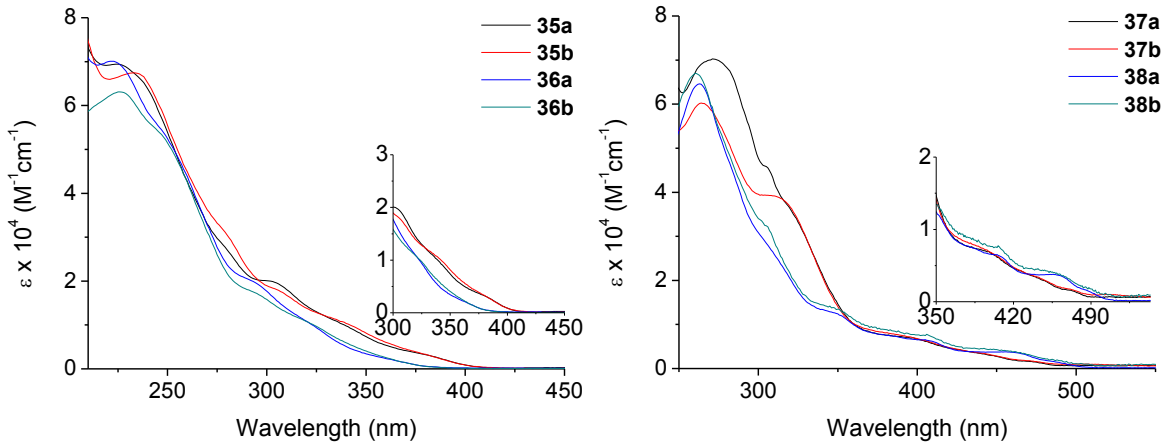

Figure 2.19: (Left) absorption spectra for complexes **35** and **36** recorded in aerated MeCN at room temperature. (Right) absorption spectra for complexes **37** and **38** recorded in aerated DCM at room temperature.

Table 2.5: Absorption spectroscopic data.

Compound	Isomer	λ_{abs} /nm (ε x 10^4 / $M^{-1}cm^{-1}$)
35[a]	**a** *meso*	224 (6.94), 280sh (2.69), 305 (1.95), 341 (0.96), 383 (0.28)
	b *rac*	234 (6.73), 281sh (2.96), 308 (1.75), 344 (0.95), 383 (0.28)
36[a]	**a** *meso*	222 (7.02), 250sh (5.19), 260sh (4.42), 294 (1.97), 326 (1.06), 364 (0.21)
	b *rac*	226 (6.32), 249sh (5.22), 295 (1.71), 323 (1.01), 365 (0.18)
37[b]	**a** *meso*	272 (7.02), 306 (4.57), 321sh (3.52), 399 (0.68), 440 (0.34), 473 (0.15)
	b *rac*	264 (6.04), 313 (3.89), 393 (0.73), 445 (0.32), 474 (0.17)
38[b]	**a** *meso*	262 (6.39), 306sh (2.81), 350 (1.26), 383 (0.75), 408 (0.64), 462 (0.36), 489 (0.16)
	b *rac*	260 (6.70), 306 (3.22), 351 (1.34), 383 (0.88), 461 (0.38)

[a]Room temperature measurements in aerated acetonitrile. [b]Room temperature measurements in aerated DCM. sh = shoulder

The diiridium complexes generally exhibit extinction coefficients larger than those of typical heteroleptic monoiridium complexes for both the LC and MLCT bands.[2,40] This can be explained by considering that a larger number of Ir centres and cyclometallating ligands should increase transition probability. Although the ^{3}MLCT bands display greater ε than some monoiridium complexes, they are not as high as for the diiridium complexes reported by Williams and Kozhevnikov (Chapter 1, complexes **21**–**23**).[32] This is likely due to a comparatively weaker SOC effect

in the diiridium complexes **35–38** presented here, as the intensity of formally forbidden ^{3}MLCT bands is proportional to SOC.[41] The higher k_r values exhibited by Williams and Kozhevnikov's complexes (an order of magnitude higher than for complexes **37** and **38** in the emission data below (Table 2.6)) also serves as evidence that they exhibit a stronger SOC effect.

The emission spectra for the diiridium complexes are presented in Figures 2.20, 2.22 and 2.23 and the key data are listed in Table 2.6. PL could not be detected for the phenylpyrazole complexes **35** and **36** at room temperature in DCM solutions. This can be explained through the thermal population of low-lying non-emissive MC excited states, which has previously been suggested to explain the properties of *fac*-Ir(ppz)$_3$, as discussed in Chapter 1.[6,42] The high E_T values of **35** and **36** (which can be estimated to be > 3 eV from the high energy onsets in the absorption data above) make a narrow MCLT–MC energy gap more likely.

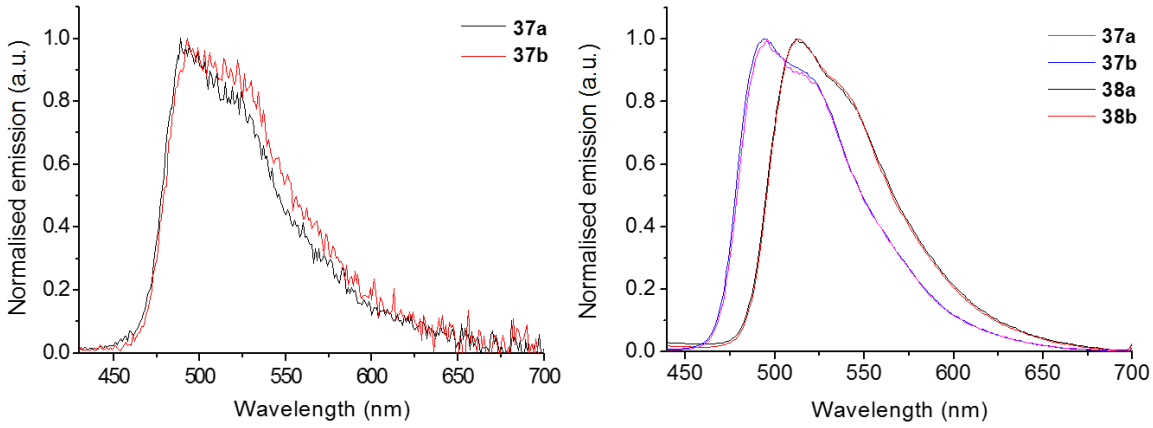

Figure 2.20: (Left) normalised emission spectra of complexes **37a** and **37b** in degassed DCM at room temperature. (Right) normalised emission spectra of complexes **37** and **38** doped into PMMA at 1 wt%. λ_{exc} = 355 nm.

In room temperature DCM solutions, complexes **37** and **38** are poorly emissive in the turquoise and green regions (PLQY < 1% and nanosecond-scale lifetimes) (Table 2.6). The weak emission of complexes **37a** and **37b** (PLQY = 0.2 ± 0.2%) is evident from the noisy emission spectra presented in Figure 2.20. This is ascribed to facile non-radiative deactivation of the excited states of **37** and **38**. This is evidenced by their non-radiative rate constants which are exceptionally high (e.g. k_{nr} = 8.3 × 10^8 s^{-1} for **38a** and **b**), even in comparison to k_{nr} for [Ir(ppy)$_2$μ-Cl]$_2$ (8.0 × 10^6 s^{-1})[37] - a well-known poorly emissive diiridium complex (PLQY = 0.5% in toluene, 0.1% in DCM).[37,43]

Drop cast films of the complexes doped into PMMA were next prepared to examine the effect of a more rigid matrix in an attempt elucidate the cause of the facile non-radiative decay. When doped into PMMA (Figure 2.20), the PLQYs increase by 2–3 orders of magnitude for complexes **37** and **38**,

respectively, with corresponding microsecond-scale lifetimes. This property is related to the comparable decreases in the values of k_{nr} for the complexes (by 2–3 orders of magnitude), whereas the values of k_r remain relatively unchanged: they are on the order of 10^5 s^{-1} for **37** and **38** in both DCM and PMMA.

Table 2.6: Summary of the key photoluminescence data for compounds **35**–**38**.

		DCM solution[a]					2-MeTHF glass[b]		Doped into PMMA 1% wt.[d]				
Ir	**Isomer**	λ_{max}^{em} /nm	PLQY /% (± 5%)[e]	τ /ns	k_r /× $10^5 s^{-1}$	k_{nr} /× 10^5 s^{-1}	λ_{max}^{em} /nm	τ /μs	λ_{max}^{em} /nm	PLQY /% (± 10%)	τ /μs	k_r /× 10^5 s^{-1}	k_{nr} /× 10^5 s^{-1}
35	**a** *meso*	Non-emissive[c]					(421, 448) 542	8.7	Non-emissive[c]				
	b *rac*						(424, 443) 591	7.7					
36	**a** *meso*						(394, 414) 552	26.2					
	b *rac*						(395) 593	7.6					
37	**a** *meso*	489	0.23	34.2	0.58	291.8	479	3.7	493	58	1.5	3.87	2.80
	b *rac*	493	0.23	51.8	0.39	192.7	481	3.6	494	68	1.6	4.25	2.00
38	**a** *meso*	514	0.03	1.2	2.50	8331	502	3.7	512	45	1.7	2.65	3.24
	b *rac*	513	0.03	1.2	2.50	8331	499	4.4	515	42	1.7	2.47	3.41

[a]Solution photoluminescence measurements were recorded in degassed DCM solutions at ca. 20 °C with an excitation wavelength of 355 nm with $Ir(ppy)_3$ as standard (Φ = 0.46).[7] [b]Measured at 77 K using an excitation wavelength of 355 nm. [c]Non-emissive is defined as PLQY < 0.03%. [d]Measured in an integrating sphere under air using an excitation wavelength of 355 nm. [e]± 5% or better. $\tau = 1/ k_{nr} + k_r$.

As ppy-based cyclometallating ligands, such as those employed in **37** and **38**, have been previously incorporated into complexes that are highly emissive in solution,[2,7] it can be concluded that the incorporation of bridging ligands is likely responsible for the low solution PL intensity of **37** and **38**. This explanation is supported by the DFT and electrochemical data above which suggest that the bridges play a significant role in the photophysical properties of the complexes. It is proposed that in room temperature DCM solutions the highly flexible bridges provide a non-radiative decay channel to quench emission via intramolecular motion. When the complexes are doped into rigid PMMA matrices, this motion is suppressed leading to large increases in PLQY. As PMMA is not as rigid as for example, a frozen glass, such a pronounced decrease in non-radiative decay compared to solution implies that a non-radiative pathway is being shut off which involves a relatively large amount of molecular motion (e.g. bridge folding). Importantly, neat films of complexes **37** and **38** drop-cast from DCM solutions are non-emissive (presumably due to triplet–triplet annihilation),[44,45] indicating that this phenomenon occurs in PMMA due to matrix-induced restricted intramolecular motion (RIM), rather than an intermolecular process between Ir complexes.

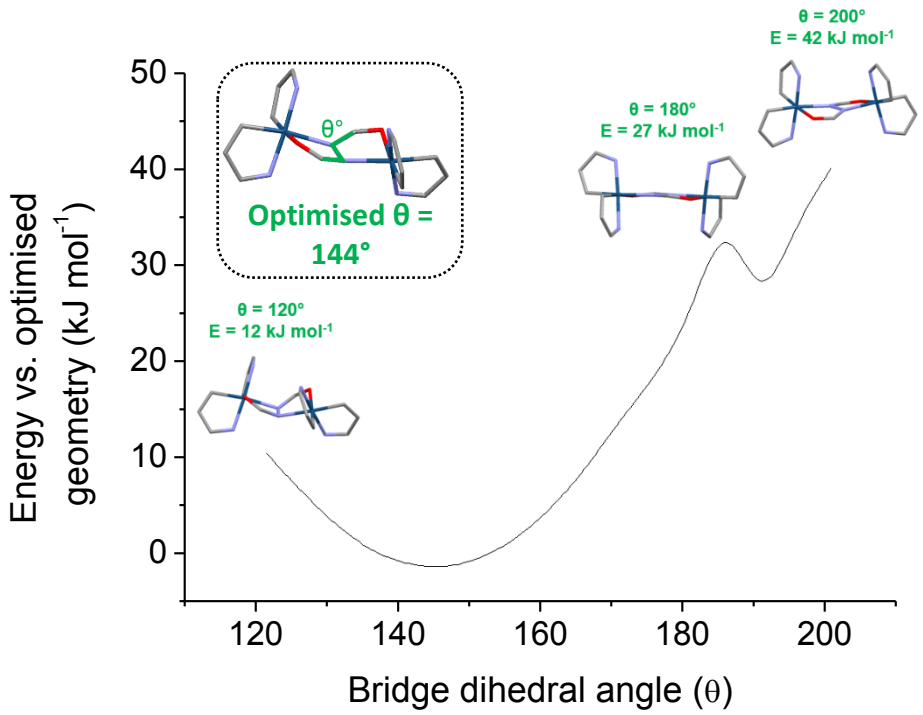

Figure 2.21: Plot of energy vs. bridge dihedral angle for **37b**. Inset: simplified optimised structure of **37b** with the CNNC dihedral labelled.

This theory was further investigated using DFT (Figure 2.21). The central CNNC dihedral angle of the ppy complex **37b** was incrementally varied while the geometry of the rest of the molecule was optimised (B3LYP/LANL2DZ:3–21G* as before). From these calculations it is possible to plot a 1D potential energy (PE) surface relating the energy of the system to the central CNNC dihedral angle to investigate bridge flexibility. The PE surface is relatively shallow: it takes only *ca.* 10 kJ mol^{-1} of energy to fold the bridge 20° from the optimised geometry in either direction, while planar form (θ = 180°) is 27 kJ mol^{-1} higher in energy than the optimised geometry (θ = 144°). The chair–chair interconversion (ring flip) of cyclohexane in solution is known to be facile at room temperature; the energy barrier for which has been estimated to be in the range of 38–59 kJ mol^{-1} and experimentally determined to be 40.6 kJ mol^{-1} from variable temperature NMR studies.[46] Therefore, while is should be noted that the data for **37b** have been obtained from calculations, they indicate that the bridging ligand should be flexible in solution at room temperature, supporting the experimental observations.

Hypsochromic shifts in emission wavelength compared to the literature compound **34** (λ_{max} PL = 521/ 523 nm)[1] (Table 2.6) are achieved through functionalisation with electron-withdrawing groups of the cyclometallating or bridging ligands in complexes **37** and **38**, respectively. These observations indicate that variation of either the bridging or cyclometallating ligands is useful to tune the colour of this diiridium system. Functionalisation of the cyclometallating ligands appears to be more

effective at blue shifting the emission, which is consistent with the fact that the bridge aryl rings are ancillary for these complexes, reducing the impact of any functionalisation.

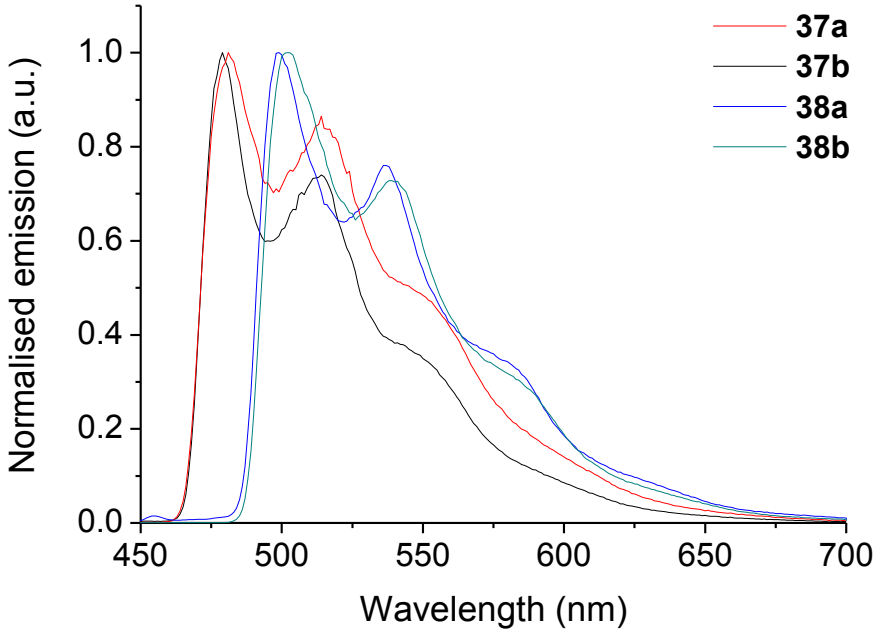

Figure 2.22: Normalised emission spectra of complexes **37** and **38** in 2-MeTHF glasses at 77 K. λ_{exc} = 355 nm.

Complexes **37** and **38** show lifetimes at 77 K in 2-MeTHF glasses increased to the microsecond-timescale (Table 2.6). This is due to a decrease in k_{nr} afforded by a reduction in ambient thermal energy at 77 K, as well as the fact that 2-MeTHF is a rigid glass at that temperature. The increase in lifetime may also be due to a reduction in k_r at low temperature, ascribed to a decrease in the population of the highest energy triplet substate (which tends to exhibit the highest k_r).[47,48,**] The low temperature emission spectra for **37** and **38** (Figure 2.22) show well resolved vibronic structures, which are a consequence of a reduction in ambient thermal energy and may also be indicative of a significant LC contribution to the excited states of the complexes.[49] The emission of **37** and **38** is also blue shifted at 77 K compared to room temperature, by 10–16 nm. This is due to a reduction in solvent relaxation at low temperature, which pushes the emitting state to higher energy in comparison to fluxional room temperature solutions.[50] Large shifts in emission wavelength at low temperature can also be indicative of MLCT character.[51] There is no significant variation in PL properties between the diastereomers for **37** and **38**.

** The values of k_r and k_{nr} at 77 K were not determined as this would require the 77 K PLQY measurement, which is experimentally very challenging.

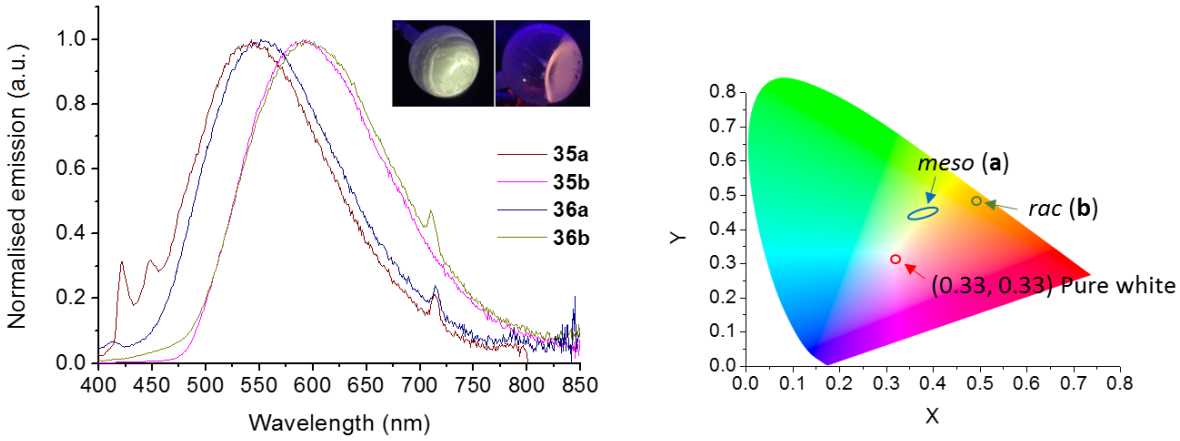

Figure 2.23: (Left) Normalised emission spectra of complexes **35** and **36** in 2-MeTHF glasses at 77 K. λ_{exc} = 355 nm. Inset: photographs of the emission from **35a** (left) and **35b** (right) under irradiation from a 365 nm UV lamp. The peaks at *ca.* 710 nm are the second-order diffraction of the scattered excitation beam. (Right) CIE_{xy} chromaticity diagram for emission from complexes **35** and **36** in 2-MeTHF glasses at 77 K. λ_{exc} = 355 nm.

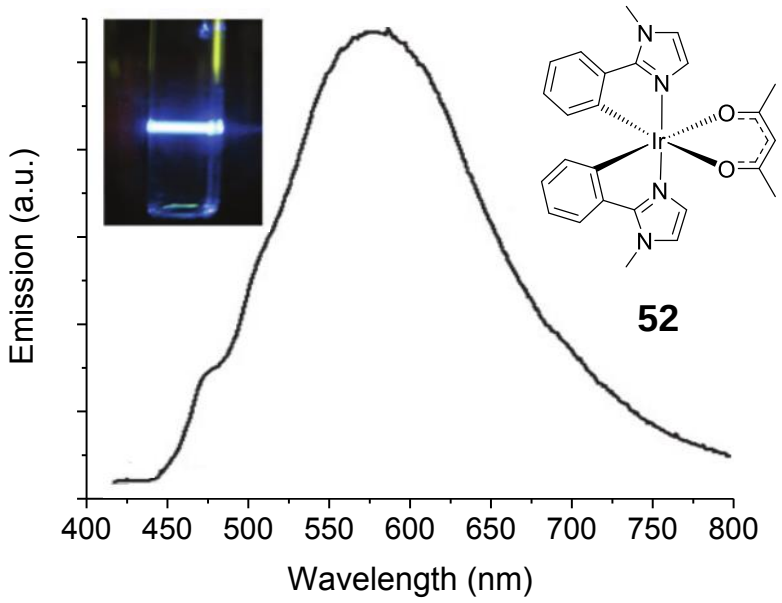

Figure 2.24: Emission spectrum of complex **52** in degassed DCM at room temperature. λ_{exc} = 355 nm. Insets: structure of complex **52** (right) and photograph of emission in DCM under excitation by a 355 nm laser (left). Adapted from ref 33 with permission from the Royal Society of Chemistry copyright 2009.

The photophysical data obtained in PMMA at room temperature and in 2-MeTHF at 77 K (Table 2.6) reinforce the proposed explanation regarding the non-emissive properties of complexes **35** and **36**. In PMMA at room temperature the complexes are non-emissive. This indicates that a rigid environment alone is insufficient to prevent non-radiative quenching, suggesting that the non-emissive properties are not solely due to bridge flexibility. However, cooling the complexes down to 77 K gives rise to emission with microsecond-scale lifetimes. This is because at low temperature

the Boltzmann distribution is altered, suppressing thermal population of the non-radiative MC states (a temperature dependent non-radiative decay pathway).[2,6]

At 77 K, other than the expected (and comparatively weak) emission at *ca.* 400–450 nm (assigned to emission from states of LC/ MLCT character involving the cyclometallating ligands)[13] intense and broad low energy emission bands (450–800 nm) centered at *ca.* 550 and 590 nm are also observed for complexes **35**/ **36a** and **35**/ **36b**, respectively (Figure 2.23). This broad emission is reminiscent of that previously reported at room temperature for the heteroleptic phenylimidazole-functionalized monoiridium complex **52** (Figure 2.24) by Nazeeruddin et al.[33] For **52** the transitions from S_0 to the lowest 3 triplet states were predicted by TD-DFT to be nearly degenerate ($S_0 \rightarrow T_1$ = 440 nm, $S_0 \rightarrow T_1$ = 433 nm and $S_0 \rightarrow T_3$ = 431 nm), involving orbitals on both the cyclometallating and ancillary ligands as acceptor orbitals. This was suspected to be highly significant and indicative of emission from multiple degenerate emissive states of mixed character. In this study TD-DFT calculations (above) yielded similar results for complexes **35a** ($S_0 \rightarrow T_1$ = 437 nm, $S_0 \rightarrow T_2$ = 429 nm, $S_0 \rightarrow T_3$ = 428 nm) and **36a** ($S_0 \rightarrow T_1$ = 417 nm, $S_0 \rightarrow T_2$ = 399 nm, $S_0 \rightarrow T_3$ = 397 nm).[††] Therefore, a similar phenomenon likely explains the broad emission from **35** and **36**. This is strengthened by the fact that complexes **35** and **36** are structurally quite close to **52** and so could feature similar photophysical properties: they are all heteroleptic Ir(III) complexes with diazole-based cyclometallating ligands. In contrast to ppz-type ligands, such as **39** and **40**, the literature contains numerous examples of room temperature emissive Ir(III) complexes featuring phenylimidazole-based cyclometallating ligands.[52–56] Therefore, it is not completely unsurprising that **35** and **36** are non-emissive at room temperature while **52** is emissive.

The wavelength of the broad bands appears to be dependent on the stereochemistry of the complexes and almost independent of substitution on the phenylpyrazole ligands, indicating that the differing molecular symmetry of diiridium diastereomers can have a significant influence on their photophysical properties. This feature is not generally observed in diiridium complexes.[21,40] It is probably related to the notably different bridge conformations between diastereomers observed via XRD and predicted by DFT, considering that TD-DFT predicts the bridges to be heavily involved in the excited states (they have both hole and electron character) for **35** and **36**. Interestingly, due to the broad emission profile the Commission Internationale de L'Éclairage (CIE_{xy}) colour coordinates for the *meso* (**a**) diastereomers (**35a** = 0.39, 0.49, **36a** = 0.35, 0.45) are approaching the

[††] Although the wavelengths for **35a** are near identical to those calculated for complex **52**, it is more significant that the $S_0 \rightarrow T_1$, $S_0 \rightarrow T_2$ and $S_0 \rightarrow T_3$ transitions have narrow energy spacings for **35a**, **36a** and **52**. This is not observed for complexes **37a** and **38a**, or in the literature for $Ir(ppy)_2acac$,[33] which all display emission profiles typical of Ir(III) phosphors and tend to feature degenerate $S_0 \rightarrow T_1$ and $S_0 \rightarrow T_2$ transitions, with the $S_0 \rightarrow T_3$ transition significantly higher in energy.

white colour coordinates of (0.33, 0.33) (see Figure 2.23). For the *rac* (**b**) diastereomers the CIE_{xy} coordinates are (0.49, 0.49) and (0.49, 0.47) for **35a** and **36b**, respectively – further into the yellow region of the spectrum.

Conclusions and future work

In conclusion, four new diarylhydrazide-bridged diiridium complexes **35**–**38** were synthesised to explore the effect of structural variation on the framework of complex **34**. The obtained diastereomers were separated and their photophysical, electrochemical and structural properties were studied.

For the ppy-functionalised complexes **37** and **38**, functionalisation of either the cyclometallating or bridging ligands with electron withdrawing groups was found to blue shift their emission in comparison to **34** through HOMO stabilisation. Their emissive properties were also found to drastically improve upon doping the complexes into solid PMMA matrices, due to matrix-induced RIM (PLQY increases of 2–3 orders of magnitude compared with their DCM solutions). The differences in electrochemical and photophysical properties between diastereomers were minimal for **37** and **38**.

In contrast, for the ppz-functionalised complexes **35** and **36** significant differences in photophysical and electrochemical properties between diastereomers were observed. They are non-emissive at room temperature due to quenching via a temperature dependent process (thermal population of MC states). Interestingly, at 77 K they exhibit broad emission which is dependent on the stereochemistry of the complexes. In the case of the *meso* (**a**) diastereomers the 77 K emission is approaching the white region of the visible spectrum.

DFT and TD-DFT calculations have provided additional insights into the photophysical properties of the complexes. Specifically, they have helped to explain the matrix dependent behaviour of **37** and **38** and the broad emission at 77 K from **35** and **36**.

The structures of the complexes were investigated via single-crystal X-ray diffraction. The geometries of the central bridging units are in excellent agreement with DFT calculations. Some rare examples of intramolecular π–π stacking between the bridging and peripheral ligands of a cyclometallated diiridium complex have also been presented. This feature, combined with the scope for new structural variations in the cyclometallating ligands and the bridges, should increase the appeal of diarylhydrazide-bridged diiridium complexes complexes as an important platform for further studies.

Further investigation into the intramolecular π–π interactions is explored in the next Chapter of this thesis. Based on the work presented in this Chapter, and that of Nazeeruddin and cooworkers,[33] complexes such as **53** (Figure 2.25) may also present an interesting avenue of research in the pursuit of diiridium complexes which emit white light at room temperature.

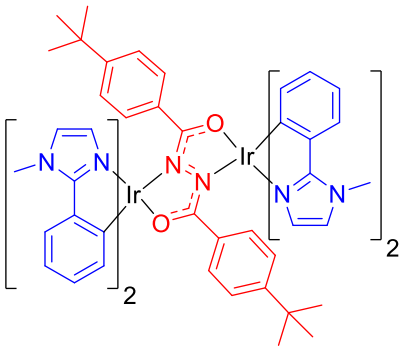

53

Figure 2.25: Proposed structure of complex **53** which may afford room temperature white light emission from a diiridium complex.

References

1 Y. Zheng, A. S. Batsanov, M. A. Fox, H. A. Al-Attar, K. Abdullah, V. Jankus, M. R. Bryce and A. P. Monkman, *Angew. Chem. Int. Ed.*, 2014, **53**, 11616–11619.

2 A. B. Tamayo, B. D. Alleyne, P. I. Djurovich, S. Lamansky, I. Tsyba, N. N. Ho, R. Bau and M. E. Thompson, *J. Am. Chem. Soc.*, 2003, **125**, 7377–7387.

3 E. Baranoff and B. F. E. Curchod, *Dalton Trans.*, 2015, **44**, 8318–8329.

4 M. A. Baldo, S. R. Forrest and M. E. Thompson, in *Organic Electroluminescence*, ed. Z. H. Kafafi, CRC and SPIE Press, 2005.

5 K. Dedeian, J. Shi, N. Shepherd, E. Forsythe and D. C. Morton, *Inorg. Chem.*, 2005, **44**, 4445–4447.

6 T. Sajoto, P. I. Djurovich, A. Tamayo, M. Yousufuddin, R. Bau, M. E. Thompson, R. J. Holmes and S. R. Forrest, *Inorg. Chem.*, 2005, **44**, 7992–8003.

7 H. Benjamin, Y. Zheng, A. S. Batsanov, M. A. Fox, H. A. Al-Attar, A. P. Monkman and M. R. Bryce, *Inorg. Chem.*, 2016, **55**, 8612–8627.

8 H. Benjamin, M. A. Fox, A. S. Batsanov, H. A. Al-Attar, C. Li, Z. Ren, A. P. Monkman and M. R. Bryce, *Dalton Trans.*, 2017, **46**, 10996–11007.

9 H. Oh, K. M. Park, H. Hwang, S. Oh, J. H. Lee, J. S. Lu, S. Wang and Y. Kang, *Organometallics*, 2013, **32**, 6427–6436.

10 J. J. Y. Lee, H. Oh, J. Kim, K.-M. Park, K. S. Yook and Y. Kang, *J. Mater. Chem. C*, 2014, 6040–6047.

11 S. Evariste, M. Sandroni, T. W. Rees, C. Roldán-Carmona, L. Gil-Escrig, H. J. Bolink, E. Baranoff and E. Zysman-Colman, *J. Mater. Chem. C*, 2014, **2**, 5793–5804.

12 T. Duan, T.-K. Chang, Y. Chi, J.-Y. Wang, Z.-N. Chen, W.-Y. Hung, C.-H. Chen and G.-H. Lee, *Dalton Trans.*, 2015, **44**, 14613–14624.

13 J. Frey, B. F. E. Curchod, R. Scopelliti, I. Tavernelli, U. Rothlisberger, M. K. Nazeeruddin and E. Baranoff, *Dalton Trans.*, 2014, **43**, 5667–5679.

14 Y. Zheng, A. S. Batsanov, R. M. Edkins, A. Beeby and M. R. Bryce, *Inorg. Chem.*, 2012, **51**, 290–297.

15 V. Sivasubramaniam, F. Brodkorb, S. Hanning, H. P. Loebl, V. van Elsbergen, H. Boerner, U. Scherf and M. Kreyenschmidt, *J. Fluor. Chem.*, 2009, **130**, 640–649.

16 I. L. Finar and D. M. Rackham, *J. Chem. Soc*, 1968, 211–214.

17 Siegrist, A. E., Patent DE1094753, 1959.

18 S. Xun, G. LeClair, J. Zhang, X. Chen, J. P. Gao and Z. Y. Wang, *Org. Lett.*, 2006, **8**, 1697–1700.

19 E. Baranoff, B. F. E. Curchod, J. Frey, R. Scopelliti, F. Kessler, I. Tavernelli, U. Rothlisberger, M. Gra and K. Nazeeruddin, *Inorg. Chem.*, 2012, **51**, 215–224.

20 U. Müller, *Symmetry Relations between Crystal Structures*, Oxford University Press, 2008.

21 C. Ulbricht, B. Beyer, C. Friebe, A. Winter and U. S. Schubert, *Adv. Mater.*, 2009, **21**, 4418–4441.

22 C. Janiak, *Dalton Trans.*, 2000, 3885–3896.

23 E. Baranoff, H. J. Bolink, E. C. Constable, M. Delgado, D. Häussinger, C. E. Housecroft, M. K. Nazeeruddin, M. Neuburger, E. Ortí, G. E. Schneider, D. Tordera, R. M. Walliser and J. A. Zampese, *Dalton Trans.*, 2013, **42**, 1073–1087.

24 P. Li, G. G. Shan, H. T. Cao, D. X. Zhu, Z. M. Su, R. Jitchati and M. R. Bryce, *Eur. J. Inorg. Chem.*, 2014, 2376–2382.

25 E. C. Constable, C. E. Housecroft, P. Kopecky, C. J. Martin, I. A. Wright, J. A. Zampese, H. J. Bolink and A. Pertegas, *Dalton Trans.*, 2013, **42**, 8086–8103.

26 A. M. Bünzli, E. C. Constable, C. E. Housecroft, A. Prescimone, J. A. Zampese, G. Longo, L. Gil-Escrig, A. Pertegás, E. Ortí and H. J. Bolink, *Chem. Sci.*, 2015, **6**, 2843–2852.

27 L. He, D. Ma, L. Duan, Y. Wei, J. Qiao, D. Zhang, G. Dong, L. Wang and Y. Qiu, *Inorg. Chem.*, 2012, **51**, 4502–4510.

28 S. Kumar, Y. Hisamatsu, Y. Tamaki, O. Ishitani and S. Aoki, *Inorg. Chem.*, 2016, **55**, 3829–3843.

29 H.-J. Cristau, P. P. Cellier, J.-F. Spindler and M. Taillefer, *European J. Org. Chem.*, 2004, **2004**, 695–709.

30 A. M'hamedi, A. S. Batsanov, M. A. Fox, M. R. Bryce, K. Abdullah, H. A. Al-Attar and A. P. Monkman, *J. Mater. Chem.*, 2012, **22**, 13529–13540.

31 K. Hanson, A. Tamayo, V. V. Diev, M. T. Whited, P. I. Djurovich and M. E. Thompson, *Inorg. Chem.*, 2010, **49**, 6077–6084.

32 R. E. Daniels, S. Culham, M. Hunter, M. C. Durrant, M. R. Probert, W. Clegg, J. A. G. Williams and V. N. Kozhevnikov, *Dalton Trans.*, 2016, **45**, 6949–6962.

33 H. J. Bolink, F. De Angelis, E. Baranoff, C. Klein, S. Fantacci, E. Coronado, M. Sessolo, K. Kalyanasundaram, M. Grätzel and M. K. Nazeeruddin, *Chem. Commun.*, 2009, 4672–4674.

34 M. Tavasli, T. N. Moore, Y. Zheng, M. R. Bryce, M. A. Fox, G. C. Griffiths, V. Jankus, H. A. Al-Attar and A. P. Monkman, *J. Mater. Chem.*, 2012, **22**, 6419.

35 X. Yang, X. Xu, J. Dang, G. Zhou, C.-L. Ho and W.-Y. Wong, *Inorg. Chem.*, 2016, **55**, 1720–1727.

36 J. Fernández-Cestau, N. Giménez, E. Lalinde, P. Montaño, M. T. Moreno and S. Sánchez, *Organometallics*, 2015, **34**, 1766–1778.

37 M. Y. Wong, G. Xie, C. Tourbillon, M. Sandroni, D. B. Cordes, A. M. Z. Slawin, I. D. W. Samuel and E. Zysman-Colman, *Dalton Trans.*, 2015, **44**, 8419–8432.

38 T. Hajra, A. J. K. Bera and V. Chandrasekhar, *Aust. J. Chem.*, 2011, **64**, 561–566.

39 A. M'hamedi, M. A. Fox, A. S. Batsanov, H. A. Al-Attar, A. P. Monkman and M. R. Bryce, *J. Mater. Chem. C*, 2017, **5**, 6777–6789.

40 S. Lamansky, P. Djurovich, D. Murphy, F. Abdel-Razzaq, H. E. Lee, C. Adachi, P. E. Burrows, S. R. Forrest and M. E. Thompson, *J. Am. Chem. Soc.*, 2001, **123**, 4304–4312.

41 A. Tsuboyama, T. Takiguchi, S. Okada, M. Osawa, M. Hoshino and K. Ueno, *Dalton Trans.*, 2004, 1115–1116.

42 X. Zhou, P. L. Burn and B. J. Powell, *Inorg. Chem.*, 2016, **55**, 5266–5273.

43 G. A. Carlson, P. I. Djurovich and R. J. Watts, *Inorg. Chem.*, 1993, **32**, 4483–4484.

44 S. Reineke, K. Walzer and K. Leo, *Phys. Rev. B - Condens. Matter Mater. Phys.*, 2007, **75**, 125328.

45 N. C. Giebink and S. R. Forrest, *Phys. Rev. B - Condens. Matter Mater. Phys.*, 2008, **77**, 235215.

46 F. R. Jensen, D. S. Noyce, C. H. Sederholm and A. J. Berlin, *J. Am. Chem. Soc.*, 1960, **82**, 1256–1257.

47 T. Sajoto, P. I. Djurovich, A. B. Tamayo, J. Oxgaard, W. A. Goddard and M. E. Thompson, *J. Am. Chem. Soc.*, 2009, **131**, 9813–9822.

48 T. Hofbeck and H. Yersin, *Inorg. Chem.*, 2010, **49**, 9290–9299.

49 A. Tsuboyama, H. Iwawaki, M. Furugori, T. Mukaide, J. Kamatani, S. Igawa, T. Moriyama, S. Miura, T. Takiguchi, S. Okada, M. Hoshino and K. Ueno, *J. Am. Chem. Soc.*, 2003, **125**, 12971–12979.

50 J. Lakowicz, *Principles of Fluorescence Spectroscopy*, Springer, 3rd edition, 2006.

51 E. S. Andreiadis, D. Imbert, J. Pécaut, A. Calborean, I. Ciofini, C. Adamo, R. Demadrille and M. Mazzanti, *Inorg. Chem.*, 2011, **50**, 8197–8206.

52 E. Baranoff, S. Fantacci, F. De Angelis, X. Zhang, R. Scopelliti, M. Grätzel and M. K. Nazeeruddin, *Inorg. Chem.*, 2011, **50**, 451–462.

53 H. Cho, J. Lee, J. I. Lee, N. S. Cho, J. H. Park, J. Y. Lee and Y. Kang, *Org. Electron.*, 2016, **34**, 91–96.

54 J. Zhuang, W. Li, W. Su, Y. Liu, Q. Shen, L. Liao and M. Zhou, *Org. Electron.*, 2013, **14**, 2596–2601.

55 T. Karatsu, M. Takahashi, S. Yagai and A. Kitamura, *Inorg. Chem.*, 2013, **52**, 12338–12350.

56 X. Yang, G. Zhou and W.-Y. Wong, *Chem. Soc. Rev.*, 2015, **44**, 8484–8575.

Chapter 3: Intramolecular π–π stacking and sky-blue emission in diarylhydrazide-bridged diiridium complexes

Introduction

In the previous Chapter intramolecular face-to-face π–π contacts between the bridge aryl groups and the phenyl groups of the peripheral cyclometallating ligands were observed in the X-ray crystal structures of the diarylhydrazide-bridged diiridium complexes **35**–**38** (Figure 2.7). This is shown again for complex **37b** in Figure 3.1. In this Chapter these interactions are tuned through structural modification, leading to marked effects on the photophysical properties of the complexes. Colour tuning is also explored to afford the first examples of sky-blue emissive bridged diiridium complexes.

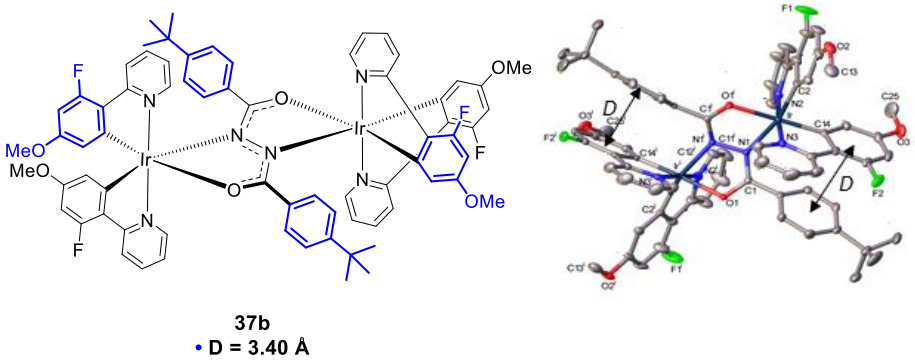

Figure 3.1: Molecular and X-ray crystal structures of **37b**. Intramolecular π–π interactions between bridging and peripheral ligands are highlighted with coloured rings and arrows. D = distance between the centroid of the bridge aryl ring and the plane of the cyclometallating ligand from single crystal XRD measurements.

π–π interactions (π–π stacking) are non-covalent interactions that are present due to some form of through-space attraction between unsaturated organic compounds on the length scale of *ca.* 3.3–3.8 Å.[1] They are of vital significance in supramolecular chemistry,[2–5] being important in molecular recognition and fulfilling key roles in the self assembly of biomacromolecules such as of DNA.[6,7] They are also manifested in small molecules. For example, intermolecular π–π stacking is responsible for the common observation that extended π systems (such as acenes) quickly become insoluble with an increase in the number of aromatic rings.[8–10] The debate over the origin of such interactions is still ogoing: electrostatics, charge-transfer interactions, van der Waals/ London

dispersion interactions and desolvation energies (the solvophobic model) have all been suggested as important factors, the contributions of which are expected to vary dependent on the systems in question.[8,11] The validity of the commonly used 'π–π stacking' term itself has also been questioned, as it implies an attractive force between two partially negatively charged (δ−) π systems (which intuitively should repel each other) and suggests some form of special interaction which cannot be explained through a consideration of other phenomena.[9,12] The work in this Chapter mainly concerns π–π interactions between electron rich and electron poor aryl systems – a situation where an electrostatic model first proposed by Hunter and Sanders generally fits well with experimental observations.[8,11,12]

π–π Interactions between aryl and perfluoroaryl groups

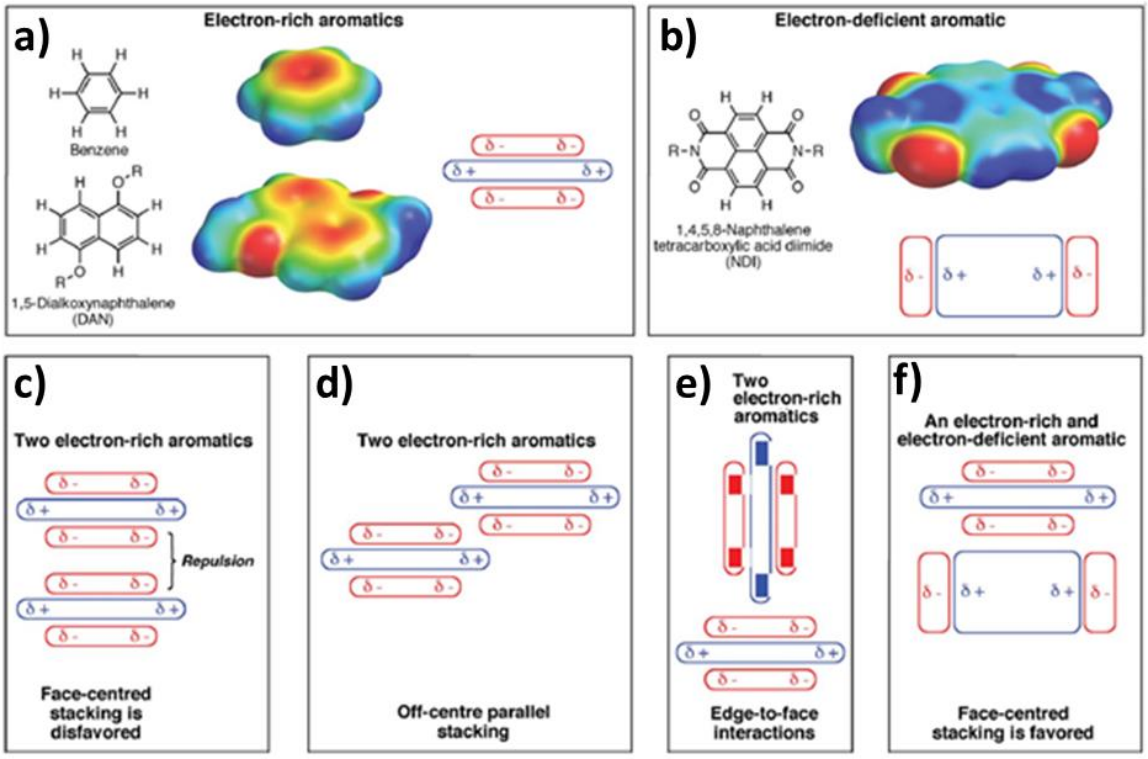

Figure 3.2: Diagrams to qualitatively describe the aromatic quadrupole moments of electron rich and electron poor aromatic molecules and how they affect the potential modes of stacking. For the electrostatic potential surfaces red is electron rich and blue is electron poor. Adapted from ref 12 with permission from the Royal Society of Chemistry copyright 2012.

The Hunter and Sanders model[8] (also referred to as the polar/pi model)[12] is primarily based on electrostatic arguments. The π electron density on benzene and most aromatic rings creates a quadrupole moment with a partial negative charge above each aromatic face and a partial positive charge (δ+) around the periphery (i.e. the H atoms on benzene) as portrayed in Figure 3.2 a).

Repulsion from the δ− regions makes face-to-face stacking unfavoured for electron-rich aromatics such as benzene (c). They instead tend to display off-centre parallel π–π stacking (d) or edge-to-face (T) stacking (CH–π interactions) (e), which both promote interactions between the δ− π systems and δ+ H atoms.

The situation changes for aromatic systems functionalised with strong electron withdrawing groups (b). The electron density is pulled away from the π system, leading to a quadrupole moment where there is a δ+ charge above each aromatic face with δ− charges on the peripheral groups. Therefore, the model predicts that face-centred stacking is favoured between electron rich and electron deficient aromatics (f).[12]

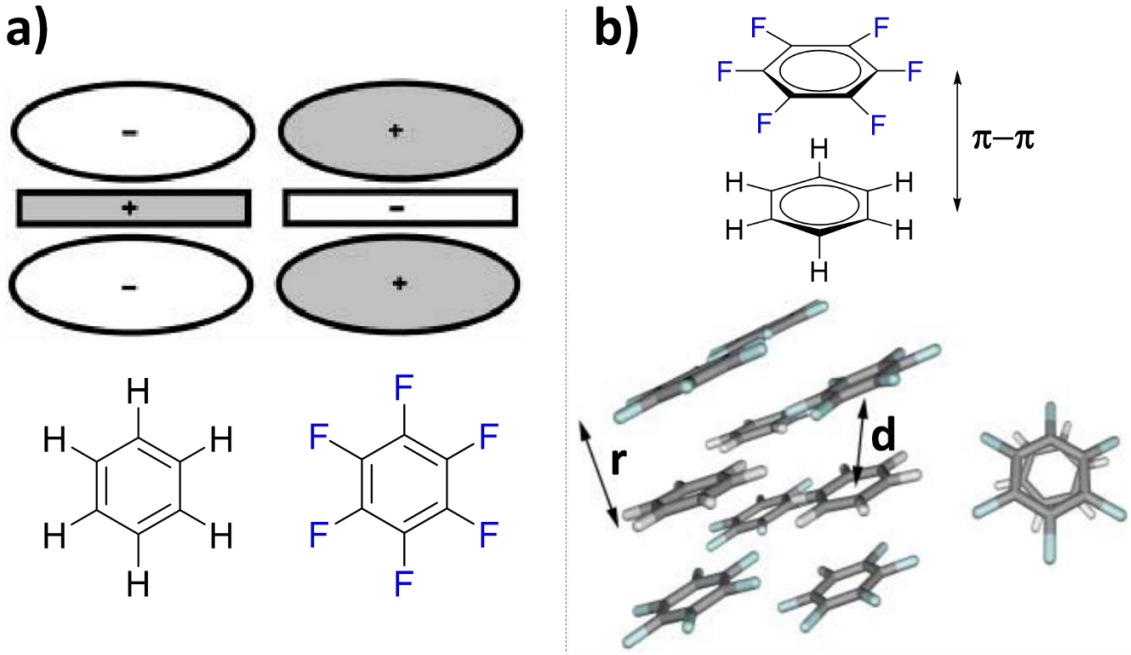

Figure 3.3: a) Molecular structures and schematics representing the quadrupole moments for benzene and perfluorobenzene. b) Diagram and X-ray crystal structure highlighting the face-to-face stacking in the 1:1 benzene/perfluorobenzene complex. r = interplanar distance (*ca*. 3.4 Å), d = intercentroid distance (*ca*. 3.7 Å). Adapted from ref 11 with permission from Wiley-VCH copyright 2003.

Such face-to-face π–π interactions are observed in the 1:1 complex of benzene/ perfluorobenzene (Figure 3.3). Due to the minimal steric influence of the fluorine atoms,[13] close interplanar distances of *ca.* 3.4 Å are observed. This arrangement contrasts with the T-shape stacking seen in the crystal structures of either component, leading to interesting physical properties.[11] The complex is solid at room temperature with a melting point of 23.7 °C, *ca.* 19 °C higher than for either of the components,[14] implying that intermolecular forces are stronger as a consequence of the face-to-

face stacking. The face-to-face stacking is due to electrostatics rather than the formation of a charge transfer complex, evident from the absence of charge transfer bands in the UV absorption spectrum of the complex.[14] However, in complexes of perfluorobenzene with more electron rich aromatics such as *N,N*-dialkylanilines, charge-transfer is observed.[15]

Cozzi and Siegel et al. have investigated intramolecular face-to-face π–π interactions using some diarylnaphthalenes.[16,17] In one study, π–π interactions between aromatic and fluoroaromatic rings were quantified.[17] The studied structures **54** and **55** are shown in Figure 3.4. The rotation barrier for the non-fluorinated ring B was estimated from ^{1}H NMR exchange data for both series. For the series **54a**–**d** the rotation barrier increases with incremental fluorination of ring A. For the series **55a**–**c** the barrier to rotation is greatest in **55c** for which ring A is the most electron withdrawn, and ring B is the most electron rich. The data for both series are consistent with an electrostatic model.

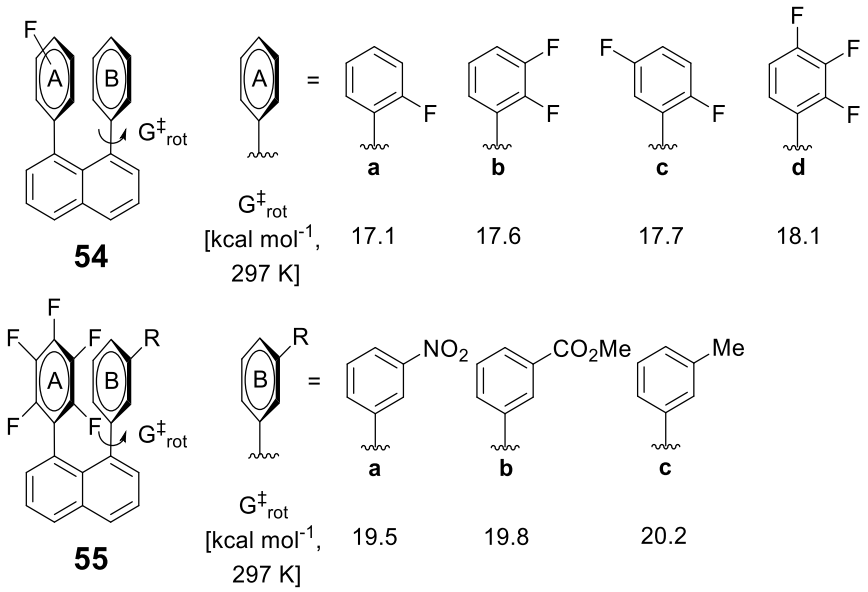

Figure 3.4: Molecular structures of diarylnaphthalenes employed to study intramolecular π–π interactions.

Hunter and co-workers studied intermolecular face-to-face π–π interactions involving heavily fluorinated rings.[18] In chemical and biological systems, studying a single interaction in isolation can in principle be extremely difficult, as any modification can lead to a change in multiple variables.[19] For example, varying an *ortho* group on an aryl system can influence both steric and electronic factors, which is one of the reasons that Hammett parameters are tabulated for *meta* and *para* substituents only.[20] One way to combat this issue for non-covalent interactions is through double mutant cycle methodology.[18,19,21,22]

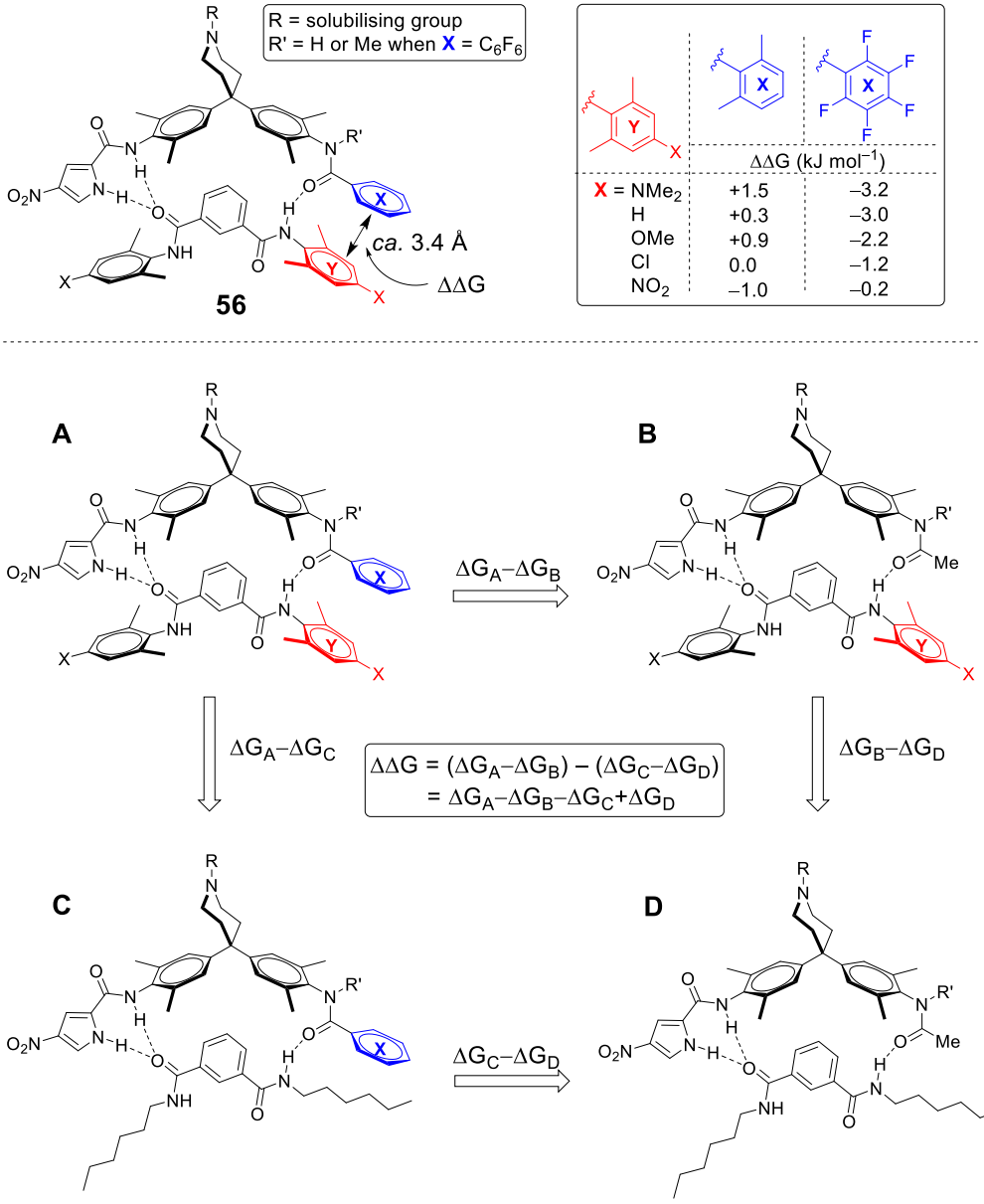

Figure 3.5: Double mutant cycle used to quantify intermolecular π–π interactions.

The cycle for a system based on **56** is presented in Figure 3.5. Direct modification of **A** to the 'single mutant' **B** cannot be used to calculate stacking free energies (ΔΔG). This is because as well as eliminating the stacking interaction, substituting ring X of **A** for a methyl group in **B** also alters the influence of secondary interactions such as hydrogen bonding. The same problem applies if ring Y is removed to give **C**. However, the secondary interactions can be quantified through removing rings X and Y simultaneously to give the 'double mutant' **D**. This is because replacing ring X for a methyl group in the transformation **C→D** only influences secondary interactions. Therefore, comparing complexes **C** and **D** enables the magnitude of the secondary interaction change in the transformation **A→B** to be quantified, meaning the difference between the two horizontal

transformations gives the magnitude of the π–π interactions in the absence of secondary effects: $\Delta\Delta G = (\Delta G_A - \Delta G_B) - (\Delta G_C - \Delta G_D)$. Comparing the vertical mutations **A→C** (changes in stacking and secondary effects) and **B→D** (changes in secondary effects only) yields the same result.

Results indicated greater stabilisation due to π–π interactions for the analogues featuring complementary electron poor and electron rich aryl rings, in agreement with a process dominated by electrostatics. An interaction between electron poor pentafluorophenyl and nitroxylyl rings was also found to be marginally attractive, which is also predicted by the model proposed by Hunter and Sanders.[8]

In conclusion, taking the benzene dimer as a model system, face-to-face π–π stacking can be promoted through substitution of one of the rings with electron withdrawing groups, which is well predicted by an electrostatic model. Fluorine atoms are particularly appealing for this task, being the most electronegative element and exerting a minimal steric effect compared to protons.[13] A wide range of fluorinated aromatic compounds is also commercially available.

Intramolecular π–π interactions in cyclometallated Ir(III) complexes

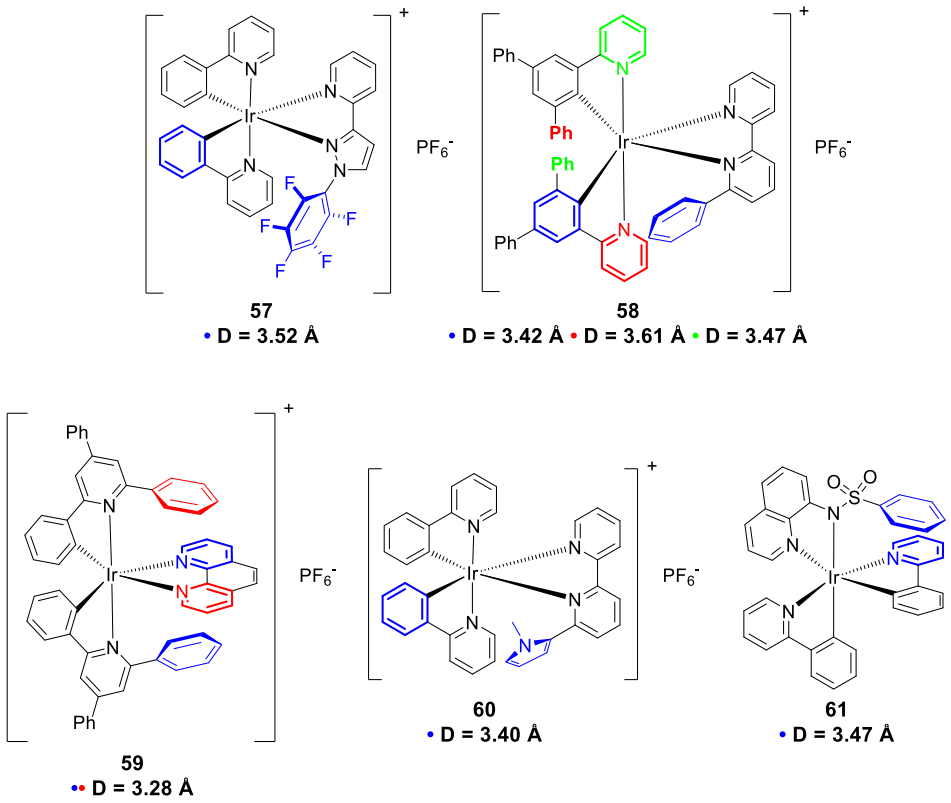

Figure 3.6: Representative iridium complexes which display intramolecular π–π stacking interactions, highlighted by the coloured rings. D = centroid–centroid distance determined by X-ray diffraction for the same-coloured rings.

Face-to-face intramolecular π–π stacking between aryl and heteroaryl rings has been reported in a few specific monoiridium complexes (**57**–**61**), the structures of which are shown in Figure 3.6.[23–27] In **57**, intramolecular π–π stacking between a cyclometallating phenyl group and a pendant pentafluorophenyl group on the ancillary ligand rigidifies the complex, leading to a reduction in k_{nr} and an order of magnitude increase in solution PLQY.[25] In complex **58**, 3-fold intramolecular π–π stacking encapsulates the Ir core, leading to an increased operational stability in LEECs.[23] For complex **59**, very close centroid–centroid distances of 3.28 Å are observed in the X-ray crystal structure. However, due to the congested structure the axial Ir–N bonds are slightly lengthened, leading to a decrease in PLQY compared to the parent $[Ir(ppy)_2phen]^+$ complex.[27] Complex **60** is a rare example which displays intramolecular π–π interactions between a cyclometallating phenyl ring and a pendant heteroaryl ring.[24] The structure is distorted by the methyl group on the pendant pyrrole, which may contribute to the poor solution PLQY (< 1% in MeCN). Complex **61** is part of an interesting series of compounds that display dual emission characteristics, although there is no indication that intramolecular π–π interactions have a significant effect on the photophysical properties.

In conclusion, there is literature precedent (particularly in complexes **57** and **58**) that intramolecular π–π interactions can serve as a tool for the modulation of the photophysical properties of Ir complexes. However, the potential of intramolecular π–π interactions to influence the photophysical properties of diiridium complexes remains unexplored, and provides the motivation for the present study.

Results and discussion

Design, synthesis and characterisation

The structures of the complexes (**62**–**70**) and ligands (**72**–**76**) studied in this Chapter are shown in Figure 3.7.

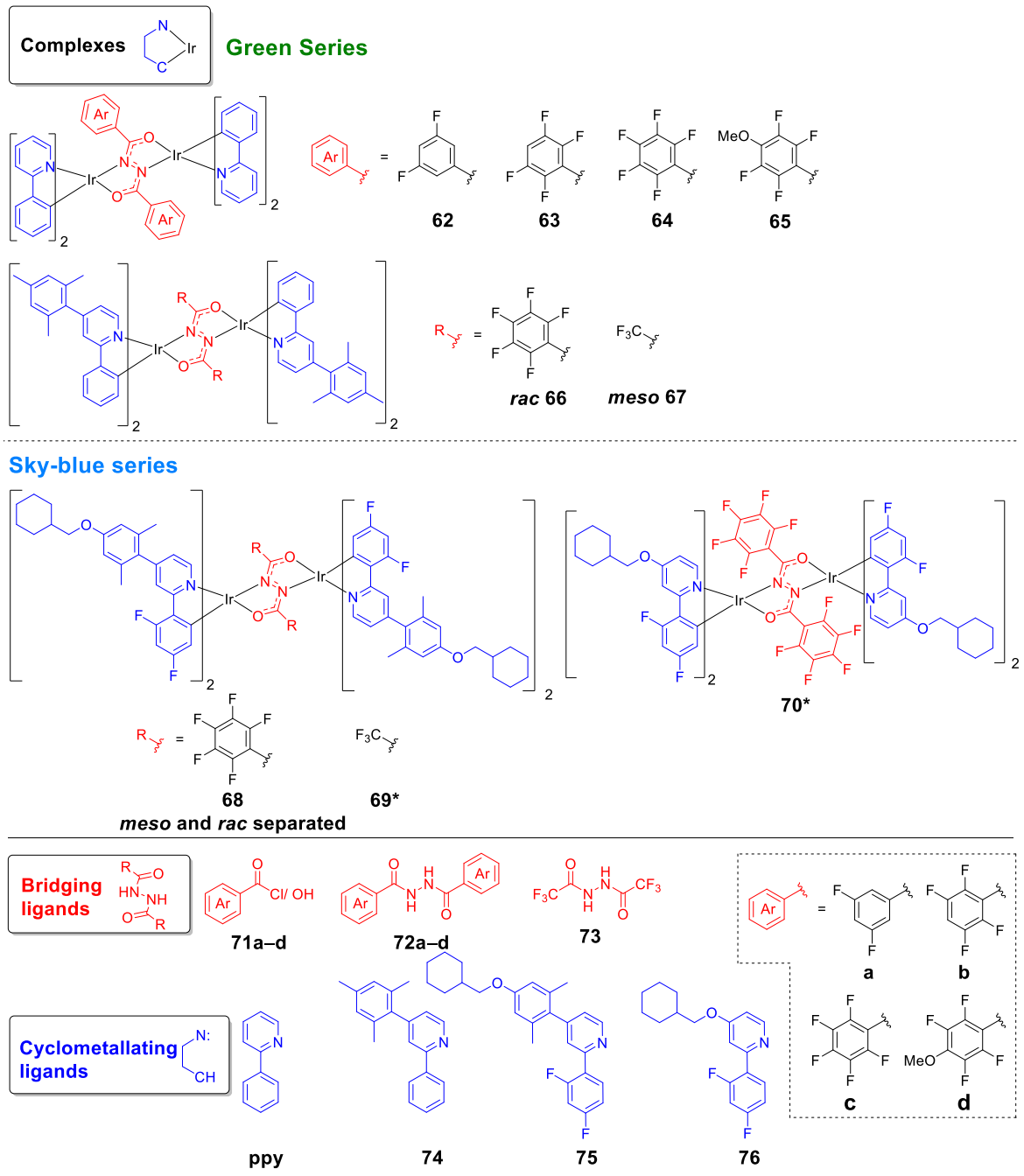

Figure 3.7: Structures of the diiridium complexes and ligands studied in this Chapter. Complexes were studied as diastereomeric mixtures unless otherwise stated. * Complexes **69** and **70** were isolated as single diastereomers; their absolute configurations are unknown.

The complexes can be broadly categorised based on the colour of their emission. Complexes **62**–**67** form the green series, whereas complexes **68**–**70** constitute the sky-blue series. The literature above indicates that fluorination of an aryl ring can encourage face-to-face π–π interactions. Therefore, complexes **62**–**64** with an increasing number of fluorine substituents on the phenyl rings of the bridge were designed, the aim being to promote intramolecular π–π interactions more extensively than in the complexes **35**–**38** studied in Chapter 2. These interactions are also expected to benefit from the fact that cyclometallated phenyl rings are comparatively electron rich, carrying a formal negative charge. This is evident in the observation that cyclometallated phenyl rings on Ir complexes undergo facile electrophilic aromatic substitution (S_EAr).[28] The methoxy-functionalised derivative **65** was also included, as in contrast to **63** and **64**, DFT calculations (discussed below) predict the bridge of **65** to be non-ancillary despite the highly fluorinated aryl rings. The analogues **67** and **69**, featuring CF_3 substituents instead of perfluoroaryl rings, were studied as model compounds for which π–π interactions involving the bridge are not possible. For derivatives **66**–**70**, the substituents on the pyridyl rings serve to enhance solubility.

For **68**–**70** the difluorophenyl rings of the ppy ligands were chosen to blue shift the emission. This is based on monoiridium precedents[29,30] and the results obtained in Chapter 2. In Chapter 2 and in the literature,[31] the diastereomers of diarylhydrazide-bridged ppy-functionalised diiridium systems were separated and minimal differences were observed in the photophysical properties of the two diastereomers. Therefore, the diiridium complexes in this Chapter were characterised and studied as diastereomeric mixtures unless otherwise stated (e.g. for complexes where only one diastereomer was isolated, or for which diastereomer separation was especially facile).

The synthetic schemes for the bridging ligands and a general scheme for the diiridium complexes are shown in Figure 3.8. The diarylhydrazide bridges **72a**–**d** were synthesised by condensation of hydrazine monohydrate with the corresponding benzoyl chlorides, which were either commercially available or prepared from the corresponding benzoic acid (**71a**–**d**). They were obtained sufficiently pure for the next step after recrystallisation. The CF_3-functionalised bridge **73** was synthesised from trifluoroacetic anhydride, which is more convenient and safer than employing gaseous trifluoroacetyl chloride.

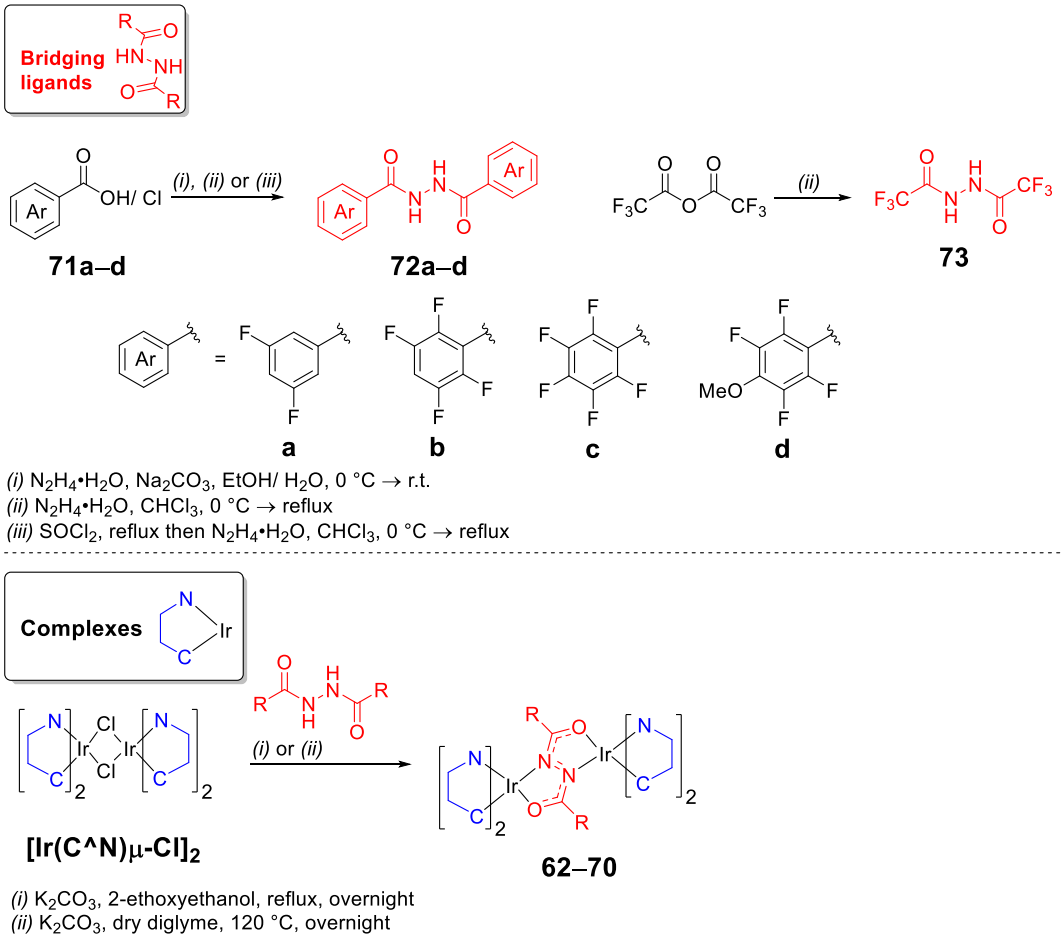

Figure 3.8: Synthetic schemes for the bridging ligands and complexes studied in this Chapter.

The diiridium complexes were obtained through heating the appropriate μ–Cl dimer and bridging ligand in a 1:1 ratio in the presence of K_2CO_3. To obtain complex **62**, which features the bis(difluorophenyl) bridge **72a**, polar protic 2-ethoxyethanol was employed as the solvent. For complexes featuring the more heavily fluorinated bridges **72b–d**, polar aprotic solvents were explored to avoid the potential for substitution of aromatic fluorine atoms through a nucleophilic aromatic substitution mechanism (S_NAr). Such substitution has been previously observed for activated aromatic fluorine atoms on Ir complexes in the presence of alkoxide ions.[32] Conditions employing either dry MeCN or 1,4-dioxane did not provide full conversion to the diarylhydrazide-bridged complexes. MALDI mass spectrometry indicated that although the bridging ligands inserted, the second bridging chloride ligand was not displaced. This problem was overcome by using dry diglyme as the solvent. It was selected as it is structurally similar to the classical 2-ethoxyethanol, while being polar aprotic and possessing a high enough boiling point to be heated to 120–140 °C, which was required for full conversion.

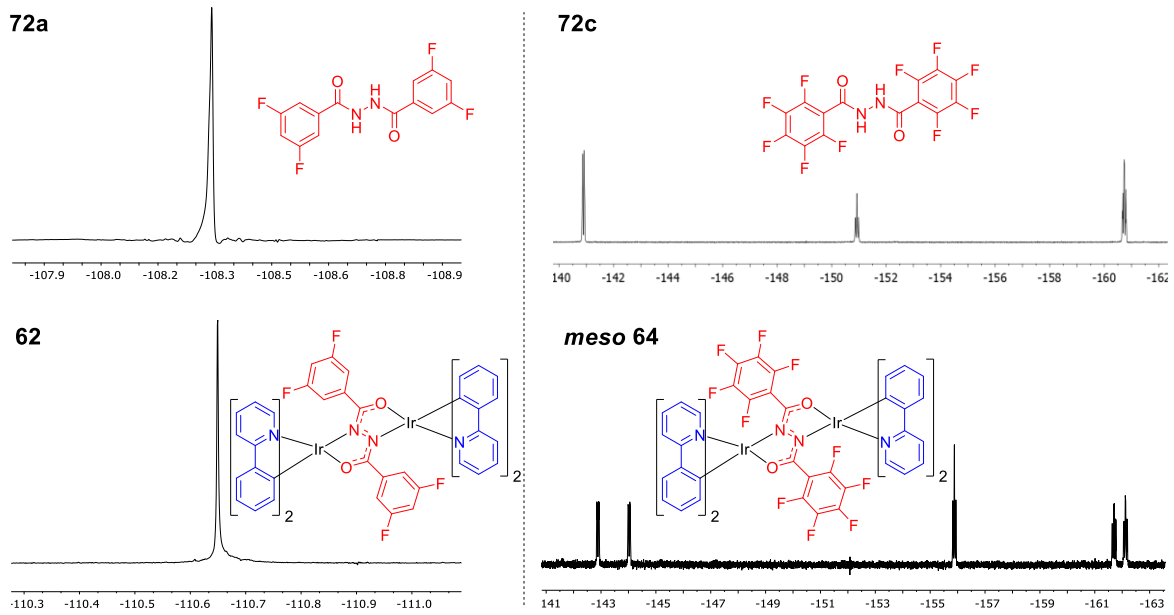

Figure 3.9: ^{19}F $\{^{1}H\}$ NMR spectra of the bridging ligands **72a** and **72c** and the complexes **62** and *meso* **64**. Chemical shifts are in ppm.

For the diarylhydrazide-bridged complexes **62**–**66**, **68** and **70** the ^{19}F NMR data are of particular interest. For the bis(difluorophenyl)hydrazide-bridged complex **62**, a single peak is observed in the ^{19}F NMR spectrum of the diastereomeric mixture (Figure 3.9). This is analogous to the spectrum of the free bridge (**72a**) and indicates that the ^{19}F environments are very similar for each diastereomer of **62**, with the bridging phenyl rings freely rotating in solution on the NMR timescale. Similar free rotation of the bridge phenyl rings is also observed for the diiridium complexes studied in Chapter 2 (**35**–**37**).*

The data for **62** contrast with that obtained for the bis(pentafluorophenyl)hydrazide-bridged complex **64**. The ligand **72c** features 3 distinct environments in its ^{19}F NMR spectrum as expected, with an integral ratio of 2:2:1 (Figure 3.9). However, the ^{19}F NMR spectrum for *meso* **64** displays a breakdown in symmetry, featuring 5 well-resolved distinct environments of equal integration (this is also observed for the *rac* isomer – Figure 3.10). This suggests that rotation of the bridging pentafluorophenyl rings is restricted in *meso* **64** at room temperature in solution.

* It is noted that for complexes **38a** and **38b**, free rotation of the bridge phenyl rings appears to be somewhat restricted from inspection of their ^{1}H and ^{19}F NMR spectra. This is attributed to the bulky CF_3 groups. However, the breakdown in symmetry observed in their ^{19}F NMR spectra is much less well resolved than for **64**.

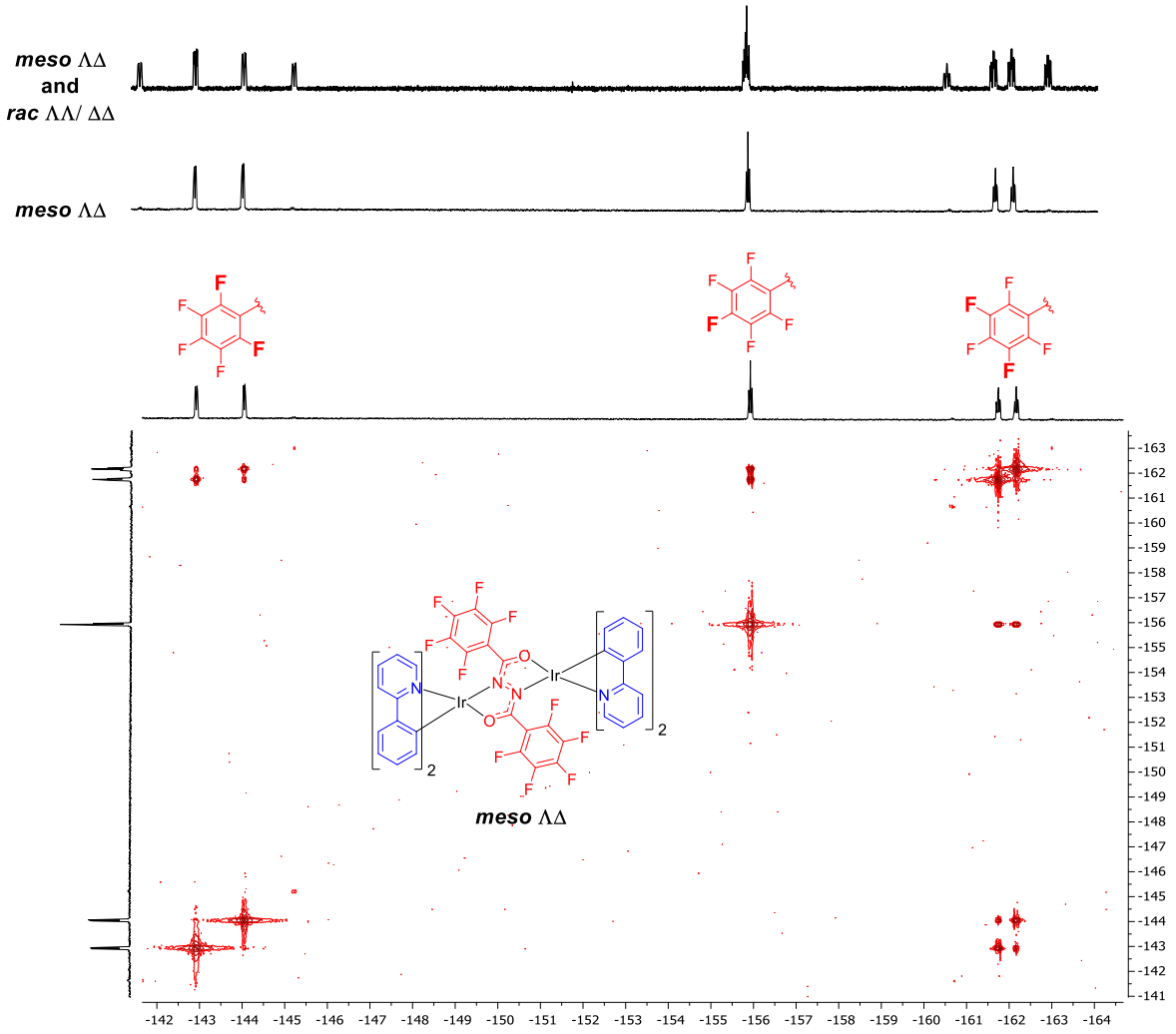

Figure 3.10: (Top) ^{19}F NMR spectrum of the diastereomeric mixture of **64** (*ca.* 5:4 molar ratio of *meso* (ΛΔ) and *rac* (ΛΛ/ ΔΔ)). (Middle) ^{19}F NMR spectrum of *meso* **64**. (Bottom) ^{19}F–^{19}F COSY NMR spectrum of *meso* **64**. Chemical shifts are in ppm.

Meso **64** was further studied by ^{19}F–^{19}F COSY NMR (Figure 3.10). Only *ortho* (^{3}J ≈ 23 Hz) and *para* (^{5}J ≈ 6 Hz) cross peaks are observed, while *meta* (^{4}J) coupling is absent. This is in agreement with the multiplicities of the signals in the 1D spectrum (in order of increasing chemical shift: apparent triplet of doublets × 2, triplet and doublet of doublets × 2). Nevertheless, although *meta* (^{4}J) coupling is absent, the data indicate that all 5 fluorine environments are on the same ring, confirming a breakdown in symmetry due to restricted rotation. *Meta* (^{4}J) ^{19}F–^{19}F coupling constants that are considerably smaller than those for *ortho* (^{3}J) and *para* (^{5}J) coupling (or even absent) have been commonly reported for heavily fluorinated aryl systems.[33–37] It has been suggested that this is because π-conjugation contributes more strongly to ^{19}F–^{19}F coupling in aromatic systems, leading to ^{5}J coupling constants that are greater than ^{4}J ones despite the increased distance.[33,37] This is in

contrast to $^{1}H–^{1}H$ coupling for instance, where the coupling component through σ bonds is stronger, resulting in a more clear distance dependence for planar aromatic systems ($^{3}J > {}^{4}J > {}^{5}J$).

These data suggest that this restriction of rotation is due to intramolecular π–π interactions. Fluorination appears to promote π–π interactions in this system to the level where it can be observed in solution through ^{19}F NMR. Steric restriction alone is unlikely to explain such well-resolved ^{19}F NMR signals, considering that fluorine atoms exert similar steric effects as protons,[13] and that the analogous difluoro complex **62** does not exhibit this effect. The ^{19}F NMR spectra of complexes **63**, **65**, **66**, **68** and **70** show the same feature as **64**. These observations indicate that a bridge tetrafluorophenyl group is sufficient to promote strong intramolecular π–π interactions in solution (**63** and **65**), and that fluorine atoms on the cyclometallating phenyl rings of ppy ligands (**68** and **70**) do not suppress them.

The bis(trifluoromethyl) bridge **73**[38] (Figure 3.7) was also investigated, as although it is strongly electron withdrawing like the perfluoroaryl bridge **72c**,[20,†] it cannot engage in intramolecular π–π stacking. Attempts to isolate a complex analogous to **64** by reacting the bridge **73** with $[Ir(ppy)_2\mu–Cl]_2$ were unsuccessful. Although MALDI mass spectrometry suggested the complex had formed, it was too insoluble to purify and characterise. As an alternative, complex **67** was synthesised (Figure 3.7), which features 4-mesityl-2-phenylpyridine (**74**) cyclometallating ligands.[39] This ligand was selected as there is literature precedent for mesityl substituents improving the solubility of cyclometallated iridium complexes while exerting minimal influence on their photophysical properties.[39–41] This is because they sit orthogonal to the cyclometallating ligand plane, precluding conjugation. The schemes for the syntheses of **74** and the other non-commercially available cyclometallating ligands studied in this Chapter (**75** and **76**) are shown in Figure 3.11.

Complex **67** was isolated as a diasteromerically pure *meso* sample (confirmed below by X-ray diffraction, Figure 3.12) in 61% yield. No *rac* diastereomer was detected in the crude reaction mixture. This stereoselectivity is surprising as DFT calculations (below) predict the *rac* diastereomer to be the more thermodynamically stable (by 9.5 kJ mol^{-1}). This is the also case for other diiridium systems (likely due to increased interligand steric clash in the *meso* forms as mentioned in Chapter 2).[31,42,43] Attempts to isomerise **67** photochemically (5 W TLC lamp irradiating a DCM solution) or

[†] The σ_{meta}, σ_{para} and inductive/ field factor (F) values for C_6F_5 and CF_3 are 0.26, 0.27, 0.27 and 0.43, 0.54, 0.38, respectively. Therefore, CF_3 is expected to be the stronger electron-withdrawing group.[20]

thermally (refluxing ethylene glycol) were unsuccessful, as previously reported for other diiridium diastereomers.[42] Nevertheless, the combined stereoselectivity and high yield is convenient.

To allow a direct comparison with complex **67**, complex **66** (the mesityl-functionalised analogue of complex **64**) (Figure 3.7) was also synthesised. Interestingly, the presence of mesityl groups leads to a larger difference in the solubilities of the diastereomers of **66** compared to **64**, making them trivial to separate by column chromatography. However, the extremely poor solubility of *meso* **66** prevented its purification; therefore, only *rac* **66** is studied here (stereochemistry confirmed by X-ray diffraction, Appendix Figure A10). It is noteworthy that *meso* **66** is less soluble than complex **64** despite the presence of mesityl groups, in contrast to the expectation based on previous reports.[40,41,43] This could tentatively be based on the increased aspect ratio of *meso* **66**, which would be expected if the bridging OCNNCO unit is planar as calculated for the *meso* diastereomers in Chapter 2 and below. This could promote packing in the solid state, decreasing solubility.

In Chapter 2 it was shown that colour tuning of the emission of diarylhydrazide-bridged diiridium complexes within the range λ_{max} 520–490 nm can be achieved through functionalisation of either the bridge or cyclometallating phenyl rings with electron withdrawing groups.[31,42] Therefore, simultaneous functionalisation of both moieties with electron withdrawing groups might afford blue / sky-blue diiridium complexes, which to date remain elusive. In this Chapter the first examples of sky-blue emissive diiridium complexes (**68**–**70**) are introduced (Figure 3.7).

Initial attempts focussed on combining the classic blue-shifting cyclometallating dfppy or 2-(2,4-difluorophenyl)-4-mesitylpyridine[41] ligands with the bis(pentafluorophenyl)/(trifluoromethyl) bridges **72c** and **73** (Figure 3.7). However, this was unsuccessful. Although MALDI mass spectrometric data were promising, the extremely poor solubility of the products prevented their isolation and characterisation. To enhance solubility the new dfppy derivative **75** (Figure 3.7) was envisaged, wherein the mesityl group is replaced by a methylenecyclohexylether-functionalised xylyl group. The methylenecyclohexyl group was selected as it should offer the beneficial solubilising properties of a branched alkyl group while being achiral. This is vital as chiral solubilising groups such as 2-ethylhexyl chains would add an extra 4 chiral centres, substantially increasing the number of possible stereoisomers. Additionally, the xylyl spacer in **75** serves as a rigid non-conjugated linker to limit the electronic influence of the electron-donating ether group.

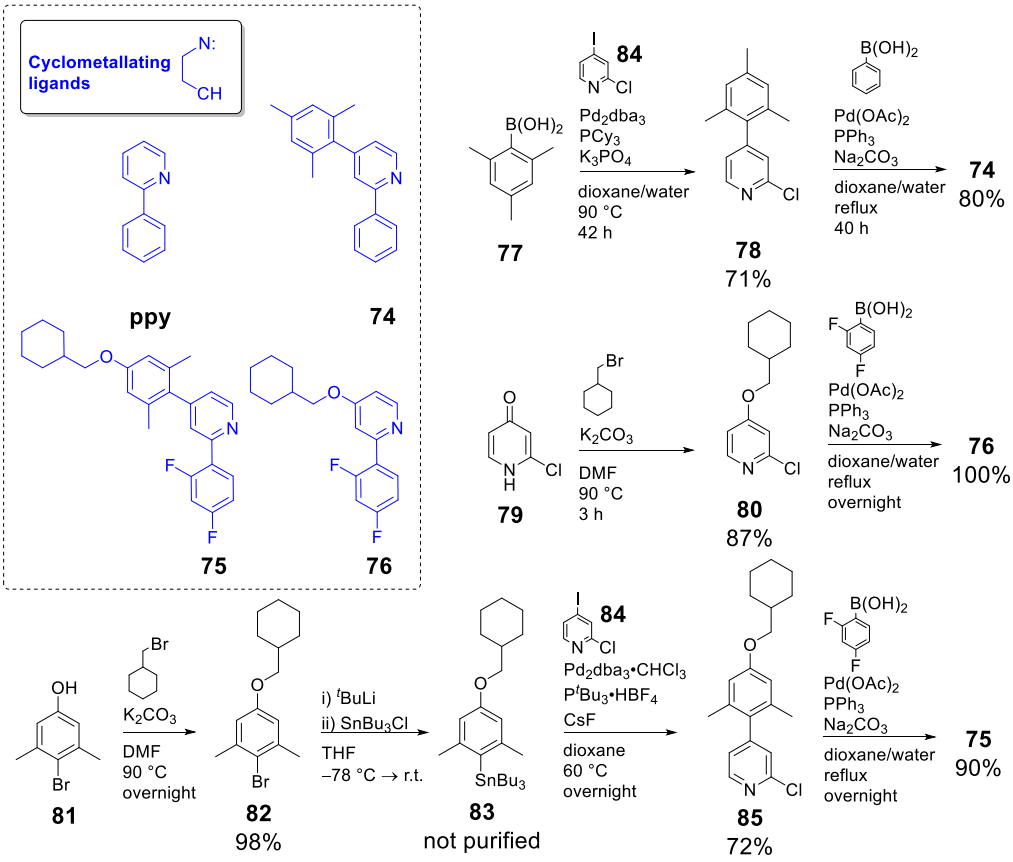

Figure 3.11: Synthetic schemes for the cyclometallating ligands studied in this Chapter.

The synthesis of **75** (Figure 3.11) started with etherification of the xylenol **81** with bromomethylcyclohexane to obtain the aryl ether **82** in 98% yield. Subsequent trapping of the lithiated derivative of **82** with $SnBu_3Cl$ afforded the stannane **83**. This was coupled with 4-iodo-2-chloropyridine (**84**) in a Stille reaction to chemoselectively obtain the 2-chloropyridine derivative **85**. Finally, Suzuki-Miyaura coupling of **85** with 2,4-difluorophenylboronic acid afforded **75** in 90% yield. Initial attempts to proceed via a boronic acid to obtain **85** rather than a stannane were troublesome. This was firstly due to poor isolated yields of the boronic acid analogue of **83** (< 20%), and secondly due to extensive deborylation when attempts were made to subsequently couple it. Therefore, Stille methodology was employed in the synthesis of the key intermediate **85**. The ligand **76** (Figure 3.7) was also synthesised (Figure 3.11) to investigate the effect of directly functionalising the pyridyl moiety with the methylenecyclohexylether group, which is expected to destabilise the LUMO and further blue shift emission. **76** was synthesised from **79** via a sequential etherification and cross coupling strategy analogous to ligand **75**.

Analogous to the mesityl-functionalised complex **66**, the diastereomers *rac* **68** (stereochemistry confirmed by X-ray diffraction below, Figure 3.12) and *meso* **68** were easily separated. The

improved solubility imparted by the methylenecyclohexylether groups allowed both diastereomers to be fully characterised. As observed for **67**, the bis(trifluoromethyl) bridge **73** resulted in only a single diastereomer for complex **69** (Figure 3.7). These two examples (**67** and **69**) suggest that bis(alkyl)hydrazide bridges may be useful ligands for obtaining diiridium complexes from racemic μ-dichloro dimers without the formation of diastereomeric mixtures. This is complementary to using enantiomerically pure dichloro-bridged dimers, as reported for other systems.[39,44]

Complex **70** was isolated as a single diastereomer: the absolute configuration is unknown. A second diastereomer was observed by NMR but could not be isolated.

X-ray crystal structures[‡]

The π–π interactions were studied in the solid state through X-ray crystallography. Single crystals were grown for complexes **62** and **64**–**68** (the details are included in the experimental section). The X-ray crystal structures of **62**, **64**, **65**, **67** and **68** are displayed in Figure 3.12. Relevant parameters are listed in Table 3.1. Additional crystallographic figures are included in the Appendix (Figures A10 and A11).

Structures **62** and **66**–**68** contained disordered CH_2Cl_2 or CD_2Cl_2 of crystallisation. Two solvent-free polymorphs of **65** formed concomitantly; in α-**65** the molecule lies on a crystallographic twofold axis while in β-**65** (as in **66** and **68**) it has no crystallographic symmetry. The structural features broadly correlate with what is observed for the diiridium complexes studied in Chapter 2. Each Ir atom has distorted octahedral coordination, with the N atoms of the two C^N cyclometallating ligands occupying axial positions, *trans* to one another.[45,31] Again, in the *meso* complexes the hydrazide moieties are planar, while in the *rac* isomers they are folded (by 7 to 24°) along the central N–N bond into two planar OCNN chelating fragments. The chelated Ir atoms can be coplanar with, or displaced from, their planes, but this does not affect the bonding pattern significantly. The aryl substituents (*A*) on the bridging ligands are oriented approximately perpendicular to the hydrazide planes (thus precluding π-conjugation) and are stacked face-to-face (π–π) with the phenyl ring (*B*) of a cyclometallating ligand (Figure 3.12). It is noteworthy that this is expected to shorten the effective conjugation length of the bridge and is beneficial for shifting emission towards the blue (see below).

[‡] All X-ray crystal structures were solved by Dr Andrei Batsanov.

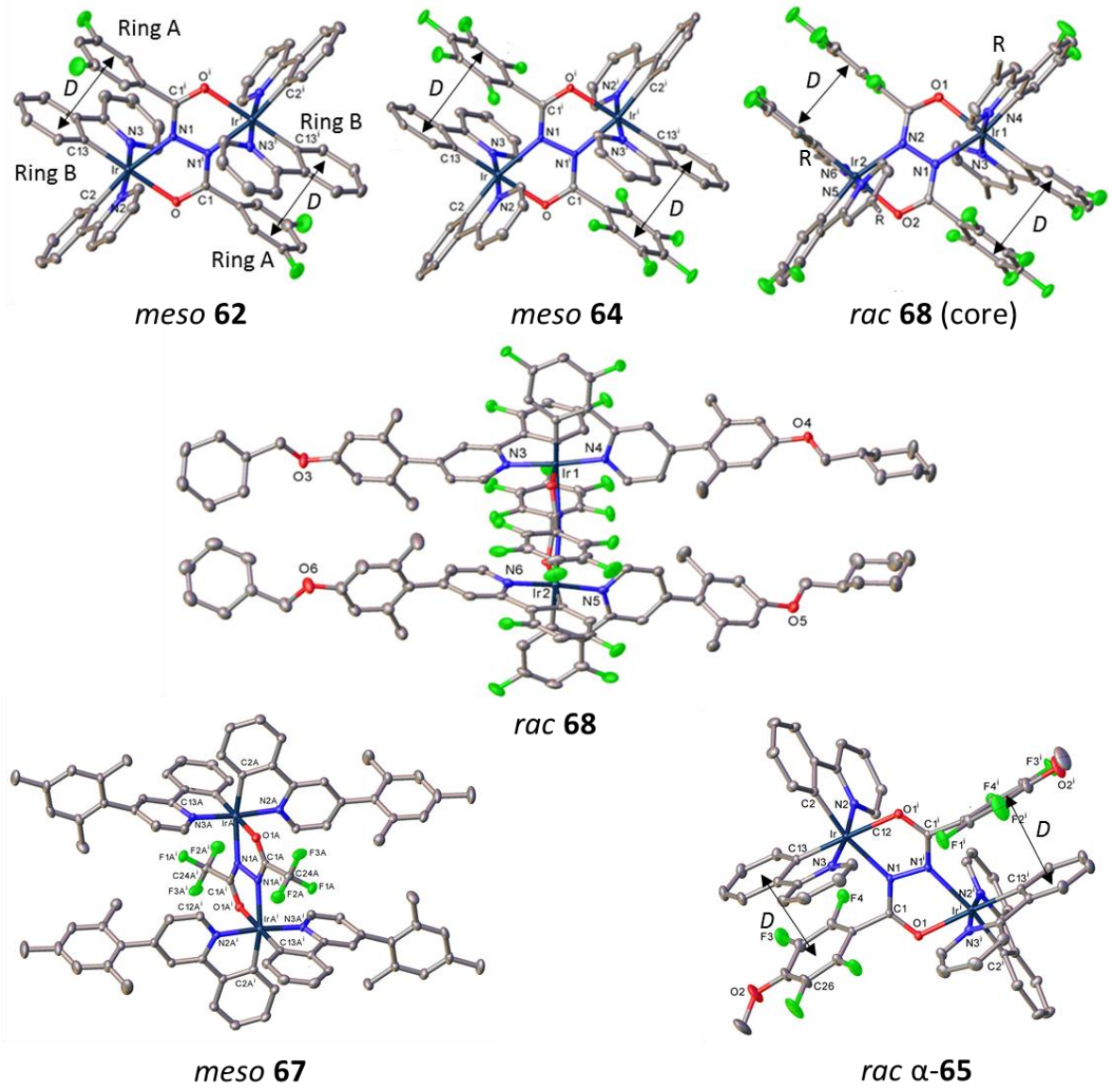

Figure 3.12: X-ray molecular structures of *meso* **62**, *meso* **64**, *rac* α–**65** (ΔΔ), *rac* **68** (ΔΔ) and one of the crystallographically non-equivalent molecules of *meso* **67**. Thermal ellipsoids are drawn at the 50% probability level, H atoms and solvent of crystallisation are omitted for clarity. Primed atoms are generated by a crystallographic inversion centre (**62**, **64** and **67**) or a twofold axis (*rac* α–**65**). For the core of *rac* **68**, the R groups denote the xylyl substituents. Vector *D* identifies intramolecular π–π interactions (see Table 3.1).

The average stacking distance is closer (*D* = 3.31 vs. 3.45 Å) and significantly more parallel (Θ = 7.1 vs. 14.5°) than for the analogues in Chapter 2 which feature *t*-Bu and CF_3 substitutuents on the bridging aryls. This is a direct consequence of fluorination of the bridge (*A*) rings, both because it promotes face-to-face stacking, and due to the comparatively small size of the fluorine atom. The complexes studied here appear to demonstrate the closest intramolecular π–π stacking reported

for cyclometallated iridium complexes.[42,23–27] Interestingly, the X-ray data suggest that molecule **67**, which lacks intramolecular stacking, is much less rigid (as expected). In the crystal there are two crystallographically non-equivalent molecules which display different conformations (see Appendix, Figure A11).

Table 3.1: Selected geometrical parameters of diiridium complexes (bond distances in Å).

	meso **62** $3CH_2Cl_2$	*meso* **64**	*rac* α-**65**	*rac* β-**65**	*rac* **66** $2CH_2Cl_2$	*meso* **67** $5CH_2Cl_2$[a]	*rac* **68** $2.25CD_2Cl_2$
Space group	$P\bar{1}$	$I4_1/a$	$C2/c$	$P2_1/n$	$P\bar{1}$	$P\bar{1}$	$P\bar{1}$
Mol. symmetry	C_i	C_i	C_2	--	--	C_i	--
Ir centres	ΔΛ	ΔΛ	ΔΔ, ΛΛ	ΔΔ, ΛΛ	ΔΔ, ΛΛ	ΔΛ	ΔΔ, ΛΛ
Ir---Ir, Å	5.091	5.089	5.117	5.062	5.082	5.147, 5.152	5.070
Ir–C (*trans*-O)	1.998(2)	2.006(6)	2.001(2)	1.994(4)	1.992(7)	1.994(3)	1.988(4)
Ir–C (*trans*-N)	2.001(2)	1.994(6)	1.997(2)	2.002(4)	2.000(7)	1.992(3)	1.996(4)
Ir–N, stacked	2.032(2)	2.005(6)	2.040(1)	2.033(3)	2.033(5)	2.029(3)	2.035(3)
Ir–N, non-stacked	2.042(2)	1.973(6)	2.044(1)	2.031(3)	2.037(5)	2.042(3)	2.031(3)
Bridge geometry							
OCNNCO folding, °	planar	planar	6.8	24.3	14.3	planar	17.9
Ir displacement, Å	0.01	0.23	0.06	0.28, 0.39	0.26, 0.20	0.52, 0.00	0.17, 0.24
Ir–O	2.152(2)	2.161(2)	2.156(1)	2.147(3)	2.142(5)	2.144(2)	2.127(3)
Ir–N	2.171(2)	2.170(3)	2.180(1)	2.164(3)	2.169(5)	2.214(2)	2.175(3)
N–N	1.438(3)	1.435(5)	1.439(2)	1.443(4)	1.448(6)	1.445(2)	1.436(4)
N–C	1.312(3)	1.308(4)	1.314(2)	1.307(5)	1.305(8)	1.310(4)	1.301(5)
C–O	1.286(2)	1.279(4)	1.283(2)	1.275(4)	1.279(8)	1.268(4)	1.278(4)
Intramolecular stacking (π–π)							
Θ, °[b]	8.5	5.9	13.5	6.9, 8.7	4.6, 6.0	--	6.2, 3.4
D, Å[c]	3.32	3.24	3.42	3.39, 3.35	3.33, 3.30	--	3.27, 3.19

[a] contains two crystallographically non-equivalent centrosymmetric dimers; [b] interplanar angle between ring *A* of the bridging ligand and ring *B* of the cyclometallating ligand (see Figure 3.12); [c] distance between the plane of ring *B* and the centroid of ring *A*.

Computational study

Electronic structure calculations were carried out for **62**–**70** to gain further insight into experimental observations. The optimised S_0 geometries were calculated at the B3LYP/LANL2DZ:3–21G* level to allow direct comparison with literature and the data presented in Chapter 2 (i.e. complexes **34**–**38**).[31,46] For complexes **68**–**70** the methylene cyclohexylether groups were substituted for methoxy groups to shorten calculation times. The geometries of the central hydrazide fragments are in good agreement with the XRD results discussed above (planar for the *meso* forms and more twisted for the *rac* diastereomers).

Molecular orbital calculations were carried out to provide insight into the localisation of the FMOs. Reasonable agreement is observed between diastereomers for all complexes. FMO plots for complexes **62**, **64**, **67** and **68** are shown in Figure 3.13 as examples which highlight the extent to which the FMO localisation varies within the series. Additional FMO plots are included in the Appendix (Figures A12–A20). For all complexes the LUMOs are localised on the cyclometallating

ligands, particularly the pyridyl moieties.[31,42] In contrast, the localisation of the HOMOs varies more significantly between complexes: in some cases the HOMO contribution from the bridge centre is high (diastereomer average ≥ 30%) (complexes **62**, **65**, **68** and **70**), whereas in other cases it is considerably less (diastereomer average < *ca.* 15%), for which the bridging ligands are likely to display ancillary character (complexes **63**, **64**, **66**, **67** and **69**). The data are listed in Table 3.2.

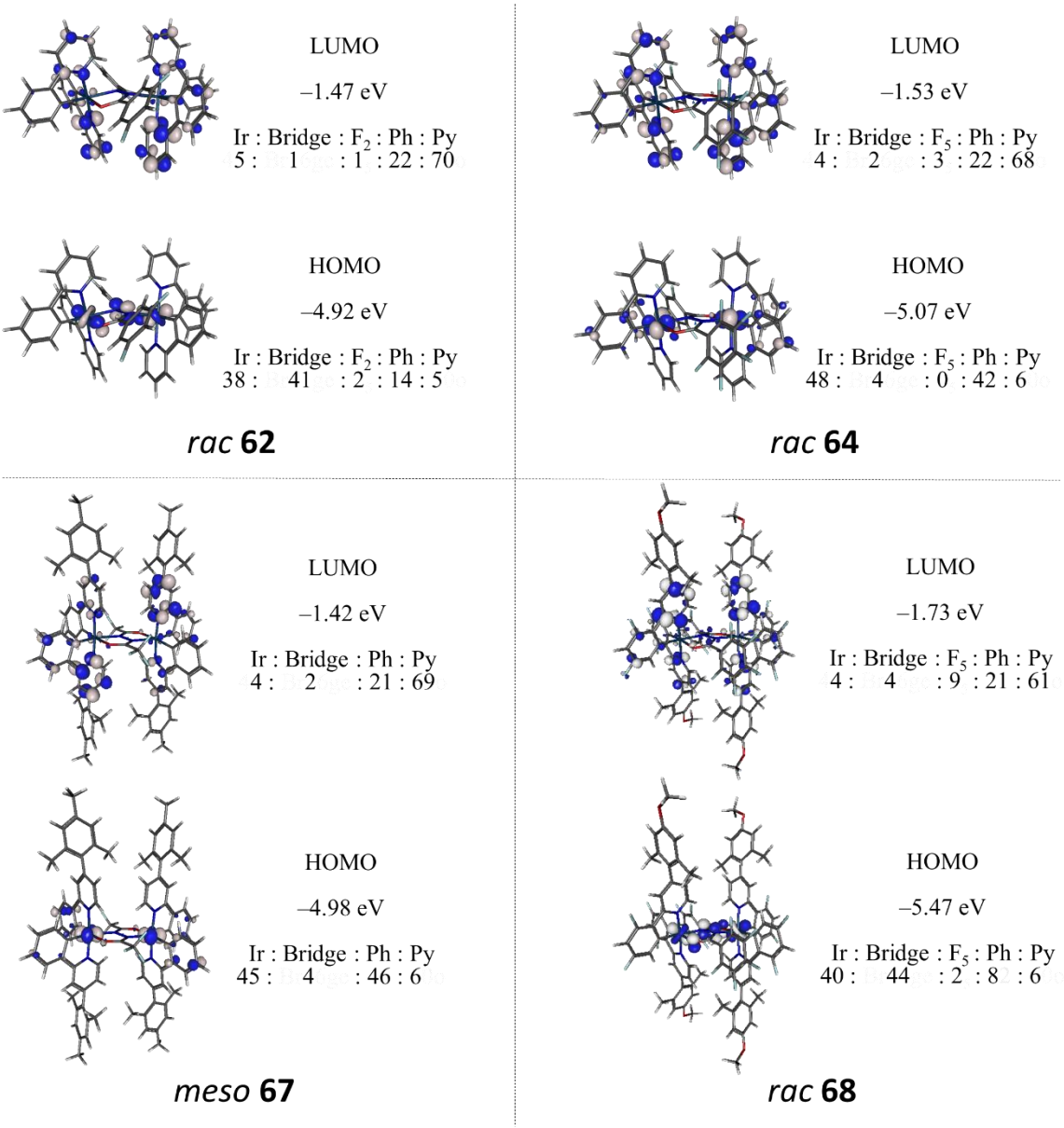

Figure 3.13: Molecular orbital compositions for *rac* **62**, *rac* **64**, *meso* **67** and *rac* **68**. The orbital contributions are percentages and the HOMO and LUMO energies were calculated at B3LYP/LANL2DZ:3–21G*. Bridge = central bridge OCNNCO fragment; F_n = fluorinated bridge aryl rings; Ph = cyclometallating ligand phenyl groups; Py = cyclometallating ligand pyridyl groups.

For complex **62** the HOMO has significant contributions from the Ir centres, the central component of the hydrazide bridge and the cyclometallating phenyl moieties, analogous to the predictions for the ppy-functionalised diiridium complexes in Chapter 2 (**35**–**38**).[31,42] Further fluorination of the bridging aryl rings decreases the bridge HOMO contributions for complexes **63** (octafluoro) and **64** (decafluoro). As a result, their HOMOs are primarily localised on the Ir centres and the cyclometallating phenyl groups, with their bridges expected to behave as ancillary ligands. As complex **65** also features methoxy groups on the bridging unit, the effect of the electron withdrawing fluorine atoms is somewhat negated. Consequently, the bridge still features notable HOMO localisation (32% average). Complexes **64** and **66** feature very similar HOMO contributions, suggesting that functionalisation with mesityl groups has a negligible electronic effect, as expected.[40,41] Lowering the π orbital energies of the cyclometallating ligands of complexes **68** and **70** through fluorination strongly shifts their HOMOs onto the bridging ligands so that the cyclometallating phenyl moieties have very low HOMO contributions (average of both diastereomers < 15% for both complexes). There is negligible frontier orbital (HOMO or LUMO) contribution from the bridge aryl rings for all complexes featuring diarylhydrazide bridges, even upon perfluorination.

Table 3.2: Summary of the HOMO compositions for the most stable minima of the complexes.

Complex	Isomer	Ir	Bridge centre	Bridge aryl	Ph[a]	Py[b]
62	*meso*	42%	28%	1%	23%	6%
	rac	38%	41%	2%	14%	5%
63	*meso*	45%	18%	1%	31%	5%
	rac	48%	4%	0%	42%	6%
64	*meso*	45%	16%	1%	33%	5%
	rac	48%	4%	0%	42%	6%
65	*meso*	45%	20%	1%	29%	5%
	rac	40%	44%	2%	9%	5%
66	*meso*	44%	22%	1%	28%	6%
	rac	47%	4%	0%	42%	6%
67	*meso*	45%	4%	-	46%	6%
	rac	45%	3%	-	46%	6%
68	*meso*	42%	35%	1%	15%	5%
	rac	40%	44%	2%	8%	6%
69	*meso*	45%	4%	-	44%	7%
	rac	45%	4%	-	44%	7%
70	*meso*	42%	42%	1%	9%	6%
	rac	42%	46%	1%	4%	7%

[a]Phenyl moieties of the cyclometallating ligands; [b]Pyridyl moieties of the cyclometallating ligands.

For complexes **67** and **69** the bridging ligands display negligible HOMO contributions (average of both diastereomers = 4% for both complexes) and are expected to behave as ancillary ligands,

regardless of cyclometallating ligand fluorination. This is indicative of the shorter conjugation length (and hence lower π orbital energy) of the bis(trifluoromethyl) bridge **73** compared to the diarylhydrazide bridges studied here.

The findings in Chapter 2 for complexes **35** and **36** indicate that sole consideration of the HOMO and LUMO is not always sufficient when discussing the lowest energy excited states of diarylhydrazide-bridged diiridium complexes. Therefore, TD-DFT calculations were carried out to explore the influence of the interesting FMO contributions of complex **66** (which should also be representative of **64**) and **70**. The data obtained for the lowest energy triplet states of **66** and **70** are listed in Table 3.3. The dominant transitions contributing to each state (≥ *ca.* 20%) are included. The compositions of the relevant orbitals (HOMO−5 – LUMO+5/6) of **66** and **70** are tabulated in the Appendix (Tables A1 and A2).

Table 3.3: Summary of the TD-DFT data for **66** and **70**.

Transition	**66**				**70**			
	meso		*rac*		*meso*		*rac*	
	Main orbital contribution	**λ/ nm**	**Main orbital contribution**	**λ/ nm**	**Main orbital contribution**	**λ/ nm**	**Main orbital contribution**	**λ/ nm**
$S_0 \rightarrow T_1$	HOMO → LUMO	483	HOMO → LUMO	472	HOMO → LUMO, HOMO-2 → LUMO	423	HOMO → LUMO, HOMO → LUMO+1	446
$S_0 \rightarrow T_2$	HOMO → LUMO+1, HOMO-1→ LUMO	482	HOMO → LUMO+1	472	HOMO → LUMO+1	422	HOMO-1 → LUMO+2	418
$S_0 \rightarrow T_3$	HOMO-1 → LUMO+3, HOMO → LUMO+2	461	HOMO → LUMO+2	463	HOMO → LUMO+6	413	HOMO-1 → LUMO, HOMO-2 → LUMO+2	418
$S_0 \rightarrow T_4$	HOMO-1 → LUMO+2, HOMO → LUMO+3	460	HOMO → LUMO+3	462	HOMO-2 → LUMO+2, HOMO-1 → LUMO+2	407	HOMO-2 → LUMO+3	413
$S_0 \rightarrow T_5$	-	-	-	-	HOMO-1 → LUMO+3	407	HOMO-1 → LUMO+3	412

Complex **66** was investigated to ascertain whether the bridging ligand behaves in an ancillary nature as the FMO data (Table 3.2) suggest. The diastereomers of complex **66** each feature 4 triplet states

that are relatively close in energy (≤ 20 nm) and so may be relevant to their emitting states. For complex meso **66**, no large contribution from the central hydrazide fragment of the bridge is encountered above the HOMO−2 orbital. The main transitions in Table 3.3 for *meso* **66** involve the HOMO and HOMO−1 as donor orbitals (bridge contributions ≤ 2%) with no HOMO−2 contribution. For *rac* **66**, no significant bridge contribution is encountered until the HOMO−1. The transitions in Table 3.3 for *rac* **66** do not involve any orbitals below the HOMO (4% bridge contribution). Also, pentafluorophenyl character is not encountered below the LUMO+4 for both diastereomers of **66**, for which none of the transitions in Table 3.3 involve orbitals above the LUMO+3. Therefore, the TD-DFT data for both diastereomers of complex **66** suggest that the bridging unit does not feature substantial hole or electron character in the excited state, and so behaves as an ancillary ligand.

Complex **70** was investigated as it features electron donating methylenecyclohexyl ether groups directly functionalised onto the pyridyl moieties, which increases their π* orbital energies.[47] Therefore, although there is negligible LUMO contribution from its pentafluorophenyl groups, of the complexes featuring the perfluoroaryl bridge **72c**, complex **70** is most likely to have some electron character on the bridge pentafluorophenyl groups in the excited state.

For complex *meso* **70** the 5 lowest energy triplet states are relatively similar in energy (≤ 20 nm). The transitions for *meso* **70** in Table 3.3 involve either the LUMO, LUMO+1, LUMO+2, LUMO+3 or LUMO+6 as acceptor orbitals. All of these orbitals feature insignificant pentafluorophenyl contribution (≤ 3%) other than the LUMO+6 (30%) which is involved the transition to T_3. For complex *rac* **70** there is an energy gap of *ca*. 30 nm between the T_1 and T_2 states. Therefore, DFT predicts that the higher energy triplet states are likely to be less important with regards to the emitting state. Nevertheless, for the first five triplet states, the transitions for *meso* **70** involve either the LUMO, LUMO+1, LUMO+2 or LUMO+3 as acceptor orbitals. The highest contribution of the pentafluorophenyl groups to any of these orbitals is still rather low, at 15%.

In summary, from the TD-DFT data for both diastereomers, other than for the $S_0 \rightarrow T_3$ transition for *meso* **70** (LUMO+6 = 30% pentafluorophenyl character), the contributions from the pentafluorophenyl groups to the 5 lowest triplet states are very small. Therefore, it is reasonable to conclude that the pentafluorophenyl groups of complex **70** are unlikely to play a large part in its excited state, making them ancillary. Based on these data for **66** and **70**, it should be reasonable to state that the bridge aryl groups are expected to behave in an ancillary nature for all the diarylhydrazide-bridged complexes (**62**–**66**, **68** and **70**) studied in this Chapter.

Electrochemical study

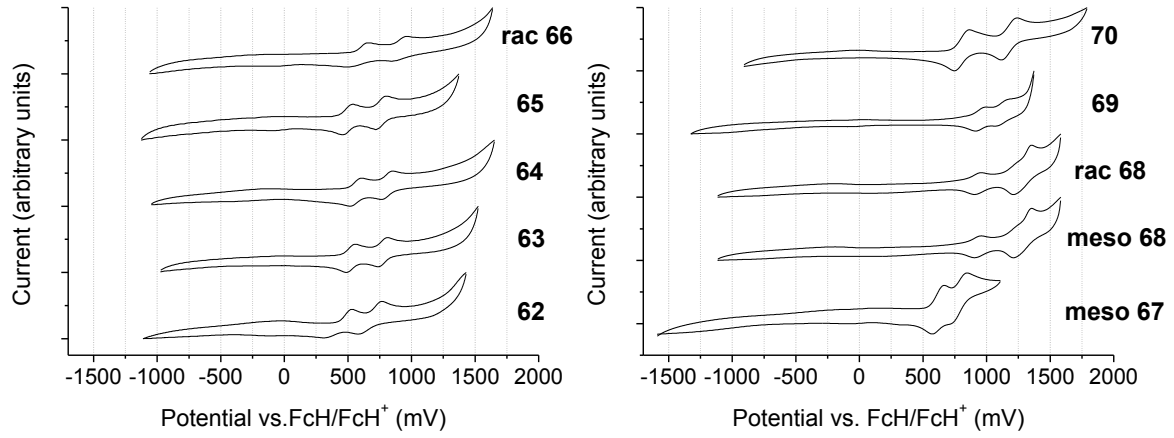

Figure 3.14: Cyclic voltammograms in 0.1 M *n*-Bu_4NPF_6/ DCM showing the oxidation processes for complexes **62**–**70**.

Complexes **62**–**70** were studied by CV to obtain their oxidation and reduction potentials. The data are listed in Table 3.4 and voltammograms for the oxidation processes are shown in Figure 3.14. All complexes display two electrochemically reversible oxidation waves. These represent sequential oxidation of the iridium centres (Ir^{3+}/ Ir^{4+} redox couples), which are electronically coupled via the conjugated bridging units (or potentially through-space) and so are electrochemically inequivalent. Both oxidation processes were shown to be chemically reversible over 10 cycles for a complex from both the green (*rac* **66**) and sky-blue (**70**) series (Figure 3.15). All complexes display irreversible reductions (the voltammograms are included in the Appendix, Figure A21).

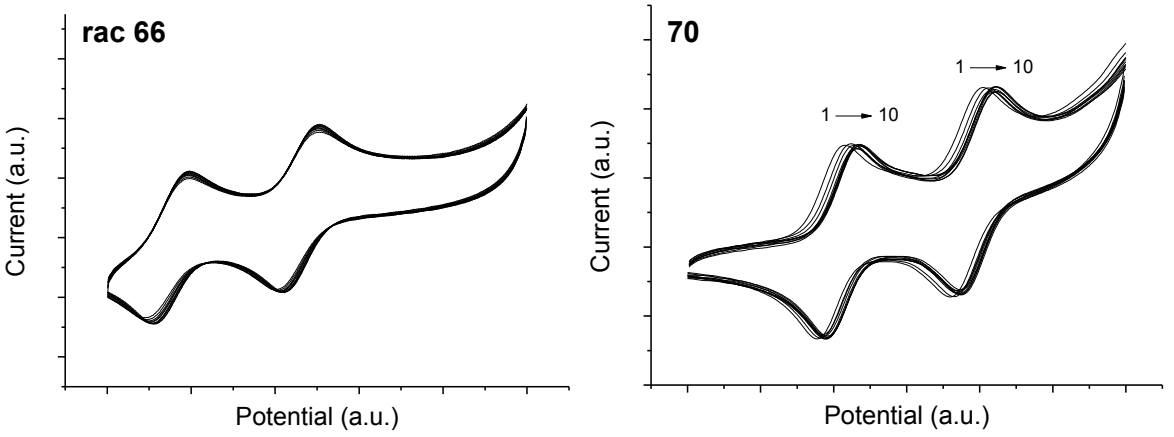

Figure 3.15: Cyclic voltammograms in 0.1 M *n*-Bu_4NPF_6/ DCM showing the oxidation processes for complexes *rac* **66** and **70** over 10 consecutive scans. The potential axis is arbitrary due to the absence of internal ferrocene. The oxidation potentials slightly drift due to the use of a quasireference electrode.

Complex **62**, which features 4 fluorine atoms on the bridging unit, displays the lowest $E^{ox(1)}$. As expected, increasing to 8 (complex **63**) and 10 electron-withdrawing fluorine atoms (complex **64**) results in successively higher oxidation potentials. Due to the addition of electron-donating methoxy groups to the octafluoro bridging unit, the oxidation potential of complex **65** is slightly decreased by 0.02 V compared to complex **63**. A relatively small variation in oxidation potentials (0.04 V) across the series **62**–**65** supports DFT predictions that the bridges in **63** and **64** behave as ancillary ligands. Complexes **62**–**65**, which vary only in the extent of bridge fluorination, all feature very similar peak splittings ($\Delta E_{1/2}$ ca. 0.25 V), indicating similar electronic coupling between the Ir centres for this series.

Table 3.4: Electrochemical data for complexes **62**–**70** referenced to $E_{1/2}$ FcH/ FcH^+ = 0.00 V.

Complex	Isomer	$E^{ox(1)}$ /V E_{pa}/ E_{pc} [$E_{1/2}$]	$E^{ox(2)}$ /V E_{pa} /E_{pc} [$E_{1/2}$]	$\Delta E_{1/2}$ /V[a]	E^{red}_{onset} /V[b]	HOMO /eV[c]	LUMO /eV[d]
62	*mixture*	0.53/ 0.31 [0.42]	0.77/ 0.58 [0.67]	0.25	−2.38	–5.22	–2.42
63	*mixture*	0.56/ 0.49 [0.52]	0.81/ 0.74 [0.77]	0.25	−2.18	–5.32	–2.62
64	*mixture*	0.61/ 0.52 [0.56]	0.85/ 0.76 [0.81]	0.25	−2.37	–5.36	–2.43
65	*mixture*	0.54/ 0.46 [0.50]	0.80/ 0.72 [0.76]	0.26	−2.29	–5.30	–2.51
66	*rac*	0.66/ 0.49 [0.58]	0.96/ 0.84 [0.90]	0.32	−2.37	–5.38	–2.43
67	*meso*	0.67/ 0.57 [0.62]	0.85/ 0.72 [0.78]	0.16	−2.44	–5.42	–2.36
68	*meso*	0.96/ 0.90 [0.93]	1.36/ 1.21 [1.28]	0.35	−2.16	–5.73	–2.66
	rac	1.00/ 0.93 [0.97]	1.43/ 1.23 [1.33]	0.36	−2.14	–5.77	–2.64
69	*	0.99/ 0.91 [0.95]	1.18/ 1.07 [1.12]	0.17	−2.15	–5.75	–2.65
70	*	0.87/ 0.75 [0.81]	1.24/ 1.12 [1.18]	0.37	−2.19	–5.61	–2.61

[a] Peak splitting between $E^{ox(1)}$ and $E^{ox(2)}$. [b] All reductions are electrochemically irreversible. [c] HOMO levels calculated from CV potentials by HOMO = –4.8 + (–$E_{1/2}^{ox(1)}$), using ferrocene as the standard. [d] LUMO levels calculated from CV potentials by LUMO = –4.8 + (–E^{red}_{onset}), using ferrocene as the standard. * Complexes **69** and **70** were isolated as single diastereomers; their absolute configurations are unknown.

Functionalising the ppy ligands of complex **66** with mesityl groups does not significantly influence $E^{ox(1)}$ (an increase of only 0.02 V is observed compared to complex **64**), suggesting that they have a minimal electronic effect (as expected).[40,41] However, it is interesting that for **66** $E^{ox(2)}$ is shifted to a significantly higher potential compared to complex **64** (0.90 V vs. 0.81 V) leading to a larger $\Delta E_{1/2}$ value of 0.32 V for **66** compared to 0.25 V for **64**. A tentative explanation is that the mesityl groups could sterically interact over the bridging unit (evident from the X-ray crystal structures in Figure 3.12). This is expected to increase molecular rigidity and could hinder any structural rearrangement to the dication (if such rearrangement is required), thereby increasing $E^{ox(2)}$ of **66** compared to the more flexible complex **64**.

The oxidation potential of **67** is higher than that of **66** by 0.04 V, suggesting that the bis(trifluoromethyl)-functionalised bridge (**73**) is more strongly electron withdrawing than the bis(pentafluorophenyl) bridge (**72c**) (In agreement with their differing Hammett parameters).[20] The $\Delta E_{1/2}$ value obtained for **67** (0.16 V) is also half of that observed for **66**, implying weaker communication between the two iridium centres. This is in line with the ancillary nature of the bridge predicted by DFT (Table 3.2) and implies that the bridge has greater ancillary character in **67** than **66**. However, the infrared spectra for **66** and **67** (Figure A22) interestingly display identical C=O stretch energies (1614 cm^{-1}), implying very similar bonding modes for the bridges in both complexes.

The addition of fluorinated cyclometallating ligands to complexes *meso* **68** and *rac* **68** further shifts their oxidation potentials to more positive values. This is as expected from DFT, which predicts high HOMO contributions from the cyclometallating phenyl rings of the parent complex **66** (Table 3.2). The $\Delta E_{1/2}$ values for *meso* **68** and *rac* **68** are also greater than for complex **66** (by 0.03/ 0.04 V). This may be due to the reduced ancillary character of the bis(pentafluorophenyl) bridge in these complexes, which is predicted in the DFT above. Complex **69** has an oxidation potential almost identical to those displayed by *meso* **68** and *rac* **68**, indicating very similar HOMO energies. Analogous to the relationship between complexes **66** and **67**, complex **69** displays a much lower $\Delta E_{1/2}$ value than either diastereomer of complex **68**, which suggests a higher ancillary character of the bis(trifluoromethyl) bridge (and so weaker Ir---Ir communication), as inferred by DFT.

The first oxidation potential of **70** is cathodically shifted compared to complexes **68** (by *ca.* 0.1 V). This is due to the absence of the xylyl spacer which electronically decouples the electron donating methylenecyclohexylether group from the ppy ligands. Complex **70** also has the largest $\Delta E_{1/2}$ value (0.37 V), in agreement with DFT which predicts the bridging unit to feature the highest HOMO contribution of the series.

The reduction potentials for **62**–**70** were also estimated by CV. All complexes display irreversible reductions. This adds error to their accurate determination, complicating the detailed analysis of any trends. A similar situation has been previously encountered in the study of monoiridium complexes by Baranoff and Nazeeruddin et al.[48] Nevertheless, the reduction onsets for the complexes **62**–**70** are in the range of −2.1 – −2.4 V vs. FcH/ FcH^+, which is a reasonable fit with their emission energies (discussed below) and also similar to those reported for ppy-based monoiridium complexes.[49] Generally, functionalisation of the cyclometallating ligands of **68**–**70** with electron-withdrawing fluorine atoms decreases their reduction potentials compared to those of complexes

62–**67** as expected.[49] The reduction potential for **70** is marginally greater than for **68** and **69** (−2.19 V vs. −2.14/ −2.16 V and −2.15 V), which is expected from the DFT data upon direct functionalisation of the LUMO-bearing pyridyl moieties with electron-donating methylenecyclohexyl ether groups.

Photophysical properties[§]

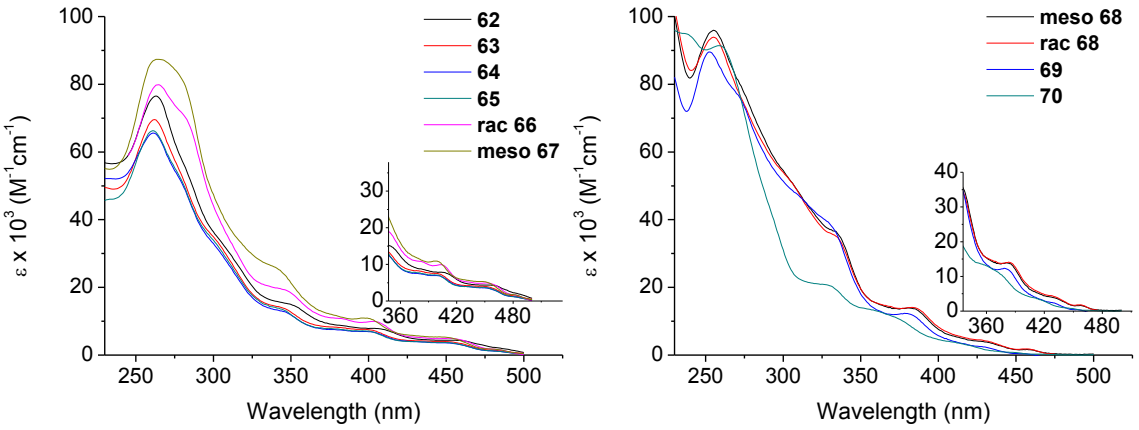

Figure 3.16: Absorption spectra for complexes **62**–**70** recorded in aerated DCM at room temperature. Insets are expansions of the *ca.* 350–500 nm regions.

Table 3.5: Absorption spectroscopic data for complexes **62**–**70** and FIrpic recorded in aerated DCM at room temperature.

Complex	Isomer	λ_{abs} /nm ($\varepsilon \times 10^3$ / $M^{-1}cm^{-1}$)
62	*mixture*	263 (77), 285sh (52), 310sh (30), 352 (15), 408 (7.5), 460 (4.3)
63	*mixture*	262 (70), 305sh (32), 345 (14), 380 (8.3), 400 (7.5), 455 (3.9)
64	*mixture*	261 (66), 281sh (50), 303sh (33), 345 (14), 400 (7.2), 453 (3.9)
65	*mixture*	262 (66), 281sh (50), 305sh (30), 347 (13), 377 (7.7), 401 (7.0), 451 (3.7)
66	*rac*	264 (80), 282 (70), 348 (19), 381 (11), 404 (10), 455 (5.5)
67	*meso*	265 (87), 281sh (81), 343 (25), 400 (11), 452 (5.4)
68	*meso*	255 (96), 274sh (79), 305sh (51), 336 (36), 384 (14), 430 (4.2), 460 (1.7)
	rac	255 (94), 276sh (73), 205sh (51), 335 (35), 386 (14), 430 (4.4), 460 (1.7)
69	*	252 (89), 272sh (77), 312sh (46), 331 (38), 382 (12), 429 (2.5), 457 (0.5)
70	*	239 (95), 259 (91), 291sh (44), 328 (21), 360 (13), 374 (11), 416 (3.3)
FIrpic	-	277 (50), 301 (34), 304 (33) 337sh (14), 357sh (8.9), 400 (6.2), 454 (0.8)[a]

[a]Values taken from ref 51. *Single diastereomer of unknown absolute configuration. sh = shoulder. For FIrpic structure see Figure 1.12.

The absorption spectra for the diiridium complexes are shown in Figure 3.16 and the data are tabulated in Table 3.5. The spectra display profiles typical for cyclometallated iridium complexes.

[§] Solution PLQYs and τ were measured by Dr Yu-ting Hsu.

As in Chapter 2, the bands below *ca.* 300 nm are assigned to ^{1}π–π* transitions, whereas the weaker bands that extend to *ca.* 500 nm are attributed to transitions to ^{1}MLCT and ^{3}MLCT states.[29,50] The green-emitting complexes **62**–**65** display similar λ_{max} (i.e. ^{1}LC band) extinction coefficients to the ppy-functionalised diiridium complexes (**34** and **35**) studied in Chapter 2 (ε = *ca.* 65–80 × 10^3 / M^{-1}cm^{-1}). The addition of mesityl groups in **66**–**69** results in a hyperchromic shift of the ^{1}LC bands to $\varepsilon \geq 80 \times 10^3$ / M^{-1}cm^{-1}, presumably because they can contribute to high energy ^{1}π–π* transitions. A similarly high extinction coefficient for **70** may be due to the electron donating alkoxy group.

The PL properties of **62**–**70** were studied at room temperature in DCM and PMMA matrices and at 77 K in 2-MeTHF glasses. The spectra are shown in Figures 3.17–3.19 and the key photophysical data are listed in Table 3.6. Complex **62** is non-emissive in DCM solution at room temperature, while being highly emissive (PLQY = 61 ± 10%) when doped into a rigid PMMA matrix. This is consistent with the data for complexes **34** and **35**, for which the flexible central bridging unit (that DFT predicts to have significant HOMO character) provides a pathway for non-radiative quenching of the excited state in solution, which can be inhibited by doping the complex into a rigid host matrix.

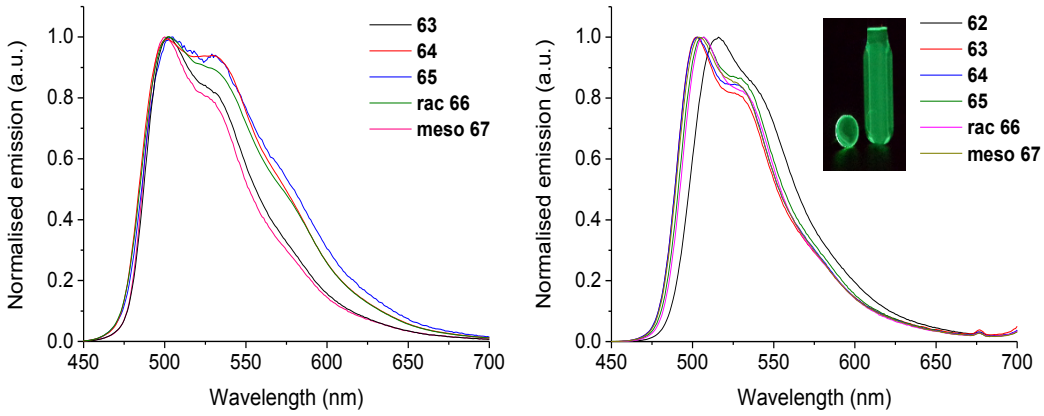

Figure 3.17: Normalised emission spectra for the green series. (Left) Spectra of complexes **63**–**67** in degassed DCM solutions at room temperature (λ_{exc} 355 nm). (Right) Spectra of complexes **62**–**67** doped into PMMA at 1 wt.% at room temperature. Inset: photograph of emission from a doped PMMA film and degassed DCM solution of *rac* **66** under irradiation from a 365 nm UV lamp.

Complexes **63**–**65** have significantly different photophysical properties than **62**. They are highly emissive in solution as well as in PMMA, with very similar PLQY values in both media. It is likely that this is due to rigidification of **63**–**65** by intramolecular π–π stacking,[25] which prevents bridge folding by restricting rotation of the bridge aryl rings. This is observed in the

solution ^{19}F NMR spectra of **63**–**65** and removes the requirement to impede bridge flexibility by using a rigid matrix such as PMMA. Another possible explanation is that for complexes with an ancillary bridging unit (Table 3.2) such as **63** and **64**, motion of the bridge does not provide as efficient a non-radiative pathway to the ground state in solution. However, as complex **65** features a non-ancillary bridge with notable HOMO character while still exhibiting a high solution PLQY (78 ± 5%), it is evident that intramolecular π–π stacking is the main reason for high solution PLQYs in highly fluorinated diarylhydrazide-bridged diiridium complexes.

The emission spectra of **63**–**65** are blue shifted compared to **62** (by *ca.* 10 nm in PMMA) (Figure 3.17). This is a result of HOMO stabilisation through further fluorination of the bridging units (in agreement with electrochemical data, Table 3.4). Complexes **63**–**65** exhibit near identical CIE_{xy} coordinates in PMMA of (0.25, 0.62/0.63) in the green region of the spectrum. The E_T values for **63**–**65** (obtained from the 77 K emission spectra, Figure 3.19) are also nearly identical (2.56–2.57 eV). These data provide additional experimental support for the DFT prediction that the bridges in **63** and **64** behave as ancillary ligands.

The mesityl groups in *rac* **66** result in a significant increase in k_{r} compared to complex **64** in DCM solution (5.30 vs. 3.40 × 10^5 s^{-1}) and in PMMA (5.18 vs. 4.41 × 10^5 s^{-1}). This leads to a small increase in solution PLQY (88 ± 5% for *rac* **66** vs. 76 ± 5% for complex **64**), whereas the PLQYs in PMMA for **64** and *rac* **66** are very similar (71 ± 10% and 72 ± 10%, respectively). The incorporation of mesityl groups has been reported to increase PLQYs and k_{r} values in monoiridium systems.[40,41] As the mesityl groups in *rac* **66** exert a minimal electronic effect,[40,41] the CIE_{xy} coordinates (in both DCM an PMMA) and E_T values for **64** and *rac* **66** are nearly identical.

Complex *meso* **67** is moderately emissive in DCM solution (PLQY = 22 ± 5%), while being highly emissive in PMMA (PLQY = 66 ± 10%). This is due to an order of magnitude decrease in k_{nr} upon doping the complex into PMMA (Table 3.6), and can be attributed to a higher molecular flexibility due to the lack of intramolecular π–π interactions, which is also inferred from the XRD data (discussed above). While *meso* **67** is not rigidified by intramolecular π–π interactions, it is still emissive in solution, albeit to a lesser extent than *rac* **66**. This could be related to the ancillary nature of the bridging ligand (predicted by DFT), which may reduce the efficiency of non-radiative quenching through bridge motion, as mentioned above.

Table 3.6: Summary of the key photoluminescence data for complexes **62–70** and FIrpic.

		DCM solution[a]					2-MeTHF glass[b]		Doped into PMMA 1% wt.[c]				
Ir	**Isomer**	**$\lambda_{max\ em}$ /nm [CIE_{xy}]**	**PLQY /% (± 5%)**	**τ /μs**	**k_r /× 10^5 s^{-1}**	**k_{nr} /× 10^5 s^{-1}**	**$\lambda_{max\ em}$ /nm ($\lambda_{10\%\ em}$ /nm)[d] [E_T /eV][e]**	**τ /μs**	**$\lambda_{max\ em}$ /nm [CIE_{xy}]**	**PLQY /% (± 10%)**	**τ /μs**	**k_r /× 10^5 s^{-1}**	**k_{nr} /× 10^5 s^{-1}**
62	*mixture*	Non-emissive[f]					500 (490) [2.53]	3.62	516 [0.28, 0.64]	61	1.81	3.37	2.15
63	*mixture*	503 [0.27, 0.61]	66	1.84	3.61	1.83	492 (484) [2.56]	3.41	503 [0.25, 0.62]	59	2.00	2.95	2.05
64	*mixture*	499 [0.30, 0.58]	76	2.24	3.40	1.07	492 (482) [2.57]	3.55	503 [0.25, 0.62]	71	2.08	3.41	1.39
65	*mixture*	505 [0.31, 0.58]	78	2.09	3.73	1.05	493 (485) [2.56]	3.33	507 [0.25, 0.63]	66	2.02	3.27	1.68
66	*rac*	502 [0.30, 0.58]	88	1.66	5.30	0.72	494 (485) [2.56]	2.67	507 [0.25, 0.63]	72	1.39	5.18	2.01
67	*meso*	500 [0.26, 0.60]	22	0.34	6.41	22.7	491 (483) [2.57]	2.30	504 [0.25, 0.63]	66	1.14	5.79	2.98
68	*meso*	470 [0.18, 0.36]	48	0.69	6.93	7.48	461 (455) [2.72]	2.24	470 [0.16, 0.33]	65	1.19	5.46	2.94
	rac	470 [0.18, 0.36]	47	0.73	6.49	7.23	463 (456) [2.72]	1.78	472 [0.15, 0.33]	60	1.18	5.51	3.39
69	*	470 [0.16, 0.33]	4[g]	0.07	5.77	135	462 (454) [2.73]	1.92	471 [0.15, 0.33]	46	1.12	4.11	4.82
70	*	459 [0.20, 0.28]	2[h]	0.11	1.64	89.3	451 (441) [2.81]	2.24	460 [0.15, 0.24]	69	1.62	4.26	1.91
FIrpic[i]	-	468 [0.19, 0.37]	73	1.85	3.95	1.46	463 [2.62][j]	2.24[j]	470sh, 493 [0.15, 0.33]	74	1.69	4.38	1.54

*Single diastereomer of unknown absolute configuration. sh = Shoulder. [a]Solution photoluminescence measurements were recorded in degassed DCM solutions at *ca.* 20 °C with an excitation wavelength of 355 nm with quinine sulfate in 0.5 M H_2SO_4 as standard (Φ = 0.546).[51] [b]Measured at 77 K using an excitation wavelength of 355 nm. [c]Measured in an integrating sphere under air using an excitation wavelength of 355 nm. [d]Wavelength at 10% intensity on the blue edge of the spectrum obtained at 77 K. [e]Estimated using $E_T = hc/\lambda_{10\%\ em}$. [f]Non-emissive is defined as PLQY < 0.05%. [g]Error = ± 4%. [h]Error = ± 2%. [i]All FIrpic data were obtained in-house for direct comparison unless otherwise stated. [j]Values taken from ref 76. $\tau = 1/k_{nr} + k_r$. For FIrpic structure see Figure 1.12.

Complexes *rac* **66** and *meso* **67** display quite similar theoretical (Table 3.2), electrochemical (Table 3.4) and photophysical (Table 3.6) properties. The largest difference between the two complexes is the presence/ absence of intramolecular π–π interactions and their solution PLQY values. Therefore, a direct comparison serves as good evidence that intramolecular π–π interactions contribute significantly to the high solution PLQYs of the diarylhydrazide-bridged complexes.

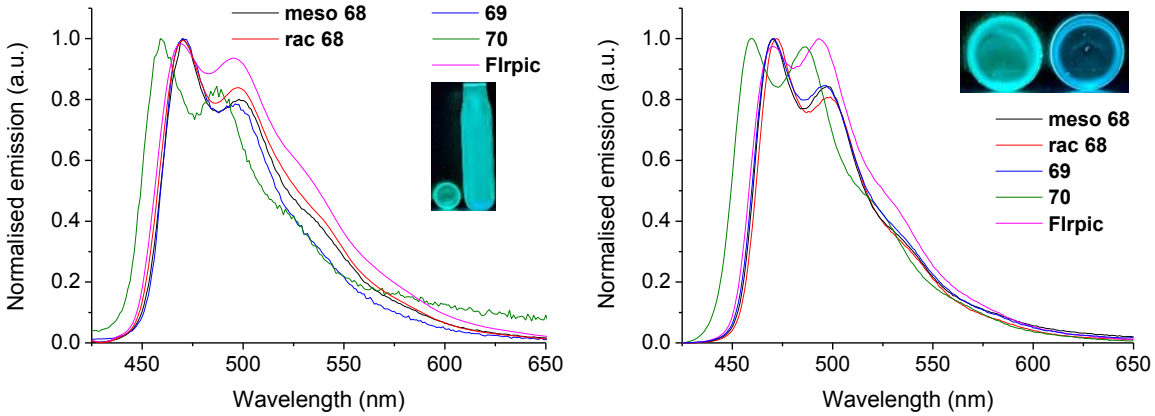

Figure 3.18: Normalised emission spectra for the sky-blue series (**68**–**70**) and FIrpic. (Left) spectra in degassed DCM solutions at room temperature (λ_{exc} 355 nm). (Right) Spectra of complexes doped into PMMA at 1 wt.% at room temperature. Insets: (left) photograph of emission from a doped PMMA film and degassed DCM solution of *rac* **68** under irradiation from a 365 nm UV lamp. (Right) photograph of the emission from doped PMMA films of *rac* **68** (left) and **70** (right) under irradiation from a 365 nm UV lamp. For FIrpic structure see Figure 1.12.

Incorporation of the fluorinated cyclometallating ligand **75** into the diastereomers *meso* **68** and *rac* **68** shifts their emission into the sky-blue region (Figure 3.18). In DCM both diastereomers have PLQYs of 47/ 48 ± 5% with CIE_{xy} coordinates (0.18, 0.36) marginally lower than the archetypal sky-blue emitter FIrpic[30,52] (0.19, 0.37) (Figure 1.12). This is observed despite their λ_{max} values being red shifted compared to FIrpic by 2 nm, and so is related to their narrower full width at half maximum (FWHM) values because of diminished $v_{0,1}$ vibronic shoulders: FWHM FIrpic = 82 nm, *meso* **68** = 63 nm, *rac* **68** = 69 nm. Sharp emission is consistent with high molecular rigidity,[53] which in this case is expected to be afforded by the intramolecular π–π interactions (observed in the ^{19}F NMR spectra of both diastereomers).

Molecular rigidity also influences the Huang-Rhys factor (S_M), which is proportional to the degree of structural distortion which occurs in the excited state of a molecule relative to the ground state.[54] S_M values were estimated for FIrpic, *meso* **68** and *rac* **68** from the relative

heights of the $v_{0,0}$ and $v_{0,1}$ peaks in their 77 K emission spectra (Figure 3.19, FIrpic spectrum analysed from ref. 52).[54,55] The following values were obtained: FIrpic = 0.7, *meso* **68** = 0.4, *rac* **68** = 0.5 (1 s.f.). These values indicate a lower intensity vibronic progression for the rigid diiridium complexes compared to FIrpic, which is vital for obtaining high colour purity.

Similarly, favourable photophysical properties are also observed for *meso* **68** and *rac* **68** when doped into PMMA: high PLQYs of 60/ 65 ± 10% (FIrpic 74 ± 10%) and comparatively narrow FWHM values of 55/ 56 nm (FIrpic 67 nm) (Figure 3.18). These comparatively narrow emission spectra are significant as the complexes are predicted to feature non-ancillary bridging ligands (see the DFT discussed above), which will likely lead to excited states with noteworthy ILCT character. ILCT character leads to more diffusely localised excited states and hence broader, less structured emission profiles.[55,56,53] The rigidifying effect of the intramolecular π–π interactions may be counteracting this, promoting sharper emission bands. These data indicate that diiridium complexes can be used as a platform for developing sky-blue phosphors with improved colour purity.

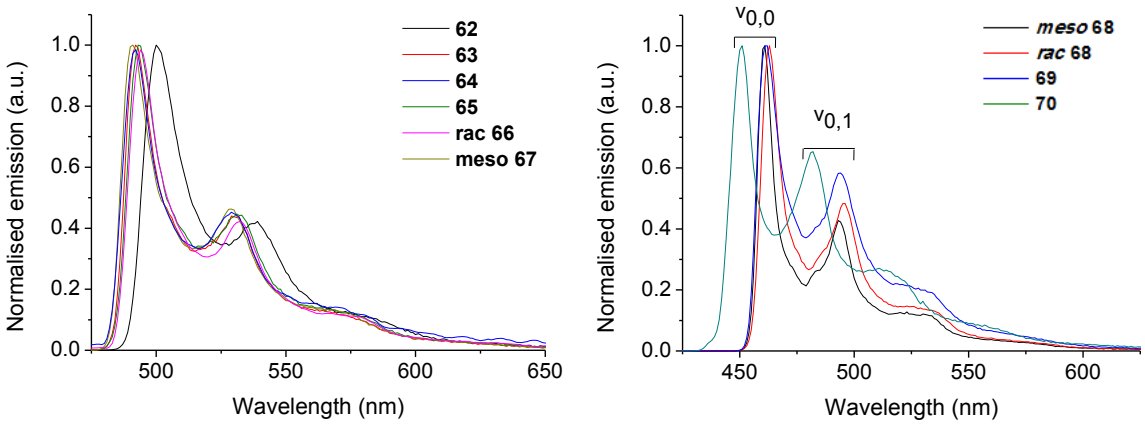

Figure 3.19: Normalised emission spectra of complexes **62–70** in 2-MeTHF glasses at 77 K (λ_{exc} 355 nm). $v_{0,0}$ and $v_{0,1}$ peaks are labelled for the sky-blue series (**68–70**).

Both diastereomers of **68** display higher k_r values than FIrpic (by *ca.* 20–40%) under directly comparable conditions in both DCM solution and PMMA. This results in notably shorter τ values in PMMA (where the complexes exhibit similar quantum yields to FIrpic) of 1.18/ 1.19 µs (vs. 1.69 µs for FIrpic). This may be related to the dinuclear nature of the complexes.[57,58] The strong Ir---Ir communication observed by CV (Table 3.4), is evidence that both Ir centres influence the excited state.

Enhanced radiative rate constants compared to monoiridium analogues have been reported for green to red diiridium complexes, which may be due to augmented spin-orbit coupling.[59,58,57,43] Blue phosphors tend to possess excited states with more LC character than green emitting complexes (see Chapter 1),[60,61,54] which is an indication of poorer LC/ MLCT state mixing (lower MLCT character) and can lead to inherently lower k_{r} values and so longer τ. The data obtained here indicate that diiridium complexes are also promising systems for developing sky-blue phosphors with higher k_{r} values and therefore shorter τ, which is a highly sought-after property.[62]

In a similar manner to the relationship between *rac* **66** and *meso* **67**, complex **69** is an analogue of **68** which cannot exhibit intramolecular π–π interactions between the cyclometalating and bridging ligands. As a result, **69** displays a low solution PLQY of 4 ± 4%. In PMMA its PLQY increases to 46 ± 10%, which is ascribed to a restriction of intramolecular motion, evident from the substantial decrease in k_{nr} (Table 3.6). The PLQY of **69** in PMMA is, however, significantly lower than those for either diastereomer of **68** (60/ 65 ± 10%). This is due to: 1) a substantially higher k_{nr} value, which crucially indicates that the intramolecular π–π interactions are also beneficial for obtaining high solid state PLQY values in diiridium complexes, and 2) a lower k_{r} value. This may be related to the smaller Ir---Ir coupling observed for **69** in the electrochemistry compared to **68** (Table 3.4 - $\Delta E_{1/2}$ is 190 mV smaller). Despite the lack of rigidifying intramolecular π–π interactions, **69** exhibits sharp emission similar to **68** (FWHM in PMMA = 57 nm) (Figure 3.18). This is ascribed to the ancillary nature of the bis(trifluoromethyl) bridge **73** in complex **69**, which contrasts with the non-ancillary nature of **72c** in complex **68**. This is expected to limit the ILCT character of the excited state, sharpening emission. The estimated S_M value for **69** is 0.6 (1 s.f.): larger than for either diastereomer of **68**, but still smaller than for FIrpic. These data indicate that incorporating ancillary bridges may also be a route towards sharpening sky-blue phosphorescence from diiridium complexes.

The emission from complex **70** is shifted deeper into the blue than for **68** or **69**, which is attributed to the LUMO-destabilising methylenecyclohexylether groups. As well as being tentatively observed in the reduction potentials above (Table 3.4), this can also be concluded from the more reliable oxidation potential data which indicate that the HOMO of **15** is shallower than for **13** or **14**. When doped into PMMA, **70** displays a PLQY of 69 ± 10%, which is comparable to the value obtained for FIrpic under the same experimental

conditions. Importantly, the colour is more blue: **70** emits at λ_{max} 460 nm, pushing the CIE_{xy} coordinates to a total value below 0.4 (0.15, 0.24), compared to FIrpic (470 nm; 0.15, 0.33). Complex **70** also displays a τ of 1.62 μs in PMMA, which is short in a doped film for an Ir complex with total CIE_{xy} < 0.4/ λ_{max} ≤ 460 nm and a high PLQY.[40,63–66] This can be attributed to the high k_r, which is perhaps related to the strong Ir---Ir coupling observed by CV ($\Delta E_{1/2}$ = 370 mV). Despite the presence of rigidifying intramolecular π–π interactions (observed in the ^{19}F NMR spectrum), the PLQY for **70** in DCM solution is low (2 ± 2%). This fits a trend of decreasing solution PLQY with increasing emission energy in the complexes *rac* **66** (λ_{max} = 502 nm, PLQY = 88 ± 5%), **68** (λ_{max} = 470 nm, PLQY = 47/ 48 ± 5%) and **70** (λ_{max} = 459 nm, PLQY = 2 ± 2%) due to incremental order of magnitude increases in their k_{nr} values (0.72, 7.23/ 7.48 and 89.3 × 10^5 s^{-1}). In contrast, all three complexes exhibit high PLQYs (> 60%) and similar k_{nr} values (1.91–3.39 × 10^5 s^{-1}) when doped into PMMA. Therefore, it appears that as the excited state energy increases, the rigidifying effect of the intramolecular π–π interactions is overcome and their capability to promote emission in solution is reduced.

Conclusions and future work

In this Chapter the chemistry of diiridium complexes have been developed in new ways with the series of highly fluorinated hydrazide-bridged complexes: 1) The use of intramolecular π–π interactions as an innovative non-covalent tool to influence the photophysical properties of diiridium complexes, and 2) the first examples of highly phosphorescent sky-blue diiridium complexes.

Complexes **62**–**67** represent an ideal platform for investigating intramolecular π–π interactions between aryl and perfluoroaryl rings in organometallic systems, in the solid state (by XRD) and also in solution (by ^{19}F NMR spectroscopy). These interactions are shown to be an effective way to rigidify diiridium complexes, which leads to significant and advantageous effects on their photophysical properties. Electrochemical and computational studies (DFT and TD-DFT) have also contributed to the understanding of these systems.

This knowledge, together with that acquired from Chapter 2, was then applied to the rational design and synthesis of the sky-blue emitting diiridium complexes **68**–**70**. They possess high PLQYs, λ_{max} as low as 460 nm (CIE_{x+y} < 0.4), high k_r, relatively short τ, and in some cases, notably sharp emission. Emission in the sky-blue region from diiridium complexes with conjugated bridging ligands is unprecedented. It has been accomplished in

this Chapter through the synergistic choice of bridging and cyclometallating ligands. The key role of the bridge is clear as there are reports of diiridium complexes bearing dfppy-type peripheral ligands for which sky-blue emission was not achieved.[67–71] Although diiridium systems have shown promise as high performing phosphors in the lower energy range (from red through to green),[31,42,59,58,57,72,43,73] to the best of our knowledge no complex displaying λ_{max} (PL) below *ca.* 490 nm at room temperature has been reported prior to this work.[42,**] The results presented in this Chapter greatly extend the versatility of luminescent diiridium complexes through shifting phosphorescence into the sky-blue region of the visible spectrum with the aid of tailored non-covalent interactions. They indicate that if diiridium complexes are correctly designed, their colour versatility is potentially comparable to monoiridium systems.

The goal of future research is to design and implement further structural modifications that could shift the emission of diiridium complexes deeper into the blue region. A blue shift of the emission from **70** is possible through using a ligand such as **86** (Figure 3.20), although it would be an incremental improvement as the HOMO of **70** is not localised on its cyclometallating ligands. Another possibility would be to move towards ligand designs that do not feature aromatic C–F bonds, which are known to be a source of instability in Ir complexes.[74] This could be accomplished through using cyclometallating and bridging ligands such as **87**[75] and **88**, which may still promote the intramolecular π–π interactions.

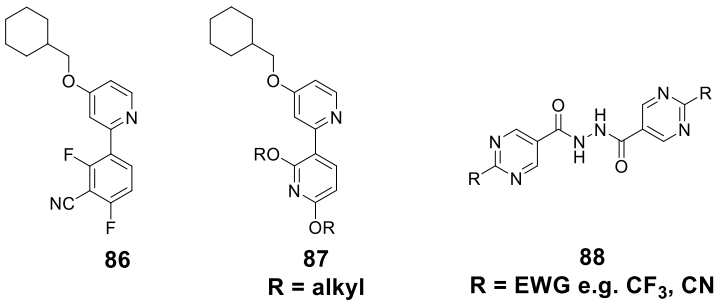

Figure 3.12: Structures of possible ligands for future work.

** Mazzanti and co-workers have reported a fluorinated diiridium complex with a vibronic sideband at 477 nm. However, the λ_{max} is *ca.* 510 nm and the emission extends out to 800 nm.[71]

References

1 C. Janiak, *Dalton Trans.*, 2000, 3885–3896.
2 D. Philp and J. F. Stoddart, *Angew. Chem. Int. Ed. Engl.*, 1996, **35**, 1154–1196.
3 B. L. Schottel, H. T. Chifotides and K. R. Dunbar, *Chem. Soc. Rev.*, 2008, **37**, 68–83.
4 J. W. Steed and J. L. Atwood, *Supramolecular Chemistry*, Wiley, 2nd edition, 2009.
5 K. Müller-Dethlefs and P. Hobza, *Chem. Rev.*, 2000, **100**, 143–167.
6 P. Hobza and J. Sponer, *Chem. Rev.*, 1999, **99**, 3247–3276.
7 P. Hobza and J. Cerny, *Phys. Chem. Chem. Phys.*, 2007, **9**, 5291–5303.
8 C. A. Hunter and J. K. M. Sanders, *J. Am. Chem. Soc.*, 1990, **112**, 5525–5534.
9 S. Grimme, *Angew. Chem. Int. Ed.*, 2008, **47**, 3430–3434.
10 K. S. Kim, P. Tarakeshwar and J. Y. Lee, *Chem. Rev.*, 2000, **100**, 4145–4185.
11 E. A. Meyer, R. K. Castellano and F. Diederich, *Angew. Chem. Int. Ed.*, 2003, **42**, 1210–1250.
12 C. R. Martinez and B. L. Iverson, *Chem. Sci.*, 2012, **3**, 2191–2201.
13 J. Wang, J. Luis, C. Pozo, A. E. Sorochinsky, S. Fustero, V. A. Soloshonok and H. Liu, *Chem. Rev.*, 2014, **114**, 2432–2506.
14 C. R. Patrick and G. S. Prosser, *Nature*, 1960, 187, 1021.
15 T. G. Beaumont and K. M. C. Davis, *Nature*, 1968, **218**, 865.
16 F. Cozzi, M. Cinquini, R. Annuziata and J. S. Siegel, *J. Am. Chem. Soc.*, 1993, 5330–5331.
17 F. Cozzi, F. Ponzini, R. Annunziata, M. Cinquini and J. S. Siegel, *Angew. Chem. Int. Ed. Engl.*, 1995, **34**, 1019–1020.
18 S. L. Cockroft, C. A. Hunter, K. R. Lawson, J. Perkins and C. J. Urch, *J. Am. Chem. Soc.*, 2005, **127**, 8594–8595.
19 H. Adams, F. J. Carver, C. A. Hunter, J. C. Morales and E. M. Seward, *Angew. Chem. Int. Ed. Engl.*, 1996, **35**, 1542–1544.
20 C. Hansch, A. Leo and R. W. Taft, *Chem. Rev.*, 1991, **91**, 165–195.
21 S. L. Cockroft and C. A. Hunter, *Chem. Soc. Rev.*, 2007, **36**, 172–188.
22 A. Camara-Campos, D. Musumeci, C. A. Hunter and S. Turega, *J. Am. Chem. Soc.*, 2009, **131**, 18518–18524.
23 A. M. Bünzli, E. C. Constable, C. E. Housecroft, A. Prescimone, J. A. Zampese, G. Longo, L. Gil-Escrig, A. Pertegás, E. Ortí and H. J. Bolink, *Chem. Sci.*, 2015, **6**, 2843–2852.
24 E. C. Constable, C. E. Housecroft, P. Kopecky, C. J. Martin, I. A. Wright, J. A. Zampese, H. J. Bolink and A. Pertegas, *Dalton Trans.*, 2013, **42**, 8086–8103.
25 L. He, D. Ma, L. Duan, Y. Wei, J. Qiao, D. Zhang, G. Dong, L. Wang and Y. Qiu, *Inorg. Chem.*, 2012, **51**, 4502–4510.
26 S. Kumar, Y. Hisamatsu, Y. Tamaki, O. Ishitani and S. Aoki, *Inorg. Chem.*, 2016, **55**, 3829–3843.
27 P. Li, G. G. Shan, H. T. Cao, D. X. Zhu, Z. M. Su, R. Jitchati and M. R. Bryce, *Eur. J. Inorg. Chem.*, 2014, 2376–2382.
28 S. Aoki, Y. Matsuo, S. Ogura, H. Ohwada, Y. Hisamatsu, S. Moromizato, M. Shiro and M. Kitamura, *Inorg. Chem.*, 2011, **50**, 806–818.
29 A. B. Tamayo, B. D. Alleyne, P. I. Djurovich, S. Lamansky, I. Tsyba, N. N. Ho, R. Bau and M. E. Thompson, *J. Am. Chem. Soc.*, 2003, **125**, 7377–7387.
30 A. F. Rausch, M. E. Thompson and H. Yersin, *J. Phys. Chem. A*, 2009, **113**, 5927–5932.
31 Y. Zheng, A. S. Batsanov, M. A. Fox, H. A. Al-Attar, K. Abdullah, V. Jankus, M. R. Bryce and A. P. Monkman, *Angew. Chem. Int. Ed.*, 2014, **53**, 11616–11619.
32 H. Oh, K.-M. Park, H. Hwang, S. Oh, J. H. Lee, J.-S. Lu, S. Wang and Y. Kang, *Organometallics*, 2013, **32**, 6427–6436.
33 S. Berger, S. Braun and H.-O. Kalinowski, *NMR Spectroscopy of the Non-Metallic Elements*, Wiley, 1st edition, 1997.

34 R. E. Banks and R. N. Haszeldine, *J. Chem. Soc*, 1967, 1822–1826.
35 E. Klauke, L. Oehlmann and B. Baasner, *J. Fluor. Chem.*, 1982, **21**, 495–513.
36 J. Zhou, M. W. Kuntze-Fechner, R. Bertermann, U. S. D. Paul, J. H. J. Berthel, A. Friedrich, Z. Du, T. B. Marder and U. Radius, *J. Am. Chem. Soc.*, 2016, **138**, 5250–5253.
37 R. J. Abraham, D. B. Macdonald and E. S. Pepper, *J. Am. Chem. Soc.*, 1968, **90**, 147–153.
38 R. Jana, B. Sarkar, D. Bubrin, J. Fiedler and W. Kaim, *Inorg. Chem. Commun.*, 2010, **13**, 1160–1162.
39 D. R. Martir, C. Momblona, A. Pertegás, D. B. Cordes, A. M. Z. Slawin, H. J. Bolink and E. Zysman-Colman, *ACS Appl. Mater. Interfaces*, 2016, **8**, 33907–33915.
40 A. F. Henwood, A. K. Bansal, D. B. Cordes, A. M. Z. Slawin, I. D. W. Samuel and E. Zysman-Colman, *J. Mater. Chem. C*, 2016, **4**, 3726–3737.
41 V. N. Kozhevnikov, Y. Zheng, M. Clough, H. A. Al-Attar, G. C. Griffiths, K. Abdullah, S. Raisys, V. Jankus, M. R. Bryce and A. P. Monkman, *Chem. Mater.*, 2013, **25**, 2352–2358.
42 D. G. Congrave, Y. Hsu, A. S. Batsanov, A. Beeby and M. R. Bryce, *Organometallics*, 2017, **36**, 981–993.
43 A. M'hamedi, M. A. Fox, A. S. Batsanov, H. A. Al-Attar, A. P. Monkman and M. R. Bryce, *J. Mater. Chem. C*, 2017, **5**, 6777–6789.
44 S.-Y. Yao, Y.-L. Ou and B.-H. Ye, *Inorg. Chem.*, 2016, **55**, 6018–6026.
45 C. Ulbricht, B. Beyer, C. Friebe, A. Winter and U. S. Schubert, *Adv. Mater.*, 2009, **21**, 4418–4441.
46 A. M'hamedi, A. S. Batsanov, M. A. Fox, M. R. Bryce, K. Abdullah, H. A. Al-Attar and A. P. Monkman, *J. Mater. Chem.*, 2012, **22**, 13529–13540.
47 I. R. Laskar, S.-F. Hsu and T.-M. Chen, *Polyhedron*, 2005, **24**, 189–200.
48 E. Baranoff, S. Fantacci, F. De Angelis, X. Zhang, R. Scopelliti, M. Grätzel and M. K. Nazeeruddin, *Inorg. Chem.*, 2011, **50**, 451–462.
49 J. Frey, B. F. E. Curchod, R. Scopelliti, I. Tavernelli, U. Rothlisberger, M. K. Nazeeruddin and E. Baranoff, *Dalton Trans.*, 2014, **43**, 5667–5679.
50 S. Lamansky, P. Djurovich, D. Murphy, F. Abdel-Razzaq, H. E. Lee, C. Adachi, P. E. Burrows, S. R. Forrest and M. E. Thompson, *J. Am. Chem. Soc.*, 2001, **123**, 4304–4312.
51 H. Benjamin, Y. Zheng, A. S. Batsanov, M. A. Fox, H. A. Al-Attar, A. P. Monkman and M. R. Bryce, *Inorg. Chem.*, 2016, **55**, 8612–8627.
52 E. Baranoff and B. F. E. Curchod, *Dalton Trans.*, 2015, **44**, 8318–8329.
53 T. Fleetham, G. Li, Z. Q. Zhu and J. Li, *SID Symp. Dig. Tech. Pap.*, 2015, **46**, 411–414.
54 J. Li, P. I. Djurovich, B. D. Alleyne, M. Yousufuddin, N. N. Ho, J. C. Thomas, J. C. Peters, R. Bau and M. E. Thompson, *Inorg. Chem.*, 2005, **44**, 1713–1727.
55 G. Li, T. Fleetham, E. Turner, X. C. Hang and J. Li, *Adv. Opt. Mater.*, 2015, **3**, 390–397.
56 K. Dedeian, J. Shi, N. Shepherd, E. Forsythe and D. C. Morton, *Inorg. Chem.*, 2005, **44**, 4445–4447.
57 R. E. Daniels, S. Culham, M. Hunter, M. C. Durrant, M. R. Probert, W. Clegg, J. A. G. Williams and V. N. Kozhevnikov, *Dalton Trans.*, 2016, **45**, 6949–6962.
58 P.-H. Lanoë, C. M. Tong, R. W. Harrington, M. R. Probert, W. Clegg, J. A. G. Williams and V. N. Kozhevnikov, *Chem. Commun.*, 2014, **50**, 6831–6834.
59 G. Li, Y. Wu, G. Shan, W. Che, D. Zhu, B. Song, L. Yan, Z. Su and M. R. Bryce, *Chem. Commun.*, 2014, **50**, 6977–6980.
60 M. A. Baldo, S. R. Forrest and M. E. Thompson, in *Organic Electroluminescence*, ed. Z. H. Kafafi, CRC and SPIE Press, 2005.
61 L. Yang, F. Okuda, K. Kobayashi, K. Nozaki, Y. Tanabe, Y. Ishii and M.-A. Haga, *Inorg. Chem.*, 2008, **47**, 7154–7165.
62 S. Haneder, E. Da Como, J. Feldmann, J. M. Lupton, C. Lennartz, P. Erk, E. Fuchs, O. Molt, I.

Münster, C. Schildknecht and G. Wagenblast, *Adv. Mater.*, 2008, **20**, 3325–3330.
63 C.-H. Yang, M. Mauro, F. Polo, S. Watanabe, I. Muenster, R. Frohlich and L. De Cola, *Chem. Mater.*, 2012, **24**, 3684–3695.
64 T. Duan, T.-K. Chang, Y. Chi, J.-Y. Wang, Z.-N. Chen, W.-Y. Hung, C.-H. Chen and G.-H. Lee, *Dalton Trans.*, 2015, **44**, 14613–14624.
65 H. J. Park, J. N. Kim, H. Yoo, K. Wee, S. O. Kang and D. W. Cho, *J. Org. Chem.*, 2013, **78**, 8054–8064.
66 T. B. Fleetham, L. Huang, K. Klimes, J. Brooks and J. Li, *Chem. Mater.*, 2016, **28**, 3276–3282.
67 G. Nasr, A. Guerlin, F. Dumur, L. Beouch, E. Dumas, G. Clavier, F. Miomandre, F. Goubard, D. Gigmes, D. Bertin, G. Wantz and C. R. Mayer, *Chem. Commun.*, 2011, **47**, 10698–10700.
68 F. Lafolet, S. Welter, Z. Popović and L. De Cola, *J. Mater. Chem.*, 2005, **15**, 2820–2828.
69 R. D. Costa, G. Fernandez, L. Sanchez, N. Martín, E. Ortí and H. J. Bolink, *Chem. Eur. J.*, 2010, **16**, 9855–9863.
70 X. Yuan, S. Zhang and Y. Ding, *Inorg. Chem. Commun.*, 2012, **17**, 26–29.
71 E. S. Andreiadis, D. Imbert, J. Pécaut, A. Calborean, I. Ciofini, C. Adamo, R. Demadrille and M. Mazzanti, *Inorg. Chem.*, 2011, **50**, 8197–8206.
72 X. Yang, Z. Feng, J. Zhao, J.-S. Dang, B. Liu, K. Zhang and G. Zhou, *ACS Appl. Mater. Interfaces*, 2016, **8**, 33874–33887.
73 X. Yang, X. Xu, J. Dang, G. Zhou, C.-L. Ho and W.-Y. Wong, *Inorg. Chem.*, 2016, **55**, 1720–1727.
74 V. Sivasubramaniam, F. Brodkorb, S. Hanning, H. P. Loebl, V. van Elsbergen, H. Boerner, U. Scherf and M. Kreyenschmidt, *J. Fluor. Chem.*, 2009, **130**, 640–649.
75 J. Frey, B. F. E. Curchod, R. Scopelliti, I. Tavernelli, U. Rothlisberger, M. K. Nazeeruddin and E. Baranoff, *Dalton Trans.*, 2014, **43**, 5667–5679.
76 E. Baranoff, B. F. E. Curchod, F. Monti, F. Steimer, G. Accorsi, I. Tavernelli, U. Rothlisberger, R. Scopelliti, M. Grätzel and M. K. Nazeeruddin, *Inorg. Chem.*, 2012, **51**, 799–811.

Chapter 4: 1,2-Diarylimidazole cyclometallating ligands in hydrazide-bridged diiridium complexes

Introduction

Fac-homoleptic monoiridium complexes with 1,2-diarylimidazole ligands currently constitute the state-of-the-art in terms of stable sky-blue Ir complexes for OLED applications.[1,2] Within the literature, such ligands have attracted limited attention in heteroleptic complexes[3–5] and do not appear to have been applied to diiridium systems. Building on the work covered in Chapter 3, in this Chapter 1,2-diarylimidazole ligands are investigated as cyclometallating ligands within our hydrazide-bridged diiridium system to obtain sky-blue emission. This enables an extension to the structural diversity of sky-blue diiridium complexes.

2-Phenylimidazole cyclometallating ligands in Ir(III) complexes

In this section, recent progress in the application of 2-phenylimidazole cyclometallating ligands to monoiridium complexes is reviewed as a foundation for their application to diiridium complexes within this Chapter.

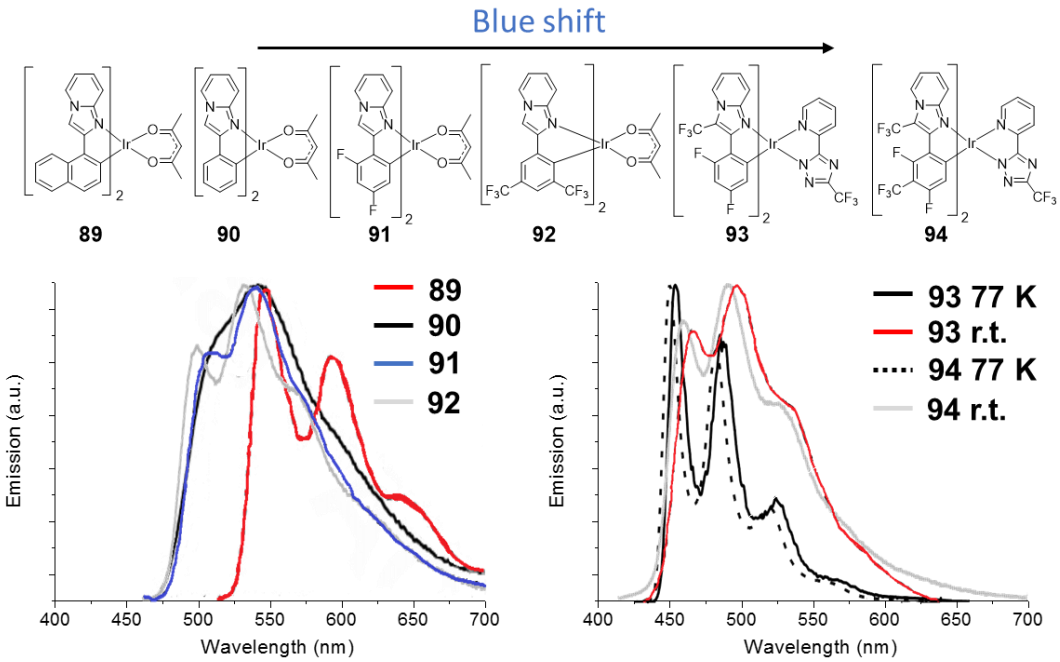

Figure 4.1: Molecular structures of complexes **89**–**94** and their emission spectra in DCM at room temperature or 2-MeTHF at 77 K. The spectra for **89**–**92** were recorded in DCM at room temperature. Adapted from reference 5 with permission from the American Chemical Society copyright 2007.

Yamashita and co-workers reported a systematic series of heteroleptic monoiridium complexes (**89**–**94**) (Figure 4.1) featuring aryl imidazo[1,2-*a*]pyridine cyclometallating ligands.[5] Emission was tuned from the orange to sky-blue using structural modifications known from ppy precedents: namely, incorporation of fluorine atoms *meta* to the Ir–C bond, inclusion of inductive electron withdrawing groups *para* to the Ir–C bond, and the use of electron withdrawn pyridylazolate ancillary ligands. However, the complexes display low room temperature solution PLQYs (≤ 6%) and rather long τ (> 5 μs). As the emission spectra feature well-resolved vibronic features, this is potentially due to a low MLCT contribution to the emissive states. In complexes **93** and **94**, DFT predicts that the HOMOs are localised on both the cyclometallating phenyl and imidazole π orbitals as well as the Ir centre, while the LUMO is localised on the pyridyl moiety of the ancillary ligand. Therefore, functionalisation of both the phenyl and imidazole components of the cyclometallating ligands with electron withdrawing groups leads to blue shifts in emission due to HOMO stabilisation. As the emission of the parent complex **90** is consecutively blue shifted through modification of the cyclometallating and ancillary ligands, the relative intensities of the first ($v_{0,0}$) and second ($v_{0,1}$) vibronic bands in the emission spectra (Figure 4.1) become increasingly inverted, leading to poor colour purity. This is a common problem associated with phenylimidazole cyclometallating ligands.[1] Even at 77 K, the estimated S_M values for **93** and **94** are rather large (0.8 1 s.f.).

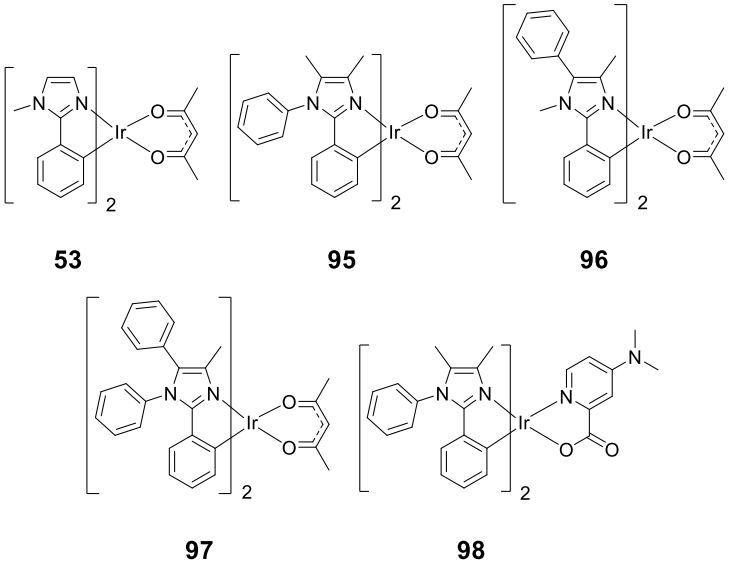

Figure 4.2: Molecular structures of complexes **53** and **95**–**98**.

Baranoff and Nazeeruddin et al. investigated a series of heteroleptic complexes (**53**[6] and **95**–**98**) featuring 2-phenylimidazole cyclometallating ligands (Figure 4.2).[3] Complex **53** exhibits broad emission which spans the visible spectrum and results in white emission. It was previously discussed in detail in Chapter 2. Functionalisation of the parent complex **53** perturbs the degenerate LUMO

levels of the cyclometallating and ancillary ligands, resulting in sharper (although still comparatively broad and featureless) emission. Notably, functionalising the imidazole moieties with bulky aryl groups also results in improved solution PLQYs (95% for complex **97**), which could be due to rigidification of the complexes or a solvent shielding effect. Analogously to the report by Yamashita,[5] DFT calculations predict that the HOMO and LUMO orbitals are smeared over the cyclometallating ligands, being less spatially separated than for complexes with ppy-based ligands.

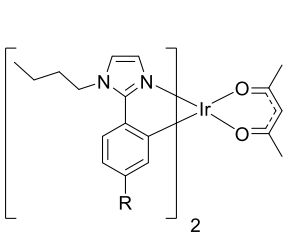

99a R = OCH_3, 458 nm, 0.02%
b R = F, 455 nm, 0.04%
c R = CF_3, 492 m, 28%

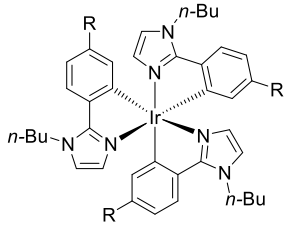

100a R = OCF_3, 454 nm, 53%
b R = F, 446 nm, 60%
c R = CF_3, 483 nm, 40%

Figure 4.3: Molecular structures of complexes **99** and **100** with their 77 K $v_{0',0}$ wavelengths and room temperature solution PLQYs (all measured in 2-MeTHF).

Karatsu and colleagues investigated some hetero- (**99a–c**) and *fac*-homoleptic (**100a–c**) complexes.[4] The structures of the complexes are shown in Figure 4.3, together with their 77 K $v_{0',0}$ emission wavelengths and room temperature solution PLQYs. The heteroleptic complexes (**99a–c**) are practically non-emissive at room temperature in solution, other than **99c** which features a red-shifting trifluoromethyl group *para* to the phenyl–imidazole bond. This is rationalised through the DFT data presented for **99b** and **99c** in Table 4.1. Poorly emissive **99b** features degenerate LUMO (localised on the cyclometallating ligand) and LUMO+1 (localised on the acac ancillary ligand) orbitals. Therefore, emission can potentially be quenched through a state localised on the acac moiety (the same is observed for **99a**). For **99c** the energy levels of the cyclometallating ligand are stabilised, therefore: 1) both the LUMO and LUMO+1 do not feature significant acac character, and 2) the LUMO+2, which does feature acac character, is 0.5 eV higher in energy than the LUMO. Consequently, a similar quenching mechanism does not apply to **99c** which is fairly emissive (PLQY = 28%) at room temperature in solution.

The homoleptic complexes (**100a–c**) are more intensely emissive (PLQYs of ≥ 40%). This is due to replacement of the acac ligand with a cyclometallating ligand, which both removes the acac-based quenching pathway and should lead to a greater ligand field splitting. Blue shifting the emission in the order **100c** (CF_3) → **100a** (OCF_3) → **100b** (F) leads to incremental increases in the intensities of the $v_{0,1}$ emission bands at room temperature so that in **100b** it is more intense than the $v_{0,0}$ band

(Figure 4.4). The S_M values (from the 77 K emission spectra) also increase in the same order (**100c** = 0.4, **100a** = 0.5, **100b** = 0.8 1 s.f.). These data suggest that the change in room temperature spectral profile with increasing emission energy is likely not due to a temperature dependent pathway which becomes more accessible upon blue shifting the emission. This would be expected if **100a–c** displayed similar S_M values at 77 K.[7] They also suggest that blue shifting the emission increases the structural distortion encountered in the excited state.

Table 4.1: FMO data obtained for phenylimidazole complexes and *fac*-Ir(ppy)$_3$ by Karatsu et al. Obtained at the B3LYP/LANL2DZ level, no basis set was specified.

Complex	Orbital	Ir	Ph[a]	Im/ Py[b]	acac	E (eV)
fac-Ir(ppy)$_3$	LUMO	0.2%	25.9%	73.5%	-	1.47
	HOMO	52.8%	38.9%	8.2%	-	4.95
99b	LUMO+2	3.6%	42.3%	39.7%	14.4%	0.74
	LUMO+1	1.4%	7.5%	7.4%	83.7%	0.87
	LUMO	2.1%	51.9%	45.6%	0.4%	0.88
	HOMO	46.4%	38.4%	10.2%	5.0%	4.86
99c	LUMO+2	2.2%	1.2%	1.0%	95.6%	1.05
	LUMO+1	2.8%	60.3%	34.3%	2.6%	1.41
	LUMO	1.6%	62.3%	35.7%	0.4%	1.54
	HOMO	48.8%	36.8%	8.6%	5.8%	5.16
100a	LUMO	0.5%	57.0%	42.5%	-	1.19
	HOMO	53.2%	31.8%	15.0%	-	5.11
100b	LUMO	0.6%	53.6%	45.8%	-	0.77
	HOMO	52.4%	32.8%	14.8%	-	4.73
100c	LUMO	0.4%	64.1%	35.5%	-	1.49
	HOMO	56.0%	30.7%	13.3%	-	5.11

[a]Phenyl groups of the cyclometallating ligands; [b]pyridyl or imidazolyl groups of the cyclometallating ligands.

DFT predicts similar contribution from the Ir centres to the HOMOs of the homoleptic complexes as for *fac*-Ir(ppy)$_3$ (Table 4.1). However, with respect to the cyclometallating ligands the FMOs are less spatially separated, analogous to the other examples above.[3,5]

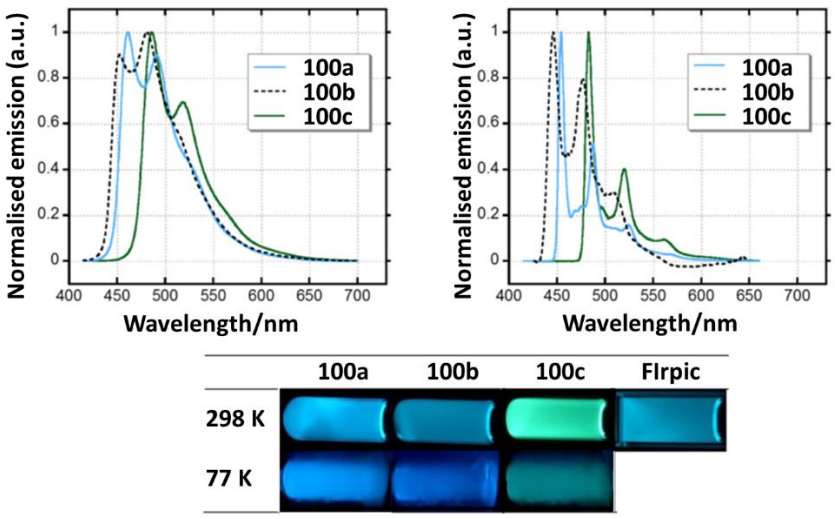

Figure 4.4: Emission spectra for complexes **100a–c** recorded in 2-MeTHF at room temperature and 77 K. Insets are photographs of emission under a UV lamp. Adapted from ref 4 with permission from the American Chemical Society copyright 2013.

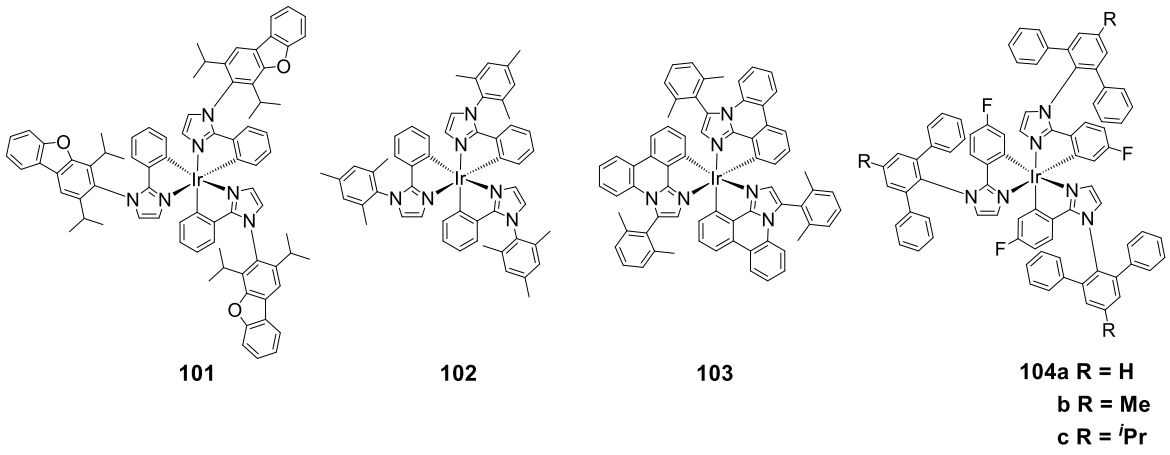

Figure 4.5: Structures of *fac*-homoleptic 2-phenylimidazole complexes.

Monoiridium complexes based on 2-phenylimidazole cyclometallating ligands have received significant interest within the OLED community, particularly *fac*-homoleptic complexes such as **101–104** (Figure 4.5) which avoid the incorporation of comparatively labile non-cyclometallated ancillary ligands.[1] Bulky aryl moieties have been widely incorporated as pendant groups, which afford high PLQYs, prevent aggregation by improving host miscibility and improve stability. Complex **101** incorporates pendant dibenzofuran groups. These aid hole transport, which is beneficial in helping to alleviate hole trapping, which is a common problem encountered with blue-emitting Ir complexes in OLEDs.[8] The complex **101** exhibits a PLQY of 52% with a PL λ_{max} of 475 nm (both in MeCN). Under directly comparable conditions, the OLED lifetime to half luminance (T_{50}) for a

vacuum processed device containing **101** was 5.8 h compared to 0.1 h for FIrpic (Figure 1.12), while displaying a good EQE of 20%. Complex **102** features pendant mesityl groups. It displays a PLQY of 61% with a short τ of 1.5 μs and λ_{max} of 474 nm. Record sky-blue Ir complex EQEs of >30% were reported for the complex, although rather broad emission results in poor CIE_{xy} coordinates (0.18, 0.41).[9,10] Complex **103** takes a step towards improving the colour purity of 2-phenylimidazole complexes through the incorporation of a rigid fused phenanthridine ligand structure.[11] Although only OLED data was reported for the complex, devices afforded improved CIE_{xy} coordinates of (0.15, 0.29) due to a diminished intensity of the $v_{0,1}$ band. This is likely because the fused structure restricts distortion of the ligand in the excited state. A long device lifetime to 80% luminance (T_{80}) of 616 ± 10 h was also reported. This is significant considering that the device lifetimes for sky-blue ppy-based complexes are typically only a few hours.[1] Complexes **104a–c** feature monofluorinated cyclometallating ligands with pendant bulky terphenyl groups that are functionalised by various alkyl chains.[12] They display PLQYs of 38–50% with $v_{0,0}$ emission bands around 460 nm (both in DCM). However, although it blue shifts the emission, fluorination inverts the intensity of their $v_{0,0}$ and $v_{0,1}$ bands, resulting in PL λ_{max} values of 487 nm. Consequently, the CIE_{xy} coordinates for **104a–c** (0.17, 0.28) are no better than those reported for the non-fluorinated complex **103.** Improved OLED stability was reported for **104a** (T_{80} = *ca*. 50 h) for which R = H.

In conclusion, the literature reveals that although DFT predicts notably different FMO localisation in phenylimidazole complexes compared to their ppy analogues, the same strategies can be applied to blue shift their emission with regards to substitution on the cyclometallating phenyl moieties.

Functionalisation of phenylimidazole ligands to obtain PL λ_{max} below *ca.* 450 nm tends to result in an inversion of the $v_{0,0}$ and $v_{0,1}$ band intensities so that the $v_{0,1}$ band is the major peak, weakening colour purity. Consequently, phenylimidazole-functionalised complexes have received less attention than their ppy-functionalised counterparts. This effect is not exclusive to phenylimidazole complexes: a similar increase in the intensity of the $v_{0,1}$ band alongside blue shifting of emission is also observed for ppy complexes, although it tends to not become comparable in intensity to the $v_{0,0}$ band until wavelengths deeper into the blue (λ_{max} below *ca.* 440 nm).[13,14] To date, no clear explanation has been offered in the literature for this property in phenylimidazole complexes. However, as it occurs upon blue shifting the emission, and is also seen for ppy complexes (albeit to a lesser extent), it is likely related to the increasing ^{3}LC character of the excited state. In such situations, the less well-defined spatial separation of the FMOs of phenylimidazole ligands may explain why the effect is more pronounced than in ppy complexes. A similar effect has also been reported upon shifting the PL below ca. 450 nm for Ir complexes featuring phenyltriazole cyclometallating ligands, for which poorer FMO spatial separation is also predicted by DFT.[15] The

fact that this effect is less pronounced in complex **103**, which has a highly rigid fused ligand structure, also supports that this effect is related to LC states.

Nonetheless, phenylimidazole functionalised Ir complexes are interesting. They have afforded greatly improved stability in sky-blue OLEDs, while their structural versatility has yet to be exhaustively explored.

Results and discussion

Design, synthesis and characterisation

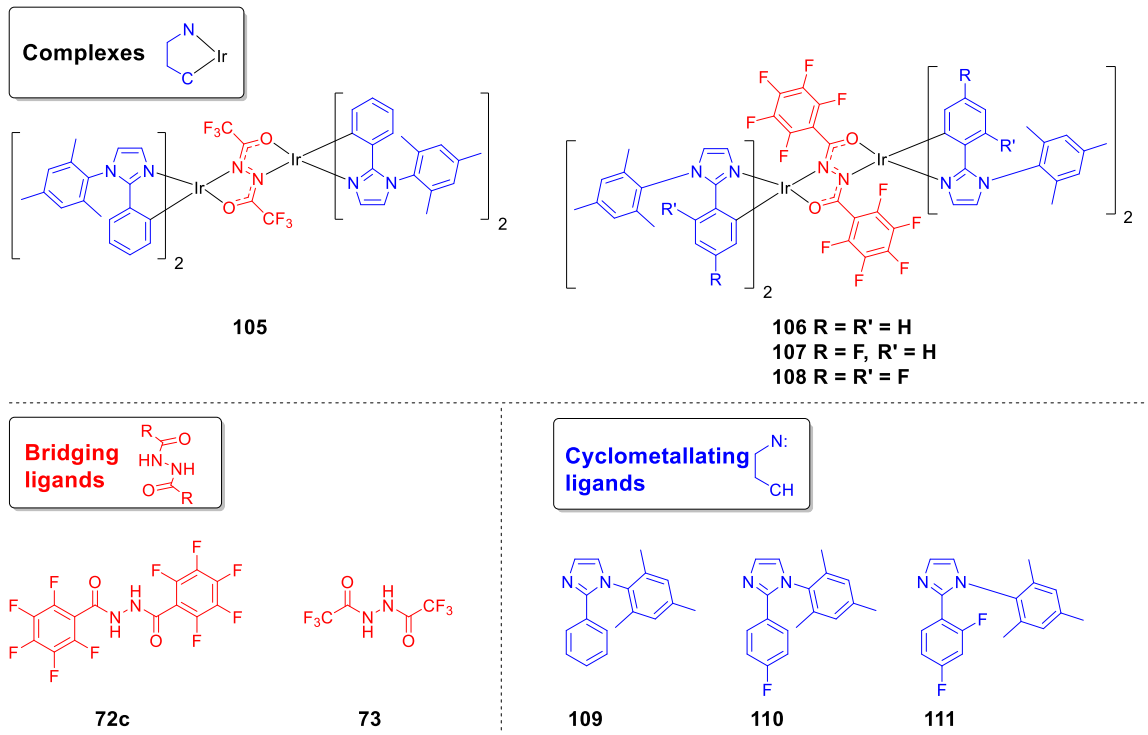

Figure 4.6: Structures of the diiridium complexes and ligands studied in this Chapter. Complexes were studied as diastereomeric mixtures unless otherwise stated

The structures of the new complexes (**105–108**) and ligands (**72c**, **73** and **109–111**) are shown in Figure 4.6. Ir complexes possessing 1,2-diarylimidazole-based ligands are very topical as they afford relatively stable sky-blue OLEDs.[11] Nevertheless, they are comparatively under-studied compared to ppy-based systems and have not been applied to diiridium complexes. In this Chapter, the compatibility of 2-phenylimidazole ligands with our bridges **72c** and **73** was assessed to develop new sky-blue diiridium complexes. The mesityl-functionalised parent ligand **109** was selected as bulky aryl groups on the 1 position of 1,2-diarylimidazoles enhance PLQYs,[3] and due to the favourable properties of its homoleptic complex **102**.[9,10] Mesityl groups are also not as excessively bulky as the other examples in Figure 4.5, which was expected to aid ligand synthesis and decrease steric congestion in the resulting diiridium complexes, making their formation more likely.

The parent ligand **109** was applied to the complexes **105** and **106** to screen the bis(trifluoromethyl) and bis(pentafluorophenyl) bridges **72c** and **73**. Based on the photophysical results obtained for these initial complexes (discussed below), and the interesting π–π interactions observed in Chapter 3 for complexes featuring **72c**, complexes **107** and **108** were then designed, which have incremental fluorination of their cyclometallating ligands (**110** and **111**). This was expected to blue shift emission through HOMO stabilisation. Although there is literature precedent for fluorination blue shifting the emission onset of 2-phenylimidazole complexes while diminishing colour purity, work reported in Chapter 2 has shown that the bridging unit can significantly alter the photophysical properties of diiridium complexes compared to their mononuclear analogues. Therefore, it is of interest to investigate such a series on a diiridium platform.

The synthesis of the bridging ligands **72c** and **73** is discussed in Chapter 3. The synthesis of the cyclometallating ligands **109–111** was accomplished via a transition metal catalyst-free route shown in Figure 4.7.[16]

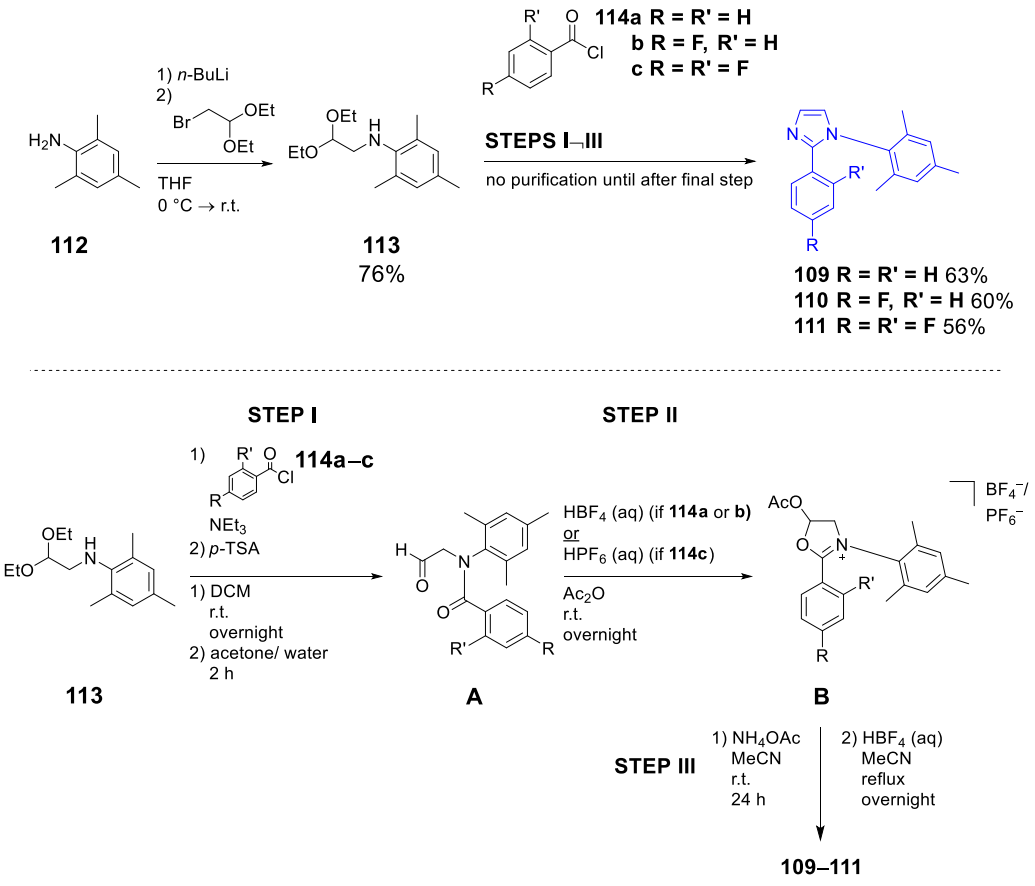

Figure 4.7: Synthetic scheme for **109–111**.

The acetal intermediate **113** was obtained from 2,4,6-trimethylaniline (**112**) after lithiation and subsequent treatment with bromoacetaldehyde diethylacetal. **113** was then treated with the

various benzoyl chlorides **114a–c** in a three-step procedure. The first step is a one-pot procedure consisting of a nucleophilic substitution of **114a–c** by **113**, followed by an *in-situ* acetal deprotection with *para*-toluenesulfonic acid (*p*-TSA) to afford the dicarbonyl intermediates **A**. Subsequent cyclisations with acetic anhydride in the presence of HBF_4 provided the oxazolium tetrafluoroborate salts **B**, which were isolated via filtration after precipitation. In the synthesis of the difluoro derivative **111**, the high solubility of the tetrafluoroborate salt prevented its facile isolation. This was overcome through synthesising the hexafluorophosphate salt, which readily precipitated when the reaction mixture was poured into diethyl ether. The salts **B** were then treated with NH_4OAc as a source of ammonia to install the second imidazole nitrogen atom. Subsequent dehydration/ aromatisation with HBF_4 afforded the cyclometallating ligands **109–111** in 56–63% yields after flash chromatography on *ca.* 2 g scales.

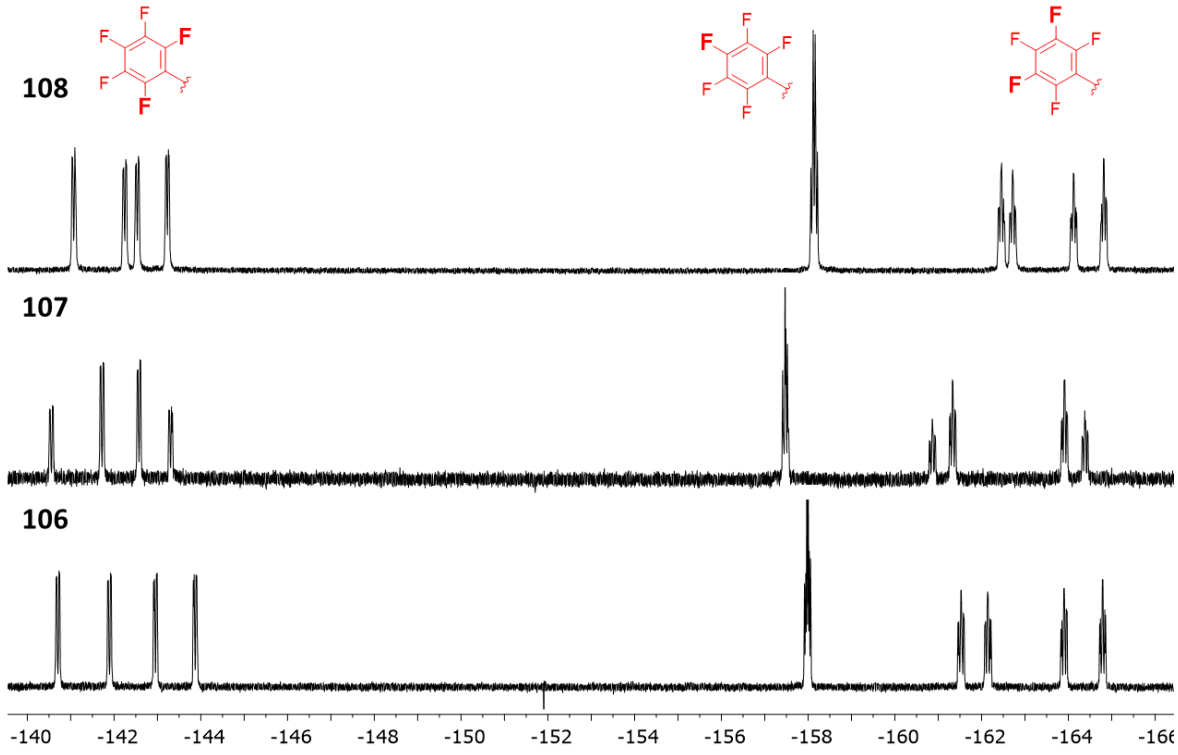

Figure 4.8: Expansions of the C_6F_5 regions of the ^{19}F $\{^1H\}$ spectra of **106–108**. Diastereomeric ratios: **106** *ca.* 1:1, **107** *ca.* 1:0.6, **108** *ca.* 1:0.9. Ten environments are seen in each spectrum, corresponding to restricted rotation of the C_6F_5 groups in solution for both diastereomers.

The complexes **105–108** were synthesised from the corresponding bis(μ–Cl) dimers in either 2-ethoxyethanol or dry diglyme in the same manner as discussed for complexes **62–70** in Chapter 3. A single diastereomer was formed for **105**, as observed for analogues in Chapter 3 incorporating the bridge **73**. The complexes **106–108** were isolated and studied as diastereomeric mixtures as they could not be easily separated. Analogous to complexes **62–66**, **68** and **70** in Chapter 3, the

pentafluorophenyl rings of **72c** promote intramolecular π–π interactions in **106**–**108**, which can be seen in the solution ^{19}F NMR spectra in Figure 4.8.

X-ray crystal structures[*]

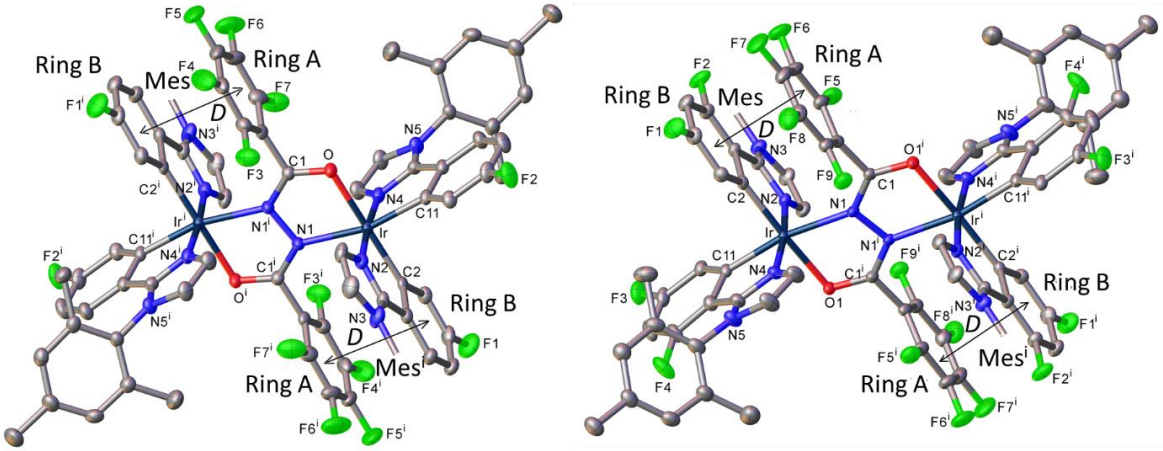

meso **107** *meso* **108**

Figure 4.9: X-ray molecular structures of *meso* **107** and *meso* **108**. Thermal ellipsoids are drawn at the 50% probability level, H atoms, solvent of crystallisation and some mesityl groups (Mes) are omitted for clarity. Primed atoms are generated by a crystallographic inversion centre. Vector *D* identifies intramolecular π–π interactions (see Table 4.2).

Table 4.2: Selected geometrical parameters of diiridium complexes (bond distances in Å).

	meso **107** $6CH_2Cl_2$	*meso* **108** 2MeOH
Space group	*C2/c*	*Pbca*
Mol. symmetry	C_i	C_i
Ir centres	ΔΛ	ΔΛ
Ir---Ir, Å	5.022	5.065
Ir–C (*trans*-O)	2.003(4)	2.003(3)
Ir–C (*trans*-N)	2.012(4)	2.016(3)
Ir–N, stacked	2.020(3)	2.018(2)
Ir–N, non-stacked	2.019(3)	2.040(2)
Bridge geometry		
OCNNCO folding, °	planar	planar
Ir displacement, Å	0.086	0.208
Ir–O	2.119(3)	2.130(2)
Ir–N	2.144(3)	2.159(2)
N–N	1.434(4)	1.437(3)
N–C	1.306(6)	1.305(4)
C–O	1.279(4)	1.287(3)
Intramolecular stacking (π–π)		
Θ, °[a]	3.5	3.0
D, Å[b]	3.30	3.26

[a] Interplanar angle between ring *A* of the bridging ligand and ring *B* of the cyclometallating ligand (see Figure 4.9); [b] distance between the plane of ring *B* and the centroid of ring *A*.

The single-crystal X-ray crystal structures of the *meso* diastereomers of **107** and **108** are displayed in Figure 4.9. Relevant parameters are listed in Table 4.2. *Meso* **107** crystallised as a DCM

[*] All X-ray crystal structures were solved by Dr Andrei Batsanov.

hexasolvate when hexane vapour was slowly diffused into its saturated DCM solution. Via a similar procedure diffusing MeOH into THF, *meso* **108** crystallised as a MeOH disolvate. The *meso* diastereomers preferentially crystallised from solutions of diastereomeric mixtures as they have a greater propensity to crystallise due to their inversion centre symmetry.

The Ir centres in both structures display distorted octahedral coordination. The N atoms of the two C^N cyclometallating ligands occupy axial positions with respect to the bridge plane, and are *trans* to one another.[17,18] As was observed for the *meso* diastereomers in Chapters 2 and 3, the central hydrazide moieties of *meso* **107** and *meso* **108** are planar, and the aryl substituents (*A*) on the bridging ligands are oriented approximately perpendicular to the hydrazide planes and are stacked face-to-face (π–π) with the phenyl ring (*B*) of a cyclometallating ligand (Figure 4.9). The stacking is closer and more parallel in *meso* **107** compared to *meso* **108** (*D* = 3.0 vs. 3.5 Å, Θ = 3.26 vs. 3.30°). The average parameters for *meso* **107** and *meso* **108** (*D* = 3.28 Å, Θ = 3.25°) are also similar to those found for *rac* **68** in Chapter 3 (D = 3.23 Å, Θ = 4.80°), while being closer and more parallel than for the Chapter 3 analogues (**62**, **64**–**66**) which do not feature cyclometallating ligand fluorination (*D* = 3.34 Å, Θ = 7.73°). Therefore, the combined X-ray data for *rac* **68**, *meso* **107** and *meso* **108** suggest that incremental fluorination of the cyclometallating ligands up to the difluoro level promotes intramolecular π–π interactions in diarylhydrazide-bridged diiridium complexes.

Computational study

Electronic structure calculations were carried out on **105**–**108** at the B3LYP/LANL2DZ:3–21G* level to gain insight into the photophysical properties of the complexes and facilitate comparison with the diiridium complexes studied in Chapters 2 and 3. In contrast to the data presented in Chapters 2 and 3, in the optimised structures of **105**–**108** the central hydrazide fragments are predicted to be close to planar for both the *meso* and *rac* diastereomers (for **35**–**38** and **62**–**70** in Chapters 2 and 3 only the *meso* forms feature planar bridges). This is likely due to the sterically congested structures, and agrees with the X-ray data presented above for *meso* **107** and *meso* **108**. The optimised geometries of the *rac* forms of **105**–**108** cannot be compared with X-ray diffraction as no *rac* structures have been solved. Such similar optimised geometries for the *rac* and *meso* diastereomers may explain why they could not be separated.

The predicted FMO contributions are listed in Table 4.3. Generally, there is a good agreement between diastereomers, and so FMO plots for *meso* **105**–**108** are presented in Figure 4.10 (The FMO plots for the *rac* diastereomers are included in the Appendix, Figures A23 and A24). For the diastereomers of **105**, the HOMOs are primarily localised on the Ir centres, the central hydrazide fragments of the bridging ligands and the cyclometallating ligands, while the LUMOs are

cyclometallating ligand-based. The spatial separation of the FMOs on the cyclometallating ligands is less defined than for the ppy analogues in Chapters 2 and 3, i.e. the LUMO contribution is split nearly equally between the phenyl and imidazole moieties. This is in good agreement with studies on mononuclear complexes featuring similar cyclometallating ligands.[3–5]

Table 4.3: Summary of the HOMO and LUMO compositions for the most stable minima of the complexes.

Complex	Isomer	Orbital	Ir	Bridge centre	Bridge aryl	Ph[a]	Im[b]
105	*meso*	LUMO	3%	1%	-	49%	47%
		HOMO	45%	14%	-	33%	8%
	rac	LUMO	2%	1%	-	43%	53%
		HOMO	46%	34%	-	13%	46%
106	*meso*	LUMO	2%	7%	58%	17%	17%
		HOMO	44%	41%	1%	7%	8%
	rac	LUMO	2%	3%	50%	23%	22%
		HOMO	44%	40%	1%	8%	7%
107	*meso*	LUMO	1%	9%	67%	11%	11%
		HOMO	43%	43%	1%	6%	7%
	rac	LUMO	1%	4%	67%	14%	14%
		HOMO	43%	42%	1%	7%	7%
108	*meso*	LUMO	2%	8%	56%	17%	18%
		HOMO	42%	45%	1%	5%	8%
	rac	LUMO	1%	4%	71%	12%	11%
		HOMO	43%	44%	1%	6%	6%

[a]Phenyl moieties of the cyclometallating ligands [b]Imidazolyl moieties of the cyclometallating ligands

The FMO distributions for **106–108** notably contrast with those predicted for the Chapter 3 ppy-based complexes **64**, **66**, **68** and **70** (which also contain the bridge **72c**). The HOMOs are localised on the Ir centres and the central hydrazide fragments of the bridging ligands in a similar manner. However, the LUMOs are primarily localised on the bridge pentafluorophenyl groups for **106–108**. Presumably, this is due to the electron rich nature of the imidazole heterocycles, which forces the LUMO onto the strongly electron accepting pentafluorophenyl groups. This is also manifested experimentally in the estimated reduction potentials of **106–108** (below), which are notably more negative than those of the ppy-complexes **64**, **66**, **68** or **70**. As a result, the cyclometallating ligands of **106–108** are not major FMO contributors (HOMO and LUMO contributions from the cyclometallating ligands are ≤ 20%).

To determine the significance of the unusual FMO distributions of **106–108**, a TD-DFT study was carried out to gain insight into the nature of their lowest energy excited states. Although the LUMOs have significant pentafluorophenyl character, they may not be directly involved in the lowest energy triplet states. This is evident from the TD-DFT data obtained for **35** and **36** in Chapter 2, for which the T_1 states are predicted to primarily involve HOMO → LUMO+4 transitions rather than HOMO → LUMO.

The TD-DFT data for **105** are included in the Appendix (Table A5).[†] The data for both diastereomers of the least (**106**) and most (**108**) fluorinated **72c**-bridged derivatives **106** and **108** are presented in Table 4.4 (the data for **107** show the same trends and are included in the Appendix, Table A5). The two largest contributing transitions to each state (≥ *ca*. 20%) are included.

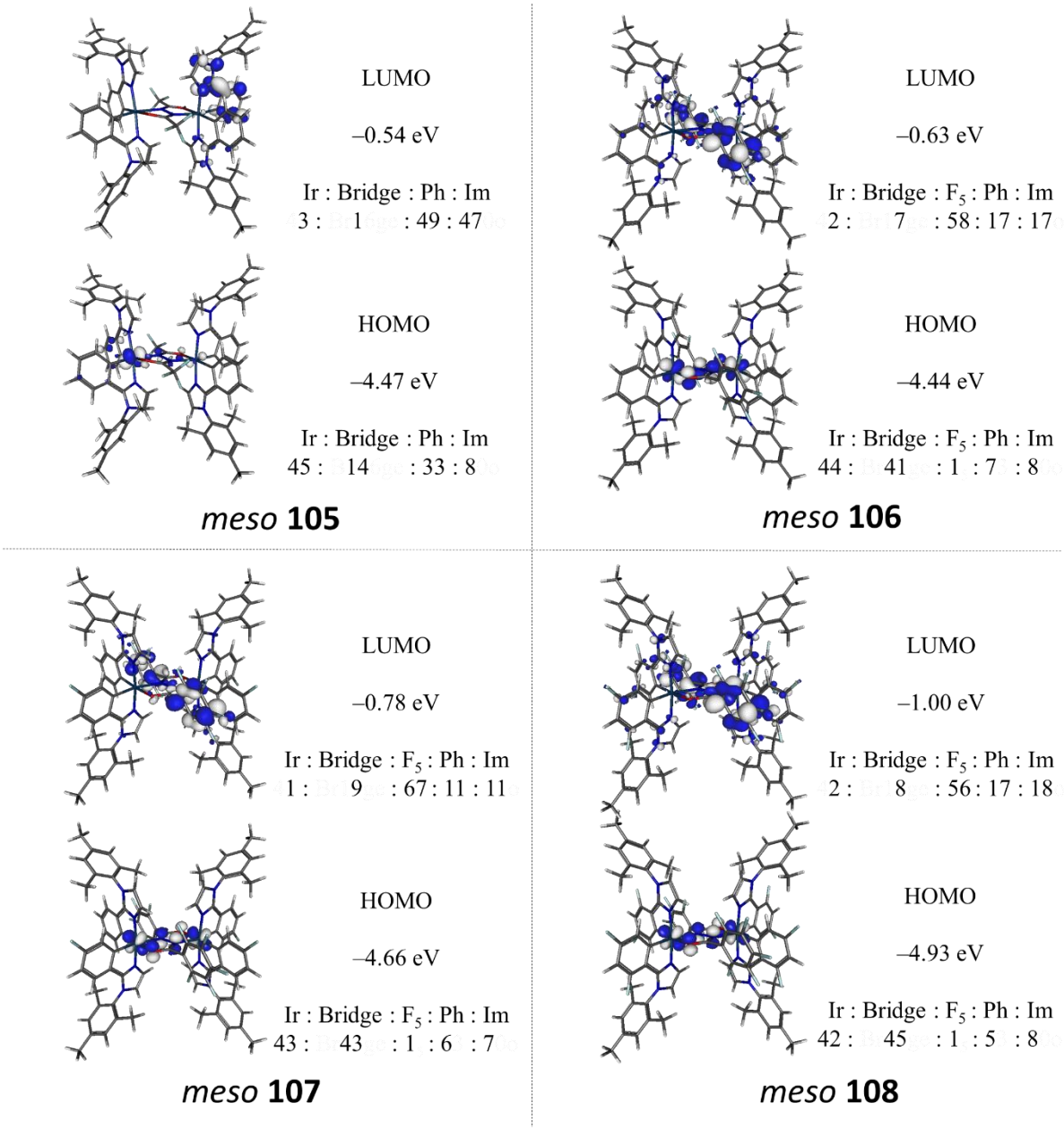

Figure 4.10: Molecular orbital compositions for *meso* **105**–**108**. The orbital contributions are percentages and the HOMO and LUMO energies were calculated at B3LYP/LANL2DZ:3–21G*. Bridge = central bridge OCNNCO fragment; F_n = fluorinated bridge aryl rings; Ph = cyclometallating ligand phenyl groups; Im = cyclometallating ligand imidazolyl groups.

[†] These data are relatively complex with contributions to the T_1 states from many transitions. In summary the hole is primarily localised on the Ir centres, the bridge and the cyclometallating ligands, while the electron is localised on the cyclometallating ligands, i.e. similar with what would be expected from a HOMO → LUMO transition.

Table 4.4: Summary of the TD-DFT data for **106** and **108**.

Transition	106				108			
	meso		*rac*		*meso*		*rac*	
	Main orbital contribution	**λ/ nm**	**Main orbital contribution**	**λ/ nm**	**Main orbital contribution**	**λ/ nm**	**Main orbital contribution**	**λ/ nm**
$S_0 \rightarrow T_1$	HOMO → LUMO	429	HOMO-1 → LUMO+3, HOMO → LUMO+1	426	HOMO → LUMO	420	HOMO-1 → LUMO+3	409
$S_0 \rightarrow T_2$	HOMO-2 → LUMO+3, HOMO → LUMO+1	425	HOMO-1 → LUMO+1, HOMO → LUMO+3	425	HOMO → LUMO+1	410	HOMO-1 → LUMO+2, HOMO → LUMO+3	409
$S_0 \rightarrow T_3$	HOMO → LUMO+3, HOMO-2 → LUMO+2	423	HOMO-1 → LUMO+4, HOMO-2 → LUMO+1	417	HOMO → LUMO+3, HOMO-2 → LUMO+1	408	HOMO-1 → LUMO+4, HOMO-2 → LUMO+5	403
$S_0 \rightarrow T_4$	HOMO-1 → LUMO+2	416	HOMO-2 → LUMO+4	417	HOMO-1 → LUMO+4, HOMO-2 → LUMO+2	402	HOMO-2 → LUMO+4	403
$S_0 \rightarrow T_5$	HOMO-1 → LUMO+4	415	HOMO → LUMO+17	413	HOMO-1 → LUMO+2, HOMO-2 → LUMO+4	401	HOMO → LUMO+8	402

Both diastereomers of the complexes **106–108** feature 5 triplet states that are relatively close in energy (≤ 20 nm). A number of these states may, therefore, be relevant when considering the emissive states of **106–108**.[6] Such a large number of near-degenerate states, many of which have significant contributions from multiple transitions, complicates detailed analysis of the data. However, it can be noted that as well as a HOMO → LUMO transition, many of the relevant transitions in Table 4.4 involve contributions from higher energy unoccupied (LUMO+1 – LUMO+3), and the lower energy occupied (HOMO−1 and HOMO−2) orbitals. Contributions for the HOMO−5 – LUMO+5 orbitals are tabulated in the Appendix (Tables A3 and A4). Particularly, while the LUMO+2 and LUMO+3 orbitals of **106–108** generally include some pentafluorophenyl character, their cyclometallating ligand character is much higher than for the LUMOs (≥ 50%, as high as 100%). The HOMO−1 and HOMO−2 orbitals for all complexes are almost exclusively based on the Ir atoms and cyclometallating ligands (*ca.* 50:50 in all cases). Therefore, while it is likely that the pentafluorophenyl substituents are somewhat involved in the excited states of **106–108**, TD-DFT predicts that the cyclometallating ligands are more involved in their emitting states than is implied

by a simple FMO analysis.[4,12] This analysis is in agreement with the photophysical data below, such as the observation that the profiles of the PL spectra for **106**–**108** are very similar to those of homoleptic 2-phenylimidazole complexes.

Electrochemical study

The oxidation and reduction processes for **105**–**108** were studied by CV. The data are listed in Table 4.5. The oxidation voltammograms are presented in Figure 4.11 and the reduction voltammograms are included in the Appendix (Figure A25). Due to electronic coupling between the Ir centres, all complexes display two oxidation waves (analogous to the data presented in Chapters 2 and 3). Both oxidations are electrochemically reversible for all complexes. All reduction processes are electrochemical irreversible.

Table 4.5: Electrochemical data for complexes **105**–**108** referenced to $E_{1/2}$ FcH/ FcH^+ = 0.00 V.

Complex	$E^{ox(1)}$ /V E_{pa}/ E_{pc} [$E_{1/2}$]	$E^{ox(2)}$ /V E_{pa} /E_{pc} [$E_{1/2}$]	$\Delta E_{1/2}$ /V[a]	E^{red}_{onset} /V[b]	HOMO /eV[c]	LUMO /eV[d]
105	0.38/ 0.29 [0.34]	0.65/ 0.55 [0.60]	0.26	–2.82	–5.14	–1.98
106	0.33/ 0.24 [0.30]	0.73/ 0.62 [0.67]	0.37	–2.95	–5.10	–1.85
107	0.55/ 0.43 [0.49]	0.95/ 0.84 [0.89]	0.40	–2.89	–5.29	–1.91
108	0.72/ 0.63 [0.68]	1.18/ 1.05 [1.12]	0.44	–2.76	–5.48	–2.04

[a] Peak splitting between $E^{ox(1)}$ and $E^{ox(2)}$. [b] All reductions are electrochemically irreversible. [c] HOMO levels calculated from CV potentials by HOMO = –4.8 + ($-E_{1/2}^{ox(1)}$), using ferrocene as the standard. [d] LUMO levels calculated from CV potentials by LUMO = –4.8 + ($-E^{red}_{onset}$), using ferrocene as the standard.

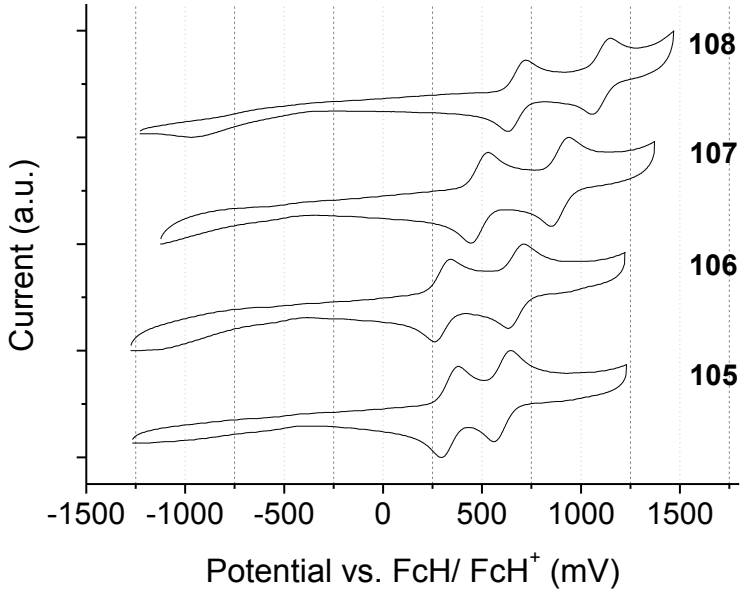

Figure 4.11: Cyclic voltammograms in 0.1 M *n*-Bu_4NPF_6/ DCM showing the oxidation processes for complexes **105**–**108**.

The first oxidation potential of **105** is more positive than for **106** (by 0.04 V). This is analogous to the relationship between complexes **66** and **67** in Chapter 3, and reinforces the conclusion that the bridge **73** is more strongly electron withdrawing than **72c**. Sequential fluorination of the cyclometallating ligands in the series **106**–**108** leads to successive increases in their oxidation potentials as expected. Complexes **105**–**108** display higher HOMOs than their Chapter 3 ppy-analogues (**66**–**70**), which is attributed to the more electron rich nature of imidazole in comparison to pyridine.

The bis(trifluoromethyl) (**73**)-bridged complex **105** displays a greater peak splitting than its ppy-analogue **67** ($\Delta E_{1/2}$ of 0.26 V vs. 0.16 V). This is attributed to the substantial bridge contribution to the HOMO of **105** (predicted by DFT), in contrast to the ancillary bridge of **67**. The DFT data above also predict increasing bridge HOMO contributions upon successive fluorination in the series **106**–**108**. This is manifested in an incremental increase of their $\Delta E_{1/2}$ values.

In a similar manner to the complexes studied in Chapter 3, the irreversible nature of the reductions for **105**–**108** adds error to their determination. However, there are some clear qualitative trends in the data. The reduction onsets for **105**–**108** are significantly more negative (by > 0.5 V) than for their sky-blue ppy analogues (**68**–**70**). They are also comparable to the values reported for heteroleptic mononuclear complexes functionalised with 2-arylimidazole ligands.[3] The reduction potential for **105** is less negative than for **106**, i.e. **105** is easier to reduce, in-line with the more highly electron withdrawing nature of the bridge **73** and the higher first oxidation potential of **105**. Sequential fluorination in the series **106**–**108** leads to consecutively less negative reduction potentials as the complexes become more electron poor.

Photophysical properties

The photophysical data for complexes **105**–**108** are listed in Table 4.6. The absorption spectra for **105**–**108** shown in Figure 4.12 display features typical of cyclometallated iridium complexes. There are intense bands below *ca.* 300 nm which correspond to population of LC states, while the weaker bands extending out to *ca.* 450 nm are assigned to ^{1}MLCT and ^{3}MLCT transitions.[19,20] The extinction coefficients are broadly higher than for similar mononuclear 2-phenylimidazole complexes.[3] However, they are lower than for the mesityl-functionalised ppy-complexes **66**–**69** (Chapter 3). This is more prominent for the LC bands, and so could be related to the presence of the imidazole groups in **105**–**108**.

Table 4.6: Summary of the key photophysical data for complexes **105–108**.

	DCM solution	2-MeTHF glass[a]		Doped into PMMA 1% wt.[b]				
Ir	**λ_{abs} /nm (ε × 10^3 / $M^{-1}cm^{-1}$)**	**$\lambda_{max\ em}$ /nm ($\lambda_{10\%\ em}$ /nm)[c] [E_T /eV][d]**	**τ /µs**	**$\lambda_{max\ em}$ /nm [CIE_{xy}]**	**PLQY /% (± 10%)**	**τ /µs**	**k_r /× 10^5 s^{-1}**	**k_{nr} /× 10^5 s^{-1}**
105	258 (59), 288sh (34), 323 (21), 349 (16), 372 (9), 402 (5), 457 (0.3)	466 (458) [2.71]	3.88	469sh, 500 [0.20, 0.40]	11	1.82	0.60	4.89
106	260 (55), 287sh (34), 327 (16), 355 (12), 378sh (7.6), 459 (0.4)	469 (459) [2.70]	4.02	470sh, 501 [0.20, 0.39]	55	2.80	1.96	1.61
107	260 (51), 284sh (36), 315sh (20), 340 (14), 365sh (7.6), 384 (4.6), 442 (0.1)	456 (442) [2.81]	5.35	456sh, 486 [0.18, 0.31]	47	4.15	1.13	1.28
108	261 (52), 283sh (33), 315 (17), 338 (12), 360sh (6.9), 379sh (3.4), 443 (0.2)	449sh, 480 (440) [2.82]	5.21	452sh, 480 [0.18, 0.27]	52	4.55	1.14	1.05

sh = Shoulder. [a]Measured at 77 K using an excitation wavelength of 355 nm. [b]Measured in an integrating sphere under air using an excitation wavelength of 355 nm. [c]Wavelength at 10% intensity on the blue edge of the spectrum obtained at 77 K. [d]Estimated using $E_T = hc/\lambda_{10\%\ em}$. $\tau = 1/k_{nr} + k_r$.

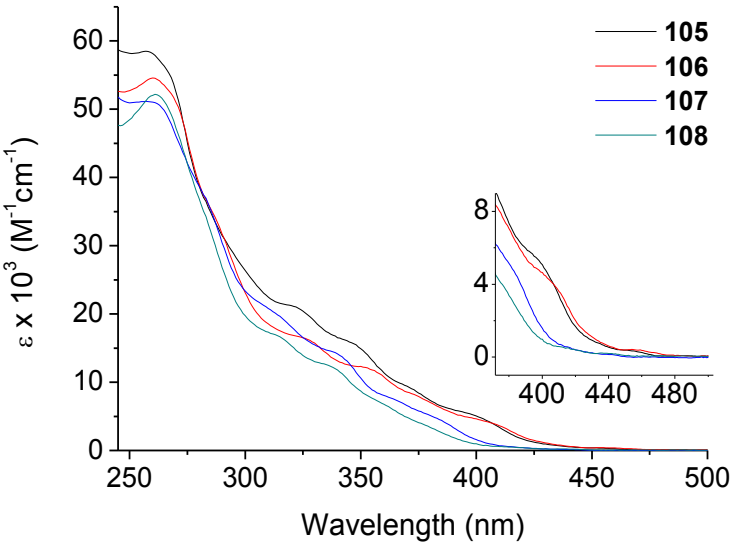

Figure 4.12: Absorption spectra for complexes **105–108** recorded in aerated DCM at room temperature. (Inset) expansions of the *ca.* 400–500 nm region.

The emission spectra for **105–108** doped into PMMA at room temperature, and in 2-MeTHF at 77 K are shown in Figure 4.13. All the complexes **105–108** are non-emissive in DCM solution at room temperature with PLQYs ≤ 0.05%. This is evidently due to facile non-radiative deactivation of their excited states, and occurs despite the intramolecular π–π interactions observed in the ^{19}F NMR spectra for **106–108**. This absence of emission in solution is presumably related in some way to the dinuclear nature of the complexes and the presence of bridging ligands, as the homoleptic mononuclear complex of ligand **109** (complex **102**, Figure 4.5) is highly emissive in solution.[9,10]

There are also examples of heteroleptic monoiridium complexes functionalised with bulky 1,2-diarylimidazole ligands that are highly emissive in solution.[3]

In contrast, all the complexes are emissive at room temperature when doped into PMMA. The observation that the complexes are emissive in PMMA but not in solution is ascribed to quenching through motion of the bridging units (as for **37** and **38** in Chapter 2).[21] This could be anticipated for **105** which does not feature rigidifying π–π interactions, but is more surprising for **106–108**. Complexes **106–108** all feature E_T values greater than 2.7 eV (estimated from the 77 K emission spectra in Figure 4.13). In Chapter 3, it was observed that the solution PLQYs of complexes **66**, **68** and **70** (bridged by **72c**) are inversely proportional to their emission energies (and E_T), despite their similar PLQYs in PMMA. This may be because higher energy excited states are more likely to transfer sufficient energy to vibrational modes to overcome rigidification by the intramolecular π–π interactions, promoting non-radiative decay in solution. A similar explanation could explain the lack of emission in solution for **106–108**, which have comparatively high E_T values.

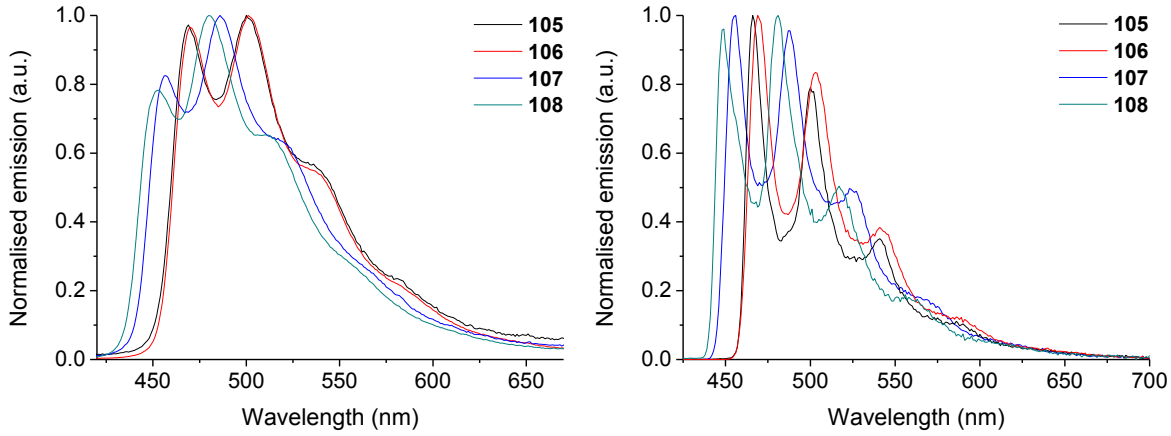

Figure 4.13: Emission spectra for complexes **105–108**. (Left) spectra of complexes doped into PMMA at 1 wt.% at room temperature. (Right) spectra of complexes in 2-MeTHF glasses at 77 K (λ_{exc} 355 nm).

The complexes **105–108** emit in the blue-green region. The emission from **105** is marginally bluer than for **106**, in agreement with electrochemical data (above) which predicts **105** to have a lower HOMO. Incremental fluorination in the series **106–108** successively blue shifts their emission maxima, as expected. For all complexes the emission is relatively broad (FWHM *ca.* 100 nm) and the $v_{0,1}$ peak is dominant, increasing in intensity in relation to the $v_{0,0}$ band with an increase in emission energy. Consequently, even though the $v_{0,0}$ band for **108** is blue shifted in PMMA compared to that of complex **70** (452 vs. 460 nm for **70**), the CIE_{xy} coordinates of **108** are less blue: CIE_{xy} **108** = (0.18, 0.27), **70** = (0.15, 0,24), FIrpic = (0.15, 0.33) (Figure 1.12). This is a property typical

of phosphors featuring 1,2-diarylimidazole ligands,[4,12] and it is interesting to note that it is not significantly altered through the incorporation of rigidifying intramolecular π–π interactions.

The emission spectra recorded at 77 K in 2-MeTHF for **105**–**108** are broader than for ppy-based analogues (Chapter 3). There are distinct vibronic features, and minimal rigidochromic shifts on cooling (≤ 3 nm) compared to the room temperature emission spectra recorded in PMMA. This implies strong LC contributions to the excited states of **105**–**108**.[22] The Huang-Rhys factors are also large: **105** = 0.8, **106** = 0.8, **107** = 1.0 and **108** > 1.0 (1 s.f.). These are notably larger than for the complexes **62**–**70** studied in Chapter 3 (0.4–0.6), implying that the excited states of **105**–**108** are highly distorted compared to their ground states. This may be related to the non-emissive properties of **106**–**108** in solution. It can be noted that complexes **63**–**68** (Chapter 3), which are highly emissive in solution, have S_M values of ≤ 0.5. In contrast, complexes **105**–**108** and complexes **37** and **38** (Chapter 2) which are all non-emissive in solution, have S_M values ≥ 0.7 (1 s.f.). Complexes **69** and **70** (Chapter 3) which are weakly emissive in solution, have intermediary S_M values of 0.5–0.6. This implies that there is an inverse relationship between the Huang-Rhys factor and the solution PLQY for hydrazide-bridged diiridium complexes.

The PLQY of **105** in PMMA is notably lower than for **106**–**108** (11 ± 10% vs. *ca.* 50 ± 10%). This is ascribed to an absence of rigidifying intramolecular π–π interactions as the k_{nr} value is larger for **105** (4.89 vs. 1.61 × 10^5 s^{-1} for **106**). The phosphorescence lifetimes of **106**–**108** are notably longer than for their ppy-analogues in Chapter 3, which have similar or greater PLQYs. For example, while **108** has a very similar E_T to complex **70** (2.82 vs. 2.81 eV), its τ is over twice as long (4.55 vs. 1.62 μs). This is related to the substantially lower k_{r} of **108** (1.14 × 10^5 s^{-1} vs. 4.26 × 10^5 s^{-1} for **70**), which is a consequence of a lower MLCT contribution to the excited state of **108**. This is likely due to high LC character, which is evident from well-resolved vibronic features in the PMMA emission spectrum of **108**: the $v_{0,0}$, $v_{0,1}$ and $v_{0,2}$ bands are all well-resolved for **108** (Figure 4.13), whereas for **70** the $v_{0,2}$ band is less well-defined in the PMMA emission spectrum, appearing as a shoulder (Chapter 3, Figure 3.18). Such LC character is not necessarily restricted to the cyclometallating ligands, as DFT/TD-DFT data suggest that the excited state may be significantly bridge-centred. The τ values in the series **106**–**108** also increase as the emission is shifted further towards the blue. This can be ascribed to a typical increase in the LC character of the excited state upon blue shifting the emission (see Chapter 1).[23–25]

During the synthesis and purification of complexes **105**–**108** it was noted that they are emissive under UV irradiation (365 nm) in the solid state as powders. Consequently, the complexes display typical aggregation-induced phosphorescent emission (AIPE) behaviour.[26,27] This can be observed

by titrating water into THF solutions of the complexes to induce precipitation/ aggregation, which promotes emission. The emission intensity increases as the THF fraction decreases. Spectra for complexes **106** and **108** are shown in Figure 4.14 as representative examples (the spectra for **105** and **107** also display AIPE and are included in the Appendix, Figure A26). This property contrasts with what is observed for complexes **37** and **38** (Chapter 2), for which neat films are non-emissive, and is ascribed to the presence of the bulky (and ancillary) mesityl groups. In the solid state they increase the distances between the emissive 'cores' of the complexes, suppressing triplet-triplet annihilation as a quenching pathway (which otherwise would dominate, as for the unshielded complexes **37** and **38**).[28,29] The mechanism which results in solid state emission from **105**–**108** is principally no different from that which promotes emission in PMMA films. The minor difference is that intramolecular motion is restricted due to intermolecular interactions between neighbouring complexes, rather than between the complexes and a PMMA host.

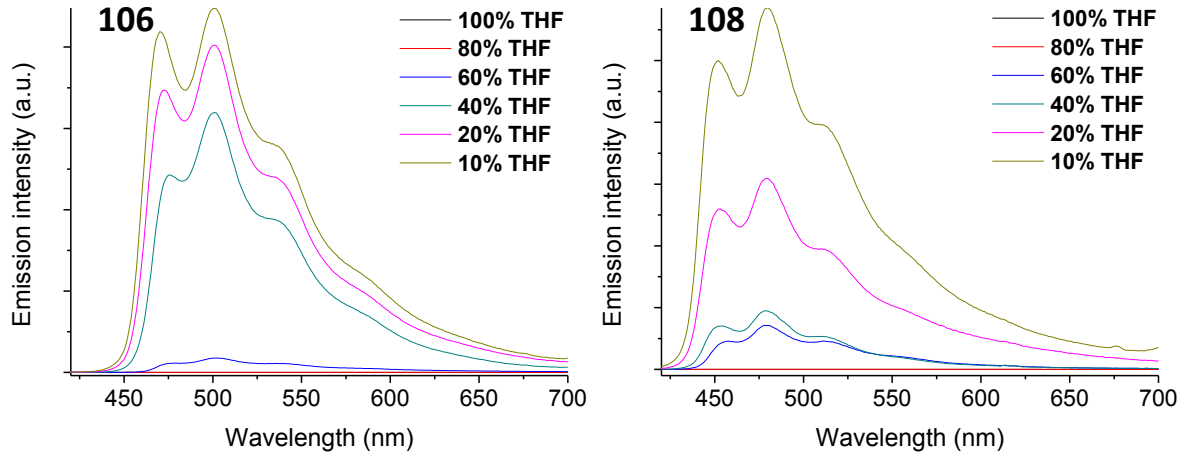

Figure 4.14: Emission spectra for THF solutions of complexes **106** and **108** upon incremental titration of water to induce precipitation (λ_{exc} 355 nm). THF fraction is percentage volume.

Conclusions and future work

In this Chapter, diarylhydrazide-bridged diiridium complexes have been further developed through the incorporation of bulky 1,2-diarylimidazole cyclometallating ligands. Complex **108** displays CIE_{xy} coordinates deeper into the blue than FIrpic: CIE_{xy} **108** = (0.18, 0.27), FIrpic = (0.15, 0.33). To the best of our knowledge, **105**–**108** are also the first diiridium complexes that show strong AIPE behaviour in the blue-green region. Previous examples are predominantly in the orange and red regions as a consequence of their highly conjugated bridging units.[30–32] The data presented in this Chapter are, therefore, complementary to those presented for the ppy-based complexes in Chapter 3, while increasing the structural diversity of sky-blue diiridium complexes and substantially broadening the colour range of dinuclear iridium AIPE emitters.

However, there are some differences (which are potentially disadvantageous) in the photophysical properties of **105**–**108** compared to the ppy complexes studied in Chapter 3. Intramolecular π–π interactions between the bridging (**72c**) and cyclometallating (**109**–**111**) ligands (which can be seen by both XRD and solution NMR) are insufficient to promote emission in solution for **106**–**108**. In PMMA **105**–**108** also exhibit poor colour purity. This is related to their PL spectral profiles, which are very broad with strong vibronic features. They also feature rather long phosphorescence lifetimes (> 4 μs for **107** and **108**). The PL data collected at room temperature and 77 K suggest that these properties are related to large LC contributions to the excited states of **105**–**108**. Electrochemical studies have helped to rationalise the structure-property relationships of the complexes. Although the data is complex, a combined DFT/ TD-DFT study supports strong LC contributions to the excited states of **105**–**108.** It also indicates that the bridge pentafluorophenyl groups are somewhat involved, in contrast to the complexes presented in Chapter 3 for which they are ancillary.

A practical limitation of complexes **105**–**108** is their poor colour purity. Rigidifying phenylimidazole chelates by incorporating a fused ligand structure has been successful for improving the colour purity of monoiridium complexes.[11] A similar strategy could be applied to diiridium complexes such as **112** (Figure 4.15) in future work.

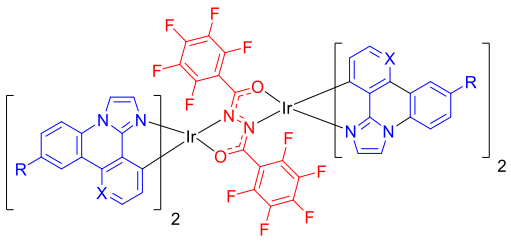

112 X = CH or N
R = solubilising group

Figure 4.14: Proposed structures for future diiridium complexes.

References

1 Y. Im, S. Y. Byun, J. H. Kim, D. R. Lee, C. S. Oh, K. S. Yook and J. Y. Lee, *Adv. Funct. Mater.*, 2017, **27**, 1603007–1603031.

2 W. Song and J. Y. Lee, *Adv. Opt. Mater.*, 2017, **5**, 1600901–1600913.

3 E. Baranoff, S. Fantacci, F. De Angelis, X. Zhang, R. Scopelliti, M. Grätzel and M. K. Nazeeruddin, *Inorg. Chem.*, 2011, **50**, 451–462.

4 T. Karatsu, M. Takahashi, S. Yagai and A. Kitamura, *Inorg. Chem.*, 2013, **52**, 12338–12350.

5 S. Takizawa, J. Nishida, T. Tsuzuki, S. Tokito and Y. Yamashita, *Inorg. Chem.*, 2007, **46**, 4308–4319.

6 H. J. Bolink, F. De Angelis, E. Baranoff, C. Klein, S. Fantacci, E. Coronado, M. Sessolo, K. Kalyanasundaram, M. Grätzel and M. K. Nazeeruddin, *Chem. Commun.*, 2009, 4672–4674.

7 T. Fleetham, G. Li and J. Li, *Adv. Mater.*, 2017, **29**, 1601861–1601877.

8 J. Lee, H.-F. Chen, T. Batagoda, C. Coburn, P. I. Djurovich, M. E. Thompson and S. R. Forrest, *Nat. Mater.*, 2016, **15**, 92–98.

9 K. Udagawa, H. Sasabe, C. Cai and J. Kido, *Adv. Mater.*, 2014, **26**, 5062–5066.

10 K. Udagawa, H. Sasabe, F. Igarashi and J. Kido, *Adv. Opt. Mater.*, 2016, **4**, 86–90.

11 Y. Zhang, J. Lee and S. R. Forrest, *Nat. Commun.*, 2014, **5**, 1–7.

12 H. Cho, J. Lee, J. I. Lee, N. S. Cho, J. H. Park, J. Y. Lee and Y. Kang, *Org. Electron.*, 2016, **34**, 91–96.

13 S. J. Lee, K. Park, K. Yang and Y. Kang, *Inorg. Chem.*, 2009, **48**, 1030–1037.

14 Y. Feng, X. Zhuang, D. Zhu, Y. Liu, Y. Wang and M. R. Bryce, *J. Mater. Chem. C*, 2016, **4**, 10246–10252.

15 S. Lo, C. P. Shipley, R. N. Bera, R. E. Harding, A. R. Cowley, P. L. Burn and I. D. W. Samuel, *Chem Mater.*, 2006, **18**, 5119–5129.

16 M. Micksch, M. Tenne and T. Strassner, *European J. Org. Chem.*, 2013, 6137–6145.

17 C. Ulbricht, B. Beyer, C. Friebe, A. Winter and U. S. Schubert, *Adv. Mater.*, 2009, **21**, 4418–4441.

18 Y. Zheng, A. S. Batsanov, M. A. Fox, H. A. Al-Attar, K. Abdullah, V. Jankus, M. R. Bryce and A. P. Monkman, *Angew. Chem. Int. Ed.*, 2014, **53**, 11616–11619.

19 A. B. Tamayo, B. D. Alleyne, P. I. Djurovich, S. Lamansky, I. Tsyba, N. N. Ho, R. Bau and M. E. Thompson, *J. Am. Chem. Soc.*, 2003, **125**, 7377–7387.

20 S. Lamansky, P. Djurovich, D. Murphy, F. Abdel-Razzaq, H. E. Lee, C. Adachi, P. E. Burrows, S. R. Forrest and M. E. Thompson, *J. Am. Chem. Soc.*, 2001, **123**, 4304–4312.

21 D. G. Congrave, Y. Hsu, A. S. Batsanov, A. Beeby and M. R. Bryce, *Organometallics*, 2017, **36**, 981–993.

22 E. S. Andreiadis, D. Imbert, J. Pécaut, A. Calborean, I. Ciofini, C. Adamo, R. Demadrille and M. Mazzanti, *Inorg. Chem.*, 2011, **50**, 8197–8206.

23 M. A. Baldo, S. R. Forrest and M. E. Thompson, in *Organic Electroluminescence*, ed. Z. H. Kafafi, CRC and SPIE Press, 2005.

24 L. Yang, F. Okuda, K. Kobayashi, K. Nozaki, Y. Tanabe, Y. Ishii and M.-A. Haga, *Inorg. Chem.*, 2008, **47**, 7154–7165.

25 J. Li, P. I. Djurovich, B. D. Alleyne, M. Yousufuddin, N. N. Ho, J. C. Thomas, J. C. Peters, R. Bau and M. E. Thompson, *Inorg. Chem.*, 2005, **44**, 1713–1727.

26 S. Reineke, K. Walzer and K. Leo, *Phys. Rev. B - Condens. Matter Mater. Phys.*, 2007, **75**, 125328.

27 N. C. Giebink and S. R. Forrest, *Phys. Rev. B - Condens. Matter Mater. Phys.*, 2008, **77**, 235215.

Chapter 5: Intramolecular π–π stacking in monoiridium complexes featuring a chiral oxazoline ancillary ligand

Introduction

In Chapter 3 it was shown that ancillary perfluoroaryl groups can significantly alter the photophysical properties of cyclometallated diiridium complexes through promoting intramolecular π–π stacking. This Chapter describes the synthesis and characterisation of diastereomeric monoiridium complexes which incorporate a chiral 2-phenoxyoxazoline ligand as the 3rd 'ancillary' ligand.* This ligand has a pendant pentafluorophenyl group to promote intramolecular π–π interactions. The π–π interactions lead to diastereoselectivity, facile separation of diastereomers, and also influence the photophysical properties of the complexes.

Phenoxyoxazole ligands in Ir(III) complexes

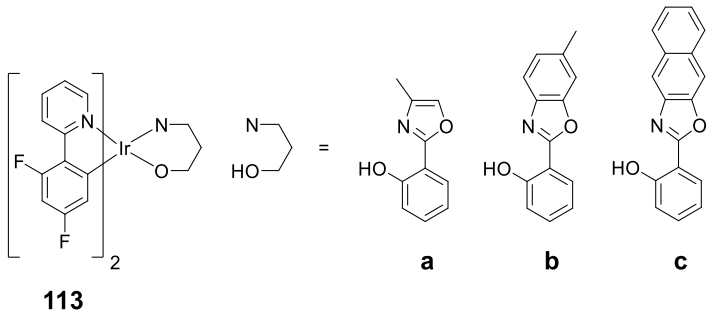

113

Figure 5.1: Molecular structures of complexes **113a–c**.

Kim, Park and co-workers reported a series of heteroleptic complexes of dfppy cyclometallating ligands (**113a–c**, Figure 5.1).[1] Monoanionic 2-phenoxyoazole-derived ancillary ligands were incorporated, which coordinate the Ir centre through a 6-membered O^N chelate, in contrast to the 5-membered chelates of cyclometallating ligands such as ppy. The triplet energy of the ancillary ligand was incrementally decreased in the order **113a–c** with oxazole, benzoxazole and naphthoxazole moieties, respectively; emission was tuned from green (λ_{max} PL = 500 nm) to yellow (550 nm). The complexes **113a–c** all have similar PLQYs in toluene (36–43%). However, the phosphorescence lifetimes increase across the series: **113a** = 1.65 μs, **b** = 7.25 μs, **c** = 9.88 μs which can be ascribed to a decrease in the MLCT character of the excited states across the series. Lowering

* In this Chapter the term 'ancillary ligand' is often used as a matter of convention to denote the 3rd (non-cyclometallating) ligand. In a literal sense a ligand is only ancillary if it features no FMO character and is, therefore, not directly involved in the excited state.

the triplet energy of the ancillary ligand increases its effectiveness as an excited state trap. This increases the ancillary ligand-based ^{3}LC character of the excited state, leading to longer τ.

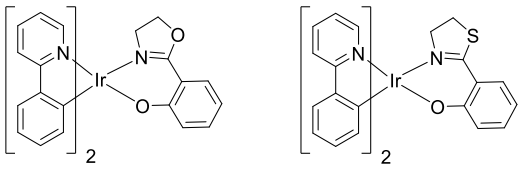

114 **115**

Figure 5.2: Molecular structures of complexes **114** and **115**.

Our group has also investigated similar complexes with 2-phenoxyoxazoline (**114**) and 2-phenoxythiazoline (**115**) ancillary ligands (Figure 5.2).[2] In DCM solution, complex **114** is a green emitter (λ_{max} PL = 527 nm) with a PLQY of 55%. In comparison, **115** displays a broader emission profile which is red shifted into the yellow (λ_{max} PL = 558 nm) and its PLQY is lower (27%). These observations were ascribed to a greater ILCT and ancillary ligand-centred (LC) character for the excited state of **115**. The complexes were incorporated into vacuum-processed OLEDs. The EL λ_{max} values for the complexes are very similar (530–540 nm). However, the devices display notably different FWHM values (**114** = 70 nm, **115** = 110 nm). This leads to significantly different CIE_{xy} coordinates: **114** displays green EL (0.35, 0.61), whereas **115** displays yellow EL (0.46, 0.50). **114** yielded the best performing device, with a peak EQE of 17.1%. DFT predicts that the HOMOs are primarily localised on the Ir centres and the phenoxy moieties of the ancillary ligands, with minimal contribution from the cyclometallating ligands. The LUMOs are primarily localised on the pyridyl rings of the cyclometallating ligands.

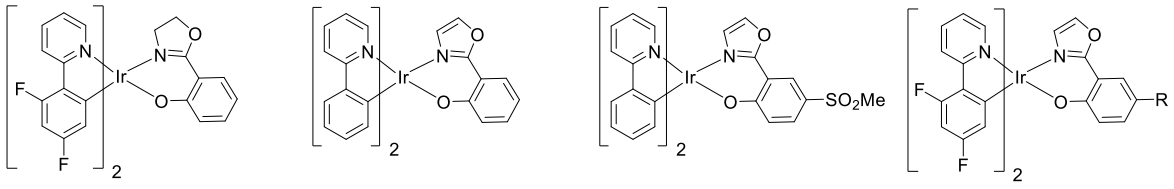

116 **117** **118** **119**, R = SO_2Me; **120**, R = CF_3

Figure 5.3: Molecular structures of complexes **116–120**.

In a follow-up study, a wider series (**116–120**) was investigated to probe the structure-property relationships in complexes featuring 2-phenoxyoxazole/ oxazoline ligands (Figure 5.3).[3] Replacement of the ppy ligands of **114** (Figure 5.2) with dfppy (**116**) blue shifts the PL λ_{max} from 527 to 506 nm. Although only a very small HOMO contribution from the cyclometallating phenyl groups of **114** is predicted by DFT, fluorine atoms positioned *meta* to the Ir–C bond can still be employed

to blue shift emission. This is because they stabilise the Ir t_{2g} orbitals, destabilising the MLCT state. Replacement of the oxazoline moiety of **114** with an oxazole heterocycle (**117**) leads to a small blue shift in emission (of 6 nm) due to HOMO stabilisation (which is observed in the electrochemistry). This implies that the increased conjugation of oxazole makes it a stronger electron withdrawing group. Functionalisation of the position *para* to the phenoxy group with a strongly electron withdrawing sulfone group in complex **118** also lowers the HOMO, resulting in a blue shift: **117** λ_{max} PL = 521 nm, **118** λ_{max} PL = 508 nm. Complexes **119** and **120** display λ_{max} PL of 476 and 479 nm, respectively, indicating that the three above design tactics: 1) dfppy cyclometallating ligands, 2) an oxazole heterocycle, and 3) an electron withdrawing group *para* to the phenoxy group, can be combined to obtain an additive blue shift in emission. The solution PLQYs are in the range of 42–73% (in DCM) and roughly increase with emission energy due to decreasing k_{nr}, in accordance with the bandgap law. The FMO compositions for **116**–**120** are predicted by DFT to be very similar to those of the parent complex **114.**

Monari, Bandini, Ceroni and colleagues investigated a series of heteroleptic monoiridium complexes functionalised with chiral 2-phenoxyoxazoline ancillary ligands (**123**–**126**) (Figure 5.4).[4] The enantiomerically pure oxazoline ligands **121** (S) and **122** (R) were reacted with racemic (ΛΛ/ ΔΔ) bis μ–Cl dimers to obtain the monoiridium complexes as diastereomeric mixtures (Λ_S and Δ_S for **123** and **125**, Λ_R and Δ_R for **124** and **126**) in *ca.* 1:1 ratios which were separated. After resolution, the enantiomeric purity of the diastereomers was confirmed by circular dichroism spectroscopy. However, the majority of the electrochemical and photophysical characterisation was carried out on diastereomeric mixtures. In solution (MeCN) the complexes are emissive (PLQYs of 51–81%) with PL λ_{max} of 497–524 nm. The most heavily fluorinated complex **126** displays the highest energy emission, indicating that fluorine atoms *meta* to the phenoxy group blue shift the emission. This is analogous to what is observed for dfppy-type cyclometallating ligands when fluorine atoms are positioned *meta* to the Ir–C bond.[5] The single crystal structures of Λ_S-**123**, Λ_S-**125** and Δ_R-**126** all feature some intramolecular π–π stacking between the pendant phenyl group of the ancillary ligand and the pyridyl moiety of a cyclometallating ligand, as demonstrated for Λ_S-**123** in Figure 5.4 (3.65 Å). No crystal structures were presented for any of the diastereomers for which the pendant phenyl group is expected to be proximal to a cyclometallated phenyl (i.e. Δ_S-**123,** Λ_R-**124**, Δ_S-**125** or Λ_R-**126**). Therefore, the presence of any intramolecular π–π interactions in those forms was not determined.

In summary, 2-phenoxyoxazoline/ oxazole ancillary ligands are interesting building blocks that have been incorporated into a range of cyclometallated monoiridium complexes. They generally have significant frontier orbital contribution, and the phenoxy ring can be functionalised to tune the emission wavelength in a similar manner to cyclometallating phenyl groups and obtain highly

emissive complexes with excited states of mixed character. As a result, 2-phenoxyoxazole ancillary ligands have been functionalised alongside the cyclometallating ligands to tune the emission wavelength in the range of *ca.* 550–475 nm.

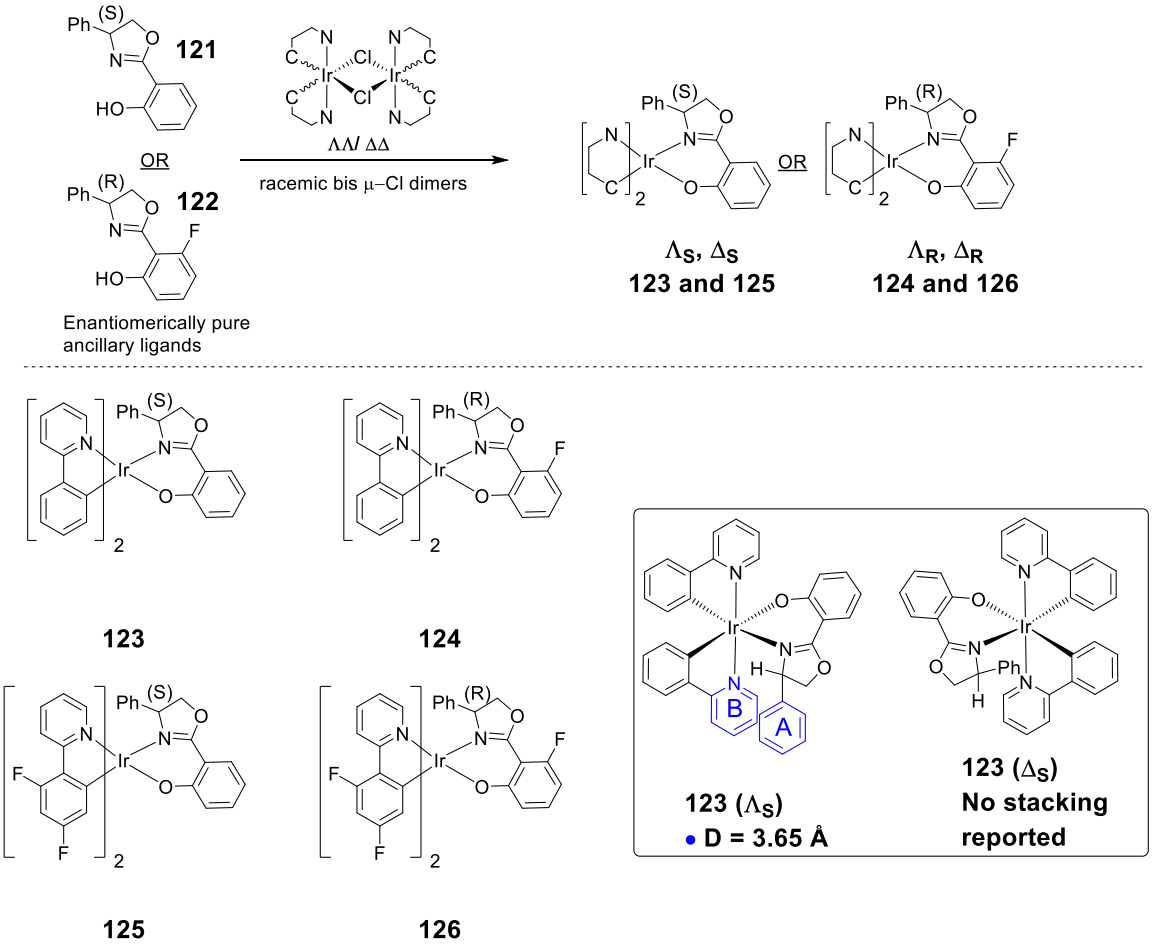

Figure 5.4: Molecular structures of complexes **121**–**124**. Intramolecular π–π interactions are highlighted with coloured rings. D = distance between the centroid of the pendant phenyl ring (A) and the plane of the pyridine ring (B) from single crystal XRD measurements.

However, there is further significance in the trend that the phenoxy ring tends to feature substantial HOMO contribution. Although not a limitation for obtaining highly emissive complexes, this occurs as phenoxy is fundamentally more electron rich than a cyclometallated phenyl ring. Therefore, the HOMO levels of complexes with 2-phenoxyoxazoline/ oxazole ancillary ligands will likely never be as deep as for homoleptic ppy-based cyclometallated complexes, or heteroleptic complexes with true ancillary ligands. This makes it unlikely that deep blue phosphors will be developed on such a platform.

Results and discussion

Design, synthesis and characterisation

The new diastereomeric complexes **132a** and **132b** (Figure 5.5) were designed based on complexes **120** (Figure 5.3) and **123–126** (Figure 5.4) to explore the influence of intramolecular π–π interactions in blue-green monoiridium complexes. The CF_3 functionalisation on the ancillary ligand **131** was selected in combination with dfppy cyclometallating ligands to blue shift the emission (based on **120**). The pendant pentafluorophenyl group on **131** introduces a second chiral centre and should promote intramolecular π–π stacking compared to the phenyl-functionalised analogues **123–126**, based on the data discussed in Chapter 3. Studies on diastereomeric mono- and diiridium complexes have shown that the photophysical properties of the stereoisomers are often similar (literature[6–10] and Chapters 2/ 3). However, for **132a** and **132b** any intramolecular π–π interactions were expected to be different for each diastereomer due to the differing orientation of the pentafluorophenyl rings with respect to the cyclometallating ligands. Therefore, provided that they could be separated, it was anticipated that **132a** and **132b** would be an interesting platform for improving our understanding of how intramolecular π–π interactions involving perfluoroaryl groups can influence the photophysical properties of Ir phosphors.

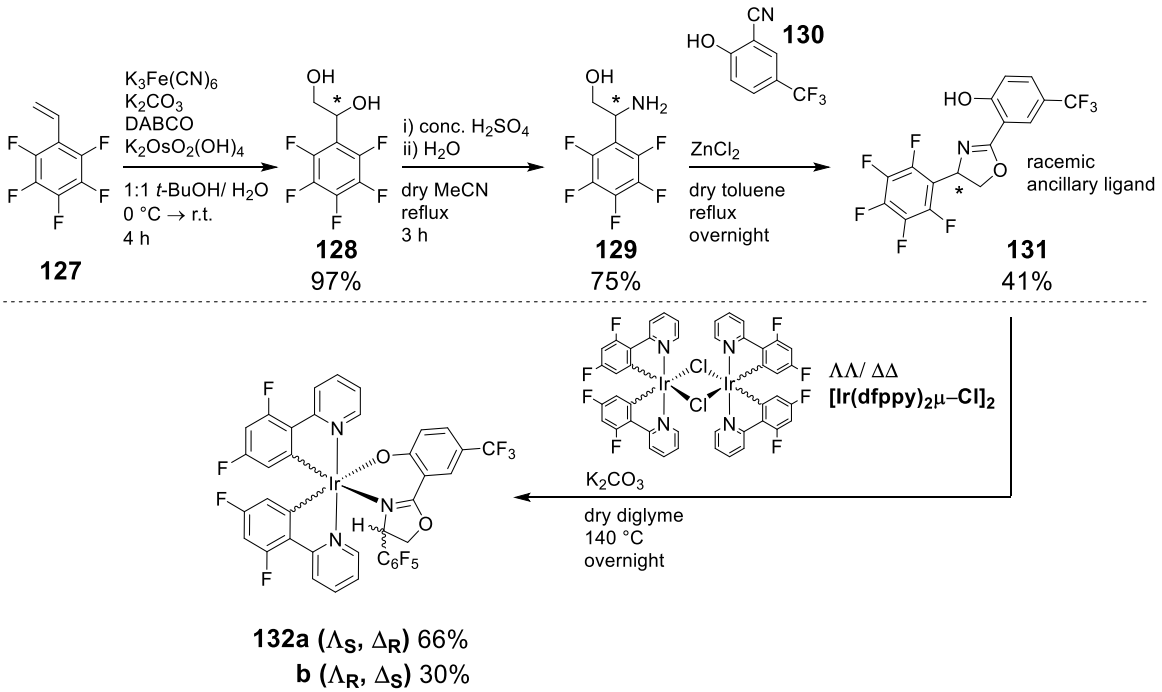

Figure 5.5: Synthetic schemes for the synthesis of the ancillary ligand **131** and complexes **132a** and **132b**.

The ancillary ligand **131** was synthesised starting from pentafluorostyrene (**127**) (Figure 5.5). Dihydroxylation to the racemic vicinal diol **128** was accomplished using catalytic potassium osmate dihydrate with $K_3Fe(CN)_6$ as a stoichiometric oxidant.[11] **128** was then heated in acetonitrile in the

presence of H_2SO_4 to regioselectively convert it into the aminoethanol derivative **129**.[11] A final $ZnCl_2$-catalysed condensation with the commercially available phenol **130** afforded racemic **131** in 41% yield. This yield is very similar to that reported for the ligand **122** (40%) (Figure 5.4), which has a pendant phenyl group.[4] Therefore, this procedure is tolerant of the highly electron-withdrawn aminoethanol derivative **129**.

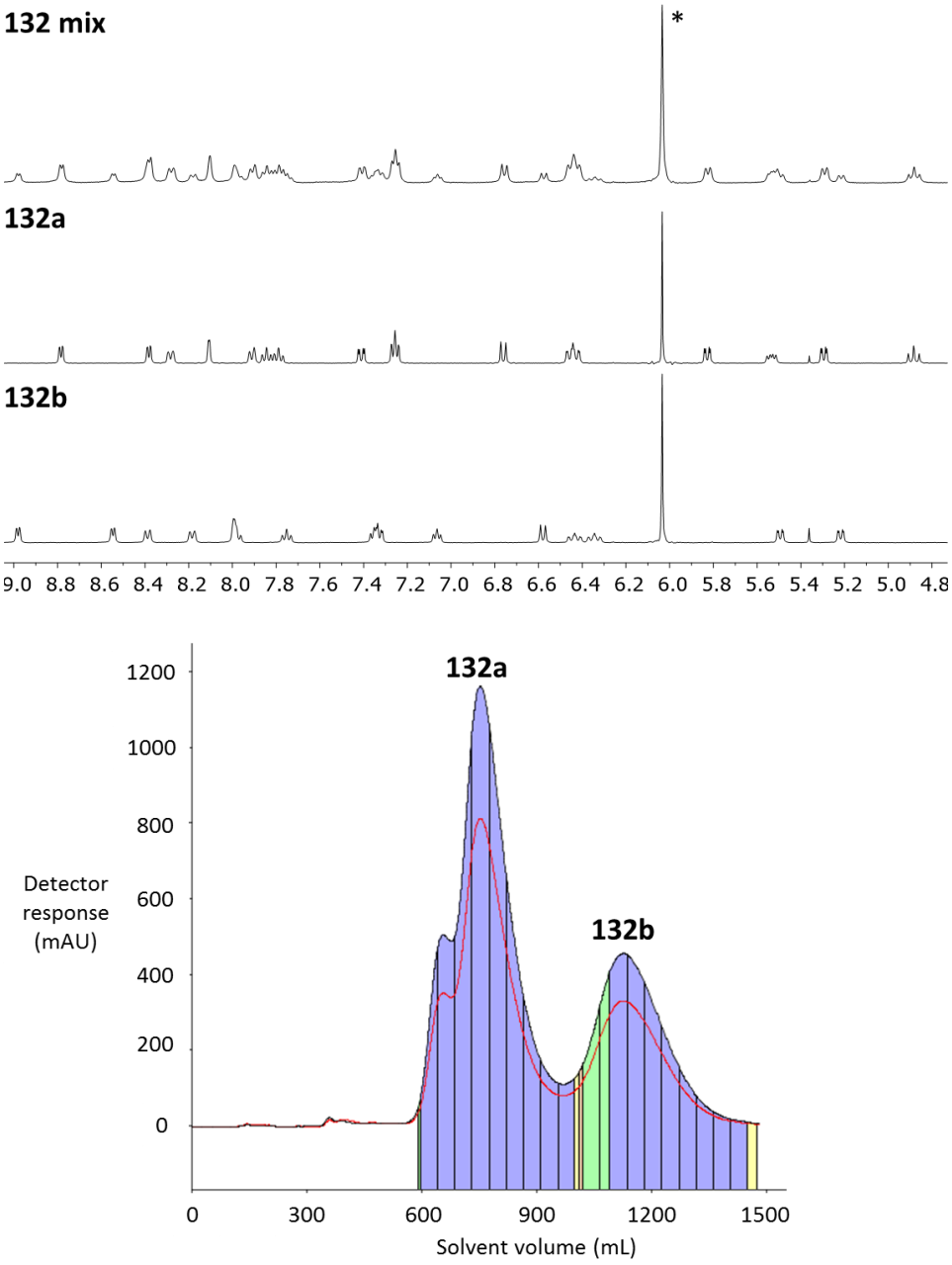

Figure 5.6: (Top) Aromatic regions of the ^{1}H NMR spectra of crude **132** and the resolved diastereomers **132a** and **132b** in D_2-1,1,2,2-tetrachloroethane to highlight the *ca.* 2:1 diastereomeric ratio, * = residual D_1,H_1-1,1,2,2-tetrachloroethane in the NMR solvent, chemical shifts are in ppm. (Bottom) Trace of the UV detector output from a Biotage© Isolera flash chromatography system to highlight the diastereomeric ratio.

Racemic **131** was then treated with the racemic dimer $[Ir(dfppy)_2\mu–Cl]_2$ under basic conditions in dry diglyme to afford the diastereomers **132a** and **132b** as racemic mixtures of enantiomers (Figure 5.5). The diastereomers were easily separated via column chromatography and isolated in yields of 66% (**132a**) and 30% (**132b**). Therefore, conversion of the μ–Cl dimer to the monoiridium complexes was near-quantitative. Analysis of the crude reaction mixture by ^{1}H NMR indicated a similar diastereomeric ratio, i.e. *ca.* 2:1, as seen in the UV detector output from the Biotage© Isolera flash chromatography system which was used to resolve the diastereomers (Figure 5.6).

The diastereoselectivity is reproducible as the same ratio was obtained when the reaction was repeated. It is likely related to the presence of the pendant pentafluorophenyl group as there is no diastereoselectivity for the literature analogues **123**–**126** (Figure 5.5), which have phenyl groups. We propose that the more favourable intramolecular π–π stacking interactions in **132a** are responsible for the observed ratio of diastereomers, which are investigated in the XRD and variable temperature NMR studies below.

X-ray crystal structures[†]

Table 5.1: Selected geometrical parameters (bond distances in Å).

	132a[a]	**132b**
Space group	*P2$_1$/n*	*I4$_1$/a*
Stereochemistry	Δ_R/ Λ_S	Δ_S/ Λ_R
Bonds to cyclometallating ligands		
Ir–C (*trans*-O)	1.99(1)/ 2.00(1)	1.994(3)
Ir–C (*trans*-N)	2.01(1)/ 2.00(1)	1.999(3)
Ir–N, stacked	2.026(9)/ 2.02(1)	2.028(2)
Ir–N, non-stacked	2.06(1)/ 2.04(1)	2.049(2)
Bonds to ancillary ligand		
Ir–O	2.117(8)/ 2.134(7)	2.137(2)
Ir–N	2.140(8)/ 2.14(1)	2.165(2)
Deviation of phenoxy plane from Ir–N1–O1 coordination plane, °	25.0/ 24.2	33.8
Intramolecular stacking (π–π)		
Θ, °[b]	5.0/ 6.7	7.8
D, Å[b]	3.30	3.33

[a] Contains two crystallographically non-equivalent molecules. [b] Interplanar angle between pendant pentafluorophenyl ring *A* of the ancillary ligand and ring *B* of the cyclometallating ligand (pyridine for **132a**, phenyl for **132b** - see Figure 5.6); [b] distance between the plane of ring *B* and the centroid of ring *A*.

The single crystal X-ray structures of complexes **132a** and **132b** are shown in Figure 5.6 and relevant parameters are listed in Table 5.1. Slow diffusion of hexane vapour into saturated DCM solutions afforded solvent-free racemic crystals of **132a** and **132b**. The crystals of **132a** consist of the Δ_R and

[†] All X-ray crystal structures were solved by Dr Andrei Batsanov.

Λ_S enantiomers, whereas the crystals of **132b** contain Δ_S and Λ_R. The crystal of **132a** contains two crystallographically non-equivalent molecules.

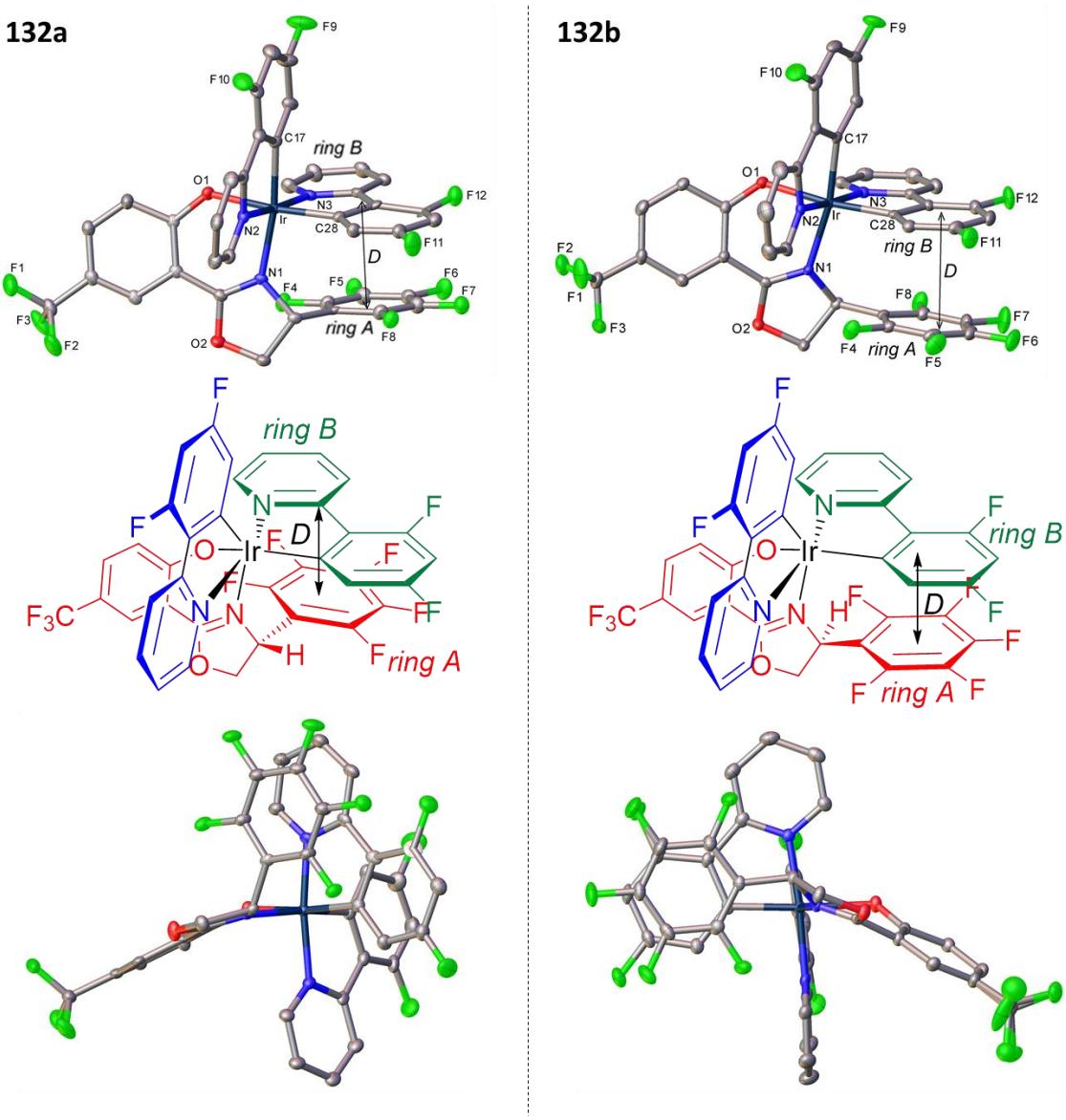

Figure 5.6: (Top) X-ray crystal structures of one of the crystallographically non-equivalent forms of Δ_R-**132a** and Δ_S-**132b** highlighting intramolecular π–π interactions. Thermal ellipsoids are drawn at the 50% probability level and H atoms are omitted for clarity. Vector D identifies intramolecular π–π interactions (see Table 5.1 and discussion in the text). (Middle) Molecular structures drawn in the same projection as the top X-ray crystal structures to clarify the differing stereochemistry of the diastereomers. Cyclometallating ligands are drawn in green and blue while the ancillary ligands are drawn in red. (Bottom) X-ray crystal structures of Λ_S-**132a** and Δ_S-**132b** projected along the ancillary ligand Ir–N–O coordination plane.

Both complexes **132a** and **132b** have distorted octahedral coordination about their Ir centres as expected, with the N atoms of the cyclometallating ligands occupying positions axial to the plane of the phenoxyoxazoline ligand coordination, and *trans* to each other. The phenoxyoxazoline ligand **131** coordinates via a 6-membered N^O chelate as expected.[2]

The structures of **132a** and **132b** each feature intramolecular π–π interactions between the pendant pentafluorophenyl group and one of the cyclometallating ligands. For **132a** the interaction is slipped face-to-face between the pentafluorophenyl group and the pyridyl component of a cyclometallating ligand, analogous to the reports for Λ_S **123**, Λ_S **125** and Δ_R **126** (Figure 5.4).[4] The stacking is closer than for Λ_S **123** (3.30 Å vs. 3.65 Å) due to perfluorination of the pendant aryl group as intended.

For the diastereomer **132b**, close intramolecular stacking (3.33 Å) is also observed, although, in contrast to **132a**, it is between the pendant pentafluorophenyl group and one of the cyclometallating phenyl moieties. The face-to-face overlap is greater (less slipped) than for **132a**. However, the stacking in **132b** is not as close and is less parallel (**132a** Θ = 5.0/ 6.7°, *D* = 3.30 Å, **132b** Θ = 7.8°, *D* = 3.33 Å). The stacking in both **132a** and **132b** is facilitated via distortion of the ancillary ligand from its coordination plane to increase the intramolecular π–π overlap. For **132a**, the plane of the phenoxy ring is bent from the ancillary ligand's Ir–N–O coordination plane by 24.2/ 25.0°, whereas it is distorted by 33.8° for **132b**.[‡] Therefore, the stacking in **132b** appears to be marginally weaker than for **132a** while also requiring a greater structural distortion of the ancillary ligand to facilitate it. This is presumably an indication that the intramolecular π–π interactions are more favourable in **132a**, which is reinforced by the diastereoselectivity of the complex formation and the variable temperature NMR data below.

Variable temperature ^{19}F NMR

The intramolecular π–π interactions in **132a** and **132b** were also studied in solution by ^{19}F NMR spectroscopy to compliment the single crystal X-ray data. At room temperature in D_2-1,1,2,2-tetrachloroethane both diastereomers exhibit 5 ^{19}F environments between *ca.* 140–160 ppm of equal integration, which are assigned to the pentafluorophenyl groups (Figure 5.7). The presence of 5 distinct environments is ascribed to a breakdown in molecular symmetry, due to intramolecular π–π stacking which restricts rotation of the pentafluorophenyl groups in solution. This is similar to the findings for the diiridium complexes in Chapters 3 and 4. *Meta* ^{19}F–^{19}F coupling also appears to be absent, as observed in Chapters 3 and 4. Both diastereomers **132a** and **132b** display well-resolved triplets corresponding to the pentafluorophenyl 4 positions at room temperature (Figure 5.7). However, whereas the signals corresponding to the 2, 3, 4 and 5 positions are sharp for **132a**, they are broader and less well defined for **132b**. This suggests that rotation of the

[‡] The interplanar the angles for complexes **116** and **120** (which do not have pendant aryl groups to undergo π–π stacking) are 15.6° and 5.8°, respectively. The interplanar angle for Λ_S **123** (which has a pendant phenyl group) is 14.4°. These values are all substantially more planar than for **132a** and **132b**.

pentafluorophenyl group at room temperature is more restricted (i.e. exchange is slower) for **132a**. This was further investigated using variable temperature ^{19}F NMR spectroscopy.

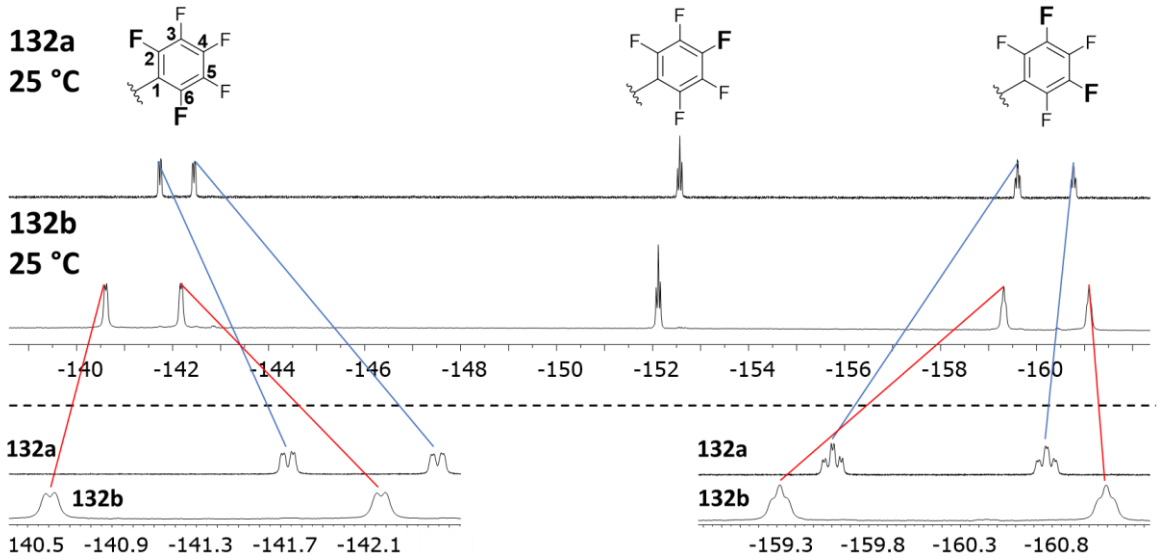

Figure 5.7: (Top) Expansions of the pentafluorophenyl regions (*ca.* 140–160 ppm) of the ^{19}F NMR spectra of **132a** and **132b** and the corresponding atom numbering scheme, recorded at 25 °C in D_2-1,1,2,2-tetrachloroethane. (Bottom) Expansions to highlight that the signals from the 2, 3, 5 and 6 environments are more sharply resolved for **132a**.

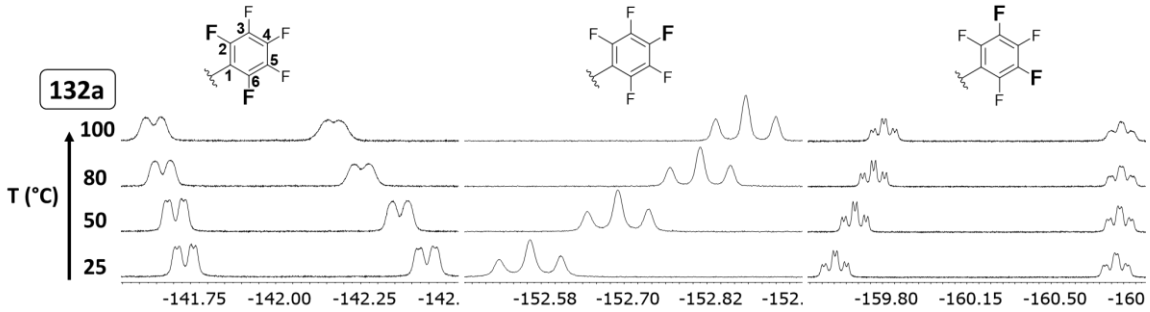

Figure 5.8: Expansions of the pentafluorophenyl regions (*ca.* 140–160 ppm) of the ^{19}F NMR spectrum of **132a** with the atom numbering scheme, recorded at temperatures between 25–100 °C in D_2-1,1,2,2-tetrachloroethane.

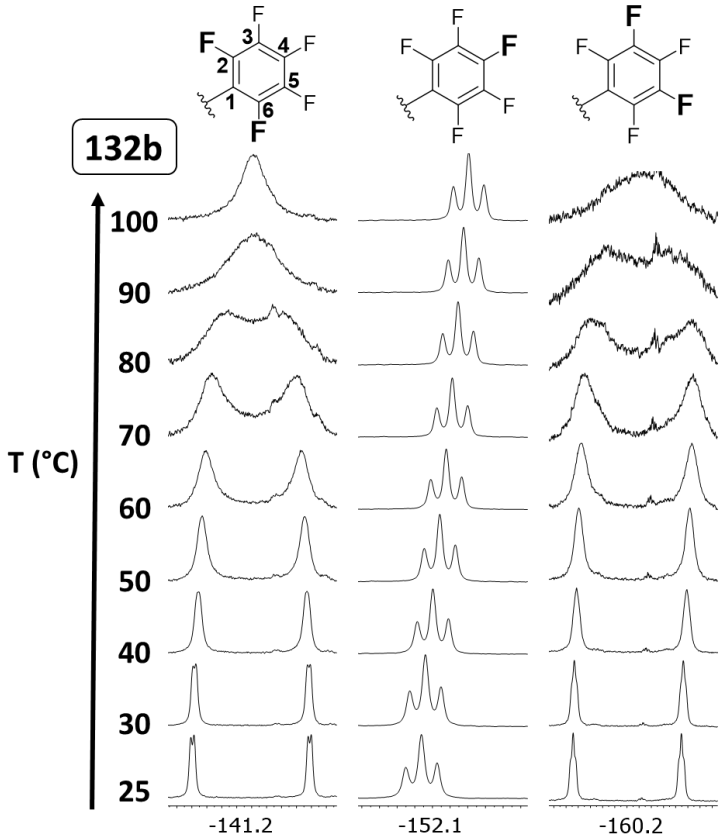

Figure 5.9: Expansions of the pentafluorophenyl regions (*ca.* 140–160 ppm) of the ^{19}F NMR spectrum of **132b** with the atom numbering scheme recorded at temperatures between 25–100 °C in D_2-1,1,2,2-tetrachloroethane.

The ^{19}F NMR spectra recorded for **132a** and **132b** in D_2-1,1,2,2-tetrachloroethane within the temperature range of 25–100 °C are shown in Figures 5.8 and 5.9, respectively. For both diastereomers no significant change is observed in the shape of the triplets corresponding to the 4 positions across the entire temperature range. This is expected as their coupling to the neighbouring ^{19}F environments should be relatively independent of the rate at which the pentafluorophenyl rings are rotating.

For **132a** the signals corresponding to the 2 and 6 positions slightly broaden so that they resolve to doublets upon heating to 100 °C (they resolve to doublets of doublets at 25 °C) (Figure 5.8). They also move towards one another – their frequency difference ($\delta\nu$) is *ca.* 330 Hz at 25 °C, which decreases to *ca*. 250 Hz at 100 °C. However, at 100 °C they are still far from their coalescence point. Similarly, the signals corresponding to the 3 and 5 positions also broaden upon heating, although qualitatively to a lesser extent as they resolve to apparent triplets of doublets across the entire investigated temperature range. $\delta\nu$ also decreases from *ca.* 550 Hz at 25 °C to *ca.* 460 Hz at 100 °C. These changes indicate that the rate at which the pendant pentafluorophenyl ring rotates increases with temperature. However, as none of the signals are close to coalescing upon heating to 100 °C,

it is concluded that exchange is slow across the entire studied temperature range and a significant energetic barrier exists for rotation of the pendant pentafluorophenyl ring of **132a**.

The variable temperature NMR data for **132b** (Figure 5.9) contrast with those obtained for **132a**, as the rate of exchange for **132b** increases more drastically with temperature. The signals corresponding to the 2 and 6 positions (δv at 25 °C = *ca.* 740 Hz) and the 3 and 5 positions (δv at 25 °C = *ca.* 835 Hz) coalescence at *ca.* 85 °C and *ca.* 95 °C, respectively. This is because upon heating the pentafluorophenyl ring of **132b** starts to rotate sufficiently fast that the 2 and 6 positions become indistinguishable on the NMR timescale.[§] The same applies to the 3 and 5 positions. As this is observed for **132b**, but not **132a**, it is concluded that the energetic barrier for rotation of the pentafluorophenyl ring in **132b** is smaller. This suggests that the intramolecular π–π interactions are more effective at restricting rotation of the pendant pentafluorophenyl ring in **132a**, although sterics cannot be completely disregarded.

For dynamic systems such as **132a** and **132b**, it is possible to extract useful physical parameters such as exchange rates and activation energies by using variable temperature NMR. This can be achieved through carrying out a complete line shape analysis which involves comparing the line shapes of the spectra at varying temperatures with simulated spectra. However, this can require a large expenditure of time and effort.[12] In the case of **132a** and **132b**, it is qualitatively clear that the energy barrier to rotation of the perfluoroaryl ring is significantly larger for **132a**, which is attributed to more favourable intramolecular π–π interactions. Therefore, the detailed experiments that would be required to determine accurate physical parameters are unlikely to afford any significant additional understanding of the system.

However, as some signals coalescence within the solvent temperature window for **132b**, it is possible to use an approximate method to estimate the rate constants of exchange (k_{coal}) at the coalescence temperatures (T_{coal}) using Equation 5.1,[12] where $\delta v_{r.t.}$ is the difference in frequency between the two exchanging environments at room temperature.

$$k_{coal} = \delta v_{r.t.} \frac{\pi}{\sqrt{2}} = 2.22 \delta v_{r.t.} \quad (5.1)$$

According to equation 5.1, for a given coalescence temperature the rate of exchange (rate of pentafluorophenyl rotation in this case) is proportional to $\delta v_{r.t.}$. This makes it even more significant that the signals for **132b** coalesce at below 100 °C while the signals for **132a** do not, as the $\delta v_{r.t.}$

[§] In this case "NMR timescale" refers to the millisecond timescale, determined from the k_{coal} values calculated using Equation 5.1.

values for **132b** are significantly larger than for **132a** (740 Hz vs. 330 Hz for the 2 and 6 positions, and 835 Hz vs. 550 Hz for the 3 and 5 positions).

For the signals corresponding to the 2 and 6 positions of **132b**, T_{coal} = *ca*. 85 °C and δv = 740 Hz. For the signals corresponding to the 3 and 5 positions T_{coal} = *ca*. 95 °C, while δv = 835 Hz. Using these values, the approximate rates of exchange at 85 °C and 95 °C for **132b** are calculated to be 1600 s^{-1} and 1900 s^{-1} (2 s.f.), respectively.

Using the same parameters, it is possible to apply the Eyring equation (Equations 5.2 and 5.3) to approximately estimate the free energy barrier ($\Delta G^{\ddagger}$) for exchange at the coalescence temperatures.[12]

$$\Delta G^{\ddagger} = RT\left[23.76 - \ln\left({}^{k}/_{T}\right)\right] \tag{5.2}$$

$$\Delta G^{\ddagger} = RT_{coal}\left[22.96 + \ln\left({}^{T_{coal}}/_{\delta v_{r.t.}}\right)\right] \tag{5.3}$$

Using Equation 5.3, a $\Delta G^{\ddagger}$ value of 70 kJ mol^{-1} (1 s.f.) is estimated for **132b** from the data obtained at either coalescence temperature. It should be emphasised that this obtained value for the energy barrier is temperature dependent due to the entropy term ($\Delta S^{\ddagger}$) in Equation 5.4,[12] which may limit its usefulness outside the coalescence temperatures.

$$\Delta G^{\ddagger} = \Delta H^{\ddagger} - T\Delta S^{\ddagger} \tag{5.4}$$

Nevertheless, as the rotation of the pendant pentafluorophenyl ring in **132b** is an intramolecular process, and the complex is rather rigid, $\Delta S^{\ddagger}$ may be small. Therefore, while further detailed investigation is required to accurately determine the energy barrier at room temperature, 70 kJ mol^{-1} may be a useful rough figure. It is noted that this value is comparable to the room temperature $\Delta G^{\ddagger}$ values reported by Cozzi and Siegel et al. for rotation of intramolecularly-stacked perfluoroaryl rings in diarylnaphthalenes, which are in the range of 80 kJ mol^{-1} (20 kcal mol^{-1}) (see Chapter 3).[13,14]

In summary, the intramolecular π–π interactions between the pendant pentafluoroaryl rings and cyclometallating ligands in **132a** and **132b** are strong enough to restrict rotation of the pendant ring in solution. This can be observed through a breakdown in the symmetry of their ^{19}F NMR spectra. From the room temperature and variable temperature NMR data for both systems, it can be concluded that the barrier to rotation in **132a** is significantly greater than for **132b**. This is ascribed to stronger intramolecular π–π interactions, in agreement with the XRD data above. As some signals coalescence at below 100 °C for **132b**, a value of 70 kJ mol^{-1} could be roughly estimated for $\Delta G^{\ddagger}$,

which is comparable to previously reported literature values.[13,14] These data also strengthen the conclusion that the diastereoselectivity of the complex formation is due to the stronger intramolecular π–π interactions in **132a**.

Computational study

Electronic structure calculations were carried out on the diastereomers **132a** and **132b** to explore their molecular orbitals and to support their electrochemical and photophysical properties (discussed below). The optimised S_0 geometries were calculated at the B3LYP/LANL2DZ:6–31G* level to allow direct comparison with our previous studies on the analogues **114**–**120** (Figures 5.2 and 5.3).[2,3] Due to the lower molecular weights of these monoiridium complexes, a more complex basis set than 3–21G* that was used for the diiridium complexes studied in Chapters 2–4 can be applied, while still affording similar or shorter calculation times.

The optimised S_0 geometry for **132b** features a more distorted phenoxyoxazole ancillary ligand than **132a**, in agreement with the XRD data above. The optimised structure for **132a** is 2.3 kJ mol^{-1} higher in energy than the optimised structure of **132b**, suggesting that while there is diastereoselectivity for **132a** under the reaction conditions employed here, it is not the thermodynamic product. No attempts were made to thermally isomerise **132a**, as it was suspected that heating it to > 200 °C in a polar protic solvent such as glycerol (the common conditions for thermal isomerisation of cyclometallated Ir complexes[15]) would lead to substitution of the aromatic fluorines and/ or decomposition. The significant differences in the variable temperature emission data (discussed below) for **132a** and **132b** when irradiated with a 405 nm laser for *ca.* 1 h suggest that they cannot be easily photoisomerised.

Table 5.2: Orbital contributions for complexes **132a** and **132b**.

Complex	Orbital	Ir	Ph[a]	Py[b]	Phenoxy	Oxazoline	C_6F_5[c]
	LUMO+2	1%	0%	3%	42%	35%	19%
	LUMO+1	4%	21%	73%	1%	0%	0%
132a	LUMO	4%	25%	69%	0%	1%	1%
	HOMO	25%	11%	3%	55%	5%	0%
	HOMO-1	36%	35%	6%	21%	2%	0%
	LUMO+2	1%	1%	2%	42%	36%	18%
	LUMO+1	4%	23%	71%	1%	1%	0%
132b	LUMO	4%	24%	70%	0%	1%	1%
	HOMO	25%	12%	3%	55%	5%	0%
	HOMO-1	36%	33%	6%	23%	2%	0%

[a]Phenyl moieties of the cyclometallating ligands; [b]Pyridyl moieties of the cyclometallating ligands; [c]Pendant pentafluorophenyl group of the ancillary ligand

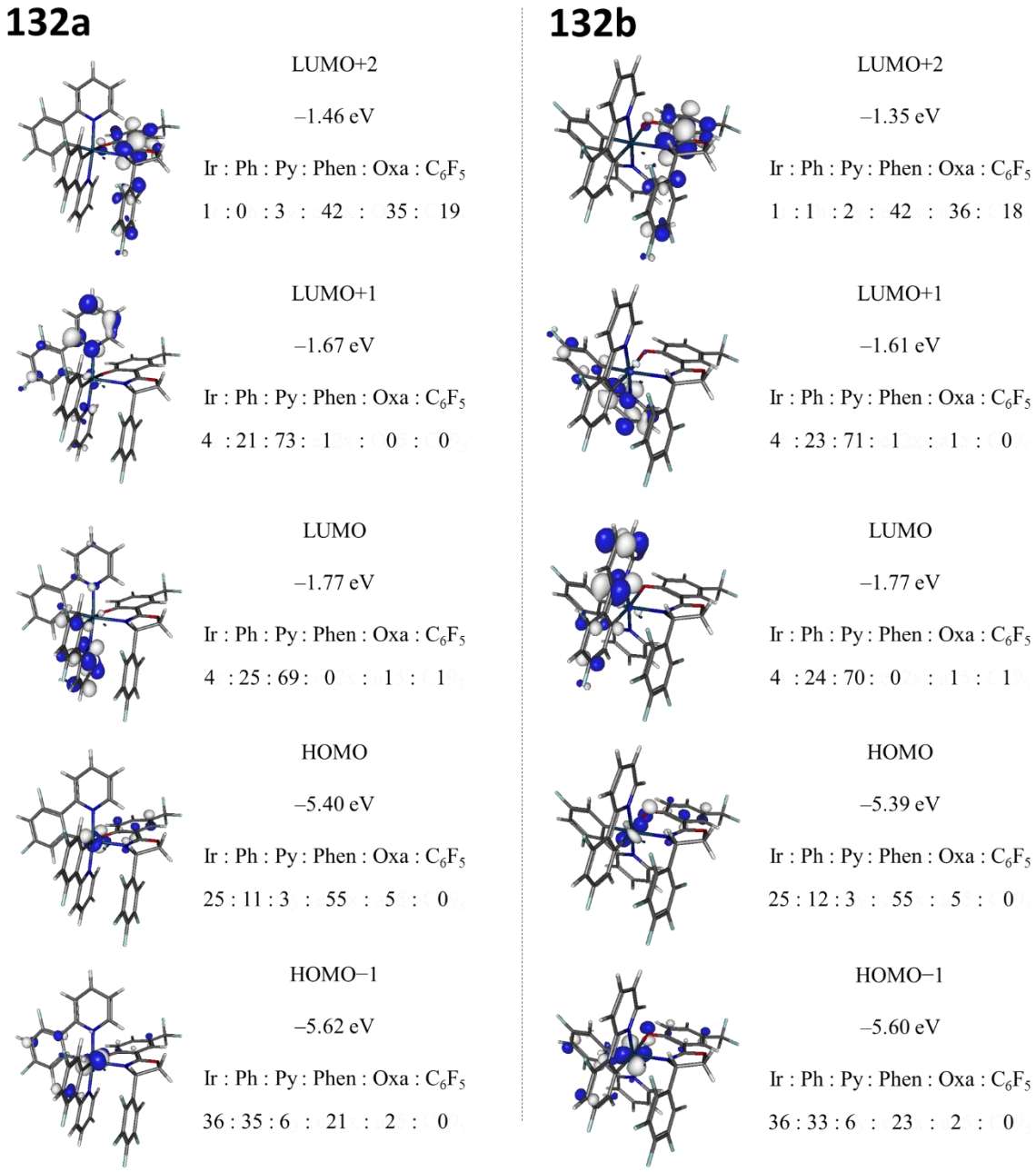

Figure 5.10: Molecular orbital compositions for **132a** and **132b**. The orbital contributions are percentages and the orbital energies were calculated at B3LYP/LANL2DZ:6–31G*. Phen = ancillary ligand phenoxy group; Oxa = ancillary ligand oxazole group; Ph = cyclometallating ligand phenyl groups; Py = cyclometallating ligand pyridyl groups; C_6F_5 = pendant pentafluorophenyl.

The molecular orbital compositions of the HOMO−1 – LUMO+2 orbitals for **132a** and **132b** (which are relevant to the TD-DFT below) are listed in Table 5.2 and the molecular orbital plots are shown in Figure 5.10.

The HOMO−1 – LUMO+2 compositions are near identical for both complexes. The HOMOs are primarily localised on the phenoxy moieties of the ancillary ligands (55%) and the Ir atoms (25%),

with small contributions from the cyclometallating phenyl groups (*ca.* 10%). This suggests that the CF_3 and oxazoline-functionalised phenoxy moiety is more electron rich than a cyclometallated dfppy ring. The LUMOs are almost exclusively localised on the cyclometallating ligands with *ca.* 70% and 25% contributions from the pyridyl and phenyl moieties, respectively. Therefore, the FMO contributions for **132a** and **132b** are in good agreement with those reported for the literature analogues **119** and **120** (Figure 5.3).[3] It should be noted that functionalisation of its non-conjugated oxazoline ring with a strongly electron-accepting pendant pentafluorophenyl ring appears to be insufficient to shift the LUMOs of **132a** and **132b** onto the ancillary ligand **131**.

For both complexes, the localisation of the LUMO+1 is practically identical to that of the LUMO, while the LUMO+2 is primarily ancillary ligand-based – they feature *ca.* 40% and 35% contributions from the phenoxy and oxazoline groups, respectively, while also being somewhat localised on the pendant pentafluorophenyl moieties (*ca.* 20%). For both complexes the HOMO−1 is primarily of Ir and cyclometallating phenyl character (*ca.* 35% contribution from each) with some localisation on the phenoxy moieties of the ancillary ligands (*ca.* 20%).

TD-DFT was employed to simulate the absorption spectra of **132a** and **132b**. The spectra calculated for the first 200 singlet states are included in Figure 5.11. The spectral profiles of the calculated spectra are generally in good agreement with experimental data. The calculated absorption onsets are shifted to lower energies than the experimental data (by *ca.* 25 nm), albeit to a smaller extent than that encountered for the diiridium complex **35a** in Chapter 2 (*ca.* 50 nm).

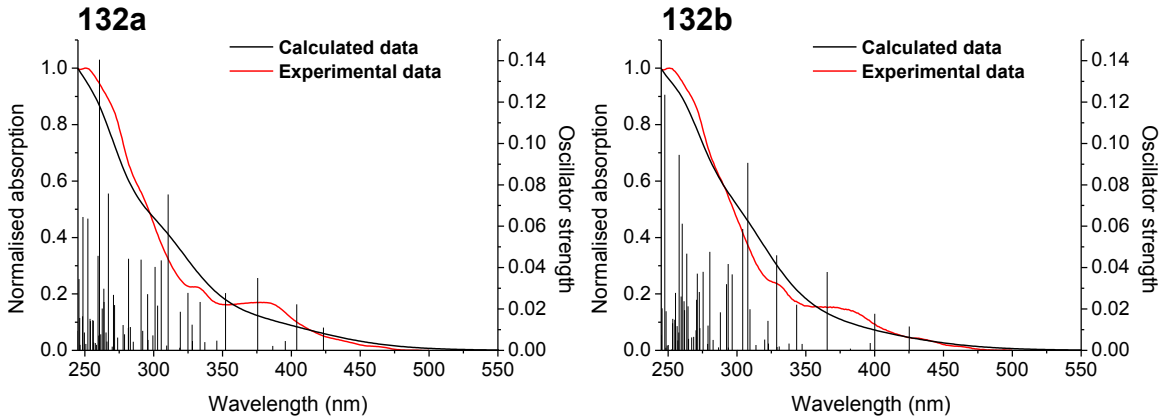

Figure 5.11: Simulated and experimental absorption spectra for complexes **132a** and **132b**. Experimental data were obtained in aerated DCM.

The lowest energy singlet and triplet states were also investigated at the S_0 geometries for **132a** and **132b**. The data for the three lowest energy triplet and singlet excited states for each complex are tabulated in Table 5.3. The dominant transitions contributing to each state (≥ *ca.* 20%) are

included. The transitions to the lowest energy singlet states ($S_0 \rightarrow S_1$) for each complex primarily consist of HOMO → LUMO transitions, while the transitions to the second and third singlet states ($S_0 \rightarrow S_2$ and $S_0 \rightarrow S_3$) also involve the LUMO+1 and HOMO−1 orbitals. This is in good agreement with the data for the analogues **116**–**120** (Figure 5.3).[3]

Table 5.3: Summary of the TD-DFT data for **132a** and **132b**.[a]

Transition	132a		132b	
	Main orbital contribution	**λ/ nm (ƒ)**	**Main orbital contribution**	**λ/ nm (ƒ)**
$S_0 \rightarrow T_1$	HOMO → LUMO+2	463	HOMO-1 → LUMO, HOMO→ LUMO	460
$S_0 \rightarrow T_2$	HOMO-1 → LUMO, HOMO→ LUMO	456	HOMO → LUMO+2	449
$S_0 \rightarrow T_3$	HOMO-1 → LUMO+1	442	HOMO-1 → LUMO+1	440
$S_0 \rightarrow S_1$	HOMO→ LUMO	423 (0.011)	HOMO→ LUMO	425 (0.012)
$S_0 \rightarrow S_2$	HOMO → LUMO+1	404 (0.022)	HOMO-1 → LUMO, HOMO → LUMO+1	400 (0.018)
$S_0 \rightarrow S_3$	HOMO-1 → LUMO	395 (0.005)	HOMO → LUMO+1, HOMO-1 → LUMO	397 (0.004)

[a]ƒ = oscillator strength. It is only included for singlet transitions as it is zero for all triplet transitions

For each of the complexes **132a** and **132b**, there are three triplet states within *ca.* 20 nm of each other, while the two lowest energy triplet states are within *ca.* 10 nm. From consideration of the lowest 2/ 3 triplet states of the complexes it is evident that their emissive states are likely to be broadly delocalised, with mixed LC (on both the cyclometallating and ancillary ligands), MLCT (metal → cyclometallating ligand/ ancillary ligand) and ILCT (ancillary ligand → cyclometallating ligand) character. For **132a** the transition to the lowest energy triplet state ($S_0 \rightarrow T_1$) is primarily of HOMO → LUMO+2 character, while the second triplet state ($S_0 \rightarrow T_2$) involves both HOMO−1 → LUMO and HOMO → LUMO transitions. For **132b** the same transitions are involved, although the ordering of the states is inverted (Table 5.3). The small variation observed in the spectral profiles of **132a** and **132b** below (most prominent in PMMA - Figure 5.14) may be related to this. However, as the experimentally determined photophysical parameters for **132a** and **132b** (λ_{max}, E_T, PLQY and τ – see below) are very similar, it is likely that their emission originates from analogous states. Therefore, the inversion of the character of the $S_0 \rightarrow T_1$ and $S_0 \rightarrow T_2$ transitions in the TD-DFT may not be significant.

Electrochemical study

The oxidation and reduction potentials for **132a** and **132b** were obtained via cyclic voltammetry. The voltammograms are shown in Figure 5.12 and the key data are listed in Table 5.4. Each complex

displays an electrochemically reversible oxidation and irreversible reduction. There is a small variation in the oxidation potentials of **132a** and **132b** (30 mV), which is unsurprising considering that similar differences in the oxidation potentials of diastereomeric iridium complexes were observed earlier in this thesis (Chapters 2 and 3) and have been reported in the literature.[6,7] The oxidation potentials of **132a** and **132b** (0.78 V and 0.81 V, respectively) are lower than for FIrpic (*ca.* 0.9 V in the literature which was reproduced in-house) (Figure 1.12).[5] This is in agreement with the DFT above which predicts the HOMO to be primarily localised on the more electron rich phenoxy moiety rather than the dfppy ligands. The HOMOs of **132a** and **132b** are marginally more negative (by 30–90 mV) than for the analogues **119** and **120** (Figure 5.3),[3] which is rationalised through the presence of strongly electron withdrawing pentafluorophenyl groups. The lack of HOMO contribution from the pentafluorophenyl rings in **132a** and **132b** is, however, expected to limit this effect. Both oxidation processes were shown to be chemically reversible over 10 cycles for **132a** and **132b** (Figure 5.13).

Table 5.4: Electrochemical data for complexes **132a** and **132b** referenced to $E_{1/2}$ FcH/ FcH^+ = 0.00 V.

Complex	E^{ox} /V E_{pa}/ E_{pc} [$E_{1/2}$]	E^{red}_{onset} /V[a]	HOMO /eV[b]	LUMO /eV[c]	E_g[d]
132a	0.88/ 0.69 [0.78]	–2.37	–5.58	–2.43	3.15
132b	0.87/ 0.74 [0.81]	–2.35	–5.61	–2.45	3.16

[a]All reductions are electrochemically irreversible. [b]HOMO levels calculated from CV potentials by HOMO = –4.8 + (–$E_{1/2}^{ox}$), using ferrocene as the standard. [c]LUMO levels calculated from CV potentials by LUMO = –4.8 + (–E^{red}_{onset}), using ferrocene as the standard. [d]Estimated electrochemical HOMO–LUMO gap.

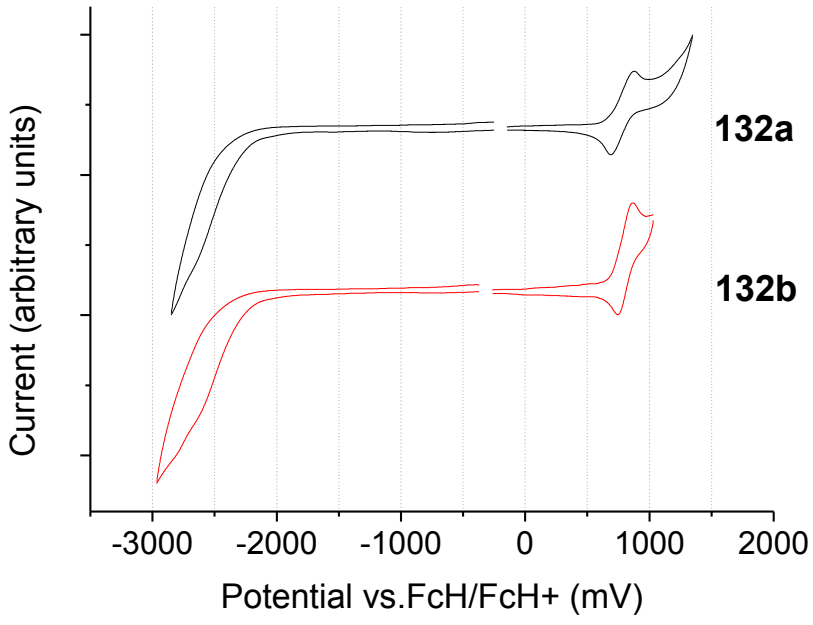

Figure 5.12: Cyclic voltammograms in 0.1 M *n*-Bu_4NPF_6/ THF showing the oxidation and reduction processes for complexes **132a** and **132b**.

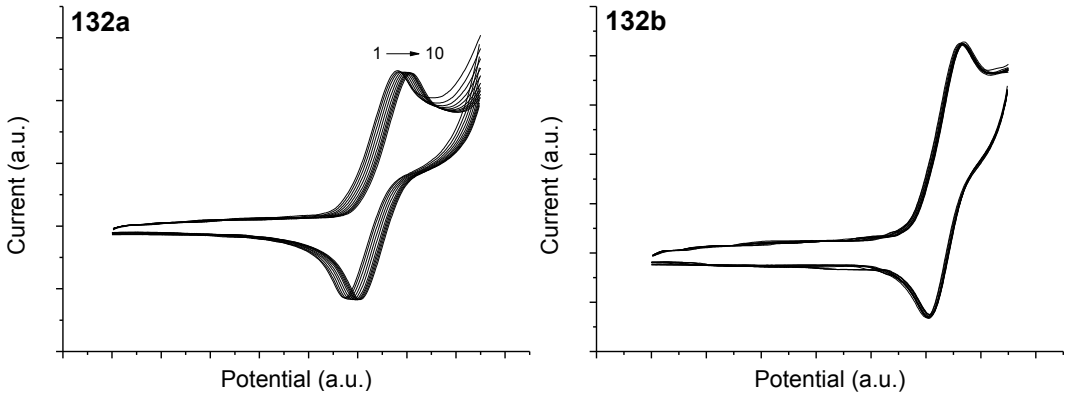

Figure 5.13: Cyclic voltammograms in 0.1 M *n*-Bu_4NPF_6/ THF showing the oxidation processes for complexes **132a** and **132b** over 10 consecutive scans. The potential axis is arbitrary due to the absence of internal ferrocene. The oxidation potentials slightly drift due to the use of a quasireference electrode.

The estimated reduction potentials for **132a** and **132b** are typical for ppy-based cyclometallated heteroleptic monoiridium complexes (i.e. within *ca.* 2.2–2.8 V).[5] While their irreversible nature adds error to their accurate determination, it is clear from the voltammograms (Figure 5.12) that the reduction potentials for **132a** and **132b** are similar (within 20 mV), as expected. Because of their similar oxidation and reduction potentials, the electrochemical band gaps (E_g) for **132a** and **132b** are near identical.

Photophysical properties

The absorption and emission spectra for **132a** and **132b** are shown in Figure 5.14 and the key photophysical data are listed in Table 5.5. The absorption spectra (DCM) for both diastereomers are very similar, as expected, and exhibit spectral profiles and extinction coefficients typical of cyclometallated monoiridium complexes.[5,15]

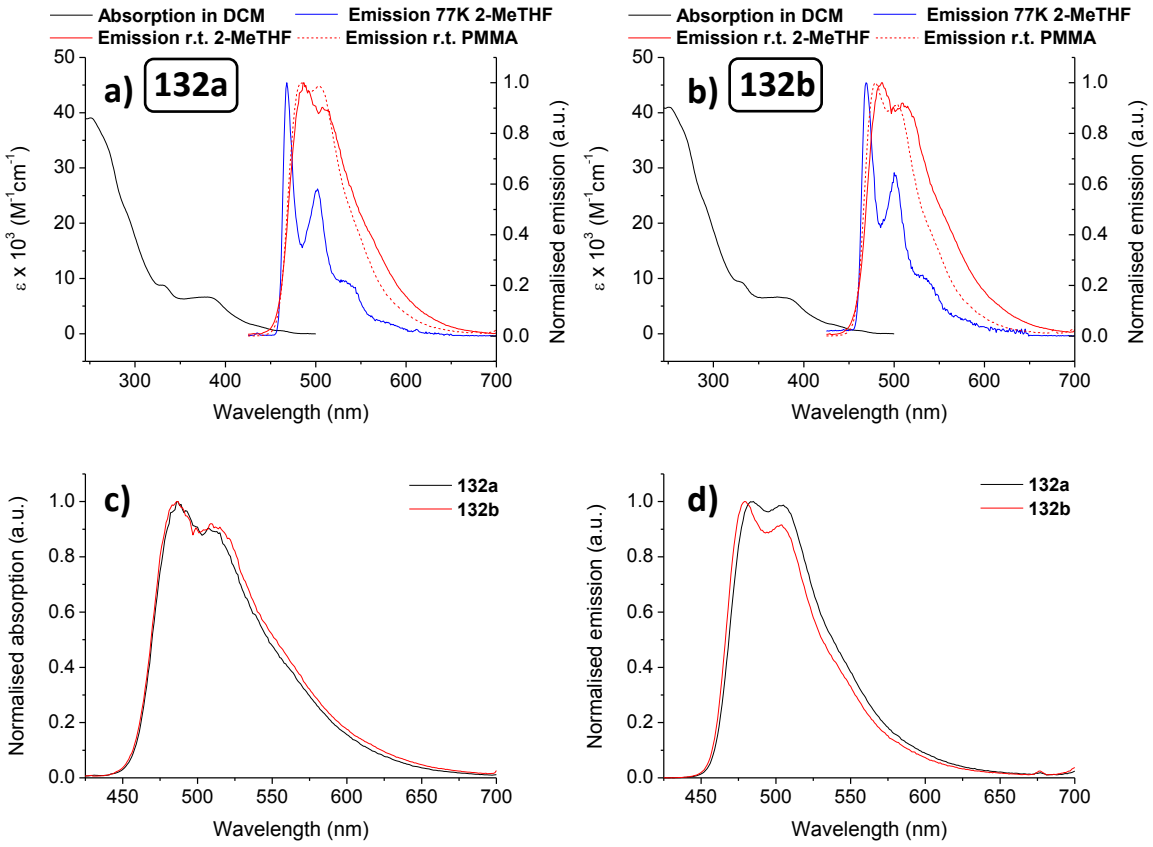

Figure 5.14: a) Absorption and emission spectra for **132a**; b) absorption and emission spectra for **132b**; c) emission spectra for **132a** and **132b** recorded in degassed 2-MeTHF at room temperature; d) emission spectra for **132a** and **132b** doped into PMMA at 1 wt.% at room temperature (λ_{exc} 355 nm).

The PL properties of **132a** and **132b** in degassed room temperature 2-MeTHF solution can be considered identical within experimental error. They each display essentially the same spectral profiles (Figure 5.14 c)) with FWHM values of *ca.* 80 nm. They also feature PLQYs of *ca*. 50%** and phosphorescence lifetimes around 1.5 µs, which fall within the range reported for the analogues **114–120**[2,3] (Figures 5.2 and 5.3), and are typical of heteroleptic phosphorescent monoiridium

** The PLQY of FIrpic under directly comparable experimental conditions in 2-MeTHF is 73 ± 5 %, i.e. the same as reported in Chapter 3 in DCM. Therefore, the solution PLQY data presented here are directly comparable with those in Chapter 3.

complexes.[5,16,17] **132a** and **132b** display the same 77 K emission spectra in 2-MeTHF, with estimated Huang-Rhys factors and E_T of 0.6 (1 s.f.) and 2.70 eV, respectively.

Table 5.5: Summary of the key photophysical data for complexes **132a** and **132b**.

	DCM solution	**2-MeTHF solution[a]**				
Complex	**λ_{abs} /nm ($\varepsilon \times 10^3$ / $M^{-1}cm^{-1}$)**	**$\lambda_{max\ em}$ /nm [CIE_{xy}]**	**PLQY /% (± 5%)**	**τ /μs**	**k_r /× 10^5 s^{-1}**	**k_{nr} /× 10^5 s^{-1}**
132a	251 (39), 270sh (33), 291sh (22), 332 (8.7), 383 (6.5), 439sh (1.3), 464 (0.5), 490 (0.1)	487 [0.23, 0.49]	51	1.56	3.27	3.14
132b	252 (41), 269sh (36), 290sh (23), 332 (9.0), 384 (6.3), 438sh (1.4), 465 (0.5), 490 (0.1)	487 [0.24, 0.49]	50	1.54	3.25	3.25
	2-MeTHF glass[b]		**Doped into PMMA 1% wt.[c]**			
Complex	**$\lambda_{max\ em}$ /nm ($\lambda_{10\%\ em}$ /nm)[d] [E_T /eV][e]**	**τ /μs**	**$\lambda_{max\ em}$ /nm [CIE_{xy}]**	**PLQY /% (± 10%)**	**τ /μs**	**k_r /× 10^5 s^{-1}**	**k_{nr} /× 10^5 s^{-1}**
132a	468 (459) [2.70]	2.79	485 [0.18, 0.46]	67	1.72	3.90	1.92
132b	469 (459) [2.70]	2.49	479 [0.17, 0.42]	60	1.73	3.47	2.31

sh = Shoulder. [a]Solution photoluminescence measurements were recorded in degassed 2-MeTHF solutions at *ca.* 20 °C with an excitation wavelength of 355 nm with quinine sulfate in 0.5 M H_2SO_4 as standard (Φ = 0.546).[16] [b]Measured at 77 K using an excitation wavelength of 355 nm. [c]Measured in an integrating sphere under air using an excitation wavelength of 355 nm. [d]Wavelength at 10% intensity on the blue edge of the spectrum obtained at 77 K. [e]Estimated using $E_T = hc/\lambda_{10\%\ em}$. $\tau = 1/k_{nr} + k_r$.

When doped into PMMA both diastereomers **132a** and **132b** feature longer τ values of *ca.* 1.7 μs. The PLQYs are slightly increased to 60/ 67%, although within experimental error they are similar to the solution values. This can mainly be attributed to decreases in k_{nr}, which can be attributed to the more rigid PMMA matrix, although there is also a small increase in k_r for both complexes (Table 5.5).

While the PLQYs and lifetimes of **132a** and **132b** are very similar in PMMA, a noteworthy difference is observed in their spectral profiles, which could be related either to the higher rigidity of PMMA in comparison to 2-MeTHF, or its polarity. The PL λ_{max} values are blue shifted compared to those recorded in 2-MeTHF (by 2 nm for **132a** and 8 nm for **132b**). The emission spectra of both **132a** and **132b** also sharpen upon doping into PMMA, i.e. they display FWHM values of *ca.* 70 nm and 65 nm, respectively, vs. 80 nm for both diastereomers in 2-MeTHF. In addition, the vibronic shoulder is more resolved for **132b**, although less intense (Figure 5.14 d)). These data could imply that in PMMA the emitting state of **132b** features greater LC character than for **132a**, and result in a total CIE_{xy} coordinate value for **132b** 0.05 units lower (0.17, 0.42) than for **132a** (0.18, 0.46). These observations indicate that in PMMA, the stronger intramolecular π–π interactions in **132a** do not

lead to sharper emission, which may have been anticipated due to the presumed higher molecular rigidity of **132a**.

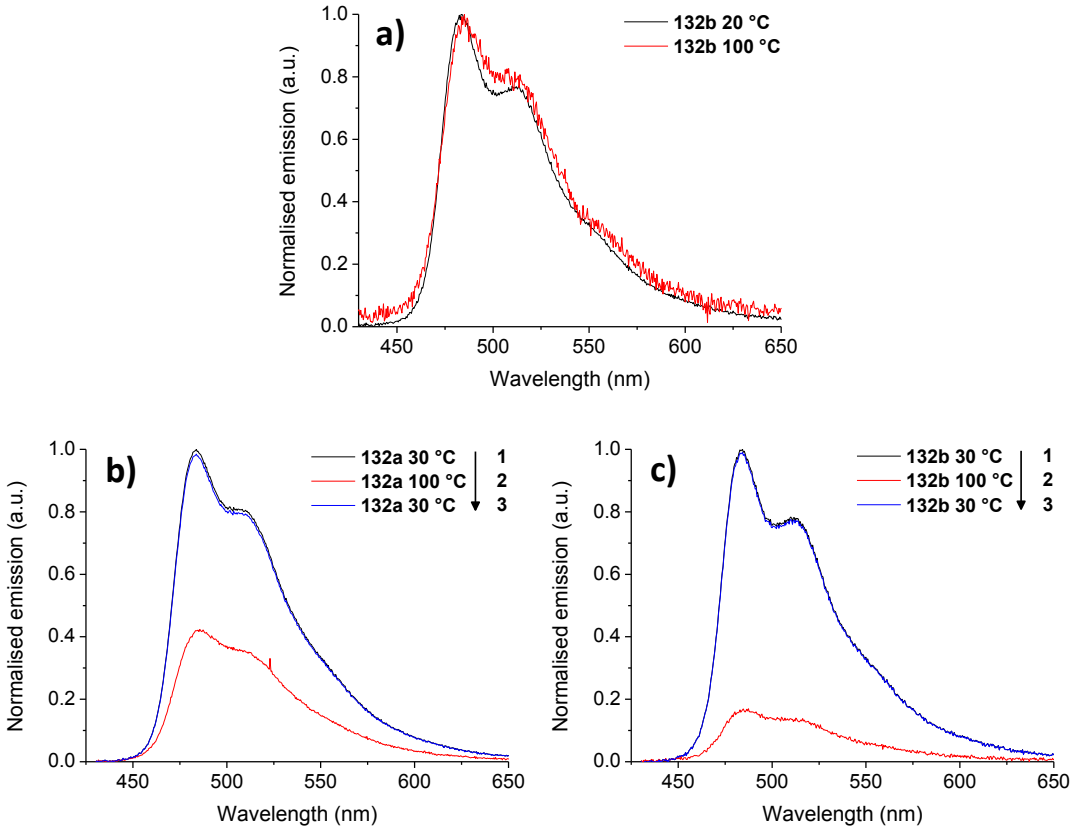

Figure 5.15: a) Normalised emission spectra for **132b** recorded at 20 °C and 100 °C; b) and c) Emission spectra upon cycling between 30 °C and 100 °C for **132a** and **132b**, respectively (normalised to the initial spectrum recorded at 30 °C). All spectra are recorded in degassed xylenes (λ_{exc} 405 nm). Temperatures are ± 5 °C.

The variable temperature NMR data (above) for **132a** and **132b** indicate that they behave differently in solution upon heating due to the differing barriers to rotation of their pendant pentafluorophenyl rings. Therefore, the PL properties of the diastereomers between 20–100 °C were investigated (Figure 5.15). Initially 1,1,2,2-tetrachloroethane was selected as a solvent for consistency with the variable temperature NMR experiments. However, **132b** decomposed upon heating in 1,1,2,2-tetrachloroethane, possibly due to traces of acid (HCl) in the solvent, or because the complex is unstable in 1,1,2,2-tetrachloroethane under prolonged (> *ca.* 15 min) irradiation from a 405 nm laser while heated. Mixed xylene was selected as an alternative solvent, due to its high boiling point and because it was expected to be more photostable. Both **132a** and **132b** are also sufficiently soluble in xylenes for PL measurements.

The spectra for **132a** and **132b** in xylenes are sharper than those recorded in 2-MeTHF with more defined vibronic bands. This suggests higher LC character and may be related to the lower polarity of xylenes. The emission spectra for **132b** recorded at 20 °C and 100 °C (Figure 5.15 a)) have very similar spectral profiles, suggesting that the emission originates from the same state regardless of temperature and the rate of rotation of the pendant pentafluorophenyl ring.

The emission spectra for **132a** and **132b** upon cycling the temperature between 30–100 °C are shown in Figures 5.15 b) and c), respectively. Upon heating from 30→100 °C the emission intensities for both complexes decrease. This observation is not due to decomposition or ingress of oxygen as the initial spectral intensities are retained upon cooling back to 30 °C. A decrease in the emission intensities of **132a** and **132b** upon heating implies the existence of a temperature dependent non-radiative pathway which becomes more accessible at higher temperatures. This has been commonly reported for cyclometallated iridium complexes and has been ascribed to the thermal population of low-lying MC states (see Chapter 1).[18,19]

Upon heating from 30→100 °C the integrated emission intensity for **132a** drops to 44% of its initial intensity, whereas it drops to 18% for **132b**. Both complexes have the same solution PL λ_{max}, display identical E_T and have the same coordination environment about their Ir centres. Therefore, the energy gaps between the MC and emitting states for **132a** and **132b** are expected to be very similar, meaning that non-radiative deactivation via thermally-accessible MC states alone cannot explain such a significant difference in the temperature dependence of their PL properties. The variable temperature ^{19}F NMR data above indicate that rotation of the pendant pentafluorophenyl rings in **132b** and **132a** is a temperature dependent process, and that there is a smaller energy barrier to rotation in **132b**. Therefore, such rotation can be expected to constitute a more easily populated non-radiative pathway for **132b** than **132a**, which leads to a more substantial decrease in emission intensity upon heating for **132b** and explains the observed differences in the variable temperature PL data.

Conclusions and future work

In conclusion, a chiral phenoxyoxazoline ancillary ligand was exploited in the synthesis of the diastereomeric monoiridium complexes **132a** and **132b**, which were separated and their photophysical, structural and electrochemical properties studied.

The chiral ancillary ligand features a pendant pentafluorophenyl ring which engages in intramolecular π–π stacking with either the pyridyl (**132a**) or phenyl (**132b**) group of a cyclometallating ligand. This is the main difference between the diastereomers which are otherwise very similar, as indicated by their electrochemical and computational data. This makes them an

ideal platform to build on the work presented in Chapters 3 and 4, and gain further insight into the effect of intramolecular π–π interactions involving perfluoroaryl rings in cyclometallated iridium complexes. The interactions were studied in solution through variable temperature ^{19}F NMR spectroscopy, and in the solid state through single crystal X-ray diffraction. Both sets of data indicate that the π–π interactions in **132a** are significantly more favourable. It is noted that the stronger intramolecular π–π interactions in **132a** lead to appreciable diastereoselectivity during complex formation (2:1 ratio of **132a** to **132b**).

132a and **132b** display very similar photophysical parameters (PLQYs and phosphorescence lifetimes) in both 2-MeTHF and PMMA. However, the emission spectrum for **132b** in PMMA is sharper and marginally blue shifted compared to that of **132a**. Importantly, this indicates that stronger intramolecular π–π interactions in cyclometallated iridium complexes do not necessarily guarantee sharper emission spectra with improved colour purity.

Our collaborators are currently exploring the application of **132a** and **132b** in vacuum-processed OLEDs. The potential to control the intramolecular π–π interactions through varying the level of fluorination on **131** could also provide a prospective application for these complexes and analogues as viscosity probes. **132b**, which features intramolecular stacking between the pendant pentafluoroaryl ring and the phenyl group of a cyclometallating ligand, displays narrower emission in PMMA, but is the minor diastereomer. In future work, incorporating a tetrafluorinated ppy cyclometallating ligand with a pendant phenyl group on the ancillary ligand to obtain a 'reverse stacked' arrangement, could promote the formation of the equivalent diastereomer for **133** (Figure 5.16).

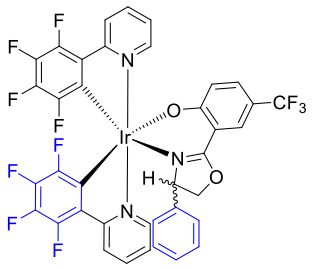

133

Figure 5.16: Proposed future structure. Intramolecular π–π stacking should be promoted between the colour rings.

References

1 Y. You, J. Seo, S. H. Kim, K. S. Kim, T. K. Ahn, D. Kim and S. Y. Park, *Inorg. Chem.*, 2008, **47**, 1476–1487.

2 K. Chao, K. Shao, T. Peng, D. Zhu, Y. Wang, Y. Liu, Z. Su and M. R. Bryce, *J. Mater. Chem. C*, 2013, **1**, 6800–6806.

3 H. Benjamin, J. Liang, Y. Liu, Y. Geng, X. Liu, D. Zhu, A. S. Batsanov and M. R. Bryce, *Organometallics*, 2017, **36**, 1810–1821.

4 E. Marchi, R. Sinisi, G. Bergamini, M. Tragni, M. Monari, M. Bandini and P. Ceroni, *Chem. Eur. J.*, 2012, **18**, 8765–8773.

5 J. Frey, B. F. E. Curchod, R. Scopelliti, I. Tavernelli, U. Rothlisberger, M. K. Nazeeruddin and E. Baranoff, *Dalton Trans.*, 2014, **43**, 5667–5679.

6 D. G. Congrave, Y. Hsu, A. S. Batsanov, A. Beeby and M. R. Bryce, *Organometallics*, 2017, **36**, 981–993.

7 X. Yang, X. Xu, J. Dang, G. Zhou, C.-L. Ho and W.-Y. Wong, *Inorg. Chem.*, 2016, **55**, 1720–1727.

8 T.-Y. Li, Y.-X. Zheng and Y.-H. Zhou, *Dalton Trans.*, 2016, **45**, 19234–19237.

9 H. Aryl, J. Feldman, G. D. Vo, C. D. Mclaren, T. C. Gehret, K. Park, S. Meth, W. J. Marshall, J. Buriak, L. M. Bryman, K. D. Dobbs, T. H. Scholz and S. G. Zane, *Organometallics*, 2015, **34**, 3665–3669.

10 Y. Zheng, A. S. Batsanov, M. A. Fox, H. A. Al-Attar, K. Abdullah, V. Jankus, M. R. Bryce and A. P. Monkman, *Angew. Chem. Int. Ed.*, 2014, **53**, 11616–11619.

11 M. Bandini, P. G. Cozzi, M. Gazzano and A. Umani-Ronchi, *Eur. J. Org. Chem.*, 2001, 1937–1942.

12 H. Günther, *NMR Spectroscopy: Basic Principles, Concepts and Applications in Chemistry*, John Wiley & Sons, Chichester, 2nd edition, 1995.

13 F. Cozzi, M. Cinquini, R. Annuziata and J. S. Siegel, *J. Am. Chem. Soc.*, 1993, **115**, 5330–5331.

14 F. Cozzi, F. Ponzini, R. Annunziata, M. Cinquini and J. S. Siegel, *Angew. Chem. Int. Ed. Engl.*, 1995, **34**, 1019–1020.

15 A. B. Tamayo, B. D. Alleyne, P. I. Djurovich, S. Lamansky, I. Tsyba, N. N. Ho, R. Bau and M. E. Thompson, *J. Am. Chem. Soc.*, 2003, **125**, 7377–7387.

16 H. Benjamin, Y. Zheng, A. S. Batsanov, M. A. Fox, H. A. Al-Attar, A. P. Monkman and M. R. Bryce, *Inorg. Chem.*, 2016, **55**, 8612–8627.

17 H. Benjamin, M. A. Fox, A. S. Batsanov, H. A. Al-Attar, C. Li, Z. Ren, A. P. Monkman and M. R. Bryce, *Dalton Trans.*, 2017, **46**, 10996–11007.

18 T. Sajoto, P. I. Djurovich, A. Tamayo, M. Yousufuddin, R. Bau, M. E. Thompson, R. J. Holmes and S. R. Forrest, *Inorg. Chem.*, 2005, **44**, 7992–8003.

19 T. Sajoto, P. I. Djurovich, A. B. Tamayo, J. Oxgaard, W. A. Goddard and M. E. Thompson, *J. Am. Chem. Soc.*, 2009, **131**, 9813–9822.

Chapter 6: Conclusions

In this thesis a number of new cyclometallated di- and monoiridium complexes were synthesised, and their structural, photophysical and electrochemical properties were studied in detail.

Analysis of the structure-property relationships of the diiridium complexes **35**–**38** in Chapter 2 revealed that the flexibility of the central diarylhydrazide bridging unit serves as a pathway for rapid non-radiative decay in solution, which can be suppressed through intermolecular means using a rigid PMMA host, enhancing Φ_{PL} by as much as 3 orders of magnitude. Through single crystal X-ray diffraction studies interesting face-to-face intramolecular π–π interactions between aryl groups on the cyclometallating bridging ligands were also observed.

Inspired by the strong face-to-face intermolecular π–π interactions that are known to exist in the 1:1 benzene/ hexafluorobenzene complex, efforts were then turned in Chapter 3 towards suppressing the bridge facilitated non-radiative decay intramolecularly. This was accomplished in complexes **62**–**66** through fluorination of the pendant bridge aryl groups to enhance the intramolecular π–π interactions. Particularly, rigidification through intramolecular π–π interactions leads to a solution Φ_{PL} of 88 ± 5% for complex **67** which features the perfluorinated diarylhydrazide bridge **72c**.

The highly electron-withdrawn nature of **72c** also made it a viable candidate as a bridge to develop the first examples of sky-blue emissive diiridium complexes. A high Φ_{PL} of 69 ± 10% at λ_{max} 460 nm was realised for complex **70** doped into PMMA. While comparison of **66**, **68** and **70** with the bis(trifluoromethyl)hydrazide (**73**)-bridged complexes **67**, **69** and **105** (Chapter 4) indicates that the intramolecular π–π interactions are useful for enhancing quantum yields in the sky-blue region in PMMA films, it is clear that they are less effective at promoting emission in solution as the emission energy is increased – the Φ_{PL} of **66** in solution is 88 ± 5% vs. 2 ± 2% for **70**.

The work in Chapter 4 concentrated on further diversification of the diiridium series to include diarylimidazole cyclometallating ligands. Significantly, complexes **105**–**108** are emissive in the sky-blue region at room temperature and constitute some of the only know examples of highly emissive (Φ_{PL} ≥ 50%) diiridium complexes that are not ppy-based.

Finally, in Chapter 5 intramolecular π–π interactions were investigated on a monoiridium platform through the diastereomeric complexes **132a** and **132b**. The intramolecular π–π interactions influenced their physical properties, enabling facile separation, and were also studied through single crystal X-ray crystallography and variable temperature NMR and photoluminescence

measurements. Their influence on the photophysical properties of **132a** and **132b** appear to be less drastic than for the diiridum complexes presented in Chapters 3 and 4.

To conclude, the work presented in this thesis helps to answer the question of whether non-covalent intramolecular π–π interactions can be of any use to help control the photophysical properties of heavy metal phosphors.

in Chapters 2–4, such interactions are very successful at enhancing emission in diiridium systems, where they rigidify the complexes to cut off a primary non-radiative decay channel which involves a comparatively large amount of molecular motion through a flexible bridging ligand. Particularly, it is shown in this thesis that intramolecular π–π interactions can add an extra dimension to the design of diiridium complexes to more thoroughly utilise their unique structural feature – the bridging ligand.

In Chapter 5, the intramolecular π–π interactions in the monoiridium diastereomers **132a** and **132b** have a less significant effect on their photophysical properties. This is likely related to the fact that the interactions are on the periphery of the complex, outside the emissive 'core', in stark contrast to the case for the diiridium complexes in Chapters 2–4.

Therefore, while they are an exciting way to rigidify complexes and tune their photophysical properties, intramolecular π–π interactions are not an entirely universal strategy to enhance photophysical performance. Consequently, while potentially a powerful tool, there is a need to rationally incorporate intramolecular π–π interactions into phosphors to utilise them to their full potential and obtain the desired effect.

Chapter 7: Experimental data

General

^{1}H, ^{13}C and ^{19}F NMR spectra were recorded on Bruker Avance 400 MHz, Varian Mercury 200, and 400 MHz, Varian Inova 500 MHz or Varian VNMRS 600 and 700 MHz spectrometers. All spectra were either referenced against the residual solvent signal or tetramethylsilane (TMS) and peak shifts are reported in ppm. Where assigned, cyclohexyl protons are labelled 'e' or 'a' to denote equatorial or axial positions, respectively. The labels 'ap. t' and 'bs' denote an apparent triplet and a broad singlet, respectively. For ^{13}C NMR assignment the labels * and # denote 2 and 3 overlapping signals, respectively. Electrospray ionisation (ESI) mass spectra were recorded on a Waters Ltd. TQD spectrometer. Atmospheric solids analysis probe (ASAP) mass spectra were recorded on a LCT premier XE spectrometer. Matrix-assisted laser desorption time-of-flight (MALDI–TOF) mass spectra were recorded on a Bruker Daltonik Autoflex II spectrometer running in positive ion reflectron mode. MALDI–TOF samples were prepared in CH_2Cl_2 (DCM) with *trans*-2-[3-(4-*tert*-butylphenyl)-2-methyl-2-propenylidene]malononitrile (DCTB) as the matrix. Elemental analyses were obtained on an Exeter Analytical Inc. CE-440 elemental analyser. Thermal analysis was run under a helium atmosphere at a rate of 10 °C min^{-1} using a Perkin-Elmer Pyris 1 instrument. Melting points were determined in open ended capillaries using a Stuart Scientific SMP3 melting point apparatus at a ramp rate of 3 °C min^{-1} and are uncorrected. Reactions requiring an inert atmosphere were carried out under argon which was first passed through a phosphorus pentoxide column. For reaction monitoring analytical thin layer chromatography (TLC) was carried out on silica gel (Merck, silica gel 60, F254) or alumina (Merck, neutral alumina 60 type E, F254) plates and visualized using UV light (254, 315, 365 nm). GCMS data were recorded on a Thermo-Finnigan Trace GCMS. Flash chromatography was carried out using either glass columns or a Biotage® Isolera One™ automated flash chromatography machine on 60 micron silica gel purchased from Fluorochem Ltd or type WN-6 neutral activity grade super I alumina purchased from Sigma Aldrich Co. All commercial chemicals were of ≥ 95% purity and were used as received without further purification. All solvents used were of analytical reagent grade or higher. Anhydrous solvents were dried through a HPLC column on an Innovative Technology Inc. solvent purification system or obtained commercially. Infrared spectra were run on solid samples on a Perkin Elmer Frontier spectrometer.

Calculations

All calculations were carried out with the Gaussian 09 package[1] by Daniel Congrave. The molecular orbital (MO) diagrams and orbital contributions were generated with the aid of Gabedit[2] and GaussSum[3] packages, respectively.

Chapters 2–4: All optimized S_0 geometries of the diiridium complexes were carried out using B3LYP[4,5] with the pseudopotential (LANL2DZ)[6–8] for iridium and 3–21G* basis set for all other atoms.[9,10] All S_0 geometries were true minima based on no imaginary frequencies found. Electronic structure calculations were also carried out on the optimised geometries at B3LYP/LANL2DZ:3–21G*.

Chapter 5: All optimized S_0 geometries of the diiridium complexes were carried out using B3LYP[4,5] with the pseudopotential (LANL2DZ)[6–8] for iridium and 6–31G* basis set for all other atoms.[9,10] All S_0 geometries were true minima based on no imaginary frequencies found. Electronic structure calculations were also carried out on the optimised geometries at B3LYP/LANL2DZ:6–31G*.

X-ray crystallography

Single crystals for all complexes were grown by Daniel Congrave. All sample preparation, experiments and the solving of all crystal structures was carried out by Dr Andrei S. Batsanov. Experiments were carried out on a Bruker 3-circle CCD diffractometer D8 Venture with a PHOTON 100 CMOS area detector, using Mo-*K*α radiation (λ=0.71073 Å) from an Incoatec IμS microsource with focusing mirrors. Crystals were cooled to 120 K using a Cryostream 700 (Oxford Cryosystems) open-flow N_2 gas cryostat. Absorption corrections were carried out by numerical integration based on crystal face indexing using the SADABS program[11] or based on the measured crystal shape, or by a semi-empirical method based on Laue equivalents and multiple scans.[12] The structures were solved by Patterson or direct methods using SHELXS software,[12] and refined by full-matrix least squares against F^2 of all data, using OLEX2[13] and SHELXL software.[15]

Electrochemistry

Cyclic voltammetry experiments were recorded using either BAS CV50W electrochemical analyzer or a PalmSens EmStat[2] potentiostat with PSTrace software. Cyclic voltammetry experiments were conducted at a scan rate of 100 mV/s. Experiments were referenced internally to ferrocene. Electrochemical processes are assigned as being electrochemically reversible based on the equal magnitudes of corresponding oxidation and reduction peaks.

Chapter 2: A three-electrode system consisting of a Pt disk (Ø = 1.8 mm) as the working electrode, a Pt wire as an auxiliary electrode and an Pt wire as a quasireference electrode was used. Experiments were conducted in either dry, degassed DCM (oxidations) or dry, degassed 1,2-dimethoxyethane (attempted reductions) solution with *n*-Bu_4NPF_6 (0.1 M) as the supporting electrolyte. Differential pulse voltammetry experiments were recorded using a PalmSens EmStat^2 potentiostat with PSTrace software. Experiments were conducted with step potentials (E step), pulse potentials (E pulse) and pulse times (t Pulse) of 5 mV, 100 mV, and 0.1 s, respectively, at a scan rate of 10 mV/s.

Chapters 3 and 4: A three-electrode system consisting of a glassy carbon disk (Ø = 2.0 mm) as the working electrode, a Pt wire as an auxiliary electrode and an Pt wire as a quasireference electrode was used. Experiments were conducted in dry, degassed DCM (oxidations) or dry, degassed THF (reductions) with *n*-Bu_4NPF_6 (0.1 M) as the supporting electrolyte.

Chapter 5: A three-electrode system consisting of a glassy carbon disk (Ø = 2.0 mm) as the working electrode, a Pt wire as an auxiliary electrode and a Pt wire as a quasireference electrode was used. Experiments were conducted in dry, degassed THF with *n*-Bu_4NPF_6 (0.1 M) as the supporting electrolyte.

Photophysical measurements

Absorption: The absorption spectra were measured on either a Unicam UV2-100 spectrometer operated with the Unicam Vision software or a Thermo Scientific Evolution 220 spectrometer with the Thermo Scientific Insight software in quartz cuvettes with a path length of 10 mm. The pure solvent (DCM or MeCN) was used for the baseline correction. The extinction coefficients were calculated using the Beer-Lambert Law, $A = \varepsilon cl$. They were measured using a titration method, whereby a stock solution of known concentration was incrementally added using a calibrated glass pipette to a cuvette of pure solvent. A minimum of 1 mg of sample was weighed out for the stock solutions, and the measurements were carried out in triplicate to minimise weighing and dilution error.

Solution photoluminescence: The photoluminescence spectra were recorded on a Horiba Jobin Yvon SPEX Fluorolog 3-22 spectrofluorometer in quartz cuvettes with a path length of 10 mm. All solutions were degassed via multiple freeze-pump-thaw cycles using a turbomolecular pump before acquisition of any spectra. For quantum yield measurements the absorption values for the samples were determined on a Unicam UV2-100 spectrometer operated with the Unicam Vision software in quartz cuvettes with a path length of 20 mm. The solution photoluminescence quantum yields

(PLQYs) of all samples were determined in triplicate by the comparative method relative to a literature standard following the literature procedure according to the following Equation 6.1:[16]

$$\Phi_x = \Phi_{Ref} \frac{Grad_x}{Grad_{Ref}} \cdot \left(\frac{\eta_x}{\eta_{Ref}}\right)^2 \quad (6.1)$$

Where "x" and "Ref" denote the material being measured and the reference compound, respectively, Φ represents the PLQY and η is the refractive index of the solvent (0.1 M H_2SO_4 = 1.333, DCM = 1.4242, 2-MeTHF = 1.406). "$Grad$" is the gradient from a plot of the integrated emission intensity (y axis) of a solution vs. $1-(10^{-A})$ (A = the absorbance of the solution). The gradient values were determined from readings on 5–8 samples with absorbance at the excitation wavelength below *ca.* 0.1 (0.2 in a 20 mm path length cuvette). Example plots from excel spreadsheets for FIrpic in DCM and a quinine sulfate standard in 0.5 M H_2SO_4 (Φ = 0.546[17]) are shown in Figure 6.1. They yield gradients of 4.26 × 10^{10} and 3.60 × 10^{10} for the sample and standard, respectively.

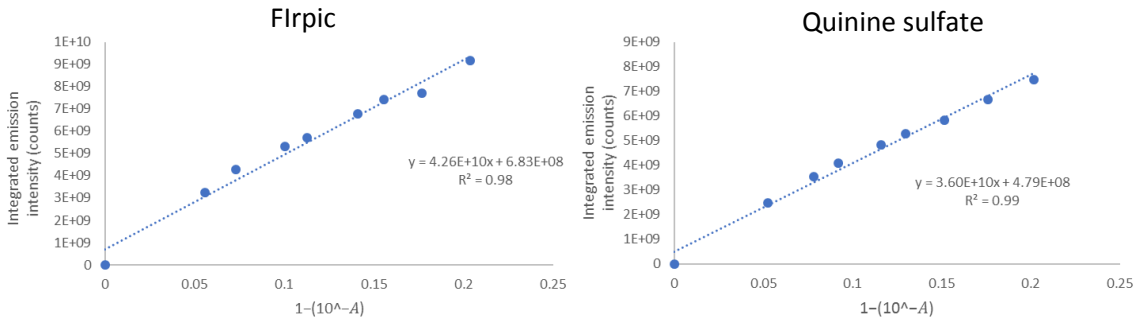

Figure 6.1: Plots of integrated emission intensity vs. $1-(10^{-A})$ for FIrpic in DCM and quinine sulfate in 0.5 M H_2SO_4.

Equation 6.1 with the inputted values is shown below, which yields a PLQY of 0.73 (73%) for FIrpic:

$$\Phi_x = 0.546 \frac{4.26}{3.60} \cdot \left(\frac{1.4242}{1.333}\right)^2$$

The relative standard error of the solution PLQY values was ≤ 5%. The absolute error may be greater. Lifetime measurements were recorded using an N_2 laser (337 nm, 10 µJ, 10 Hz) as an excitation source in a custom spectrometer which produced a 1 kHz train of pulses of 20 ns duration. The luminescence was collected at 90° and focused onto the entrance slit of a monochromator (Bethan TM 300V). The emission was detected by a photon counting PMT and the arrival times of photons at the detector determined using a multichannel scaler. The data were transferred to a PC and analysed using non-linear regression. The decay data were fitted to exponential functions. Low temperature emission spectra and lifetime data were measured in a DN1704 optical cryostat

(Oxford Instruments) with a ITC601 temperature controller (Oxford Instruments). To obtain high temperature emission spectra the sample was heated in a silicone oil bath. A 405 nm laser was focussed on the sample perpendicular to the detector of an Ocean Optics Maya Pro spectrometer. **Chapter 2:** All solution photoluminescence experiments were carried out by Dr Yu-Ting Hsu. The complexes were studied in DCM. Solution PLQYs were determined using *fac*-Irppy$_3$ as a standard, the PLQY of which (Φ = 0.46 in degassed DCM) was determined in-house vs. quinine sulfate in 0.5 M H_2SO_4 (Φ = 0.546[17]). An excitation wavelength of 355 nm was used. **Chapter 3:** All solution photoluminescence experiments were carried out by Dr Yu-Ting Hsu. The complexes were studied in DCM. Solution PLQYs were determined vs. quinine sulfate in 0.5 M H_2SO_4 (Φ = 0.546[17]) as standard. An excitation wavelength of 355 nm was used. **Chapter 5:** All solution photoluminescence experiments were carried out by Daniel Congrave. The complexes were studied in 2-MeTHF. Solution PLQYs were determined vs. quinine sulfate in 0.5 M H_2SO_4 (Φ = 0.546[17]) as standard. An excitation wavelength of 355 nm was used.

PMMA film photoluminescence: All PMMA film photoluminescence experiments were carried out by Daniel Congrave. The quantum yields of complexes doped into PMMA thin films were calculated using an integrating sphere according to the literature method.[18] They were determined in triplicate from three samples that were prepared in parallel. The calculated standard error values were ≤ 10%. The literature method is principally based on the Equation 6.2 below:

$$\Phi_{film} = \frac{Photons\ emitted}{Photons\ absorbed} \tag{6.2}$$

The main issue encountered when measuring PLQYs using an integrating sphere, particularly for a solid sample, is the presence of secondary scattering effects which can add error to the quantification of the emitted and absorbed photons. Such error can be minimised through carrying out measurements on an integrating sphere in the three configurations shown in Figure 6.2.[19]

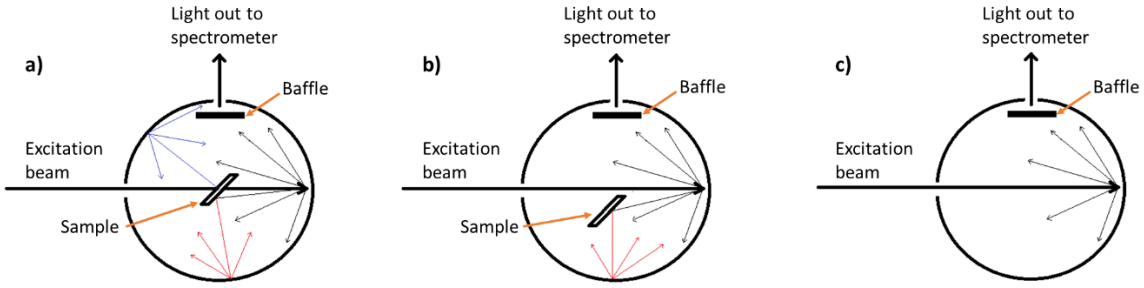

Figure 6.2: Integrating sphere configurations for a PLQY measurement on a solid sample: a) sample in excitation beam; b) sample out of excitation beam; c) empty sphere.

In configuration a) the sample is lined up so that it is the first thing to be struck by the photons of the excitation beam upon entering the sphere. When an excitation photon strikes the sample it can be absorbed before being re-emitted at a probability in accordance with its PLQY (light blue arrows – primary emission). The emitted photons then reflect around the sphere until they leave it and reach the detector. However, the excitation photon may also be transmitted by the sample (either by passing directly through it without being absorbed or via scattering), after which it will strike the side of the sphere and be reflected (thin black arrows). The reflected photon may then either leave the sphere or reflect around the interior of the sphere until it strikes the sample for a second time. At this point it could be absorbed and potentially re-emitted as secondary emission (red arrows), or transmitted again. The Spectralon^{TM} coating of the sphere interior has a transmittance of > 99% across the entire UV-Vis range. Therefore, an excitation photon may cycle around the sphere many times before it either leaves the sphere or is absorbed by the sample. Consequently, the data obtained in configuration a) correspond to not only primary absorption and emission, but also higher order processes. It is necessary to deconvolute the primary absorption and emission processes from the higher order processes, which add error to the quantification of the photons absorbed and emitted by the sample. This is achieved through carrying out experiments in configuration b). In configuration b) the sample is present in the sphere but is not aligned with the excitation beam, therefore, primary absorption and emission is not possible and only higher order processes are observed, i.e. the excitation beam must strike the side of the sphere before the sample. In configuration c) no sample is present to absorb any photons. This configuration is used to determine the maximum number of excitation photons which may reach the detector, i.e. the excitation intensity. The simplified Equation 6.3 (which is essence is the same as Equation 6.2) explains how the data obtained in configurations a), b) and c) can be used to determine the PLQY of the film:

$$\Phi_{film} = \frac{Photons\ emitted_{(a)} - (Film\ transmittance \times Photons\ emitted_{(b)})}{Film\ absorbance \times Excitation\ intensity} \quad (6.3)$$

On the top line of the equation, the film transmittance multiplied by the number of photons emitted in configuration b) quantifies all higher order luminescence in configuration a). Subtracting this from the total luminescence intensity detected in configuration a) allows quantification of the photons that are collected due to primary emission only. On the bottom line the primary absorption can be quantified through multiplying the film absorbance by the excitation intensity measured in configuration c). Equation 6.3 is based on Equations 6.4 and 6.5, which can be used to calculate the PLQY:

$$\Phi_{film} = \frac{E_{(a)} - (1 - A) \times E_{(b)}}{A \times L_{(c)}} \quad (6.4)$$

$$A = \frac{L_{(b)} - L_{(a)}}{L_{(b)}} \quad (6.5)$$

Where $E_{(x)}$ is the integrated luminescence in configuration x) and $L_{(x)}$ is the integrated intensity of the excitation beam which reaches the detector in configuration x). A is the film absorbance.

Lifetime measurements on PMMA films were recorded using an N_2 laser (337 nm, 10 µJ, 10 Hz) as an excitation source in a custom spectrometer which produced a 1 kHz train of pulses of 20 ns duration. The luminescence was collected at 90° and focused onto the entrance slit of a monochromator (Bethan TM 300V). The emission was detected by a photon counting PMT and the arrival times of photons at the detector determined using a multichannel scaler. The data were transferred to a PC and analysed using non-linear regression. The decay data were fitted to exponential functions.

Chapter 2: To prepare the films, 100 µL of a 1 mg mL^{-1} solution of the diiridium complex in DCM was added to 1 mL of a 10 mg mL^{-1} solution of PMMA in *N,N*-dimethylformamide (DMF) and the resulting solution was stirred open to air at room temperature (*ca.* 2 h). The solution was then drop-cast using a Gilson precision pipette onto a 15 x 1 mm circular quartz disk (UQG Optics Ltd., UK) in *ca.* 10 x 50 µL portions, allowing the solvent to evaporate at room temperature under air in between each addition (*ca.* 30 min – 1 h). A final 50 µL portion was then drop-cast onto the quartz disk before it was heated to *ca.* 40 °C overnight on a hot plate under air. Photophysical analysis was then immediately carried out. Data were recorded on a Horiba Jobin Yvon SPEX Fluorolog 3-22 using a custom made integrating sphere.

Chapters 3–5: To prepare the films, an adaptation of the method employed in Chapter 2 was employed. This adaptation was possible due to the improved solubility of the complexes studied in Chapters 3–5 in chlorobenzene (CB) and is experimentally simpler. The PLQY values obtained using films of complexes **64** and *rac* **66** prepared in this manner were the same (within experimental error) as those obtained using the method employed in Chapter 2. 100 µL of a 1 mg mL^{-1} solution of the diiridium complex in DCM was added to 1 mL of a 10 mg mL^{-1} solution of PMMA in CB and the resulting solution was stirred open to air at room temperature (*ca.* 2 h). The solution was then drop-cast using a Gilson precision pipette onto a 10 × 1 mm circular quartz disk (UQG Optics Ltd., UK) in a single 150 µL portion. The substrate was heated to *ca.* 40 °C overnight on a hot plate under air. Photophysical analysis was then immediately carried out. The quantum yields of complexes doped into PMMA thin films were recorded on a Horiba Jobin Yvon SPEX Fluorolog 3 using a calibrated Quanta-Φ integrating sphere – a different integrating sphere to that employed in Chapter 2, which was used in Chapters 3–5 due to timetabling issues. Within experimental error, identical values were obtained when PMMA films of complex **37b** were analysed using either sphere.

Synthetic details for Chapter 2: New diarylhydrazide-bridged diiridium complexes

General

$[Ir(ppy)_2\mu\text{–}Cl]_2$ was synthesized according to a literature procedure.[20] NMR spectra for all novel compounds are included as .pdf files on the USB stick submitted as Supporting Information.

***N*-Phenylpyrazole (39).** This compound was prepared according to a literature procedure.[21]

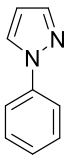

Phenylhydrazine hydrochloride (**45**) (10.0 g, 69.2 mmol, 1.00 eq.), 1,1,3,3-tetraethoxypropane (17.0 mL, 70.9 mmol, 1.02 eq.) and conc. HCl (10.0 mL) were combined in EtOH (250 mL) and refluxed for 5 h. The reaction was cooled to room temperature and the solvent evaporated under reduced pressure. The residue was purified by distillation on a Kugelrohr apparatus (95–115 °C, 0.33 mbar) to obtain *N*-phenylpyrazole (**39**) as a faint oil (9.07 g, 62.9 mmol, 91%). NMR data were in agreement with those previously reported.[22] ^{1}H NMR (400 MHz, $CDCl_3$) δ (ppm) = 7.95 (dd, *J* = 2.6, 0.7 Hz, 1H), 7.78 – 7.68 (m, 3H), 7.51 – 7.45 (m, 2H), 7.31 (tt, *J* = 7.4, 1.2 Hz, 1H), 6.49 (dd, *J* = 2.5, 1.8 Hz, 1H).

***N*-(2,4-Difluorophenyl)pyrazole (40).** This compound was prepared according to a literature procedure.[21] 2,4-difluorophenylhydrazine hydrochloride (**46**) (2.00 g, 11.1 mmol, 1.00 eq.), 1,1,3,3-tetraethoxypropane (2.45 g, 11.1 mmol, 1.00 eq.) and conc. HCl (2.0 mL) were combined in EtOH (20 mL) and refluxed for 2 h. The reaction was cooled to room temperature and the solvent evaporated under reduced pressure. The residue was purified by flash chromatography on silica gel (eluent: DCM with *ca.* 0.5% NEt_3 as additive) to obtain *N*-(2,4-difluorophenyl)pyrazole (**40**) as a faint oil (1.34 g, 7.43 mmol, 67%). NMR data were in agreement with those previously reported.[23] ^{1}H NMR (400 MHz, $CDCl_3$) δ (ppm) = 7.94–7.92 (m, 1H), 7.89 – 7.82 (m, 1H), 7.73 (d, *J* = 1.7 Hz, 1H), 7.03 – 6.96 (m, 1H), 6.48 (dd, *J* = 2.4, 1.9 Hz, 1H); ^{19}F NMR (376 MHz, $CDCl_3$) δ (ppm) = -111.51 – -111.60 (m, 1F), -120.55 – -121.22 (m, 1F).

2-(2-Fluoro-4-methoxyphenyl)pyridine (42). A solution of 2-fluoro-4-methoxyphenylboronic acid (**48**) (960 mg, 5.65 mmol, 1.00 eq.) and 2-bromopyridine (**47**) (0.60 mL, 6.29 mmol, 1.11 eq.) in dioxane (30 mL) was degassed by bubbling with argon via a needle for 30 min. An aqueous solution (4 mL) of Na_2CO_3 (760 mg, 7.17 mmol, 1.27 eq.) was next added, along with $Pd(PPh_3)_4$ (70 mg, 61 µmol, 0.1 eq.). The light yellow mixture was then degassed for a further 10 min, before being heated to 95 °C overnight under argon. The reaction mixture was cooled to room temperature and then the solvent volume was reduced to *ca.* 10 mL under reduced pressure. It was then diluted with water (*ca.* 50 mL) and extracted with DCM (3 × 50 mL). The organic extracts were combined, dried over $MgSO_4$, filtered and evaporated under reduced pressure. The crude oil was purified by distillation on a Kugelrohr apparatus. Traces of 2-bromopyridine (**47**) were distilled first (70–80 °C, *ca.* 0.75 mbar), followed by the target 2-(2-fluoro-4-methoxyphenyl)pyridine (**42**) (110–120 °C, *ca.* 0.75 mbar) as a colourless oil (1.09 g, 5.36 mmol, 95%). NMR data were in agreement with those previously reported.[17] ^{1}H NMR (400 MHz, $CDCl_3$) δ (ppm) = 8.68 (ddd, *J* = 4.9, 1.9, 1.1 Hz, 1H), 7.95 (t, *J* = 8.9 Hz, 1H), 7.76 – 7.72 (m, 1H), 7.69 (td, *J* = 8.0, 7.6, 1.9 Hz, 1H), 7.18 (ddd, *J* = 7.2, 4.9, 1.5 Hz, 1H), 6.82 (ddd, *J* = 8.9, 2.6, 0.7 Hz, 1H), 6.70 (dd, *J* = 13.2, 2.6 Hz, 1H), 3.82 (s, 3H); ^{19}F NMR (376 MHz, $CDCl_3$) δ (ppm) = -114.70 (ddd, *J* = 13.2, 8.9, 2.2 Hz, 1F).

***N*,*N*'-Bis(4-*tert*-butylbenzoyl)hydrazide (43).** 4-*tert*-Butylbenzoic acid (**49**) (12.8 g, 71.8 mmol, 1.00 eq.) was carefully added to thionyl chloride (22 ml, 300 mmol, 4.20 eq.) under an argon atmosphere. Dry DMF (0.5 mL) was then added under stirring. The mixture was heated to reflux for 4 h, at which point residual thionyl chloride and DMF were removed by vacuum distillation (*ca.* 1 mbar, room temp). The residual crude 4-*tert*-butylbenzoyl chloride (**50**) was obtained as a light yellow oil in quantitative yield which was used without further purification.

4-*tert*-Butylbenzoylchloride (**50**) (14.2 g, 72.0 mmol, 2.63 eq.) was added dropwise under an argon atmosphere to pyridine (35 mL), which was cooled in an ice bath to maintain the reaction temperature between 5–10 °C. A yellow suspension immediately formed. Hydrazine monohydrate (1.37 g, 27.4 mmol, 1.00 eq.) was then added dropwise (over *ca.* 30 min), again maintaining the reaction temperature between 5–10 °C. After stirring for 10 min at 5–10 °C the reaction mixture was heated to 90 °C (at which point total dissolution was observed) for 14 h. The resulting orange solution was cooled to room temperature and poured into water (300 mL), leading to the formation of a yellow precipitate. After being left to settle for 1 h, the precipitate was collected via filtration and washed with warm water (750 mL) to yield crude *N*,*N*'-bis(4-*tert*-butylbenzoyl)hydrazide (**43**) as a light yellow powder (9.15 g, 26.0 mmol, 95%). Trituration with boiling ethanol (250 mL) followed by filtration provided material which was pure by ^{1}H NMR as a white powder (6.70 g, 19.0 mmol, 69%). Analytical data were in agreement with those previously reported.[24] ^{1}H NMR (400 MHz, $CDCl_3$) δ (ppm) = 9.29 (bs, 2H), 7.83 (d, *J* = 8.6 Hz, 2H), 7.52 (d, *J* = 8.6 Hz, 2H), 1.37 (s, 18H); M.pt. 283–286 °C (lit. 280–281 °C).

***N*,*N'*-Bis(3,5-bis(trifluoromethyl)benzoyl)hydrazide (44).** Based on a literature procedure for analogs,[25] 3,5-bis(trifluoromethyl)benzoyl chloride (5.00 g, 18.1 mmol, 2.13 eq.) (**51**) was added dropwise under air to a stirred solution of hydrazine monohydrate (425 mg, 8.49 mmol, 1.00 eq.) in ethanol (10 mL), which was cooled in an ice bath to maintain the reaction temperature below 15 °C. A white precipitate formed immediately. Once the addition was half complete, a solution of Na_2CO_3 (954 mg, 9.00 mmol, 1.06 eq.) in water (10 mL) was added dropwise alongside the remaining 3,5-bis(trifluoromethyl)benzoyl chloride. After the addition of the reagents was completed (*ca.* 20 min), the ice bath was removed and stirring was continued at room temperature for a further 30 min. The reaction mixture was poured into water (50 mL), allowed to settle for 1 h and filtered to collect crude **44** as a white powder (4.35 g, 8.50 mmol, 100%), containing *ca.* 10 mol% of residual mono-acylated intermediate (tentatively identified by ^{1}H NMR). Analytically pure **44** was obtained via recrystallization from 5:1 v/v ethanol/ *n*-hexane mixture (60 mL) as white needles (3.91 g, 7.63 mmol, 90%). ^{1}H NMR (400 MHz, DMSO-d_6) δ (ppm) = 11.31 (s, 2H), 8.59 (s, 4H), 8.45 (s, 2H); ^{13}C NMR (101 MHz, DMSO-d_6) δ 163.3 ($C_{C=O}$), 134.7, 131.3 (q, ^{2}J = 33.4 Hz, C_{quart}), 128.8, 126.3, 123.5 (q, ^{1}J = 273.0 Hz, C_{CF3}); ^{19}F NMR (376 MHz, DMSO-d_6) δ (ppm) = -61.3 (s, 6F); MS (ASAP): *m/z* 513.0 [MH^+]. Calcd. for $C_{18}H_8F_{12}N_2O_2H^+$: 513.0; Anal. Calcd. for $C_{18}H_8F_{12}N_2O_2$: C, 42.21; H, 1.57; N, 5.47. Found: C, 42.16; H, 1.57; N, 5.57.

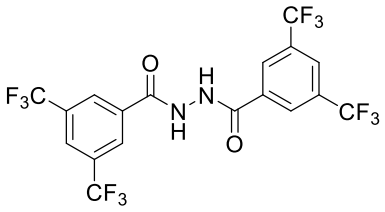

General procedure for the synthesis of the diiridium complexes 35–38. $IrCl_3 \cdot 3H_2O$ (1.00 eq.) and the cyclometallating ligand (2.20 eq.) were added to 2-ethoxyethanol (5 mL per 200 mg $IrCl_3 \cdot 3H_2O$) and the mixture was heated to reflux under an argon atmosphere for 24 h to form the dichloro-bridged diiridium intermediate *in situ*. The reaction mixture was then cooled to room temperature before addition of the bridging ligand (0.50 eq.) and K_2CO_3 (5.00 eq.). The mixture was then heated at reflux for a further 24 h before being cooled to room temperature and diluted with water (*ca*. 70 mL per 200 mg $IrCl_3 \cdot 3H_2O$) to yield a colored precipitate, which was isolated via filtration and washed with water (2 × 50 mL). The NMR assignment and ring nomenclature used for the complexes is discussed for **36b** as a representative example in Chapter 2.

Complexes 35a + b. Following the general procedure, $IrCl_3 \cdot 3H_2O$ (400 mg, 1.13 mmol, 1.00 eq.), *N*-phenylpyrazole (**39**) (360 mg, 2.50 mmol, 2.21 eq.), *N*,*N*'-bis(4-*tert*-butylbenzoyl)hydrazide (**43**) (200 mg, 0.57 mmol, 0.50 eq.) and K_2CO_3 (780 mg, 5.64 mmol, 4.99 eq.) gave a brown precipitate. The isolated solid was triturated with boiling *n*-hexane (500 mL). The hexane insoluble material was passed through a neutral alumina plug (eluent: DCM sat. K_2CO_3) and purified by fractional crystallization via liquid diffusion from saturated DCM solutions layered with *n*-hexane. This yielded the *meso* isomer (**35a**) as pale green crystals (172 mg, 0.12 mmol, 21%). ^{1}H NMR (700 MHz, $CDCl_3$) δ (ppm) = 7.97 (d, *J* = 2.8 Hz, $2H_{A3}$), 7.94 (d, *J* = 2.8 Hz, $2H_{A5}$), 7.90 (d, *J* = 2.9 Hz, $2H_{B3}$), 7.60 (d, *J* = 2.9 Hz, $2H_{B5}$), 6.94 (d, *J* = 7.8 Hz, $2H_{B8}$), 6.77 (t, *J* = 2.8 Hz, $2H_{A4}$), 6.72 (d, *J* = 7.8 Hz, $2H_{A8}$), 6.63 (t, *J* = 7.8 Hz, $2H_{B9}$), 6.58 (d, *J* = 8.1 Hz, $4H_{C3}$), 6.53 (t, *J* = 2.9 Hz, $2H_{B4}$), 6.45 (t, *J* = 7.8 Hz, $4H_{A9/B10}$), 6.38 (d, *J* = 8.1 Hz, $4H_{C2}$), 6.13 (t, *J* = 7.8 Hz, $2H_{A10}$), 5.98 (dd, *J* = 7.8, 1.3 Hz, $2H_{B11}$), 5.54 (d, *J* = 7.8 Hz $2H_{A11}$), 1.10 (s, $18H_{t\text{-}Bu}$); MS (MALDI–TOF): *m/z* 1308.4 [M^+]. Calcd. for $C_{58}H_{54}Ir_2N_{10}O_2^+$: 1308.4; Anal. Calcd. for $C_{58}H_{54}Ir_2N_{10}O_2$: C, 53.28; H, 4.16; N, 10.71. Found: C, 53.19; H, 4.15; N, 10.69. The filtrate from the trituration was mixed with celite (*ca.* 2 g) under reduced pressure and subjected to flash chromatography on silica gel (eluent: gradient *n*-hexane/ DCM sat. K_2CO_3 1:0–1:9 v/v) to yield the crude *rac* isomer (**35b**), which eluted before residual traces of the *meso* isomer. Trituration with hot methanol followed by filtration gave **35b** as a pale green powder (90 mg, 0.07 mmol, 12%). ^{1}H NMR (700 MHz, $CDCl_3$) δ (ppm) = 8.02 (dd, *J* = 2.9, 0.7 Hz, $2H_{C3}$), 8.01 (dd, *J* = 3.0, 0.7 Hz, $2H_{A3}$), 7.75 (dd, *J* = 2.1, 0.7 Hz, $2H_{A5}$), 7.37 (dd, *J* = 2.1, 0.7 Hz, $2H_{C5}$), 7.03 (dd, *J* = 7.9, 1.1 Hz, $2H_{B3}$), 6.85 (dd, *J* = 7.8, 1.2 Hz, $2H_{D3}$), 6.69 (ddd, *J* = 7.9, 7.2, 1.3 Hz, $2H_{B4}$), 6.65 – 6.57 (m, $12H_{A4,\ C4,\ E2,\ E3}$), 6.49 – 6.45 (m, $4H_{D4,\ B5}$), 6.03 (td, *J* = 7.4, 1.2 Hz, $2H_{D5}$), 5.98 (dd, *J* = 7.6, 1.3 Hz, $2H_{B6}$), 5.32 (dd, *J* = 7.4, 1.3 Hz, $2H_{D6}$),

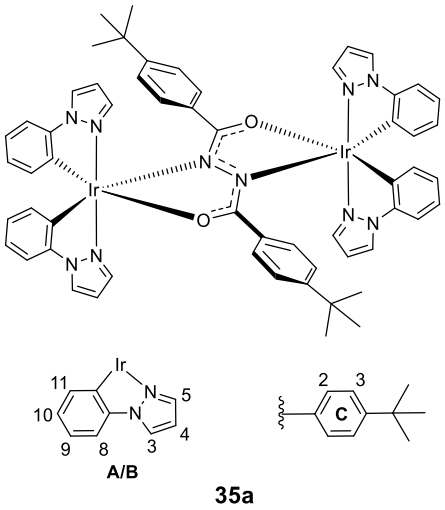

35a

1.10 (s, 18$H_{t\text{-Bu}}$); ^{13}C NMR (176 MHz, $CDCl_3$) δ (ppm) = 176.1 ($C_{C=O}$), 149.4 (C_{E1}), 143.5 (C_{B1}), 142.4 (C_{D1}), 137.7 (C_{A5}), 136.6 (C_{C5}), 134.4 (C_{B6}), 133.6 (C_{D6}), 133.4 (C_{E4}), 133.3 (C_{B2}), 133.0 (C_{D2}), 126.6 (C_{A3}), 125.5 (C_{E2}), 125.2 (C_{D5}), 124.6 (C_{C3}), 123.9 (C_{E3}), 121.2 (C_{B4}), 119.4 (C_{D4}), 110.3 (C_{B3}), 109.6 (C_{D3}), 106.6 (C_{A4}), 106.3 (C_{C4}), 34.2 ($C_{t\text{-Bu quart}}$), 31.2 ($C_{t\text{-Bu Me}}$); MS (MALDI–TOF): *m/z* 1308.4 [M^+]. Calcd. for $C_{58}H_{54}Ir_2N_{10}O_2^+$: 1308.4; Anal. Calcd. for $C_{58}H_{54}Ir_2N_{10}O_2$: C, 53.28; H, 4.16; N, 10.71. Found: C, 53.56; H, 4.36; N, 10.49.

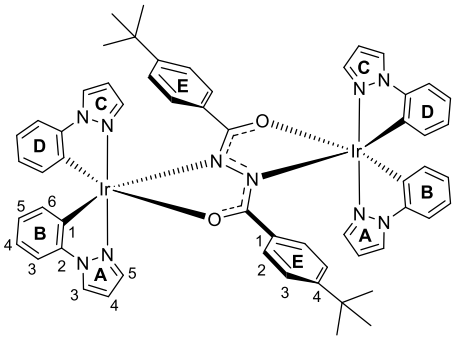

35b

Solutions sufficiently concentrated to obtain a ^{13}C NMR spectrum and determine C^N ligand orientation with respect to the bridge could not be obtained for **35a** due to its low solubility in organic solvents.

Complexes 36a + b. Following the general procedure, $IrCl_3 \cdot 3H_2O$ (340 mg, 0.96 mmol, 1.00 eq.), *N*-(2,4-difluorophenyl)pyrazole (**40**) (380 mg, 2.11 mmol, 2.20 eq.), *N*,*N*′-bis(4-*tert*-butylbenzoyl)hydrazide (**43**) (170 mg, 0.48 mmol, 0.50 eq.) and K_2CO_3 (665 mg, 4.81 mmol, 5.01 eq.) gave an off-white precipitate. The isolated solid was triturated with boiling *n*-hexane (300 mL). The hexane insoluble material was passed through a neutral alumina plug (eluent: DCM sat. K_2CO_3) and purified by fractional crystallization via liquid diffusion from saturated DCM solutions layered with *n*-hexane. This yielded the *meso* isomer (**36a**) as white crystals (130 mg, 0.09 mmol, 19%).

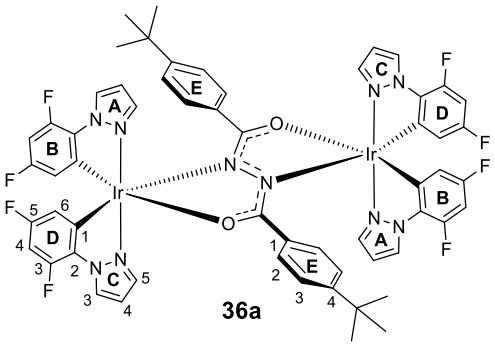

36a

^{1}H NMR (700 MHz, $CDCl_3$) δ (ppm) = 8.31 (d, *J* = 2.9 Hz, 2H_{A3}), 8.22 (d, *J* = 3.0 Hz, 2H_{C3}), 7.92 (d, *J* = 2.2 Hz, 2H_{A5}), 7.54 (d, *J* = 2.2 Hz, 2H_{C5}), 6.86 (dd, *J* = 2.9, 2.2 Hz, 2H_{A4}), 6.78 (d, *J* = 8.7 Hz, 4H_{E3}), 6.60 (dd, *J* = 3.0, 2.2 Hz, 2H_{C4}), 6.39 (d, *J* = 8.7 Hz, 4H_{E2}), 6.29 (ddd, *J* = 11.5, 8.6, 2.5 Hz, 2H_{D4}), 6.07 (ddd, *J* = 11.4, 8.6, 2.5 Hz, 2H_{B4}), 5.40 (dd, *J* = 8.5, 2.5 Hz, 2H_{D6}), 5.00 (dd, *J* = 8.7, 2.5 Hz, 2H_{B6}), 1.14 (s, 18$H_{t\text{-Bu}}$); ^{13}C NMR (176 MHz, $CDCl_3$) δ (ppm) = 176.7 ($C_{C=O}$), 159.6 (dd, *J* = 250.00, 10.51 Hz, C_{D5}), 159.0 (dd, *J* = 248.64, 11.28 Hz, C_{B5}) 150.2 (C_{E1}), 148.6 (dd, *J* = 253.03, 12.73 Hz, C_{D3}), 148.0 (dd, *J* = 251.38, 13.68 Hz, C_{B3}), 136.9 (C_{C5}), 136.2 (C_{A5}), 132.4 (C_{E4}), 130.6 (d, *J* = 15.0 Hz, C_{C3}), 130.2 (d, *J* = 14.6 Hz, C_{A3}), 127.5 (C_{D2}), 126.5 (C_{B2}), 126.03 (C_{E2}), 124.00 (C_{E3}), 115.8 (d, *J* = 18.8 Hz, C_{D1}), 115.2 (d, *J* = 18.7 Hz, C_{B1}), 107.4 (d, *J* = 2.5 Hz, C_{A4}), 107.3 (d, *J* = 2.5 Hz, C_{C4}), 97.8 (dd, *J* = 28.2, 23.4 Hz, C_{D4}), 96.4 (dd, *J* = 28.1, 23.0 Hz, C_{B4}), 34.3 ($C_{t\text{-Bu quart}}$), 31.0 ($C_{t\text{-Bu Me}}$); ^{19}F NMR (376 MHz, $CDCl_3$) δ -114.5 – -114.4 (m, 4F), -125.8 (dd, *J* = 12.0, 5.5 Hz, 2F), -126.01 (dd, *J* = 11.9, 5.3 Hz, 2F); MS (MALDI–TOF):

m/z 1452.3 [M^+]. Calcd. for $C_{58}H_{46}F_8Ir_2N_{10}O_2^+$: 1452.3; Anal. Calcd. for $C_{58}H_{46}F_8Ir_2N_{10}O_2$: C, 47.99; H, 3.19; N, 9.65. Found: C, 47.92; H, 3.20; N, 9.62. The filtrate from the trituration was mixed with celite (*ca.* 2 g) under reduced pressure and subjected to flash chromatography on silica gel (eluent: gradient *n*-hexane/DCM sat. K_2CO_3 1:0–2:3 v/v) to yield the crude *rac* isomer (**36b**), which eluted before residual traces of the *meso* isomer. Trituration with hot methanol followed by filtration gave **36b** as a white powder (105 mg, 0.07 mmol, 15%) ^{1}H NMR (700 MHz, $CDCl_3$) δ (ppm) = 8.33 (d, *J* = 3.0 Hz, $2H_{A3}$), 8.32 (d, *J* = 2.9 Hz, $2H_{C3}$), 7.76 (dd, *J* = 2.1, 0.7 Hz, $2H_{A5}$), 7.32 (dd, *J* = 2.2, 0.6 Hz, $2H_{C5}$), 6.81 (d, *J* = 8.4 Hz, $4H_{E3}$), 6.72 (dd, *J* = 3.0, 2.1 Hz, $2H_{A4}$), 6.67 (dd, *J* = 2.9, 2.2 Hz, $2H_{C4}$), 6.58 (d, *J* = 8.4 Hz, $4H_{E2}$), 6.33 (ddd, *J* = 11.5, 8.6, 2.5 Hz, $2H_{B4}$), 6.07 (ddd, *J* = 11.4, 8.6, 2.5 Hz, $2H_{D4}$), 5.42 (dd, *J* = 8.4, 2.5 Hz, $2H_{B6}$), 4.81 (dd, *J* = 8.8, 2.5 Hz, $2H_{D6}$), 1.14 (s, $18H_{t\text{-Bu}}$); ^{13}C NMR (176 MHz, $CDCl_3$) δ (ppm) = 176.4 ($C_{C=O}$), 159.6 (dd, *J* = 250.83, 11.15 Hz, C_{B5}), 158.8 (dd, *J* = 247.73, 12.08 Hz, C_{D5}), 150.7 (C_{E1}), 148.6 (dd, *J* = 251.19, 11.51 Hz, C_{B3}), 148.0 (dd, *J* = 251.19, 13.10 Hz, C_{D3}), 138.1 (C_{B1}), 137.1 (C_{D1}), 137.3 (C_{A5}), 136.3 (C_{C5}), 132.5 (C_{E4}), 130.7 (d, *J* = 14.9 Hz, C_{A3}), 129.9 (d, *J* = 14.9 Hz, C_{C3}), 127.5 (C_{B2}), 126.6 (C_{D2}), 126.5 (C_{E2}), 124.1 (C_{E3}), 116.0 (d, *J* = 19.5 Hz, C_{B6}), 115.1 (d, *J* = 20.3 Hz, C_{D6}), 107.6 (d, *J* = 2.5 Hz, C_{A4}), 107.1 (d, *J* = 2.5 Hz, C_{C4}), 97.8 (dd, *J* = 27.9, 23.4 Hz, C_{B4}), 96.3 (dd, *J* = 28.2, 23.3 Hz, C_{D4}), 34.3 ($C_{t\text{-Bu quart}}$), 31.0 ($C_{t\text{-Bu Me}}$); ^{19}F NMR (376 MHz, $CDCl_3$) δ (ppm) = -114.3 – -114.2 (m, 4F), -125.8 (dd, *J* = 12.0, 5.5 Hz, 2F), -126.8 (dd, *J* = 12.0, 5.2 Hz, 2F); MS (MALDI–TOF): *m/z* 1452.3 [M^+]. Calcd. for $C_{58}H_{46}F_8Ir_2N_{10}O_2^+$: 1452.3; Anal. Calcd. for $C_{58}H_{46}F_8Ir_2N_{10}O_2$: C, 47.99; H, 3.19; N, 9.65, Calcd. for $C_{58}H_{46}F_8Ir_2N_{10}O_2 \cdot 0.1C_6H_{14}$ (C_6H_{14} is observed in ^{1}H NMR): C, 48.20; H, 3.27; N, 9.59. Found: C, 48.44; H, 3.35; N, 9.46.

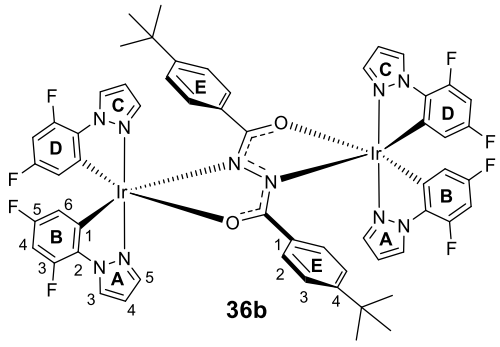

36b

Complexes 37a + b. Following the general procedure, $IrCl_3 \cdot 3H_2O$ (200 mg, 0.57 mmol, 1.00 eq.), 2-(2-fluoro-4-methoxyphenyl)pyridine (**42**) (255 mg, 1.25 mmol, 2.19 eq.), *N*,*N*'-bis(4-*tert*-butylbenzoyl)hydrazide (**43**) (100 mg, 0.28 mmol, 0.50 eq.) and K_2CO_3 (390 mg, 2.82 mmol, 4.95 eq.) gave a yellow precipitate. The isolated solid was extracted into DCM sat. K_2CO_3 (*ca.* 100 mL) and suspended onto celite (*ca.* 2 g) under reduced pressure. The residue was purified via flash chromatography on silica gel (eluent: gradient *n*-hexane/ DCM sat. K_2CO_3 1:0–3:7 v/v). First to elute was the *rac* isomer (**37b**), followed by the *meso* isomer (**37a**). Final purification by trituration with hot methanol gave the diastereomers as yellow powders:

meso **37a**: (90 mg, 0.06 mmol, 20%). ^{1}H NMR (700 MHz, $CDCl_3$) δ (ppm) = 9.00 (d, *J* = 5.3 Hz, $2H_{A6/C6}$), 8.75 (d, *J* = 5.3 Hz, $2H_{A6/C6}$), 8.10 – 8.06 (m, $4H_{A3/C3}$), 7.84 (t, *J* = 7.6 Hz, $2H_{A4/C4}$), 7.67 (t, *J* = 7.9 Hz, $2H_{A4/C4}$), 7.30 (t, *J* = 6.7 Hz, $2H_{A5/C5}$), 6.88 (t, *J* = 6.7 Hz, $2H_{A5/C5}$), 6.70 (d, *J* = 7.9 Hz, $4H_{E3}$), 6.35 (d, *J* = 7.9 Hz, $4H_{E2}$), 6.01 (dd, *J* = 14.5, 2.3 Hz, $2H_{B4}$), 5.81 (dd, *J* = 14.2, 2.3 Hz, $2H_{D4}$), 5.29 (d, *J* = 2.3 Hz, $2H_{B6}$), 5.08 (d, *J* = 2.3 Hz, $2H_{D6}$), 3.42 (s, $6H_{MeO\ B}$), 3.38 (s, $6H_{MeO\ D}$), 1.16 (s, $18H_{t\text{-}Bu}$); ^{19}F NMR (376 MHz, $CDCl_3$) δ (ppm) = -112.8 (d, *J* = 16.9 Hz, 2F), -113.3 (d, *J* = 16.5 Hz, 2F); MS (MALDI–TOF): *m/z* 1544.4 [M^+]. Calcd. for $C_{70}H_{62}F_4Ir_2N_6O_6^+$: 1544.4; Anal. Calcd. for $C_{70}H_{62}F_4Ir_2N_6O_6$: C, 54.46; H, 4.05; N, 5.44. Found: C, 54.56; H, 4.15; N, 5.33.

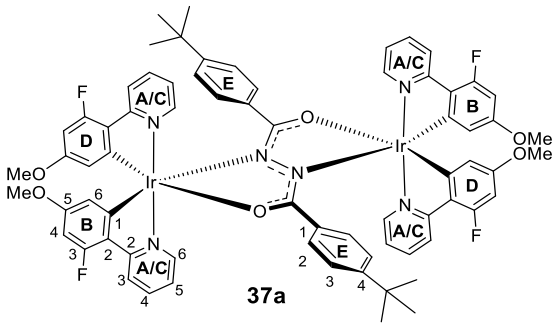

rac **37b**: (58 mg, 0.04 mmol, 13%). ^{1}H NMR (700 MHz, $CDCl_3$) δ (ppm) = 9.17 (dd, *J* = 5.2, 1.3 Hz, $2H_{A6}$), 8.24 (d, *J* = 5.4 Hz, $2H_{C6}$), 8.13 (d, *J* = 8.5 Hz, $2H_{A3}$), 7.98 (d, *J* = 8.4 Hz, $2H_{C3}$), 7.77 (td, *J* = 8.5, 1.3 Hz, $2H_{A4}$), 7.74 – 7.71 (m, $2H_{C4}$), 7.21 (ddd, *J* = 8.5, 5.2, 1.4 Hz, $2H_{A5}$), 6.93 (ddd, *J* = 8.4, 5.4, 1.4 Hz, $2H_{C5}$), 6.67 (d, *J* = 8.4 Hz, $4H_{E3}$), 6.47 (d, *J* = 8.4 Hz, $4H_{E2}$), 5.98 (dd, *J* = 14.3, 2.3 Hz, $2H_{B4}$), 5.78 (dd, *J* = 14.0, 2.3 Hz, $2H_{D4}$), 5.21 (d, *J* = 2.3 Hz, $2H_{B6}$), 5.05 (d, *J* = 2.3 Hz, $2H_{D6}$), 3.38 (s, $6H_{MeO\text{-}B}$), 3.36 (s, $6H_{MeO\text{-}D}$), 1.12 (s, $18H_{t\text{-}Bu\ Me}$); ^{13}C NMR (176 MHz, $CDCl_3$) δ (ppm) = 176.2 ($C_{C=O}$), 166.9 (d, *J* = 6.85 Hz, C_{A2}), 166.4 (d, *J* = 5.68 Hz, C_{C2}), 161.6 (d, *J* = 255.91 Hz, C_{B3}), 161.2 (d, *J* = 256.71 Hz, C_{D3}), 160.8 (d, *J* = 11.28 Hz, C_{D5}), 160.1 (d, *J* = 11.82 Hz, C_{B5}), 149.7 (C_{E1}), 148.9 (C_{A6}), 147.5 (C_{C6}), 137.2 (C_{A4}), 136.4 (C_{C4}), 132.4 (C_{E4}), 126.6 (C_{E2}), 124.5 (d, *J* = 4.85 Hz, C_{B1}), 123.6 (C_{E3}), 123.5 (d, *J* = 4.85 Hz, C_{D1}), 122.5 (d, *J* = 17.65 Hz, C_{A3}), 121.4 (d, *J* = 18.69 Hz, C_{C3}), 120.0 (C_{A5}), 119.5 (C_{C5}), 112.9 (C_{B6}), 111.6 (C_{D6}), 95.0 (d, *J* = 27.69 Hz, C_{B4}), 94.1 (d, *J* = 26.31 Hz, C_{D4}), 54.7 ($C_{OMe\text{-}D}$), 54.4 ($C_{OMe\text{-}B}$), 34.2 ($C_{t\text{-}Bu\ quart}$), 31.0 ($C_{t\text{-}Bu\ Me}$); ^{19}F NMR (376 MHz, $CDCl_3$) δ (ppm) = -112.7 (d, *J* = 14.5 Hz, 2F), -113.1 (d, *J* = 14.2 Hz, 2F); MS (MALDI–TOF): *m/z* 1544.4 [M^+]. Calcd. for $C_{70}H_{62}F_4Ir_2N_6O_6^+$: 1544.4; Anal. Calcd. for $C_{70}H_{62}F_4Ir_2N_6O_6$: C, 54.46; H, 4.05; N, 5.44. Found: C, 54.35; H, 4.22; N, 5.12.

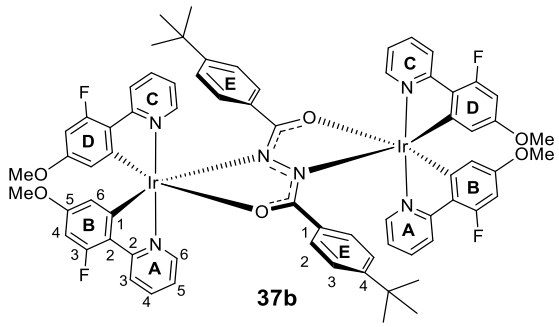

Solutions sufficiently concentrated to obtain a ^{13}C NMR spectrum and determine ligand pyridine–phenyl connectivity could not be obtained for **37a** due to its low solubility in organic solvents.

Complexes 38a + b. Following a modification of the general procedure starting directly from the

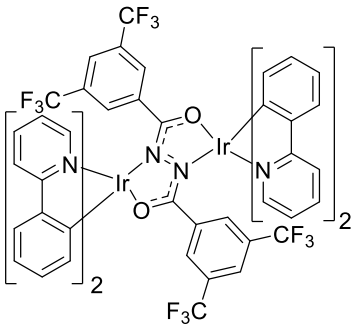

dichloro-bridged intermediate $[Ir(ppy)_2\mu–Cl]_2$ (400 mg, 0.37 mmol, 1.00 eq.) *N*,*N*'-bis(3,5-bis(trifluoromethyl)benzoyl)hydrazide (**44**) (191 mg, 0.37 mmol, 1.00 eq.) and K_2CO_3 (258 mg, 1.87 mmol, 5.00 eq.) a yellow precipitate was obtained. The isolated solid was then extracted into DCM sat. K_2CO_3 (*ca.* 100 mL) and mixed with celite (*ca.* 2 g) under reduced pressure. The residue was purified via flash chromatography on silica gel (eluent: *n*-hexane/ DCM sat. K_2CO_3 1:1) and both diastereomers were collected as a single fraction. After evaporation of the solvent under reduced pressure, the yellow residue was refluxed in toluene (*ca.* 600 mL) for 10 min before being filtered hot through a glass sinter. The filtrate was then reduced in volume by *ca.* 50 mL and filtered again while hot. This process of reducing the volume by 50 mL followed by hot filtration was repeated a further two times before all of the isolated solids were combined and washed with pentane to afford the *meso* isomer (**38a**) (78 mg, 0.05 mmol, 14%) as a yellow powder. ^{1}H NMR (700 MHz, CD_2Cl_2) δ (ppm) = 9.01 (dd, *J* = 5.5, 1.3 Hz, $2H_{A6}$), 8.76 (dd, *J* = 5.6 Hz, $2H_{B6}$), 7.98 – 7.94 (m, $2H_{A4}$), 7.84 – 7.78 (m, $6H_{A3,B3.B4}$), 7.53 (ddd, *J* = 7.2, 5.5, 1.4 Hz, $2H_{A5}$), 7.47 (bs, $2H_{C2\,or\,6}$), 7.43 (dd, *J* = 7.0, 1.3 Hz, $2H_{B9}$), 7.27 (s, $2H_{C4}$), 7.16 – 7.09 (m, $4H_{A9,B5}$), 6.75 (t, *J* = 7.0 Hz, $2H_{B10}$), 6.59 (ddd, *J* = 8.2, 7.0, 1.3 Hz, $2H_{B11}$), 6.48 (td, *J* = 7.7, 1.2 Hz, $2H_{A10}$), 6.30 (t, *J* = 7.7 Hz, $2H_{A11}$), 6.01 (bs, $2H_{C2\,or\,6}$), 5.92 (dd, *J* = 8.2, 1.2 Hz, $2H_{B12}$), 5.85 (dd, *J* = 7.7, 1.2 Hz, $2H_{A12}$); ^{19}F NMR (376 MHz, CD_2Cl_2) δ (ppm) = -63.07 (bs, 6F), -63.18 (bs, 6F); MS (MALDI–TOF): *m/z* 1512.2 [M^+]. Calcd. for $C_{62}H_{38}F_{12}Ir_2N_6O_2^+$: 1512.2; Anal. Calcd. for $C_{62}H_{38}F_{12}Ir_2N_6O_2$: C, 49.27; H, 2.53; N, 5.56. Found: C, 49.04; H, 2.55; N, 5.47. The filtrate from the hot filtrations was mixed with celite (*ca.* 2 g) under reduced pressure before being subjected to flash chromatography on silica gel (eluent: gradient *n*-hexane/ DCM sat. K_2CO_3 1:0–1:1 v/v) to yield the crude *rac* isomer (**38b**), which eluted before residual *meso* isomer. The residue was triturated with boiling methanol (*ca.* 5 mL) and the resulting suspension was cooled in a fridge before being filtered and washed with pentane to afford **38b** as a yellow powder (56 mg, 0.04 mmol, 10%). ^{1}H NMR (700 MHz, CD_2Cl_2) δ (ppm) = 9.24 (dd, *J* = 5.5, 1.4 Hz, $2H_{A6}$), 8.28 (d, 5.2 Hz, $2H_{B6}$), 7.96 – 7.91 (m, $4H_{A4,B4}$), 7.89 (d, *J* = 8.3 Hz, $2H_{A3}$), 7.75 (d, *J* = 8.1 Hz, $2H_{B3}$), 7.50 (ddd, *J* = 7.3, 5.5, 1.5 Hz, $2H_{A5}$), 7.47 (d, *J* = 7.7 Hz, $2H_{A9}$), 7.28 – 7.25 (m, $4H_{B5,C4}$), 7.09 (dd, *J* = 7.7, 1.3 Hz, $2H_{B9}$), 7.08 (bs, $2H_{C2\,or\,6}$), 6.81 (bs, $2H_{C2\,or\,6}$), 6.76 (t, *J* = 7.7 Hz, $2H_{A10}$), 6.58 (t, *J* = 7.7 Hz, $2H_{A11}$), 6.50 (t, *J* = 7.7 Hz, $2H_{B10}$), 6.36 (t, *J* = 7.7 Hz, $2H_{B11}$), 5.90 (dd, *J* = 7.7, 1.2 Hz, $2H_{A12}$), 5.85 (dd, *J* = 7.7, 1.1 Hz, $2H_{B12}$); ^{19}F NMR (376 MHz, CD_2Cl_2) δ (ppm) = -62.8 (bs, 6F), -63.2 (bs, 6F); MS (MALDI–TOF): *m/z* 1512.2 [M^+]. Calcd. for

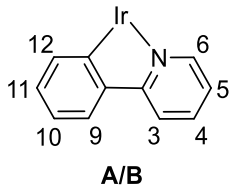

A/B

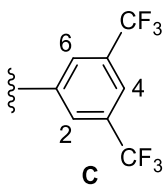

C

$C_{62}H_{38}F_{12}Ir_2N_6O_2^+$: 1512.2; Anal. Calcd. for $C_{62}H_{38}F_{12}Ir_2N_6O_2$: C, 49.27; H, 2.53; N, 5.56. Found: C, 48.94; H, 2.65; N, 5.43.

Solutions sufficiently concentrated to obtain a ^{13}C NMR spectrum could not be obtained for either complex due to low solubility in organic solvents.

Synthetic details for Chapter 3: Intramolecular π–π stacking and sky-blue emission in diarylhydrazide-bridged diiridium complexes

General

$[Ir(ppy)_2\mu\text{–}Cl]_2$[20] and 4-(2,4,6-trimethylphenyl)-2-chloropyridine[26] (**78**) were synthesised according to literature procedures. Some of the new diarylhydrazide bridges (**72b** and **72d**) could not be obtained analytically pure to ^1H NMR, even after repeated recrystallisation attempts. In such cases they were found to be sufficiently pure for the synthesis of the corresponding diiridium complexes. NMR spectra for all novel compounds are included as .pdf files on the USB stick submitted as Supporting Information.

***N*,*N*′-Bis(3,5-difluorobenzoyl)hydrazide (72a).** 3,5-Difluorobenzoyl chloride (**71a**) (5.00 g, 28.3 mmol, 2.10 eq.) was added dropwise under air to a stirred solution of hydrazine monohydrate (675 mg, 13.5 mmol, 1.00 eq.) in ethanol (10 mL), which was cooled in an ice bath to maintain the reaction temperature below 15 °C. Formation of a white precipitate was immediately observed. Once the addition was half complete, a further 30 mL of cold ethanol was added to facilitate stirring before a solution of Na_2CO_3 (1.50 g, 14.2 mmol, 1.05 eq.) in water (10 mL) was added dropwise alongside the remaining difluorobenzoyl chloride (**71a**). After the addition of the reagents was completed (*ca.* 20 min), the ice bath was removed and stirring was continued at room temperature for a further 30 min. The reaction mixture was poured into water (50 mL), allowed to settle for 1 h and filtered to collect the crude hydrazide as a white powder which was subsequently refluxed in ethanol (100 mL) for 10 min. The mixture was cooled to room temperature and then filtered to obtain *N*,*N*′-bis(3,5-difluorobenzoyl)hydrazide (**72a**) (3.19 g, 10.2 mmol, 76%). M.pt. 285–290 °C; ^1H NMR (400 MHz, DMSO-d_6) δ (ppm) = 10.84 (s, $2H_{N–H}$), 7.73 – 7.44 (m, $6H_{2+4}$); ^{13}C NMR (101 MHz, DMSO-d_6) δ (ppm) = 163.7 (t, J = 2.9 Hz, $C_{C=O}$), 162.8 (dd, J = 247.7, 12.7 Hz, C_3), 136.1 (t, J = 8.7 Hz, C_1), 111.7 – 111.2 (m, C_2), 108.1 (t, J = 25.9 Hz, C_4); $^{19}F\{^1H\}$ NMR (376 MHz, DMSO-d_6) δ (ppm) = -108.3 (s, 4F); HRMS (ASAP): *m/z* 313.0607 [MH^+]. Calcd. for $C_{14}H_9N_2O_2F_4^+$: 313.0600.

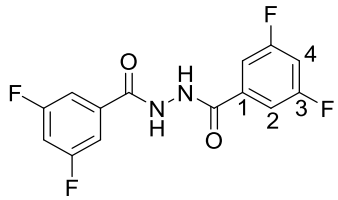

***N*,*N'*-Bis(2,3,5,6-tetrafluorobenzoyl)hydrazide (72b)** 2,3,5,6-Tetrafluorobenzoyl chloride (**71b**)

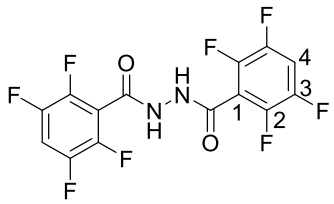

(5.00 g, 23.5 mmol, 2.13 eq.) was added dropwise under air to a stirred solution of hydrazine monohydrate (553 mg, 11.0 mmol, 1.00 eq.) in ethanol (10 mL), which was cooled in an ice bath to maintain the reaction temperature below 15 °C. Formation of a white precipitate was immediately observed. Once the addition was half complete, a solution of Na_2CO_3 (1.24 g, 11.7 mmol, 1.06 eq.) in water (10 mL) was added dropwise alongside the remaining 2,3,5,6-tetrafluorobenzoyl chloride (**71b**). After the addition of the reagents was completed (*ca.* 20 min), the ice bath was removed and stirring was continued at room temperature for a further 30 min. The reaction mixture was poured into water (50 mL), allowed to settle for 1 h and filtered to collect the crude hydrazide as a white powder (5.30 g, 13.8 mmol, 125%). The crude material was recrystallised twice from methanol/water and was obtained sufficiently pure for use in the next step (2.95 g, 7.68 mmol, 70%). M.pt. 265–269 °C; ^{1}H NMR (400 MHz, DMSO-d_6) δ (ppm) = 11.36 (s, $2H_{N–H}$), 8.22 – 8.01 (m, $2H_4$); ^{13}C NMR (101 MHz, DMSO-d_6) δ (ppm) = 156.7 ($C_{C=O}$), 147.2 – 141.8 (m, C_{2+3}), 115.8 (t, J = 20.5 Hz, $C_{1\text{ or }4}$), 109.3 (t, J = 23.5 Hz, $C_{1\text{ or }4}$); ^{19}F {^{1}H} NMR (376 MHz, DMSO-d_6) δ (ppm) = -137.9 – -138.1 (m, 4F), -141.5 – -141.6 (m, 4F); HRMS (ASAP): *m/z* 385.0224 [MH^+]. Calcd. for $C_{14}H_5N_2O_2F_8^+$: 385.0223.

***N*,*N'*-Bis(pentafluorobenzoyl)hydrazide (72c).** Pentafluorobenzoyl chloride (**71c**) (5.00 g, 21.7

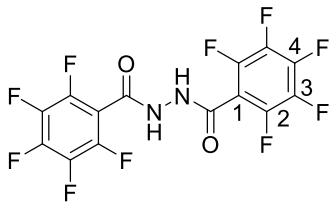

mmol, 2.13 eq.) was cautiously added dropwise under air to a stirred solution of hydrazine monohydrate (510 mg, 10.2 mmol, 1.00 eq.) in ethanol (10 mL), which was cooled in an ice bath to maintain the reaction temperature below 15 °C. Formation of a white precipitate was immediately observed. Once the addition was half complete, a further 20 mL of cold ethanol was added to facilitate stirring before a solution of Na_2CO_3 (1.15 g, 10.85 mmol, 1.06 eq.) in water (8 mL) was added dropwise alongside the remaining pentafluorobenzoyl chloride (**71c**). After the addition of the reagents was completed (*ca.* 20 min), the ice bath was removed and stirring was continued at room temperature for a further 30 min. The reaction mixture was poured into water (50 mL), allowed to settle for 1 h and filtered to collect the crude hydrazide as a white powder (3.58 g, 8.57 mmol, 84%). The crude material was recrystallised twice from methanol/water and was obtained sufficiently pure for use in the next step (2.36 g, 5.61 mmol, 55%). M.pt. 264–266 °C (lit. 270 °C[27]); ^{1}H NMR (400 MHz, DMSO-d_6) δ (ppm) = 11.41 (s, $2H_{N–H}$); ^{13}C NMR (101 MHz, DMSO-d_6) δ (ppm) = 156.0 ($C_{C=O}$), 145.4 – 136.0 (m, $C_{2–4}$), 110.5 (t, J = 21.3 Hz, C_1); ^{19}F{^{1}H} NMR (376 MHz, DMSO-d_6) δ (ppm) = -140.8 – -141.0 (m, $2F_{2\text{ or }3}$), -150.9 (t, J = 22.3 Hz, $1F_4$), -160.6 – -160.8 (m, $2F_{2\text{ or }3}$); HRMS (ASAP): *m/z* 421.0035 [MH^+]. Calcd. for $C_{14}H_3N_2O_2F_{10}^+$: 421.0035.

***N,N'*-Bis(2,3,5,6-tetrafluoro-4-methoxybenzoyl)hydrazide (72d).** 2,3,5,6-Tetrafluoro-4-methoxybenzoic acid (**71d**) (1.00 g, 4.46 mmol, 1.00 eq.) was heated to reflux in $SOCl_2$ (5 mL) with a drop of *N,N*-dimethylformamide overnight under argon. The solvent was then evaporated to obtain crude 2,3,5,6-tetrafluoro-4-methoxybenzoyl chloride which was dissolved in dry chloroform (30 mL). Hydrazine monohydrate (0.1 mL, 2.09 mmol, 0.47 eq.) was added dropwise to the chloroform solution which was cooled in an ice bath to maintain the reaction temperature below 15 °C. Formation of a white precipitate was immediately observed. After the addition was completed (*ca.* 10 min), the ice bath was removed and the mixture was heated to reflux for 2 h. It was then diluted with *n*-hexane (50 mL), allowed to settle for 1 h and filtered to collect the crude hydrazide as a white powder (650 mg, 1.46 mmol, 70% based on hydrazine monohydrate). The crude material was recrystallised from ethanol and was obtained sufficiently pure for use in the next step (260 mg, 0.59 mmol, 28% based on hydrazine monohydrate). M.pt. 252–256 °C; ^{1}H NMR (400 MHz, DMSO-d_6) δ (ppm) = 11.18 (s, $2H_{N–H}$), 4.14 (s, $6H_{OMe}$); ^{13}C NMR (101 MHz, DMSO-d_6) δ (ppm) = 156.7 ($C_{C=O}$), 145.3 – 139.0 (m, $C_{1–3}$), 108.3 (t, *J* = 21 Hz, C_4), 62.8 (C_{OMe}); ^{19}F {^{1}H} NMR (376 MHz, DMSO-d_6) δ (ppm) = -142.4 – -142.5 (m, 4F), -156.9 – -157.2 (m, 4F); HRMS (ASAP): *m/z* 445.0422 [MH^+]. Calcd. for $C_{16}H_9N_2O_4F_8^+$: 445.0435.

Bis(trifluoromethyl)hydrazide (73). Hydrazine monohydrate (2.5 mL, 51.5 mmol, 1.00 eq.) was added to dry chloroform (10 mL) under argon and cooled in an ice water bath to *ca.* 0 °C. Trifluoroacetic anhydride (21.8 mL, 155 mmol, 3.00 eq.) was then cautiously added to the mixture over the course of 1 h. A white precipitate immediately formed during the addition. Once approximately half had been added, further dry chloroform (10 mL) was added to facilitate stirring. Once the addition was complete, the mixture was refluxed under argon for 1 h, before being cooled to room temperature and filtered. The white precipitate was washed with hexane (*ca.* 50 mL) to obtain bis(trifluoromethyl)hydrazide (**73**) as a white powder (9.6 g, 43 mmol, 83%). NMR data were in agreement with those previously reported.[28] ^{1}H NMR (400 MHz, Acetone-d_6) δ (ppm) = 10.00 – 11.00 (bs, 2H); ^{19}F {^{1}H} NMR (376 MHz, Acetone-d_6) δ (ppm) = -75.82 (s, 6F).

2-Phenyl-4-(2,4,6-trimethylphenyl)pyridine (74). 4-(2,4,6-Trimethylphenyl)-2-chloropyridine

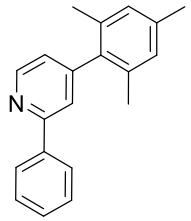

(3.36 g, 14.5 mmol, 1.00 eq.)(**78**), phenyl boronic acid (2.65 g, 21.7 mmol, 1.50 eq.) and PPh_3 (912 mg, 3.48 mmol, 24 mol%) were combined in 1,4-dioxane (45 mL). A solution of Na_2CO_3 (6.14 g, 57.9 mmol, 4.00 eq.) in water (10 mL) was then added and the mixture was degassed for 30 min. $Pd(OAc)_2$ (195 mg, 0.87 mmol, 6 mol%) was then added and the mixture was degassed for a further 10 minutes, before being heated to reflux under argon overnight. The mixture was then allowed to cool to room temperature and evaporated to near-dryness. To the residue was added water (50 mL) and DCM (50 mL). The organic layer was separated and the aqueous later was extracted thrice more with DCM (50 mL). The organic extracts were combined, dried over $MgSO_4$ and evaporated under reduced pressure. The residue was passed through a short column of silica gel (eluent: EtOAc with *ca.* 0.5% vol. NEt_3 as an additive) before being purified by distillation on a Kugelrohr apparatus (200 °C, *ca.* 9×10^{-2} mbar) to afford 2-phenyl-4-(2,4,6-trimethylphenyl)pyridine (**74**) as a faint yellow viscous oil (3.15 g, 11,52 mmol, 80%). NMR data were in agreement with those previously reported.[29] ^{1}H NMR (400 MHz, $CDCl_3$) δ (ppm) = 8.77 (dd, *J* = 5.0, 0.9 Hz, 1H), 8.09 – 8.01 (m, 2H), 7.60 (dd, *J* = 1.5, 0.9 Hz, 1H), 7.55 – 7.43 (m, 3H), 7.09 (dd, *J* = 5.0, 1.5 Hz, 1H), 7.01 (d, *J* = 0.7 Hz, 2H), 2.38 (s, 3H), 2.08 (s, 6H).

Tetrakis(2-phenyl-4-(2,4,6-trimethylphenyl)-pyridine-*C*^{2},*N*')(μ-dichloro)diiridium ([Ir(mesppy)$_2$μ-Cl]$_2$). $IrCl_3 \cdot 3H_2O$ (689 mg, 1.95 mmol, 1.00 eq.) and 2-phenyl-4(2,4,6-trimethylphenyl)-pyridine (**74**)

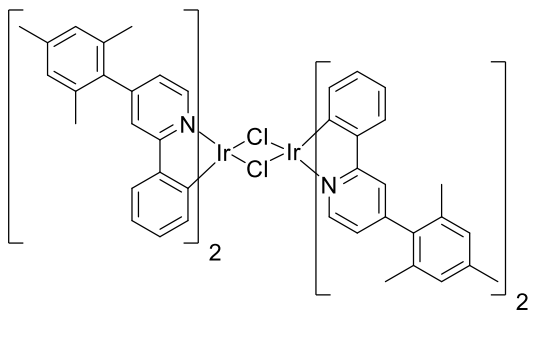

(1.18 g, 4.32 mmol, 2.21 eq.) were added to a mixture of 2-ethoxyethanol (30 mL) and water (10 mL) and heated to reflux under an argon atmosphere for 24 h. The reaction mixture was then cooled to room temperature and poured into water (*ca.* 200 mL) and cooled in a fridge for 1 h. The formed yellow precipitate was then isolated via filtration and washed sequentially with water (*ca.* 50 mL), cold methanol (5 mL), cold *n*-hexane (3 × 20 mL) and cold *n*-pentane (3 × 20 mL) to afford tetrakis(2-phenyl-4-(2,4,6-trimethylphenyl)-pyridine-*C*^{2},*N*')(μ-dichloro)diiridium (**[Ir(mesppy)$_2$μ-Cl]$_2$**). as a yellow powder (1.42 g, 0.92 mmol, 94%). NMR data were in agreement with those previously reported.[29] ^{1}H NMR (400 MHz, CD_2Cl_2) δ (ppm) = 9.70 (d, *J* = 5.9 Hz, 2H), 7.77 (d, *J* = 1.9 Hz, 2H), 7.54 (dd, *J* = 7.9, 1.4 Hz, 2H), 7.05 (d, *J* = 10.9 Hz, 4H), 6.89 – 6.82 (m, 4H), 6.71 (td, *J* = 7.9, 1.4 Hz, 2H), 5.95 (dd, *J* = 7.9, 1.1 Hz, 2H), 2.42 (s, 6H), 2.16 (s, 6H), 2.15 (s, 6H).

2-Bromo-5-(methylcyclohexyloxy)-*meta*-xylene (82). 2-Bromo-4-hydroxy-*meta*-xylene (**81**) (15.00 g, 74.6 mmol, 1.00 eq.) and K_2CO_3 (20.6 g, 149 mmol, 2.00 eq.) were combined in *N,N*-dimethylformamide (100 mL) and heated to 80 °C for 10 min under argon. Bromo(methylcyclohexane) (15.6 mL, 112 mmol, 1.50 eq.) was then added in a single portion and the mixture was heated to 90 °C overnight. The reaction mixture was cooled to room temperature and poured into water (1 L). The mixture was extracted with EtOAc/ toluene 1:1 v/v (3 × 200 mL). The organic layers were combined and washed with $HCl_{(aq)}$ (1 M, 5 × 50 mL) before being dried over $MgSO_4$ and evaporated under reduced pressure to afford a brown oil. The residue was purified via flash chromatography on silica gel (eluent: *n*-hexane). 2-Bromo-5-(methylcyclohexyloxy)-*meta*-xylene (**82**) eluted as a clear oil (21.7 g, 73.0 mmol, 98%). ^{1}H NMR (400 MHz, $CDCl_3$) δ (ppm) = 6.66 (s, 2H), 3.72 (d, *J* = 6.4 Hz, 2H), 2.40 (s, 6H), 1.93 – 1.67 (m, 6H), 1.39 – 1.17 (m, 3H), 1.05 (qd, *J* = 12.2, 3.4 Hz, 2H); ^{13}C NMR (101 MHz, $CDCl_3$) δ (ppm) = 157.8, 139.0, 117.9, 114.4, 73.6, 37.7, 29.9, 26.5, 25.8, 24.0; HRMS (ASAP): *m/z* 296.0779 [M^+]. Calcd. for $C_{15}H_{21}OBr^+$: 296.0776.

2-Tributylstannyl-5-(methylcyclohexyloxy)-*meta*-xylene (83). 2-Bromo-5-(methylcyclohexyloxy)-*meta*-xylene (**82**) (10.5 g, 33.6 mmol, 1.00 eq.) was dissolved in dry THF (250 mL) and cooled to –78 °C under argon. *t*-BuLi (1.7 M in pentane, 27 mL, 74.8 mmol, 2.22 eq.) was then added over 15 min, keeping the reaction temperature below –65 °C. The thick yellow mixture was then stirred at –78 °C for 45 min before the addition of tributyltin chloride (11.2 mL, 41.2 mmol, 1.23 eq.) over 5 min. The reaction was then warmed to room temperature overnight before being poured into hexane (200 mL). The mixture was washed with sat. $NH_4Cl_{(aq)}$ (3 × 50 mL) before being dried over $MgSO_4$, and the solvent removed under reduced pressure to afford 2-tributylstannyl-5-(methylcyclohexyloxy)-*meta*-xylene (**83**) as a pale yellow oil (17.0 g, 33.5 mmol, 100%) which was used without further purification. ^{1}H NMR (400 MHz, $CDCl_3$) δ (ppm) = 6.59 (s + (d, $^4J_{H–Sn}$ = 11.7 Hz), 2H), 3.74 (d, *J* = 6.3 Hz, 2H), 2.38 (s + (d, $^4J_{H–Sn}$ = 5.5 Hz), 6H), the aliphatic region (*ca.* 0.5–2 ppm) was not assigned due to the presence of alkyl tin impurities; HRMS (ASAP): *m/z* 505.2808 [MH^+]. Calcd. for $C_{27}H_{49}O^{116}Sn^+$: 505.2801.

2-Chloro-4-(2,6-dimethyl-4-(methylcyclohexyloxy)phenyl)pyridine (85). 2-Chloro-4-iodopyridine

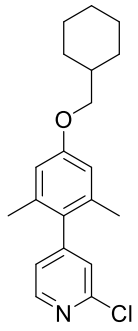

(3.00 g, 12.5 mmol, 1.00 eq.) (**84**), 2-tributylstannyl-5-(methylcyclohexyloxy)-*meta*-xylene (**83**) (8.74 g, 17.2 mmol, 1.38 eq.) and tri-*tert*-butylphosphonium tetrafluoroborate (218 mg, 0.75 mmol, 6 mol%) were added to dry dioxane (50 mL) and the resulting mixture was degassed for 40 min. Pd_2dba_3•$CHCl_3$ (388 mg, 0.37 mmol, 3 mol%) was then added to the mixture, which was degassed for a further 10 min before the addition of CsF (4.18 g, 27.5 mmol, 2.20 eq.). The red reaction mixture was subsequently stirred at room temperature for 2.5 h. Analysis of an aliquot by GC-MS at this point indicated that the desired reaction had not occurred. Further Pd_2dba_3•$CHCl_3$ (130 mg, 0.12 mmol, 1 mol%) and tri-*tert*-butylphosphonium tetrafluoroborate (73 mg, 0.25 mmol, 2 mol%) were added and the mixture was heated to 60 °C for 17 h, after which point analysis of an aliquot by GC-MS revealed complete consumption of 2-chloro-4-iodopyridine. The reaction mixture was cooled to room temperature, diluted with EtOAc (*ca.* 50 mL) and filtered through a plug of celite, which was subsequently washed with further EtOAc (2 × 50 mL). The combined filtrates were evaporated under reduced pressure and the residual crude product was purified via flash chromatography on silica gel (eluent: gradient EtOAc/ *n*-hexane 0:1–1:9 v/v with *ca.* 0.5% vol. NEt_3 as an additive) to obtain 2-chloro-4-(2,6-dimethyl-4-(methylcyclohexyloxy)phenyl)pyridine (**85**) as a brown oil (3.67 g, 11.1 mmol, 89%). Further purification by distillation on a Kugelrohr apparatus (*ca.* 110 °C, 0.1 mbar) afforded a colourless viscous oil which solidified upon standing (2.96 g, 8.97 mmol, 72%). M.pt. 72–75 °C; ^{1}H NMR (400 MHz, $CDCl_3$) δ (ppm) = 8.45 (dd, *J* = 5.0, 0.8 Hz, 1H), 7.18 (dd, *J* = 1.5, 0.8 Hz, 1H), 7.06 (dd, *J* = 5.0, 1.5 Hz, 1H), 6.68 (s, 2H), 3.78 (d, *J* = 6.4 Hz, 2H), 1.93 – 1.70 (m, 6H), 1.41 – 1.19 (m, 3H), 1.15 – 1.02 (m, 2H); ^{13}C NMR (101 MHz, $CDCl_3$) δ (ppm) = 159.0, 152.8, 151.8, 149.7, 136.5, 125.5, 124.1, 113.6, 73.4, 37.8, 29.9, 26.6, 25.8, 20.9; HRMS (ESI): *m/z* 330.1628 [MH^+]. Calcd. for $C_{20}H_{25}NOCl^+$: 330.1625.

2-(2,4-Difluorophenyl)-4-(2,6-dimethyl-4-(methylcyclohexyloxy)phenyl)pyridine (75). 2-Chloro-

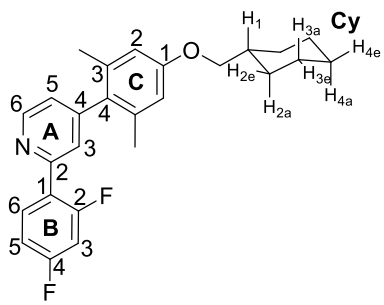

4-(2,6-dimethyl-4-(methylcyclohexyloxy)phenyl)pyridine (**85**) (617 g, 1.87 mmol, 1.00 eq.), 2,4-difluorophenyl boronic acid (443 mg, 2.81 mmol, 1.50 eq.) and PPh_3 (20.5 mg, 0.45 mmol, 24 mol%) were combined in 1,4-dioxane (6 mL). A solution of Na_2CO_3 (795 mg, 7.48 mmol, 4.00 eq.) in water (2 mL) was then added and the mixture was degassed for 15 min. $Pd(OAc)_2$ (20.5 mg, 0.11 mmol, 6 mol%) was then added and the mixture was degassed for a further 5 minutes, before being heated to reflux under argon overnight. The mixture was then allowed to cool to room temperature and evaporated to near-dryness. To the residue was added water (30 mL) and DCM

(40 mL). The organic layer was separated and the aqueous later was extracted twice more with DCM (40 mL). The organic extracts were combined, dried over $MgSO_4$ and evaporated under reduced pressure. The residue was purified by flash chromatography on silica gel (eluent: gradient EtOAc/ *n*- hexane 1:99–1:9 v/v with *ca.* 0.5% vol. NEt_3 as an additive). 2-(2,4-Difluorophenyl)-4-(2,6-dimethyl-4-(methylcyclohexyloxy)phenyl)pyridine (**75**) was obtained as a white tacky solid (678 g, 1.66 mmol, 90%). M.pt. 117–118 °C; ^{1}H NMR (600 MHz, $CDCl_3$) δ (ppm) = 8.74 (dd, *J* = 5.0, 0.9 Hz, $1H_{A6}$), 8.07 (td, *J* = 8.8, 6.6 Hz, $1H_{B6}$), 7.57 (dd, *J* = 1.5, 0.9 Hz, $1H_{A3}$), 7.07 (dd, *J* = 5.0, 1.5 Hz, $1H_{A5}$), 7.02 (dddd, *J* = 8.8, 6.6, 2.6, 1.4 Hz, $1H_{B5}$), 6.90 (ddd, *J* = 11.3, 8.8, 2.6 Hz, $1H_{B3}$), 6.68 (s, $2H_{C2}$), 3.77 (d, *J* = 6.4 Hz, $2H_{CH2Cy}$), 2.06 (s, $6H_{CMe}$), 1.92 – 1.85 (m, $2H_{CyH2e}$), 1.85 – 1.81 (m, $1H_{CyH1}$), 1.77 (dt, *J* = 13.0, 3.4 Hz, $2H_{CyH3e}$), 1.74 – 1.68 (m, $1H_{CyH4e}$), 1.32 (qt, *J* = 12.7, 3.4 Hz, $2H_{CyH3a}$), 1.22 (qt, *J* = 12.7, 3.4 Hz, $1H_{CyH4a}$), 1.07 (qd, *J* = 12.7, 3.4 Hz, $2H_{CyH2a}$); ^{13}C NMR (151 MHz, $CDCl_3$) δ (ppm) = 163.2 (dd, *J* = 250.9, 12.0 Hz, C_{B4}), 160.6 (dd, *J* = 252.8, 12.0 Hz, C_{B2}), 158.7 (C_{C1}), 152.6 (d, *J* = 2.6 Hz, C_{A2}), 149.9 (C_{A4}), 149.8 (C_{A6}), 136.7 (C_{C3}), 132.2 (dd, *J* = 9.7, 4.4 Hz, C_{B6}), 131.4 (C_{C4}), 125.7 (d, *J* = 9.4 Hz, C_{A3}), 123.9 (C_{A5}), 123.9 (dd, *J* = 12.0, 3,9 Hz, C_{B1}), 113.5 (C_{C2}), 111.9 (dd, *J* = 21.1, 3.6 Hz, C_{B5}), 104.4 (dd, *J* = 27.0, 25.3 Hz, C_{B3}), 73.4 (C_{CH2}), 37.7 (C_{Cy1}), 29.9 (C_{Cy2}), 26.5 (C_{Cy4}), 25.8 (C_{Cy3}), 21.0 (C_{Me}); ^{19}F {^{1}H} NMR (376 MHz, $CDCl_3$) δ (ppm) = -109.2 – -109.5 (m, 1F), -112.7 – - 112.8 (m, 1F); HRMS (ESI): *m/z* 408.2128 [MH^+]. Calcd. for $C_{26}H_{28}NOF_2^+$: 408.2139.

4-(Methylcyclohexyloxy)-2-chloropyridine (80). 2-Chloro-4-pyridone (**79**) (5.00 g, 38.6 mmol, 1.00 eq.) and K_2CO_3 (10.7 g, 77.2 mmol, 2.00 eq.) were combined in *N,N*-dimethylformamide (50 mL) and heated to 80 °C for 10 min under argon. Bromo(methylcyclohexane) (8.1 mL, 57.9 mmol, 1.50 eq.) was then added in a single portion and the mixture was heated to 90 °C for a further 4 h. The reaction mixture was cooled to room temperature and poured into water (200 mL). The mixture was extracted with EtOAc/ toluene 1:1 v/v (4 × 100 mL). The organic layers were combined and washed with $HCl_{(aq)}$ (1 M, 5 × 50 mL) before being dried over $MgSO_4$ and evaporated under reduced pressure to afford a brown oil. The residue was purified via flash chromatography on silica gel (eluent: EtOAc/ *n*-hexane 3:7 v/v) to obtain 4-(methylcyclohexyloxy)-2-chloropyridine (**80**) as a waxy white solid (7.55 g, 33.4 mmol, 87%). M.pt. 54–55 °C; ^{1}H NMR (400 MHz, $CDCl_3$) δ (ppm) = 8.19 (d, *J* = 5.8 Hz, 1H), 6.84 (d, *J* = 2.3 Hz, 1H), 6.75 (dd, *J* = 5.8, 2.3 Hz, 1H), 3.81 (d, *J* = 6.1 Hz, 2H), 1.93 – 1.59 (m, 6H), 1.40 – 1.15 (m, 3H), 1.14 – 0.99 (m, 2H); ^{13}C NMR (101 MHz, $CDCl_3$) δ (ppm) = 167.0, 152.5, 150.1, 110.1, 109.9, 73.9, 37.3, 29.7, 26.3, 25.7; HRMS (ESI): *m/z* 226.1001 [MH^+]. Calcd. for $C_{12}H_{17}NOCl^+$: 226.0999.

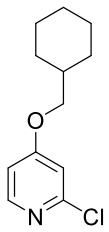

2-(2,4-Difluorophenyl)-4-(methylcyclohexyloxy)pyridine (76). 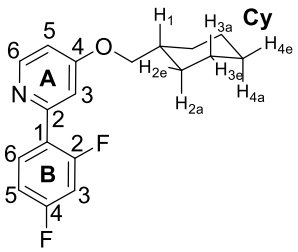

4-(Methylcyclohexyloxy)-2-chloropyridine (**80**) (2.00 g, 8.86 mmol, 1.00 eq.), 2,4-difluorophenyl boronic acid (2.10 g, 13.29 mmol, 1.50 eq.) and PPh_3 (558 mg, 2.13 mmol, 24 mol%) were combined in 1,4-dioxane (32 mL). A solution of Na_2CO_3 (3.76 g, 35.4 mmol, 4.00 eq.) in water (12 mL) was then added and the mixture was degassed for 30 min. $Pd(OAc)_2$ (120 mg, 0.53 mmol, 6 mol%) was then added and the mixture was degassed for a further 10 min, before being heated to reflux under argon overnight. The mixture was then allowed to cool to room temperature and evaporated to near-dryness. To the residue was added water (50 mL) and DCM (50 mL). The organic layer was separated and the aqueous later was extracted twice more with DCM (50 mL). The organic extracts were combined, dried over $MgSO_4$ and evaporated under reduced pressure. The residue was purified by flash chromatography on silica gel (eluent: EtOAc/ *n*- hexane 4:6 v/v with *ca.* 0.5% vol. NEt_3 as an additive). 2-(2,4-Difluorophenyl)-4-(methylcyclohexyloxy)pyridine (**76**) was obtained as a faint yellow oil which solidified on standing (2.68 g, 8.83 mmol, 100%). M.pt. 66–68 °C; ^{1}H NMR (600 MHz, $CDCl_3$) δ (ppm) = 8.49 (d, *J* = 5.7 Hz, $1H_{A6}$), 7.97 (td, *J* = 7.8, 6.6 Hz, $1H_{B6}$), 7.24 (ap. t, *J* = 2.4 Hz, $1H_{A3}$), 6.98 (tdd, *J* = 7.8, 2.5, 1.0 Hz, $1H_{B5}$), 6.90 (ddd, *J* = 11.3, 8.8, 2.5 Hz, $1H_{B3}$), 6.77 (dd, *J* = 5.7, 2.4 Hz, $1H_{A5}$), 3.84 (d, *J* = 6.3 Hz, $2H_{CH2Cy}$), 1.89 – 1.85 (m, $2H_{CyH2e}$), 1.84 – 1.81 (m, $1H_{CyH1}$), 1.78 (dt, *J* = 12.9, 3.4 Hz, $2H_{CyH3e}$), 1.73 – 1.69 (m, $1H_{CyH4e}$), 1.31 (qt, *J* = 12.7, 3.4 Hz, $2H_{CyH3a}$), 1.21 (qt, *J* = 12.7, 3.4 Hz, $1H_{CyH4a}$), 1.07 (qd, *J* = 12.7, 3.4 Hz, $2H_{CyH2a}$); ^{13}C NMR (151 MHz, $CDCl_3$) δ (ppm) = 165.7 (C_{A4}), 163.08 (dd, *J* = 250.7, 12.1 Hz, C_{B4}), 160.45 (dd, *J* = 252.4, 11.9 Hz, C_{B2}), 153.9 (d, *J* = 2.4 Hz, C_{A2}), 150.7 (C_{A6}), 132.1 (dd, *J* = 9.6, 4.5 Hz, C_{B6}), 123.9 (dd, *J* = 11.6, 3.8 Hz, C_{B1}), 111.7 (dd, *J* = 21.0, 3.7 Hz, C_{B5}), 110.9 (d, *J* = 9.1 Hz, C_{A3}), 109.0 (C_{A5}), 104.3 (dd, *J* = 27.1, 25.3 Hz, C_{B3}), 73.4 (C_{CH2}), 37.4 (C_{Cy1}), 29.8 (C_{Cy2}), 26.4 (C_{Cy4}), 25.7 (C_{Cy3}); ^{19}F{^{1}H} NMR (376 MHz, $CDCl_3$) δ (ppm) = -109.4 (d, *J* = 8.5 Hz, 1F), -112.7 (d, *J* = 8.5 Hz, 1F); HRMS (ESI): *m/z* 304.1517 [MH^+]. Calcd. for $C_{18}H_{20}NOF_2^+$: 304.1513.

Complex 62. *N*,*N*'-Bis(3,5-difluorobenzoyl)hydrazide (**72a**) (87 mg, 0.28 mmol, 1.00 eq.), $[Ir(ppy)_2\mu\text{-}Cl]_2$ (300 mg, 0.28 mmol, 1.00 eq.) and K_2CO_3 (116 mg, 0.84 mmol, 3.00 eq.) were added to 2-ethoxyethanol (15 mL) under and argon atmosphere and heated to reflux overnight. The reaction mixture was then cooled to room temperature and the solvent was removed under reduced pressure. The residue was then dissolved in DCM and suspended onto celite (*ca.* 2 g) under reduced pressure, before being subjected to flash chromatography on silica gel (eluent: gradient *n*-hexane/ DCM sat. K_2CO_3 3:7 – 0:1). The yellow band was collected and after

removing the solvent under reduced pressure, the residue was dissolved in a minimal amount of DCM (*ca*. 20 mL). Addition of methanol (*ca*. 20 mL) followed by reducing the volume of the mixture to 20 mL afforded complex **62** (275 mg, 0.21 mmol, 75%) as a yellow precipitate which was isolated via filtration and washed sequentially with methanol followed by pentane. The isolated product was a mixture of diastereomers in a *ca.* 9:1 ratio. MS (MALDI–TOF): *m/z* 1312.2 [M^+]. Calcd. for $C_{58}H_{38}F_4Ir_2N_6O_2^+$: 1312.2; Anal. Calcd. for $C_{58}H_{38}F_4Ir_2N_6O_2$: C, 53.12; H, 2.92; N, 6.41, Calcd. for $C_{58}H_{38}F_4Ir_2N_6O_2 \cdot 0.2CH_2Cl_2$: C, 52.62; H, 2.91; N, 6.33. Found: C, 52.62; H, 2.95; N, 6.27.;

Major diastereomer: ^{1}H NMR (600 MHz, CD_2Cl_2, TMS) δ (ppm) = 9.00 (ddd, *J* = 5.7, 1.6, 0.8 Hz, $2H_A$), 8.70 (dt, *J* = 5.7, 1.2 Hz, $2H_B$), 8.02 – 7.89 (m, $4H_{2A}$), 7.85 – 7.76 (m, $4H_{2B}$), 7.54 – 7.45 (m, $4H_{A,D}$), 7.36 (dd, *J* = 7.8, 1.4 Hz, $2H_C$), 7.10 (ddd, *J* = 6.7, 5.7, 2.2 Hz, $2H_B$), 6.80 (td, *J* = 7.5, 1.3 Hz, $2H_D$), 6.68 – 6.58 (m, $4H_{C,D}$), 6.41 (td, *J* = 7.8, 1.4 Hz, $2H_C$), 6.17 (tt, *J* = 9.1, 2.4 Hz, $2H_{E2}$), 6.07 – 6.00 (m, $2H_D$), 5.91 (dd, *J* = 7.8, 1.4 Hz, $2H_C$), 5.88 (s, $4H_{E4}$); ^{19}F {^{1}H} NMR (376 MHz, CD_2Cl_2) δ (ppm) = -110.65 (s, 2F).

Due to poor solubility in organic solvents, a solution sufficiently concentrated to obtain a ^{13}C NMR spectrum of the diastereomeric mixture could not be obtained. The ^{1}H NMR spectrum of the minor diastereomer could not be completely deconvoluted due to its low concentration and the presence of overlapping signals. The ^{1}H NMR spectrum of the mixture is included on the USB stick. Single crystals of the *meso* diastereomer suitable for X-ray diffraction were grown by vapour diffusion of methanol into a DCM solution of the complex.

Complex 63. *N*,*N*′-Bis(2,3,5,6-tetrafluorobenzoyl)hydrazide (**72b**) (108 mg, 0.28 mmol, 1.00 eq.) was added to dry diglyme (10 mL) with K_2CO_3 (200 mg, 1.45 mmol, 5.18 eq.) and heated to 50 °C under an argon atmosphere for 30 min to obtain a pale yellow suspension. $[Ir(ppy)_2\mu\text{-}Cl]_2$ (300 mg, 0.28 mmol, 1.00 eq.) was then added and the mixture was heated to 120 °C overnight. The reaction mixture was then cooled to room temperature and the solvent was removed under reduced pressure. The residue was dissolved in DCM and suspended onto celite (*ca.* 2 g) under reduced pressure, before being subjected to flash chromatography on silica gel (eluent: DCM sat. K_2CO_3) . The glowing yellow band was collected and after removing the solvent under reduced pressure, the residue was dissolved in a minimal amount of DCM (*ca*. 10 mL). Addition of hexane (*ca*. 20 mL) followed by reducing the volume of the mixture to 25 mL afforded complex **63** (207 mg, 0.15 mmol, 53%) as a yellow precipitate which was isolated via filtration and washed with pentane. The product

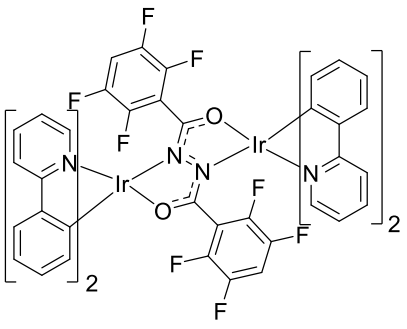

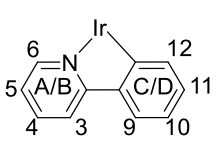

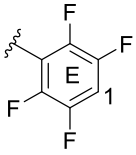

was isolated as a mixture of diastereomers in a *ca.* 9:1 ratio. MS (MALDI–TOF): *m/z* 1384.2 [M^+]. Calcd. for $C_{58}H_{34}F_8Ir_2N_6O_2^+$: 1384.2; Anal. Calcd. for $C_{58}H_{34}F_8Ir_2N_6O_2$: C, 50.36; H, 2.48; N, 6.08. Found: C, 50.06; H, 2.47; N, 6.00;

Major diastereomer: ^{1}H NMR (600 MHz, CD_2Cl_2, TMS) δ (ppm) = 9.18 (d, *J* = 5.6 Hz, $2H_{A6}$), 8.31 (d, *J* = 5.6 Hz, $2H_{B6}$), 7.97 – 7.94 (m, $2H_{A4}$), 7.93 – 7.87 (m, $6H_{A3, B4, B3}$), 7.50 (d, *J* = 7.4 Hz, $2H_{C9}$), 7.46 (ddd, *J* = 7.5, 5.6, 1.5 Hz, $2H_{A5}$), 7.37 (d, *J* = 7.2 Hz, $2H_{D9}$), 7.14 (ddd, *J* = 7.2, 5.6, 1.6 Hz, $2H_{B5}$), 6.79 (td, *J* = 7.4, 1.2 Hz, $2H_{C10}$), 6.63 – 6.59 (m, $4H_{C11, D10}$), 6.47 (td, *J* = 7.7, 1.0 Hz, $2H_{D11}$), 6.38 – 6.32 (m, $2H_{E1}$), 6.12 (d, *J* = 7.7 Hz, $2H_{D12}$), 5.91 (d, *J* = 7.4 Hz, $2H_{C12}$); ^{19}F {^{1}H} NMR (376 MHz, CD_2Cl_2) δ (ppm) =-138.37 (dd, *J* = 24.5, 12.0 Hz, 2F), -140.73 (dd, *J* = 23.0, 12.4 Hz, 2F), -141.90 (dd, *J* = 24.5, 12.4 Hz, 2F), -145.59 (dd, *J* = 23.0, 12.0 Hz, 2F).

Minor diastereomer: ^{19}F NMR (376 MHz, CD_2Cl_2) δ (ppm) =-139.55 (dd, *J* = 24.2, 11.7 Hz), -139.80 (dd, *J* = 23.4, 12.4 Hz), -143.09 (dd, *J* = 24.2, 11.7 Hz), -144.38 (dd, *J* = 23.4, 12.4 Hz).

Due to poor solubility in organic solvents, a solution sufficiently concentrated to obtain a ^{13}C NMR spectrum of the diastereomeric mixture could not be obtained. The ^{1}H NMR spectrum of the minor diastereomer could not be completely deconvoluted due to its low concentration and the presence of overlapping signals. The ^{1}H NMR spectrum of the mixture is included on the USB stick.

Complex 64. $[Ir(ppy)_2\mu\text{-}Cl]_2$ (160 mg, 0.15 mmol, 1.00 eq.) and *N*,*N*'-bis(pentafluorobenzoyl)hydrazide (**72c**) (63 mg, 0.15 mmol, 1.00 eq.) were added to dry diglyme (20 mL) and heated to 120 °C under an argon atmosphere for 24 h. The reaction mixture was then cooled to room temperature and the solvent was removed under reduced pressure. The residue was then dissolved in DCM and suspended onto celite (*ca.* 2 g) under reduced pressure, before being subjected to flash chromatography on silica gel (eluent: *n*-hexane/ DCM sat. K_2CO_3 1:1 v/v). The glowing yellow band was collected and after removing the solvent under reduced pressure, the residue was dissolved in a minimal amount of DCM (*ca*. 10 mL). Addition of hexane (*ca*. 20 mL) followed by reducing the volume of the mixture to 25 mL afforded complex **64** (70 mg, 0.05 mmol, 33%) as a yellow precipitate which was isolated via filtration and washed with pentane. The product was isolated as a mixture of diastereomers in a *ca.* 5:4 ratio (*meso:rac*). MS (MALDI–TOF): *m/z* 1420.1 [M^+]. Calcd. for $C_{58}H_{32}F_{10}Ir_2N_6O_2^+$: 1420.2; Anal. Calcd. for $C_{58}H_{32}F_{10}Ir_2N_6O_2$: C, 49.08; H, 2.27; N, 5.92. Found: C, 49.16; H, 2.31; N, 5.89.

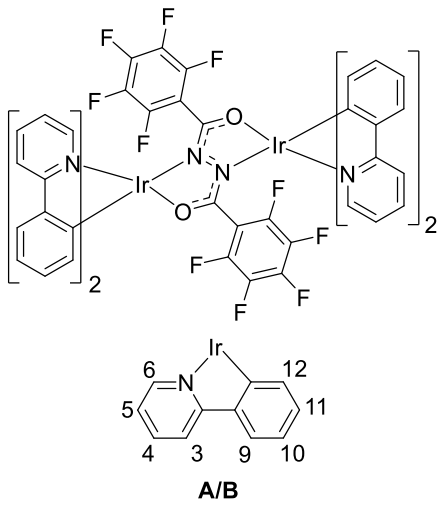

A/B

Meso diastereomer: ^{1}H NMR (700 MHz, CD_2Cl_2, TMS) δ (ppm) = 8.94 (d, *J* = 5.4 Hz, $2H_{B6}$), 8.69 (d, *J* = 5.6 Hz, $2H_{A6}$), 7.98 – 7.88 (m, $4H_{B4,B3}$), 7.81 – 7.75 (m, $4H_{A4,A3}$), 7.51 – 7.48 (m, $2H_{B5}$), 7.47 – 7.44 (m, $2H_{A9}$), 7.42 – 7.38 (m, $2H_{B9}$), 7.02 (ddd, *J* = 7.3, 5.6, 2.0 Hz, $2H_{A5}$), 6.81 – 6.77 (m, $2H_{A10}$), 6.71 – 6.67 (m, $2H_{B10}$), 6.64 – 6.59 (m, $2H_{A11}$), 6.54 – 6.48 (m, $2H_{B11}$), 6.07 (d, *J* = 7.7 Hz, $2H_{B12}$), 5.96 (dd, *J* = 7.9, 1.2 Hz, $2H_{A12}$); ^{19}F {^{1}H} NMR (376 MHz, CD_2Cl_2) δ (ppm) = -142.9 (dd, *J* = 24.2, 7.8 Hz, 2F), -144.0 (dd, *J* = 24.4, 7.8 Hz, 2F), -155.8 – -155.9 (m, 2F), -161.7 (td, *J* = 22.8, 7.8 Hz, 2F), -162.1 (td, *J* = 22.7, 7.7 Hz, 2F); ^{13}C NMR (176 MHz, CD_2Cl_2, TMS) δ (ppm) = 149.2 (C_{A6}), 147.93 (C_{B6}), 131.8 (C_{B12}), 131.5 (C_{A12}), 129.2 (C_{A11}), 128.9 (C_{B11}), 123.8 (C_{A9}), 123.8 (C_{B9}), 121.6 (C_{A10}), 121.6 (C_{B5}), 121.5 (C_{A5}), 119.6 (C_{B10}).

Rac diastereomer: ^{1}H NMR (700 MHz, CD_2Cl_2, TMS) δ (ppm) = 9.13 (d, *J* = 5.6 Hz, $2H_{B6}$), 8.27 (d, *J* = 5.4 Hz, $2H_{A6}$), 7.98 – 7.88 (m, $8H_{B4,B3,A4,A3}$), 7.51 – 7.48 (m, $2H_{A9}$), 7.47 – 7.44 (m, $2H_{B5}$), 7.42 – 7.38 (m, $2H_{B9}$), 7.14 (ddd, *J* = 7.2, 5.4, 1.5 Hz, $2H_{A5}$), 6.81 – 6.77 (m, $2H_{A10}$), 6.71 – 6.67 (m, $2H_{B10}$), 6.64 – 6.59 (m, $2H_{A11}$), 6.54 – 6.48 (m, $2H_{B11}$), 6.12 (d, *J* = 7.8 Hz, $2H_{B12}$), 5.90 (dd, *J* = 7.6, 1.1 Hz, $2H_{A12}$); ^{19}F {^{1}H} NMR (376 MHz, CD_2Cl_2) δ (ppm) = -141.6 (d, *J* = 22.6 Hz, 2F), -145.2 (d, *J* = 23.7 Hz, 2F), -155.8 – -155.9 (m, 2F), -160.5 – -160.7 (m, 2F), -162.9 – -163.1 (m, 2F); ^{13}C NMR (176 MHz, CD_2Cl_2, TMS) δ (ppm) = 149.8 (C_{B6}), 148.4 (C_{A6}), 131.8 (C_{A12}), 131.5 (C_{B12}), 129.1 (C_{A11}), 128.8 (C_{B11}), 123.5 (C_{B9}), 121.9 (C_{A5}), 121.7 (C_{A10}), 121.7 (C_{A9}), 121.5 (C_{B5}), 120.0 (C_{B10}).

Due to low solubility in organic solvents, extensive coupling to ^{19}F nuclei and overlapping signals due to the presence of two diastereomers, some of the ^{13}C NMR signals could not be unambiguously assigned. All signals that could be clearly identified in the ^{13}C, ^{1}H–^{13}C HSQC and ^{1}H–^{13}C HMBC NMR spectra are reported. The spectra are included on the USB stick. To obtain a sample of the *meso* (ΛΔ) isomer, which was used to grow crystals suitable for X-ray diffraction, the diastereomeric mixture was suspended in toluene at a concentration of 1 mg/ mL. The suspension was refluxed for 20 minutes and then hot filtered to obtain a sample of the *meso* (ΛΔ) isomer as the filtrand. Crystals were grown by layering a near-saturated DCM solution of the complex with hexane.

Complex 65. *N*,*N'*-Bis(2,3,5,6-tetrafluoro-4-methoxybenzoyl)hydrazide (**72d**) (62 mg, 0.14 mmol, 1.00 eq.) was added to dry diglyme (5 mL) with K_2CO_3 (96 mg, 0.70 mmol, 5.00 eq.) and heated to 50 °C under an argon atmosphere for 30 min to obtain a pale yellow suspension. $[Ir(ppy)_2\mu\text{-}Cl]_2$ (150 mg, 0.14 mmol, 1.00 eq.) was then added and the mixture was heated to 120 °C overnight. The reaction mixture was then cooled to room temperature and the solvent was removed under reduced pressure. The residue was then dissolved in DCM and suspended onto celite (*ca.* 2 g) under reduced pressure, before being subjected to flash chromatography on silica gel (eluent: DCM sat. K_2CO_3). The glowing yellow band was collected and after removing the solvent under reduced pressure, the residue was dissolved in a minimal amount of DCM (*ca*. 5 mL). Addition of methanol (*ca*. 20 mL) followed by reducing the volume of the mixture to *ca*. 20 mL afforded complex **65** (57 mg, 0.04 mmol, 28%) as a yellow precipitate which was isolated via filtration and washed with pentane. The product was obtained as a mixture of diastereomers in a *ca.* 5:4 ratio. MS (MALDI–TOF): *m/z* 1444.2 [M^+]. Calcd. for $C_{60}H_{38}F_8Ir_2N_6O_4^+$: 1444.2; Anal. Calcd. for $C_{60}H_{38}F_8Ir_2N_6O_4$: C, 49.93; H, 2.65; N, 5.82, Calcd. for $C_{60}H_{38}F_8Ir_2N_6O_4 \cdot 0.2CH_2Cl_2$: C, 49.51; H, 2.65; N, 5.75. Found: C, 49.50; H, 2.76; N, 5.70.

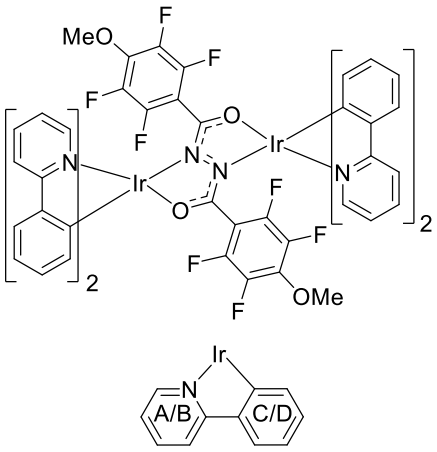

^{1}H and ^{19}F NMR

Major diastereomer*:* ^{1}H NMR (600 MHz, CD_2Cl_2, TMS) δ (ppm) = 9.16 (d, *J* = 5.6 Hz, $2H_A$), 8.27 (dt, *J* = 5.5, 1.2 Hz, $2H_B$), 7.96 – 7.86 (m, $8H_{2A,\ 2B}$), 7.50 – 7.41 (m, $4H_{A,C}$), 7.40 – 7.36 (m, $2H_D$), 7.11 (ddd, *J* = 7.3, 5.5, 1.2 Hz, $2H_B$), 6.80 – 6.75 (m, $2H_C$), 6.65 – 6.57 (m, $4H_{C,D}$), 6.50 – 6.43 (m, $2H_D$), 6.11 (d, *J* = 7.7 Hz, $2H_D$), 5.91 (dd, *J* = 7.8, 1.2 Hz, $2H_C$), 3.86 (s, $6H_{MeO}$); ^{19}F {^{1}H} NMR (376 MHz, CD_2Cl_2) δ (ppm) = -143.2 – -143.5 (m, 2F), -146.6 – -146.8 (m, 2F), -157.7 – -157.9 (m, 2F), -159.4 – -159.7 (m, 2F).

Minor diastereomer*:* ^{1}H NMR (600 MHz, CD_2Cl_2, TMS) δ (ppm) = 8.95 (dd, *J* = 5.4, 1.3 Hz, $2H_A$), 8.72 (d, *J* = 5.7 Hz, $2H_B$), 7.96 – 7.86 (m, H_{2A}), 7.79 – 7.73 (m, $4H_{2B}$), 7.50 – 7.41 (m, $H_{A,C}$), 7.40 – 7.36 (m, $2H_D$), 7.01 (ddd, *J* = 7.2, 5.7, 2.0 Hz, $2H_B$), 6.80 – 6.75 (m, $2H_C$), 6.65 – 6.57 (m, $4H_{C,D}$), 6.50 – 6.43 (m, $2H_D$), 6.06 (d, *J* = 7.7 Hz, $2H_D$), 5.96 (dd, *J* = 7.8, 1.1 Hz, $2H_C$), 3.86 (s, $6H_{MeO}$); ^{19}F {^{1}H} NMR (376 MHz, CD_2Cl_2) δ (ppm) = -144.4 – -144.7 (m, 2F), -145.5 – -145.8 (m, 2F), -158.5 – -158.9 (m, 4F).

^{13}C NMR

Diasteromeric mixture: ^{13}C NMR (151 MHz, CD_2Cl_2, TMS) δ (ppm) = 169.3, 168.8, 168.6, 168.5, 165.2, 151.5 – 148.5 (C_{ArF}), 145.0, 144.9, 143.6, 143.5, 138.1, 137.8, 137.6, 132.5, 132.3, 132.1, 132.1,

129.6, 129.6, 129.3, 129.2, 124.3, 124.3, 124.0, 124.0, 122.4, 122.3, 122.1, 122.0, 122.0, 120.2, 120.1, 119.7, 119.3, 119.3, 118.9, 62.0.

Due to low solubility in organic solvents, extensive coupling to ^{19}F nuclei and overlapping signals due to the presence of two diastereomers, some of the ^{13}C NMR signals could not be unambiguously assigned. All signals that could be clearly identified in the ^{13}C, ^{1}H–^{13}C HSQC and ^{1}H–^{13}C HMBC NMR spectra are reported. The spectra are included on the USB stick. Single crystals of the *rac* diastereomer suitable for X-ray diffraction were grown by layering a near-saturated DCM solution of the complex with hexane.

Complex *rac* **66.** *N*,*N*'-Bis(pentafluorobenzoyl)hydrazide (**72c**) (82 mg, 0.19 mmol, 1.00 eq.) was added to dry diglyme (15 mL) with K_2CO_3 (80 mg, 0.70 mmol, 2.98 eq.) and heated to 50 °C under an argon atmosphere for 30 min to obtain a pale yellow suspension. $[Ir(mesppy)_2\mu\text{-}Cl]_2$ (300 mg, 0.19 mmol, 1.00 eq.) was then added and the mixture was heated to 120 °C overnight. The reaction mixture was then cooled to room temperature and the solvent was removed under reduced pressure. The residue was then dissolved in DCM and suspended onto celite (*ca.* 2 g) under reduced pressure, before being subjected to flash chromatography on silica gel (eluent: gradient *n*-hexane/ DCM sat. K_2CO_3 9:1–1:1 v/v). First to elute was the *rac* (ΛΛ/ ΔΔ) diastereomer, which after removal of the solvent was dissolved in a minimal amount of DCM (*ca*. 5 mL). Addition of hexane (*ca*. 20 mL) followed by reducing the volume of the mixture to *ca*. 20 mL afforded complex *rac* **66** as a yellow precipitate which was isolated via filtration and washed with pentane (115 mg, 0.6 mmol, 31%). ^{1}H NMR (700 MHz, CD_2Cl_2) δ (ppm) = 9.27 (d, *J* = 5.7 Hz, $2H_{A6}$), 8.44 (d, *J* = 5.6 Hz, $2H_{B6}$), 7.71 (s, $2H_{B3}$), 7.69 (s, $2H_{A3}$), 7.46 (d, *J* = 7.7 Hz, $2H_{B9}$), 7.35 (d, *J* = 7.4 Hz, $2H_{A9}$), 7.21 (dd, *J* = 5.7, 1.7 Hz, $2H_{A5}$), 7.05 (s, $2H_{mesAr}$), 7.04 (s, $4H_{mesAr}$), 7.01 (s, $2H_{mesAr}$), 6.94 (dd, *J* = 5.6, 1.7 Hz, $2H_{B5}$), 6.80 (t, *J* = 7.7 Hz, $2H_{B10}$), 6.70 (t, *J* = 7.4 Hz, $2H_{A10}$), 6.69 – 6.65 (m, $2H_{B11}$), 6.62 (t, *J* = 7.4 Hz, $2H_{A11}$), 6.41 (d, *J* = 7.4 Hz, $2H_{A12}$), 5.99 (d, *J* = 8.4 Hz, $2H_{B12}$), 2.37 (s, $6H_{mesMe}$), 2.36 (s, $6H_{mesMe}$), 2.29 (s, $6H_{mesMe}$), 2.21 (s, $6H_{mesMe}$), 2.13 (s, $6H_{mesMe}$), 2.09 (s, $6H_{mesMe}$); ^{19}F NMR {^{1}H} (376 MHz, CD_2Cl_2) δ (ppm) = -141.9 (dd, *J* = 25.2, 7.7 Hz, 2F), -145.1 – -145.2 (m, 2F), -155.9 (t, *J* = 21.6 Hz, 2F), -160.2 – -160.4 (m, 2F), -162.9 (ddd, *J* = 23.3, 21.6, 7.9 Hz, 2F); ^{13}C NMR (176 MHz, CD_2Cl_2) δ (ppm) = 168.1 (C_{A2}), 167.9 (C_{B2}), 151.9 (C_{A4}), 151.6 (C_{B4}), 150.8 (C_{A7}), 149.8 (C_{A6}), 148.4 (C_{B6}), 147.7 (C_{B7}), 144.7 (C_{B8}), 143.0 (C_{A8}), 135.0 – 135.8 ($C_{mes\ quart}$

$_{carbons}$), 131.8 (C_{B12}), 131.7 (C_{A12}), 129.1 (C_{B11}), 128.9 (C_{A11}), 128.4 (C_{mesAr}), 128.4[#] (C_{mesAr}), 123.9 (C_{B9}), 123.6 (C_{A9}), 123.1 (C_{A5}), 122.9 (C_{B5}), 121.8 (C_{B10}), 120.5 (C_{A3}), 119.9 (C_{B3}), 119.5 (C_{A10}), 20.8* (C_{mesMe}), 20.4 (C_{mesMe}), 20.3 (C_{mesMe}), 20.1 (C_{mesMe}), 20.0 (C_{mesMe}); MS (MALDI–TOF): *m/z* 1892.3 [M^+]. Calcd. for $C_{94}H_{72}F_{10}Ir_2N_6O_2^+$: 1892.5; Anal. Calcd. for $C_{94}H_{72}F_{10}Ir_2N_6O_2$: C, 59.67; H, 3.84; N, 4.44, Calcd. for $C_{94}H_{72}F_{10}Ir_2N_6O_2{\cdot}0.4CH_2Cl_2$: C, 58.87; H, 3.81; N, 4.36. Found: C, 58.78; H, 3.73; N, 4.36. Due to low solubility in organic solvents and extensive coupling to ^{19}F nuclei, some of the quaternary ^{13}C NMR signals could not be identified. All signals that could be clearly identified in the ^{13}C, ^{1}H–^{13}C HSQC and ^{1}H–^{13}C HMBC NMR spectra are reported. The spectra are included on the USB stick. Single crystals suitable for X-ray diffraction were grown by vapour diffusion of hexane into a DCM solution of the complex. A second yellow band presumed to contain the *meso* (ΛΔ) diastereomer slowly eluted from the column after the *rac* (ΛΛ/ ΔΔ) diastereomer, but due to very low solubility it could not be isolated in an analytically pure form.

Complex *meso* **67.** Bis(trifluoromethyl)hydrazide (**73**) (43 mg, 0.19 mmol, 1.00 eq.), $[Ir(mesppy)_2\mu\text{-}Cl]_2$ (300 mg, 0.19 mmol, 1.00 eq.) and K_2CO_3 (80 mg, 0.70 mmol, 2.98 eq.) were added to 2-ethoxyethanol (15 mL) under and argon atmosphere and heated to reflux overnight. The reaction mixture was then cooled to room temperature and the solvent was removed under reduced pressure. The residue was then dissolved in DCM and suspended onto celite (*ca.* 2 g) under reduced pressure, before being subjected to flash chromatography on silica gel (eluent: gradient *n*-hexane/ DCM sat. K_2CO_3 9:1–1:1 v/v). The glowing yellow band was collected and after removing the solvent under reduced pressure, the residue was dissolved in a minimal amount of DCM (*ca*. 5 mL). Addition of hexane (*ca*. 20 mL) followed by reducing the volume of the mixture to *ca*. 20 mL afforded complex *meso* **67** as a yellow precipitate which was isolated via filtration and washed with pentane (200 mg, 0.12 mmol, 61%). A single diastereomer (ΛΔ) was obtained.

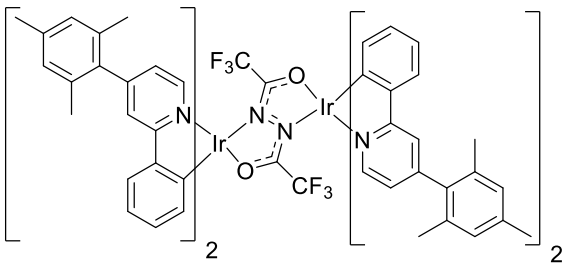

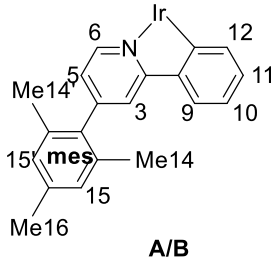

A/B

^{1}H NMR (700 MHz, THF-d_8) δ (ppm) = 8.74 (d, *J* = 5.6 Hz, $2H_{A6}$), 8.63 (d, *J* = 5.7 Hz, $2H_{B6}$), 7.84 (d, *J* = 1.9 Hz, $2H_{A3}$), 7.79 (d, *J* = 1.8 Hz, $2H_{B3}$), 7.56 (dd, *J* = 7.9, 1.3 Hz, $2H_{A9}$), 7.53 (dd, *J* = 7.6, 1.3 Hz, $2H_{B9}$), 7.25 (dd, *J* = 5.6, 1.9 Hz, $2H_{A5}$), 7.01 – 6.99 (m, $4H_{A15',B15'}$), 6.97 (s, $2H_{B15}$), 6.90 – 6.87 (m, $4H_{A15,\ B5}$), 6.70 (td, *J* = 7.6, 7.0, 1.2 Hz, $2H_{B10}$), 6.65 (ddd, *J* = 7.9, 6.9, 1.3 Hz, $2H_{A10}$), 6.57 (ddd, *J* = 7.9, 7.0, 1.3 Hz, $2H_{B11}$), 6.53 (ddd, *J* = 8.1, 6.9, 1.3 Hz, $2H_{A11}$), 6.30 (d, *J* = 8.1 Hz, $2H_{A12}$), 6.05 (dd, *J* = 7.9, 1.2 Hz,

$2H_{B12}$), 2.35 (s, $6H_{BMe16}$), 2.32 (s, $6H_{AMe16}$), 2.18 (s, $6H_{AMe14'}$), 2.15 (s, $6H_{BMe14'}$), 1.91 (s, $6H_{BMe14}$), 1.86 (s, $6H_{AMe14}$); ^{19}F {^{1}H} NMR (376 MHz, CD_2Cl_2) δ (ppm) = -67.0 (s, 6F); ^{13}C NMR (176 MHz, THF-d_8) δ (ppm) = 170.8 (C_{A2}), 169.9 (C_{B2}), 152.5 (C_{B4}), 152.3 (C_{A4}), 150.6 (C_{B6}), 150.3 (C_{A7}), 149.4 (C_{A6}), 146.5 (C_{B7}), 145.2 (C_{B8}), 145.0 (C_{A8}), 138.7 ($C_{mes\ quart}$), 138.5 ($C_{mes\ quart}$), 137.3 – 135.9 ($C_{mes\ quart\ carbons}$), 134.6 (C_{A12}), 132.9 (C_{B12}), 130.4 (C_{B11}), 130.0 (C_{A11}), 130.0* ($C_{A15',B15'}$), 129.9 (C_{B15}), 129.8 (C_{A15}), 125.7 (C_{B9}), 125.4 (C_{A9}), 124.5 (C_{B5}), 124.13 (C_{A5}), 122.7 (C_{B10}), 121.8 (C_{B3}), 121.7 (C_{A3}), 121.2 (C_{A10}), 22.0* ($C_{A16,B16}$), 21.6 (C_{A14}), 21.5 (C_{B14}), 21.5 ($C_{A14'}$), 21.4 ($C_{B14'}$); MS (MALDI–TOF): *m/z* 1696.3 [M^+]. Calcd. for $C_{84}H_{72}F_6Ir_2N_6O_2^+$: 1696.5; Anal. Calcd. for $C_{84}H_{72}F_6Ir_2N_6O_2$: C, 59.49; H, 4.28; N, 4.96, Calcd. for $C_{84}H_{72}F_6Ir_2N_6O_2 \cdot 0.5CH_2Cl_2$: C, 58.38; H, 4.23; N, 4.83. Found: C, 58.04; H, 4.25; N, 4.71. Due to low solubility in organic solvents some of the quaternary ^{13}C NMR signals could not be identified. All signals that could be clearly identified in the ^{13}C, ^{1}H–^{13}C HSQC and ^{1}H–^{13}C HMBC NMR spectra are reported. The spectra are included on the USB stick. Single crystals suitable for X-ray diffraction were grown by vapour diffusion of hexane into a THF solution of the complex.

Complexes *meso* **68** and *rac* **68.** $[Ir(COD)\mu\text{-}Cl]_2$ (200 mg, 0.30 mmol, 1.00 eq.) and 2-(2,4-difluorophenyl)-4-(2,6-dimethyl-4-(methylcyclohexyloxy)phenyl)pyridine (**75**) (534 mg, 1.32 mmol, 4.4 eq.) were added to 2-ethoxyethanol (10 mL) and heated to reflux under an argon atmosphere for 4 h. The reaction mixture was then cooled to room temperature and the solvent removed under reduced pressure. The residue was then dissolved in DCM (*ca.* 10 mL) and hexane was added (*ca.* 30 mL). The solvent volume was reduced to *ca.* 10 mL under reduced pressure. A yellow precipitate formed which was filtered and washed with pentane (*ca.* 20 mL) to isolate the intermediate μ-dichloro-bridged diiridium complex (463 mg, 0.22 mmol, 75%) which was used without further purification (^{1}H NMR data were consistent with the proposed structure). The obtained dichloro dimer was combined with *N*,*N'*-bis(pentafluorobenzoyl)hydrazide (**72c**) (94 mg, 0.22 mmol, 1.00 eq.) and K_2CO_3 (77 mg, 0.56 mmol, 2.50 eq.) and suspended in dry diglyme (15 mL) under argon. It was subsequently heated to 120 °C overnight. The reaction mixture was then cooled to room temperature and the solvent removed under reduced pressure. To the residue was added DCM (10 mL), and the resulting mixture was sonicated for 5 min. Hexane (30

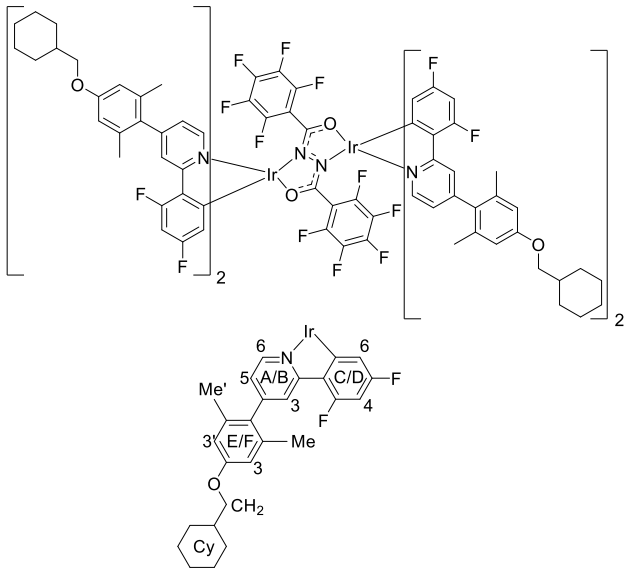

mL) was then added, before the solvent volume was reduced to *ca.* 30 mL. The mixture was filtered to obtain a yellow powder and a yellow/orange filtrate. Both the filtrate and filtrand were retained.

Filtrand

The filtrand was further purified by flash chromatography on silica gel (eluent: *n*-hexane/ DCM sat. K_2CO_3 4:6 v/v). After evaporation of the column solvent, the residue was precipitated from DCM/ hexane, filtered and washed with pentane to afford the presumed *meso* (ΛΔ) diastereomer *(meso* **68***)* (150 mg, 0.06 mmol, 21% from [Ir(COD)μ-Cl]$_2$).

Filtrate

The filtrate was evaporated and the residue was refluxed in methanol (20 mL) for 5 min. The mixture was then cooled in a freezer (−18 °C) for 1 h before being filtered to obtain a yellow precipitate, which was further purified by flash chromatography on silica gel (eluent: *n*-hexane/ toluene 6:4 v/v). After evaporation of the column solvent, the residue was precipitated from DCM/ hexane, filtered and washed with pentane to afford *rac* **68** (80 mg, 0.03 mmol, 11% from [Ir(COD)μ-Cl]$_2$).

meso **68:** ^{1}H NMR (600 MHz, CD_2Cl_2) δ (ppm) = 8.93 (d, *J* = 5.8 Hz, 2H$_{A6}$), 8.76 (d, *J* = 5.8 Hz, 2H$_{B6}$), 8.10 (s, 2H$_{A3}$), 8.01 (s, 2H$_{B3}$), 7.34 (dd, *J* = 5.8, 1.8 Hz, 2H$_{A5}$), 6.88 (dd, *J* = 5.8, 1.8 Hz, 2H$_{B5}$), 6.78 – 6.72 (m, 6H$_{E3,E3',F3'}$), 6.65 (bs, 2H$_{F3}$), 6.38 – 6.32 (m, 2H$_{C4}$), 6.31 – 6.25 (m, 2H$_{D4}$), 5.66 (dd, *J* = 8.5, 2.0 Hz, 2H$_{D6}$), 5.38 (dd, *J* = 8.9, 2.4 Hz, 2H$_{C6}$), 3.85 (d, *J* = 6.4 Hz, 4H$_{CH2}$), 3.81 (d, *J* = 6.4 Hz, 4H$_{CH2}$), 2.18 (bs, 6H$_{EMe/EMe'}$), 2.16 (bs, 6H$_{FMe/FMe'}$), 1.98 −1.90 (m, 20H$_{Cy,EMe/EMe',FMe/FMe'}$), 1.82 (td, *J* = 7.7, 3.7 Hz, 12H$_{Cy}$), 1.76 (d, *J* = 11.7 Hz, 4H$_{Cy}$), 1.41 – 1.32 (m, 8H$_{Cy}$), 1.29 – 1.26 (m, 4H$_{Cy}$), 1.18 – 1.09 (m, 8H$_{Cy}$) The ^{1}H environments on rings E and F resolve due to restricted rotation. Exchange is observed in ^{1}H–^{1}H NOESY and ^{1}H–^{1}H ROESY experiments; ^{19}F NMR (376 MHz, CD_2Cl_2) δ (ppm) = -108.0 (d, *J* = 10.2 Hz, 2F), -108.3 (d, *J* = 10.1 Hz, 2F), -109.7 (d, *J* = 10.2 Hz, 2F), -110.0 (d, *J* = 10.2 Hz, 2F), -142.0 (d, *J* = 21.2 Hz, 2F), -143.4 (d, *J* = 20.5 Hz, 2F), -154.7 (t, *J* = 20.5 Hz, 2F), -161.1 (td, *J* = 23.9, 7.5 Hz, 2F), -161.7 (td, *J* = 23.9, 21.2, 7.5 Hz, 2F); ^{13}C NMR (176 MHz, CD_2Cl_2) δ (ppm) = 148.6 (C$_{B6}$), 147.7 (C$_{A6}$), 125.0 (C$_{A3}$), 124.9 (C$_{B3}$), 123.93 (C$_{A5}$), 123.59 (C$_{B5}$), 113.8 (C$_{F3}$), 113.7$^{\#}$ (C$_{F3',E3,E3'}$), 113.6 (C$_{D6}$), 113.5 (C$_{C6}$), 98.2 (C$_{C4}$), 96.0 (C$_{D4}$), 73.5 (C$_{CH2}$), 73.43 (C$_{CH2}$), 37.8* (C$_{Cy}$), 29.9* (C$_{Cy}$), 26.6* (C$_{Cy}$), 25.8* (C$_{Cy}$), 20.7 (C$_{FMe/FMe'}$), 20.6 (C$_{EMe/EMe'}$), 20.4 (C$_{FMe/FMe'}$), 20.3 (C$_{EMe/EMe'}$); MS (MALDI–TOF): *m/z* 2428.6 [M$^+$]. Calcd. for $C_{118}H_{104}F_{18}Ir_2N_6O_6^+$: 2428.7; Anal. Calcd. for $C_{118}H_{104}F_{18}Ir_2N_6O_6$: C, 58.36; H, 4.32; N, 3.46, Calcd. for $C_{118}H_{104}F_{18}Ir_2N_6O_6{\cdot}0.3CH_2Cl_2$: C, 57.90; H, 4.30; N, 3.42. Found: C, 57.83; H, 4.34; N, 3.36.

rac **68**: ^{1}H NMR (700 MHz, CD_2Cl_2, TMS) δ (ppm) = 9.18 (d, *J* = 5.8 Hz, 2H$_{A6}$), 8.35 (d, *J* = 5.7 Hz, 2H$_{B6}$), 8.08 (s, 4H$_{A3,B3}$), 7.28 (d, *J* = 5.8 Hz, 2H$_{A5}$), 7.01 – 6.98 (m, 2H$_{B5}$), 6.76 – 6.71 (m, 8H$_{E3,E3',F3,F3'}$), 6.35 (t, *J* = 10.5 Hz, 2H$_{C4}$), 6.29 (t, *J* = 10.6 Hz, 2H$_{D4}$), 5.84 (d, *J* = 8.7 Hz, 2H$_{D6}$), 5.36 – 5.34 (m, 2H$_{C6}$), 3.82 –

3.79 (m, 8H_{CH2}), 2.30 (bs, 6$H_{FMe/FMe'}$), 2.22 (bs, 6$H_{EMe/EMe'}$), 2.11 (bs, 6$H_{FMe/FMe'}$), 2.09 (bs, 6$H_{EMe/EMe'}$), 1.89 (d, *J* = 12.8 Hz, 8H_{Cy}), 1.79 (d, *J* = 13.8 Hz, 12H_{Cy}), 1.73 (d, *J* = 12.8 Hz, 4H_{Cy}), 1.34 (q, *J* = 13.1 Hz, 8H_{Cy}), 1.29 – 1.22 (m, 4H_{Cy}), 1.09 (q, *J* = 12.8 Hz, 8H_{Cy}) The ^{1}H environments on rings E and F partially resolve due to restricted rotation. Exchange is suspected from the ^{1}H–^{1}H NOESY experiment; ^{19}F {^{1}H} NMR (376 MHz, CD_2Cl_2) δ (ppm) = -107.9 (d, *J* = 10.2 Hz, 2F), -108.5 (d, *J* = 10.2 Hz, 2F), -109.7 – -109.8 (m, 2F), -109.8 – -109.9 (m, 2F), -141.0 (d, *J* = 24.1 Hz, 2F), -144.5 (d, *J* = 22.6 Hz, 2F), -154.7 (t, *J* = 20.8 Hz, 2F), -159.9 – -160.2 (m, 2F), -161.9 (td, *J* = 22.8, 22.2, 7.7 Hz, 2F); ^{13}C NMR (176 MHz, CD_2Cl_2) δ (ppm) = 164.9 (C_{A2}), 164.4 (C_{B2}), 162.8 (d, *J* = 256 Hz, C_{D5}), 162.4 (d, *J* = 251 Hz, C_{C5}), 153.2 (C_{A4}), 153.1 (C_{B4}), 159.2* ($C_{E/F}$), 148.4 (C_{A6}), 148.1 (C_{B6}), 136.6* ($C_{E/F}$), 130.5* ($C_{E/F}$), 125.1 (C_{A3}), 124.7 (C_{B3}), 123.9 (C_{A5}), 123.7 (C_{B5}), 113.9 (C_{C6}), 113.7* ($C_{E/F}$), 113.7* ($C_{E/F}$), 113.6 (C_{D6}), 98.3 (C_{C4}), 95.9 (C_{D4}), 73.5* (C_{CH2}), 37.7* (C_{Cy}), 29.9* (C_{Cy}), 26.5* (C_{Cy}), 25.8*(C_{Cy}), 20.8 ($C_{EMe/EMe'}$), 20.6 ($C_{FMe/FMe'}$), 20.5 ($C_{FMe/FMe'}$), 20.5 ($C_{EMe/EMe'}$); MS (MALDI–TOF): *m/z* 2428.6 [M^+]. Calcd. for $C_{118}H_{104}F_{18}Ir_2N_6O_6^+$: 2428.7; Anal. Calcd. for $C_{118}H_{104}F_{18}Ir_2N_6O_6$: C, 58.36; H, 4.32; N, 3.46, Calcd. for $C_{118}H_{104}F_{18}Ir_2N_6O_6{\cdot}0.5CH_2Cl_2$: C, 57.60; H, 4.28; N, 3.40. Found: C, 57.46; H, 4.32; N, 3.42.

Due to low solubility in organic solvents and extensive coupling to ^{19}F nuclei, some of the quaternary ^{13}C NMR signals could not be identified. All signals that could be clearly identified in the ^{13}C, ^{1}H–^{13}C HSQC and ^{1}H–^{13}C HMBC NMR spectra are reported. The spectra are included on the USB stick. Crystals suitable for X-ray diffraction fell overnight from a saturated solution of the complex in CD_2Cl_2.

Complex 69. [Ir(COD)μ-Cl]$_2$ (94 mg, 0.14 mmol, 1.00 eq.) and 2-(2,4-difluorophenyl)-4-(2,6-dimethyl-4-(methylcyclohexyloxy)phenyl)pyridine (**75**) (250 mg, 0.62 mmol, 4.4 eq.) were added to 2-ethoxyethanol (5 mL) and heated to reflux under an argon atmosphere for 4 h to generate the μ-dichloro-bridged diiridium complex *in-situ*. The reaction mixture was then cooled to room temperature, before bis(trifluoromethyl)hydrazide (**73**) (34 mg, 0.14 mmol, 1.00 eq.), and K_2CO_3 (58 mg, 0.42 mmol, 3.00 eq.) were added. The reaction mixture was then heated to reflux overnight, before being cooled to room temperature and the solvent removed under reduced pressure. The residue was dissolved in DCM, suspended onto celite (*ca.* 2 g) under reduced pressure and subjected to flash chromatography on

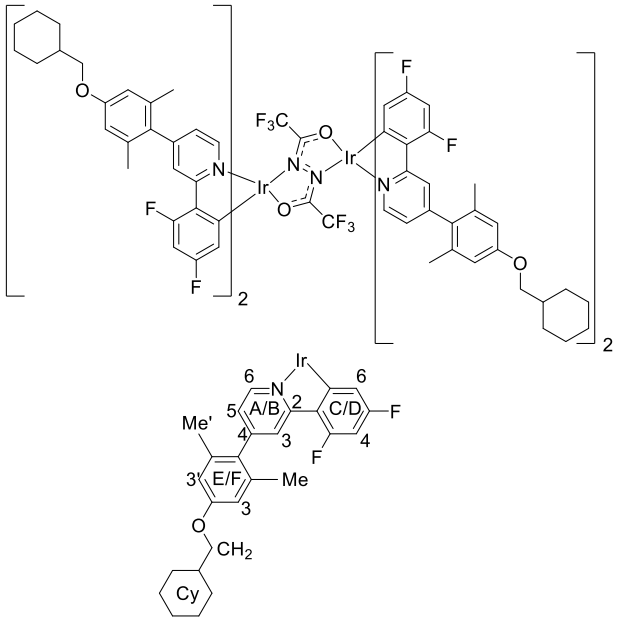

silica gel (eluent: gradient *n*-hexane/ DCM sat. K_2CO_3 8:2–2:8 v/v). The yellow band was collected and the column solvent was removed under reduced pressure. The residue was heated to reflux in THF (25 mL) for 20 min and then hot filtered to obtain a yellow powder (25 mg, 0.01 mmol, 8%). A second crop was obtained by reducing the filtrate to 10 mL and repeating the process (60 mg, 0.03 mmol, 19%). The recovered solids from both filtrations were combined to afford complex (**69**) (85 mg, 0.04 mmol, 27%) as a single diastereomer. ^{1}H NMR (700 MHz, CD_2Cl_2, TMS) δ (ppm) = 8.57 (d, *J* = 5.7 Hz, $2H_{A6}$), 8.42 (d, *J* = 5.7 Hz, $2H_{B6}$), 8.13 (s, $2H_{A3}$), 8.06 (s, $2H_{B3}$), 7.20 (dd, *J* = 5.7, 1.9 Hz, $2H_{A5}$), 6.79 (dd, *J* = 5.7, 1.9 Hz, $2H_{B5}$), 6.73 (bs, $2H_{E3}$), 6.72 (bs, $2H_{F3}$), 6.70 (bs, $2H_{F3'}$), 6.61 (bs, $2H_{E3'}$), 6.42 (ap. t, *J* = 10.2 Hz, $2H_{C4}$), 6.36 (ap. t, *J* = 10.6 Hz, $2H_{D4}$), 5.70 (dd, *J* = 9.1, 2.1 Hz, $2H_{D6}$), 5.47 (dd, *J* = 9.0, 2.4 Hz, $2H_{C6}$), 3.82 (d, *J* = 6.4 Hz, $4H_{CH2}$), 3.79 (d, *J* = 6.1 Hz, $4H_{CH2}$), 2.17 (bs, $6H_{EMe/EMe'}$), 2.14 (bs, $6H_{FMe/FMe'}$), 1.92 (bs, $6H_{FMe/FMe'}$), 1.91 – 1.81 (m, $8H_{Cy}$), 1.84 (bs, $6H_{EMe/EMe'}$), 1.82 – 1.77 (m, $12H_{Cy}$), 1.74 (d, *J* = 13.0 Hz, $4H_{Cy}$), 1.39 – 1.31 (m, $8H_{Cy}$), 1.29 – 1.23 (m, $4H_{Cy}$), 1.13 – 1.09 (m, $8H_{Cy}$) The ^{1}H environments on rings E and F resolve due to restricted rotation. Exchange is suspected from the ^{1}H–^{1}H NOESY experiment (Figure S64); ^{19}F {^{1}H} NMR (376 MHz, CD_2Cl_2) δ (ppm) = -67.0 (s, $6F_{CF3}$), -107.6 (d, *J* = 10.2 Hz, $2F_{Ar}$), -109.4 (d, *J* = 9.8 Hz, $2F_{Ar}$), -109.6 (d, *J* = 10.2 Hz, $2F_{Ar}$), -111.2 – -111.3 (m, $2F_{Ar}$); ^{13}C NMR (176 MHz, CD_2Cl_2) δ (ppm) = 165.7 (C_{A2}), 164.6 (C_{B2}), 159.2 ($C_{E\ or\ F}$), 159.1 ($C_{E\ or\ F}$), 152.9 (C_{B4}), 152.7 (C_{A4}), 148.2 (C_{B6}), 146.9 (C_{A6}), 125.1 (C_{B3}), 124.9 (C_{A3}), 123.7 (C_{B5}), 123.3 (C_{A5}), 114.7 (C_{D6}), 113.7$^{\#}$ ($C_{E3/E3'/F3'}$), 113.6 (C_{F3}), 113.6 (C_{C6}), 98.4 (C_{C4}), 96.5 (C_{D4}), 73.5 (C_{CH2}), 73.4 (C_{CH2}), 37.8* (C_{Cy}), 29.8* (C_{Cy}), 26.6* (C_{Cy}), 25.8* (C_{Cy}), 20.6 ($C_{EMe/EMe'}$), 20.6 ($C_{FMe/FMe'}$), 20.6 ($C_{FMe/FMe'}$), 20.5 ($C_{EMe/EMe'}$); MS (MALDI–TOF): *m/z* 2232.2 [M^+]. Calcd. for $C_{108}H_{104}F_{14}Ir_2N_6O_6^+$: 2232.7. Due to low solubility in organic solvents, some quaternary ^{13}C NMR signals could not be identified. All signals that could be clearly identified in the ^{13}C, ^{1}H–^{13}C HSQC and ^{1}H–^{13}C HMBC NMR spectra are reported. The spectra are included on the USB stick. A reproducible CHN analysis could not be obtained for this compound. On three runs on the same sample the carbon reading varied by over 1%.

Complex 70. $[Ir(COD)\mu\text{-}Cl]_2$ (200 mg, 0.30 mmol, 1.00 eq.) and 2-(2,4-difluorophenyl)-4-(methylcyclohexyloxy)phenyl pyridine (**76**) (366 mg, 1.21 mmol, 4.05 eq.) were added to 2-ethoxyethanol (15 mL) and heated to reflux under an argon atmosphere for 4 h. The reaction mixture was then cooled to room temperature and hexane was added (*ca.* 30 mL). The mixture was cooled in a fridge (*ca.* 3 °C) for 1 h. A yellow precipitate formed which was filtered and washed with pentane (*ca.* 20

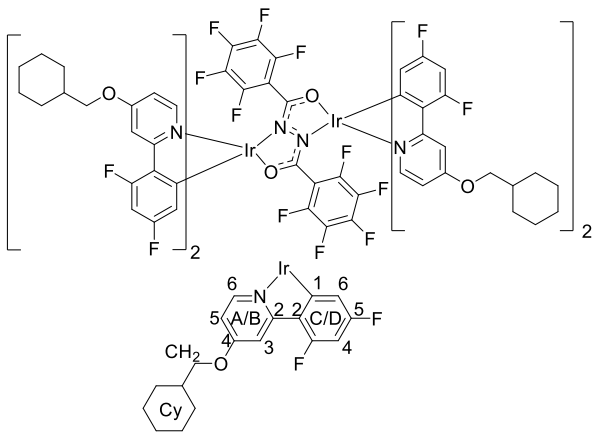

mL) to isolate the intermediate μ-dichloro-bridged diiridium complex (403 mg, 0.24 mmol, 80%) which was used without further purification (^{1}H NMR data were consistent with the proposed structure). The obtained dichloro dimer was combined with *N*,*N'*-bis(pentafluorobenzoyl)hydrazide (**72c**) (102 mg, 0.24 mmol, 1.00 eq.) and K_2CO_3 (84 mg, 0.60 mmol, 2.50 eq.) and suspended in dry diglyme (15 mL) under argon. It was subsequently heated to 120 °C overnight. The reaction mixture was then cooled to room temperature and diluted with hexane (*ca.* 70 mL). A yellow precipitate formed which was filtered and washed with pentane (*ca.* 20 mL). The obtained solid was then dissolved in DCM and suspended onto celite (*ca.* 2 g) under reduced pressure, before being subjected to flash chromatography on silica gel (eluent: *n*-hexane/ DCM sat. K_2CO_3 1:1 v/v). The faint yellow band was collected and after removing the solvent under reduced pressure, the residue was dissolved in minimal DCM (*ca*. 15 mL). Hexane was added (*ca.* 20 mL) and the volume was reduced to 20 mL After collecting the precipitate by filtration and washing with pentane complex **70** was obtained as a yellow solid (130 mg, 0.6 mmol, 22% from [Ir(COD)μ-Cl]$_2$). A single diastereomer was obtained.^{1}H NMR (700 MHz, CD_2Cl_2, TMS) δ (ppm)= 8.73 (d, *J* = 6.5 Hz, 2H$_{A6}$), 7.94 (d, *J* = 6.5 Hz, 2H$_{B6}$), 7.75 (t, *J* = 2.8 Hz, 2H$_{A3}$), 7.72 (t, *J* = 2.7 Hz, 2H$_{B3}$), 7.00 (dd, *J* = 6.5, 2.8 Hz, 2H$_{A5}$), 6.72 (dd, *J* = 6.5, 2.7 Hz, 2H$_{B5}$), 6.32 (ddd, *J* = 12.0, 9.0, 2.4 Hz, 2H$_{C4}$), 6.24 (ddd, *J* = 11.9, 9.0, 2.4 Hz, 2H$_{D4}$), 5.60 (dd, *J* = 9.0, 2.4 Hz, 2H$_{D6}$), 5.42 (dd, *J* = 8.7, 2.4 Hz, 2H$_{C6}$), 4.08 – 4.05 (m, 8H$_{CH2}$), 2.03 – 1.93 (m, 12H$_{Cy}$), 1.89 – 1.83 (m, 8H$_{Cy}$), 1.80 – 1.74 (m, 4H$_{Cy}$), 1.45 – 1.35 (m, 8H$_{Cy}$), 1.29 – 1.26 (m, 4H$_{Cy}$), 1.25 – 1.16 (m, 8H$_{Cy}$); ^{19}F NMR (376 MHz, CD_2Cl_2) δ (ppm) = -108.7 (d, *J* = 10.1 Hz, 2F), -109.4 (d, *J* = 10.0 Hz, 2F), -111.0 (d, *J* = 10.1 Hz, 2F), -111.1 (d, *J* = 10.1 Hz, 2F), -140.4 (d, *J* = 24.5 Hz, 2F), -143.9 (d, *J* = 24.0 Hz, 2F), -155.3 (t, *J* = 20.8 Hz, 2F), -160.5 – -160.8 (m, 2F), -162.1 – -162.4 (m, 2F); ^{13}C NMR (176 MHz, CD_2Cl_2, TMS) δ (ppm) = 167.4 (C$_{B2}$), 167.2 (C$_{A4\ or\ B4}$), 165.7 (C$_{A2}$), 165.1 (C$_{A4\ or\ B4}$), 162.6 (d, *J* = 255 Hz, C$_{D5}$), 162.3 (d, *J* = 251 Hz, C$_{C5}$), 160.5 (d, *J* = 266 Hz, C$_{D3}$), 160.4 (d, *J* = 263 Hz, C$_{C3}$), 150.1 (C$_{A6}$), 148.7 (B$_{B6}$), 128. 7 (C$_{C1}$), 127.15 (C$_{D1}$), 114.1 (C$_{C6}$), 113.6 (C$_{D6}$), 109.7 (C$_{A5}$), 109.6 (C$_{B5}$), 108.8 (C$_{A3}$), 108.4 (C$_{B3}$), 97.9 (C$_{C4}$), 95.6 (C$_{D4}$), 74.3 (C$_{CH2}$), 74.25 (C$_{CH2}$), 37.50 (C$_{Cy}$), 37.44 (C$_{Cy}$), 29.75 (C$_{Cy}$), 29.68 (C$_{Cy}$), 26.39 (C$_{Cy}$), 26.36 (C$_{Cy}$), 25.74* (C$_{Cy}$); MS (MALDI–TOF): *m/z* 2012.4 [M$^+$]. Calcd. for $C_{86}H_{72}F_{18}Ir_2N_6O_6^+$: 2012.3; Anal. Calcd. for $C_{86}H_{72}F_{18}Ir_2N_6O_6^+$: C, 51.34; H, 3.61; N, 4.18. Found: C, 51.23; H, 3.60; N, 4.15. Due to low solubility in organic solvents and extensive coupling to ^{19}F nuclei, some of the quaternary ^{13}C NMR signals could not be reported. All signals that could be clearly identified in the ^{13}C, ^{1}H–^{13}C HSQC and ^{1}H–^{13}C HMBC NMR spectra are reported. The spectra are included on the USB stick.

Synthetic details for Chapter 4: 1,2-Diarylimidazole cyclometallating ligands in hydrazide-bridged diiridium complexes

General

NMR spectra for all novel compounds are included as .pdf files on the USB stick submitted as Supporting Information.

***N*-(2,2-Diethoxyethyl)mesitylamine (113).** Prepared according to a literature procedure.[30] *n*-Buli

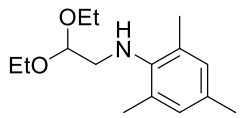

(2.5 M in hexane, 41.2 mL, 103 mmol, 1.10 eq.) was added to a solution of 2,4,6-trimethylaniline (**112**) (13.2 mL, 94.0 mmol, 1.00 eq.) in THF (150 mL) at 0 °C over 30 min. The resulting mixture was stirred at room temperature for 30 min before bromoacetaldehyde diethylacetal (15.6 mL, 103 mmol, 1.10 eq.) was added over 10 min. The reaction mixture was stirred at room temperature for 4 h. It was then poured into a mixture of sat. aq. $NaHCO_3$ and water (1:1 v/v, 200 mL). The mixture was extracted with Et_2O (3 × 150 mL). The combined extracts were washed with water (100 mL), dried over $MgSO_4$, filtered and then evaporated. The residue was distilled (100–120 °C, *ca.* 5 × 10^{-2} mbar) to furnish *N*-(2,2-diethoxyethyl)mesitylamine (**113**) as a light yellow oil (18.0 g, 71.6 mmol, 76%). NMR data were in agreement with those previously reported.[30] ^{1}H NMR (400 MHz, $CDCl_3$): δ (ppm) = 6.81 (s, 2H), 4.60 (t, *J* = 5.5 Hz, 1H), 3.72 (dt, *J* = 9.4, 7.0 Hz, 2H), 3.56 (dt, *J* = 9.3, 7.0 Hz, 2H), 3.07 (d, *J* = 5.7 Hz, 2H), 2.27 (s, 6H), 2.22 (s, 3H), 1.24 (t, *J* = 7.2 Hz, 6H).

General procedure for the synthesis of 1,2-diarylimidazoles (109–111). Based on a literature procedure.[31]

Step I. Based on *ca.* 10 mmol scale of *N*-(2,2-diethoxyethyl)mesitylamine (**113**). Triethylamine (2.00 eq.) and the benzoyl chloride derivative (**114**) (5.00 eq.) were added sequentially to a solution of *N*-(2,2-diethoxyethyl)mesitylamine (**113**) (1.00 eq.) in DCM (20 mL) under argon at 0 °C. The mixture was warmed to room temperature and stirred overnight. The solvent was then removed under reduced pressure and the residue was dissolved in acetone/ water (9:1 v/v, 20 mL). *para*-Toluenesulfonic acid (2.10 eq.) was added and the resulting mixture was heated to reflux for 2 h. The solvent was evaporated under reduced pressure and the residue was dissolved in EtOAc (80 mL). The solution was washed with sat. aq. Na_2CO_3 (2 × 50 mL). The washings were combined and extracted with EtOAc (3 × 80 mL). All organic layers were then combined, washed with water (20 mL), dried over $MgSO_4$ and filtered. After evaporation of the solvent, the residue (**A**) was used in Step II without further purification.

Step II. The product (**A**) from Step I was cautiously dissolved in acetic anhydride (15 mL). The

solution was cooled to 0 °C and aq. HBF_4 (50%, 1.20 eq.) was added slowly. The resulting mixture was stirred overnight at room temperature. It was then added dropwise to stirred diethyl ether (100 mL) to precipitate the intermediate salt **B**. Prolonged stirring, sonication or scratching was sometimes required to induce precipitation. The solid was filtered and washed with Et_2O (2 × 10 mL).

Step III. The product (**B**) from Step II was dissolved in MeCN (30 mL). NH_4OAc (1.70 eq.) was added and the solution was stirred at room temperature for 24 h. Next, aq. HBF_4 (50%, 1.70 eq.) was added and the reaction mixture was heated to reflux overnight. The solvent was evaporated under reduced pressure and the residue was dissolved in EtOAc (80 mL). The solution was washed with sat. aq. Na_2CO_3 (2 × 50 mL). The washings were combined and extracted with EtOAc (3 × 80 mL). All organic layers were then combined, washed with water (20 mL), dried over $MgSO_4$ and filtered. After evaporation of the solvent the residue was purified by flash chromatography on silica gel.

1-(2,4,6-Trimethylphenyl)-2-phenylimidazole (109). The general procedure for 1,2-diarylimidazoles was followed starting from *N*-(2,2-diethoxyethyl)mesitylamine (**113**) (6.63 g, 26.4 mmol, 1.00 eq.) and benzoyl chloride (**114a**) (18.6 g, 132 mmol, 5.00 eq.). The crude product was purified by flash chromatography on silica gel (eluent: gradient 1:0–6:4 *n*-hexane/ EtOAc v/v with *ca*. 0.5% NEt_3 as additive) to obtain 1-(2,4,6-trimethylphenyl)-2-phenylimidazole (**109**) as an off-white powder (4.40 g, 16.7 mmol, 63%). NMR analytical data were in agreement with those previously reported.[31] ^{1}H NMR (400 MHz, $CDCl_3$) δ (ppm) = 7.46 – 7.41 (m, 2H), 7.33 (d, *J* = 1.2 Hz, 1H), 7.26 – 7.20 (m, 3H), 6.99 – 6.96 (m, 2H), 6.91 (d, *J* = 1.2 Hz, 1H), 2.37 (s, 3H), 1.94 (s, 6H).

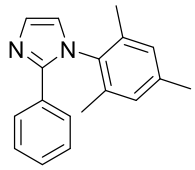

1-(2,4,6-Trimethylphenyl)-2-(4-fluorophenyl)imidazole (110). The general procedure for 1,2-diarylimidazoles was followed starting from *N*-(2,2-diethoxyethyl)mesitylamine (**113**) (3.17 g, 12.6 mmol, 1.00 eq.) and 4-fluorobenzoyl chloride (**114b**) (10.0 g, 63.0 mmol, 5.00 eq.). The crude product was purified by flash chromatography on silica gel (eluent: gradient 1:0–6:4 *n*-hexane/ EtOAc v/v with *ca*. 0.5% NEt_3 as additive) to obtain 1-(2,4,6-trimethylphenyl)-2-(4-fluorophenyl)imidazole (**110**) as an off-white powder (2.12 g, 7.56 mmol, 60%). M.pt. 107–109 °C; ^{1}H NMR (400 MHz, $CDCl_3$) δ (ppm) = 7.43 – 7.37 (m, 2H), 7.31 (d, *J* = 1.3 Hz, 1H), 6.98 (s, 2H), 6.96 – 6.88 (m, 3H), 2.37 (s, 3H), 1.93 (s, 6H); ^{13}C NMR (101 MHz, $CDCl_3$) δ (ppm) = 162.6 (d, *J* = 248.4 Hz), 145.5, 139.0, 135.2, 134.4, 129.4, 129.3, 128.6 (d, *J* = 8.2 Hz), 127.0 (d, *J* = 3.4 Hz), 121.9, 115.4 (d, *J* = 21.6 Hz), 21.1, 17.6; ^{19}F{^{1}H} NMR (376 MHz, $CDCl_3$) δ (ppm) = -113.1 (s, 1F); HRMS (ESI): *m/z* 281.1458 [MH^+]. Calcd. for $C_{18}H_{18}FN_2^+$: 281.1454.

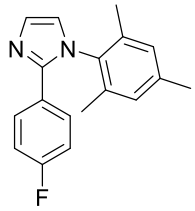

1-(2,4,6-Trimethylphenyl)-2-(2,4-difluorophenyl)imidazole (111). A modification of the general procedure for 1,2-diarylimidazoles was followed starting from *N*-(2,2-diethoxyethyl)mesitylamine (**113**) (3.33 g, 13.2 mmol, 1.00 eq.) and 2,4-difluorobenzoyl chloride (**114c**) (9.30 g, 66.0 mmol, 5.00 eq.) where aq. PF_6 (65%, 1.20 eq.) was used instead of aq. HBF_4 in step 2. The crude product was purified by flash chromatography on silica gel (eluent: gradient 1:0–4:6 *n*-hexane/ EtOAc v/v with *ca*. 0.5% NEt_3 as additive) to obtain 1-(2,4,6-trimethylphenyl)-2-(2,4-difluorophenyl)imidazole (**111**) as an off-white powder (2.22 g, 7.39 mmol, 56%). M.pt. 80.5–82 °C; ^{1}H NMR (400 MHz, $CDCl_3$) δ (ppm) = 7.37 (d, *J* = 1.3 Hz, 1H), 7.32 (td, *J* = 8.5, 6.4 Hz, 1H), 7.00 (d, *J* = 1.3 Hz, 1H), 6.89 (dd, *J* = 1.3, 0.7 Hz, 2H), 6.82 (dddd, *J* = 8.7, 7.8, 2.5, 0.7 Hz, 1H), 6.74 (ddd, *J* = 10.2, 8.9, 2.5 Hz, 1H), 2.31 (s, 3H), 1.96 – 1.93 (m, 6H); ^{13}C NMR (101 MHz, $CDCl_3$) δ (ppm) = 163.1 (dd, *J* = 251.7, 12.0 Hz), 160.3 (dd, *J* = 254.4, 12.8 Hz), 142.2 (d, *J* = 2.5 Hz), 138.6, 135.1, 133.4, 132.4 (dd, *J* = 9.7, 4.1 Hz), 129.8, 129.1, 122.1, 115.6 (dd, *J* = 14.4, 3.9 Hz), 111.4 (dd, *J* = 21.3, 3.9 Hz), 104.4 (t, *J* = 25.7 Hz), 21.0, 17.6; ^{19}F{^{1}H} NMR (376 MHz, $CDCl_3$) δ (ppm) = -108.2 (dd, *J* = 8.8, 0.9 Hz, 1F), -108.4 (dd, *J* = 8.9, 1.1 Hz, 1F); HRMS (ESI): *m/z* 299.1363 [MH^+]. Calcd. for $C_{18}H_{17}F_2N_2^+$: 299.1360.

Complex 105. $IrCl_3 \cdot 3H_2O$ (250 mg, 0.71 mmol, 1.00 eq.) and 1-(2,4,6-trimethylphenyl)-2-phenylimidazole (**109**) (390 mg, 1.49 mmol, 2.10 eq.) were added to 2-ethoxyethanol (10 mL) and the mixture was heated to reflux under an argon atmosphere for 24 h to form the dichloro-bridged diiridium intermediate *in situ*. The reaction mixture was then cooled to room temperature before addition of *N*,*N*′-bis(trifluoromethyl)hydrazide (**73**) (79 mg, 0.35 mmol, 0.50 eq.) and K_2CO_3 (147 mg, 1.06 mmol, 1.49 eq.). The mixture was then heated at reflux for a further 24 h before being cooled to room temperature. The solvent was evaporated, and the residue was purified by flash chromatography on silica gel (eluent: gradient 1:1–0:1 *n*-hexane/ DCM sat. K_2CO_3). After removing the solvent under reduced pressure, the residue was dissolved in a minimal amount of DCM (*ca*. 10 mL). Addition of hexane (*ca*. 20 mL) followed by reducing the volume of the mixture to 20 mL afforded complex **105** (400 mg, 0.24 mmol, 68%) as a light yellow precipitate which was isolated via filtration and washed with pentane. It was isolated as a single diastereomer. ^{1}H NMR (700 MHz, CD_2Cl_2, TMS) δ (ppm) = 7.28 (d, *J* = 1.5 Hz, $2H_{A5}$), 7.22 (d, *J* = 1.5 Hz, $2H_{B5}$), 7.11 – 7.07 (m, $10H_{A4,\ mesAr}$), 6.89 (d, *J* = 1.5 Hz, $2H_{B4}$), 6.61 (td, *J* = 7.5, 1.4 Hz,

$2H_{C4}$), 6.54 (ddd, *J* = 8.1, 7.2, 1.4 Hz, $2H_{D4}$), 6.49 (td, *J* = 7.5, 1.2 Hz, $2H_{C5}$), 6.43 – 6.41 (m, $4H_{D3,\ D5}$), 6.25 (dd, *J* = 7.5, 1.2 Hz, $2H_{C3}$), 6.14 – 6.12 (m, $4H_{C6,\ D6}$), 2.41 (s, $6H_{mesMe}$), 2.41 (s, $6H_{mesMe}$), 2.13 (s, $6H_{mesMe}$), 2.08 (s, $6H_{mesMe}$), 1.96 (s, $6H_{mesMe}$), 1.95 (s, $6H_{mesMe}$); ^{19}F NMR (376 MHz, CD_2Cl_2) δ (ppm) = -66.4 (s, 3F); ^{13}C NMR (176 MHz, CD_2Cl_2, TMS) δ (ppm) = 157.9 (C_{A2}), 157.1 (B_{B2}), 146.5 (C_{D2}), 144.3 (C_{C2}), 140.0* (C_{mesAr}), 135.8–135.7 ($C_{4\times mesAr}$), 135.7 (C_{C1}), 135.2 (C_{D1}), 133.8 (C_{D3}), 133.0 (C_{mesAr}), 132.8 (C_{mesAr}), 132.2 (C_{C3}), 129.4–129.3 ($C_{4\times mesAr}$), 127.7 (C_{C4}), 126.9* ($C_{B5,\ D4}$), 125.1 (C_{A5}), 121.0 ($C_{C6\ or\ D6}$), 120.7 (C_{C5}), 120.6 ($C_{C6\ or\ D6}$), 119.8 ($C_{A4,\ B4}$), 118.9 (C_{D5}), 20.9* (C_{mesMe}), 17.5* (C_{mesMe}), 17.0* (C_{mesMe}); MS (MALDI–TOF): *m/z* 1652.3 [M^+]. Calcd. for $C_{76}H_{68}F_6Ir_2N_{10}O_2^+$: 1652.5; Anal. Calcd. for $C_{76}H_{68}F_6Ir_2N_{10}O_2$: C, 55.26; H, 4.15; N, 8.48, Calcd. for $C_{76}H_{68}F_6Ir_2N_{10}O_2{\cdot}0.5CH_2Cl_2$: C, 54.23; H, 4.10; N, 8.27. Found: C, 54.40; H, 4.04; N, 8.34. Due to low solubility in organic solvents and coupling to ^{19}F nuclei, the quarternary bridge ^{13}C NMR signals were not observed. All signals that could be clearly identified in the ^{13}C, ^{1}H–^{13}C HSQC and ^{1}H–^{13}C HMBC NMR spectra are reported. The spectra are included on the USB stick. Some of the aromatic mesityl ^{13}C environments are reported as a range due to the large number of overlapping signals.

General procedure for the synthesis of the diarylhydrazide-bridged complexes (106–108). $IrCl_3{\cdot}3H_2O$ (250 mg, 0.71 mmol, 1.00 eq.) and the 1,2-diarylimidazole cyclometallating ligand (1.49 mmol, 2.10 eq.) were added to 2-ethoxyethanol (10 mL) and the mixture was heated to reflux under an argon atmosphere for 24 h to form the dichloro-bridged diiridium intermediate *in situ*. The reaction mixture was cooled to room temperature and the solvent was evaporated under reduced pressure. The residue was then dried under high vacuum. Next, *N*,*N*′-bis(pentafluorobenzoyl)hydrazide (**72c**) (149 mg, 0.35 mmol, 0.50 eq.) and K_2CO_3 (147 mg, 1.06 mmol, 1.49 eq.) were added and the mixture was suspended in dry diglyme (15 mL). It was then heated in a 120 °C heating mantle under argon overnight. The reaction was cooled to room temperature and the solvent was subsequently removed under reduced pressure. The residue was firstly purified by flash chromatography on silica gel (eluent: typically gradient *n*-hexane/ DCM sat. K_2CO_3) and then dissolved in minimal DCM (*ca*. 10 mL). Addition of hexane (*ca*. 20 mL) followed by reducing the volume of the mixture to 20 mL afforded the complexes as coloured precipitates which were isolated via filtration and washed with pentane.

Complex 106. Prepared according to the general procedure, complex **106** was obtained as a light yellow powder (460 mg, 0.25 mmol, 70%). The flash chromatography eluent was DCM sat. K_2CO_3. **106** was obtained as a diastereomeric mixture in a *ca.* 1:1 ratio. This complicates NMR assignment of the individual diastereomers making them very difficult to distinguish and so the overlapping spectra of the mixture are reported. ^{1}H and ^{13}C Signals are assigned based on whether they represent imidazole (A), phenyl (B) or mesityl (mes) environments. Coupling constants in ^{1}H NMR are ± 0.5 Hz. ^{1}H NMR (700 MHz, CD_2Cl_2, TMS) δ (ppm) = 7.64 – 7.62 (m, $2H_A$), 7.54 (d, *J* = 1.5 Hz, $2H_A$), 7.49 (d, *J* = 1.6 Hz, $2H_A$), 7.20 (d, *J* = 1.9 Hz, $2H_{mesAr}$), 7.17 (d, *J* = 1.9 Hz, $2H_{mesAr}$), 7.13 (d, *J* = 1.5 Hz, $2H_A$), 7.08 (dd, *J* = 9.6, 1.6 Hz, $10H_{2\times A,\ mesAr}$), 7.06 – 7.04 (m, $6H_{mesAr}$), 6.97 (d, *J* = 1.5 Hz, $2H_A$), 6.92 (d, *J* = 1.5 Hz, $2H_A$), 6.53 – 6.49 (m, $4H_{2\times B}$), 6.44 – 6.39 (m, $4H_{2\times B}$), 6.37 – 6.33 (m, $2H_B$), 6.33 – 6.28 (m, $8H_{4\times B}$), 6.18 – 6.11 (m, $10H_{5\times B}$), 6.10 (dd, *J* = 7.7, 1.3 Hz, $2H_B$), 6.07 (dd, *J* = 7.8, 1.3 Hz, $2H_B$), 2.43 – 2.42 (m, $12H_{mesMe}$), 2.40 (s, $6H_{mesMe}$), 2.40 (s, $6H_{mesMe}$), 2.37 (s, $6H_{mesMe}$), 2.27 (s, $6H_{mesMe}$), 2.08 (s, $6H_{mesMe}$), 2.06 (s, $6H_{mesMe}$), 2.01 – 2.00 (m, $18H_{mesMe}$), 1.82 (s, $6H_{mesMe}$); ^{19}F {^{1}H} NMR (376 MHz, CD_2Cl_2) δ (ppm) = -140.70 (dd, *J* = 24.7, 6.5 Hz, 2F), -141.89 (dd, *J* = 24.7, 7.2 Hz, 2F), -142.95 (dd, *J* = 24.5, 7.4 Hz, 2F), -143.87 (dd, *J* = 23.8, 7.5 Hz, 2F), -158.1 – - 157.9 (m, 4F), -161.53 (td, *J* = 24.1, 22.4, 7.5 Hz, 2F), -162.14 (td, *J* = 24.2, 7.5 Hz, 2F), -163.90 (td, *J* = 23.1, 7.6 Hz, 2F), -164.79 (td, *J* = 22.9, 7.2 Hz, 2F); ^{13}C NMR (176 MHz, CD_2Cl_2, TMS) δ (ppm) = 183.6* ($C_{C=O}$), 157.5 (C_A), 157.4 (C_A), 157.3 (C_A), 157.0 (C_A), 148.5 (C_B), 148.0 (C_B), 147.3 (C_B), 146.9 (C_B), 139.7 ($C_{4\times mesAr}$), 136.1* (C_B), 135.8 ($C_{4\times mesAr}$), 135.6 ($C_{4\times mesAr}$), 134.8 (C_B), 134.6 (C_B), 132.9 ($C_{4\times mesAr,\ 2\times B}$), 132.5 ($C_{2\times B}$) 129.5* ($C_{mesAr}$), 129.4$^{\#}$ (C_{mesAr}), 129.3$^{\#}$ (C_{mesAr}), 127.5 ($C_{2\times B}$), 127.2 (C_B), 127.0 (C_B), 126.7* (C_A), 125.5 (C_A), 125.4 (C_A), 120.9 ($C_{4\times B}$), 120.8 (C_B), 120.6* (C_B), 120.5 (C_A), 120.1 (C_A), 119.8 (C_A), 119.5 (C_A), 118.4 (C_B), 20.9* (C_{mesMe}), 20.8* (C_{mesMe}), 17.9* (C_{mesMe}), 17.3* (C_{mesMe}), 16.9 (C_{mesMe}), 16.8 (C_{mesMe}), 16.6 (C_{mesMe}), 16.5 (C_{mesMe}); MS (MALDI–TOF): *m/z* 1848.4 [M^+]. Calcd. for $C_{86}H_{68}F_{10}Ir_2N_{10}O_2^+$: 1848.5; Anal. Calcd. for $C_{86}H_{68}F_{10}Ir_2N_{10}O_2$: C, 55.90; H, 3.71; N, 7.58, Calcd. for $C_{86}H_{68}F_{10}Ir_2N_{10}O_2{\cdot}0.3CH_2Cl_2$: C, 55.33; H, 3.69; N, 7.48. Found: C, 55.32; H, 3.66; N, 7.46. Due to poor solubility in organic solvents and extensive coupling to ^{19}F nuclei, the ^{13}C environments corresponding to the pentafluorophenyl groups were not observed. All signals that could be clearly identified in the ^{13}C, ^{1}H–^{13}C HSQC and ^{1}H–^{13}C HMBC NMR spectra are reported. The spectra are included on the USB stick.

Complex 107. Prepared according to the general procedure, complex **107** was obtained as a light yellow powder (420 mg, 0.22 mmol, 62%). The flash chromatography eluent was DCM sat. K_2CO_3. **107** was obtained as a diastereomeric mixture in a *ca.* 1:0.6 ratio. MS (MALDI–TOF): *m/z* 1920.3 [M^+]. Calcd. for $C_{86}H_{64}F_{14}Ir_2N_{10}O_2^+$: 1920.4; Anal. Calcd. for $C_{86}H_{64}F_{14}Ir_2N_{10}O_2$: C, 53.80; H, 3.36; N, 7.30, Calcd. for $C_{86}H_{64}F_{14}Ir_2N_{10}O_2 \cdot 0.3CH_2Cl_2$: C, 53.28; H, 3.35; N, 7.20. Found: C, 53.22; H, 3.27; N, 7.20.

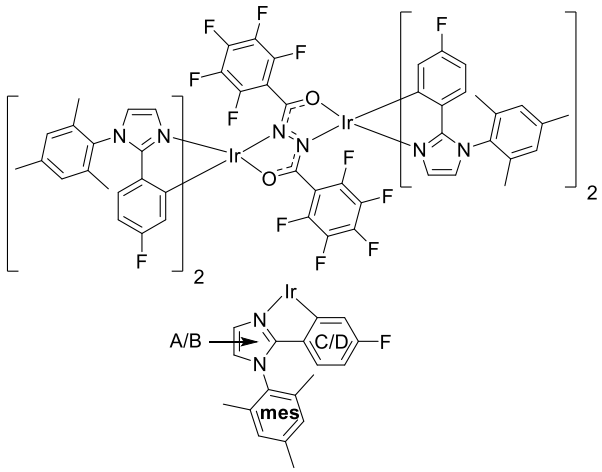

Major diastereomer: ^{1}H NMR (700 MHz, CD_2Cl_2, TMS) δ (ppm) = 7.51 (d, *J* = 1.5 Hz, $2H_A$), 7.43 (s, $2H_B$), 7.18 (s, $2H_{mesAr}$), 7.16 (d, *J* = 1.5 Hz, $2H_A$), 7.09 – 7.05 (m, $6H_{3 \times mesAr}$), 6.93 (d, *J* = 1.5 Hz, $2H_B$), 6.18 – 6.05 (m, $8H_{2 \times C,\ 2 \times D}$), 5.87 (dd, *J* = 10.2, 2.6 Hz, $2H_C$), 5.80 – 5.77 (m, $2H_D$), 2.43 (s, $6H_{mesMe}$), 2.39 (s, $6H_{mesMe}$), 2.24 (s, $6H_{mesMe}$), 2.07 (s, $6H_{mesMe}$), 2.01 (s, $6H_{mesMe}$), 1.81 (s, $6H_{mesMe}$); ^{19}F NMR (376 MHz, CD_2Cl_2) δ (ppm) = -113.13 (d, *J* = 1.4 Hz, 2F), -113.35 (d, *J* = 1.4 Hz, 2F), -141.74 (dd, *J* = 24.5, 7.6 Hz, 2F), -142.60 (dd, *J* = 23.4, 7.6 Hz, 2F), -157.4 – -157.5 (m, 2F), -161.29 (td, *J* = 24.5, 7.6 Hz, 2F), -163.90 (td, *J* = 22.7, 7.9 Hz, 2F); ^{13}C NMR (176 MHz, CD_2Cl_2, TMS) δ (ppm) = 162.6 (C!), 161.3 (C!), 156.7 (C_A), 156.8 – 156.4 (C!), 156.2 (C_B), 151.7 – 150.3 (C!), 139.9* (C_{mesAr}), 135.9 – 135.5 ($C_{4 \times mesAr}$), 132.5* (C_{mesAr}), 132.2 (C!), 131.0 (C!), 129.7 – 129.5 ($C_{4 \times mesAr}$), 126.4 (C_B), 125.2 (C_A), 120.8 (C_A), 119.8 (C_B), 118.6 (C_{C+D}), 108.0 – 107.5 (C!), 105.6 – 105.4 (C!), 20.9* (C_{mesMe}), 18.0 (C_{mesMe}), 17.3 (C_{mesMe}), 16.5* (C_{mesMe}).

Minor diastereomer: ^{1}H NMR (700 MHz, CD_2Cl_2, TMS) δ (ppm) = 7.57 (d, *J* = 1.5 Hz, $2H_A$), 7.21 (s, $2H_{mesAr}$), 7.09 (d, *J* = 1.5 Hz, $2H_A$), 7.09 – 7.05 (m, $6H_{3 \times mesAr}$), 7.04 (d, *J* = 1.5 Hz, $2H_B$), 6.98 (d, *J* = 1.5 Hz, $2H_B$), 6.18 – 6.05 (m, $8H_{2 \times C,\ 2 \times D}$), 5.80 – 5.77 (m, $2H_D$), 5.71 (dd, *J* = 10.1, 2.6 Hz, $2H_C$), 2.43 (s, $6H_{mesMe}$), 2.40 (s, $6H_{mesMe}$), 2.35 (s, $6H_{mesMe}$), 2.05 (s, $6H_{mesMe}$), 2.01 (s, $6H_{mesMe}$), 1.99 (s, $6H_{mesMe}$); ^{19}F NMR (376 MHz, CD_2Cl_2) δ (ppm) = -113.33 (s, 2F), -113.46 (s, 2F), -140.57 (dd, *J* = 24.2, 6.8 Hz, 2F), -143.33 (dd, *J* = 23.0, 6.0 Hz, 2F), -157.4 – -157.5 (m, 2F), -160.83 (td, *J* = 24.7, 8.0 Hz, 2F), -164.37 (td, *J* = 21.4, 7.3 Hz, 2F); ^{13}C NMR (176 MHz, CD_2Cl_2, TMS) δ (ppm) = 162.6 (C!), 161.3 (C!), 156.8 – 156.4 (C!), 156.7 (C_A), 156.4 (C_B), 151.7 – 150.3 (C!), 139.2* (C_{mesAr}), 135.9 – 135.5 ($C_{4 \times mesAr}$), 132.5* (C_{mesAr}), 132.2 (C!), 131.0 (C!), 129.7 – 129.5 ($C_{4 \times mesAr}$), 126.4 (C_A), 125.2 (C_B), 120.4 (C_A), 120.1 (C_B), 118.6 (C_D), 118.1 (C_C), 108.0 – 107.5 (C!), 105.6 – 105.4 (C!), 20.9* (C_{mesMe}), 18.0 (C_{mesMe}), 17.3 (C_{mesMe}), 16.8 (C_{mesMe}), 11.9 (C_{mesMe}).

Due to poor solubility in organic solvents and extensive coupling to ^{19}F nuclei, some quaternary ^{13}C environments were not observed. As many of the signals corresponding to rings C and D heavily overlap in the ^{1}H NMR spectrum of the diastereomeric mixture, their ^{13}C environments could not be unambiguously assigned to a ring or diastereomer. Such signals/ regions are labelled "!". All signals that could be clearly identified in the ^{13}C, ^{1}H–^{13}C HSQC and ^{1}H–^{13}C HMBC NMR spectra are reported. The spectra are included on the USB stick. Single crystals suitable for X-ray diffraction were grown by vapour diffusion of hexane into a DCM solution of the complex.

Complex 108. Prepared according to the general procedure, complex **108** was obtained as a tan powder (334 mg, 0.17 mmol, 47%). The flash chromatography eluent was gradient 9:1–4:6 *n*-hexane/ DCM sat. K_2CO_3 v/v. During precipitation the compound gelled, implying a propensity to interact with DCM. This is evident from the CHN result and residual DCM observed in the ^{1}H NMR spectrum of the complex after drying. **107** was obtained as a diastereomeric mixture in a *ca.* 1:0.9 ratio. MS (MALDI–TOF): *m/z* 1992.1 [M^+]. Calcd. for $C_{86}H_{60}F_{18}Ir_2N_{10}O_2^+$: 1992.4; Anal. Calcd. for $C_{86}H_{60}F_{18}Ir_2N_{10}O_2$: C, 51.86; H, 3.04; N, 7.03, Calcd. for $C_{86}H_{60}F_{18}Ir_2N_{10}O_2 \cdot 1CH_2Cl_2$: C, 50.31; H, 3.01; N, 6.74. Found: C, 50.31; H, 2.92; N, 6.79.

Major diastereomer: ^{1}H NMR (700 MHz, THF-d_8) δ (ppm) = 7.66 (d, *J* = 1.5 Hz, $2H_{A5}$), 7.31 (d, *J* = 1.5 Hz, $2H_{A4}$), 7.25 (d, *J* = 1.6 Hz, $2H_{B5}$), 7.11 (d, *J* = 2.0 Hz, $2H_{mesAr}$), 7.09 (d, *J* = 1.6 Hz, $2H_{B4}$), 7.00 (bs, $4H_{mesAr}$), 6.99 (s, $2H_{mesAr}$), 6.01 (ddd, *J* = 11.3, 8.9, 2.4 Hz, $2H_{D4}$), 5.96 (ddd, *J* = 11.5, 9.0, 2.4 Hz, $2H_{C4}$), 5.64 (dd, *J* = 9.0, 2.4 Hz, $2H_{D6}$), 5.58 (dd, *J* = 9.1, 2.4 Hz, $2H_{C6}$), 2.39 (s, $6H_{mesMe}$), 2.37 (s, $6H_{mesMe}$), 2.34 (s, $6H_{mesMe}$), 2.04 (s, $6H_{mesMe}$), 2.02 –2.00 (m, $12H_{mesMe}$); $^{19}F\{^{1}H\}$ NMR (376 MHz, THF-d_8) δ (ppm) = -105.78 (d, *J* = 7.9 Hz, 2F), -106.45 – -106.55 (m, 2F), -112.32 (d, *J* = 7.9 Hz, 2F), -112.70 – -112.80 (m, 2F), -141.07 (dd, *J* = 24.4, 6.4 Hz, 2F), -143.23 (dd, *J* = 24.4, 7.1 Hz, 2F), -158.18 – -158.28 (m, 2F), -162.45 (td, *J* = 24.3, 7.4 Hz, 2F), -164.82 (td, *J* = 22.0, 21.5, 7.1 Hz, 2F); ^{13}C NMR (176 MHz, THF-d_8) δ (ppm) = 164.3 (d, *J* = 250 Hz, C_{D5}), 164.0 (d, *J* = 250 Hz, C_{C5}), 159.0 (d, *J* = 247 Hz, C_{C3}), 158.2 (C_{A2}), 158.0 (d, *J* = 264 Hz, C_{D3}) 157.5 (C_{B2}), 140.5* (C_{mesAr}), 137.7 (C_{mesAr}), 137.6 (C_{mesAr}), 137.5 (C_{mesAr}), 137.0* (C_{mesAr}), 136.7 (C_{mesAr}), 130.6 (C_{mesAr}), 130.3 (C_{mesAr}), 130.2 (C_{mesAr}), 130.1 (C_{mesAr}), 128.4 (C_{A5}), 127.3 (C_{B4}), 124.1 (C_{A4}), 123.7 (C_{B5}), 121.0 (C_{D2}), 120.0 (C_{C2}), 116.3 (d, *J* = 16.9 Hz, C_{D6}), 116.0 (d, *J* = 16.7 Hz, C_{C6}), 98.0 (t, *J* = 25 Hz, C_{D4}), 96.2 (t, *J* = 25 Hz, C_{C4}), 22.0* (C_{mesMe}), 19.1 (C_{mesMe}), 18.5 (C_{mesMe}), 18.4 (C_{mesMe}), 18.2 (C_{mesMe}).

Minor diastereomer:

^{1}H NMR (700 MHz, THF-d_8) δ (ppm) = 7.56 (d, J = 1.5 Hz, 2H$_{A5}$), 7.51 (d, J = 1.7 Hz, 2H$_{B5}$), 7.39 (d, J = 1.5 Hz, 2H$_{A4}$), 7.17 (d, J = 1.7 Hz, 2H$_{B4}$), 7.12 – 7.10 (m, 2H$_{mesAr}$), 7.08 (s, 2H$_{mesAr}$), 7.00 – 6.97 (m, 2H$_{mesAr}$), 6.97 (s, 2H$_{mesAr}$), 6.02 – 5.98 (m, 2H$_{C4}$), 5.96 – 5.92 (m, 2H$_{D4}$) 5.74 (dd, J = 9.2, 2.3 Hz, 2H$_{D6}$), 5.61 (dd, J = 9.0, 2.4 Hz, 2H$_{C6}$), 2.40 (s, 6H$_{mesMe}$), 2.28 (s, 6H$_{mesMe}$), 2.08 (s, 6H$_{mesMe}$), 2.04 (s, 6H$_{mesMe}$), 2.02 – 1.99 (m, 6H$_{mesMe}$), 1.86 (s, 6H$_{mesMe}$); ^{19}F{^{1}H} NMR (376 MHz, THF-d_8) δ (ppm) = -105.71 (d, J = 8.0 Hz, 2F), -106.45 – -106.55 (m, 2F), -111.87 (d, J = 8.0 Hz, 2F), -112.70 – 112.80 (m, 2F), -142.25 (dd, J = 24.7, 7.7 Hz, 2F), -142.54 (dd, J = 24.7, 7.2 Hz, 2F), -158.18 – -158.28 (m, 2F), -162.72 (td, J = 23.7, 7.2 Hz, 2F), -164.12 (td, J = 23.7, 7.7 Hz, 2F); ^{13}C NMR (176 MHz, THF-d_8) δ (ppm) = 164.4 (d, J = 250 Hz, C$_{D5}$), 164.1 (d, J = 250 Hz, C$_{C5}$), 159.3 (d, J = 245 Hz, C$_{C3}$), 158.3 (d, J = 260 Hz, C$_{D3}$), 157.7 (C$_{A2 + B2}$), 140.6* (C$_{mesAr}$), 137.9 (C$_{mesAr}$), 137.6 (C$_{mesAr}$), 137.5 (C$_{mesAr}$), 137.0* (C$_{mesAr}$), 136.7 (C$_{mesAr}$), 130.5 (C$_{mesAr}$), 130.4 (C$_{mesAr}$), 130.3 (C$_{mesAr}$), 130.2 (C$_{mesAr}$), 128.5 (C$_{B5}$), 127.3 (C$_{A5}$), 124.4 (C$_{A4}$), 123.6 (C$_{B4}$), 120.9 (C$_{C2}$), 120.0 (C$_{D2}$), 116.3 (d, J = 17 Hz, C$_{D6}$), 116.0 (d, J = 16 Hz, C$_{C6}$), 98.0 (t, J = 27 Hz, C$_{C4}$), 96.0 (t, J = 26 Hz, C$_{D4}$), 21.90* (C$_{mesMe}$), 19.1 (C$_{mesMe}$), 18.5 (C$_{mesMe}$), 18.1 (C$_{mesMe}$), 17.8 (C$_{mesMe}$).

Due to poor solubility in organic solvents and extensive coupling to ^{19}F nuclei, some quaternary ^{13}C environments were not observed (bridge carbons, C1 and D1). All signals that could be clearly identified in the ^{13}C, ^{1}H–^{13}C HSQC and ^{1}H–^{13}C HMBC NMR spectra are reported. The spectra are included on the USB stick. Single crystals suitable for X-ray diffraction were grown by vapour diffusion of methanol into a THF solution of the complex.

Synthetic details for Chapter 5: Intramolecular π–π stacking in monoiridium complexes featuring a chiral oxazoline ancillary ligand

General

[Ir(dfppy)$_2$μ–Cl]$_2$ was synthesized according to a literature procedure.[20] NMR spectra for all novel compounds are included as .pdf files on the USB stick submitted as Supporting Information.

***rac*-1-(Pentafluorophenyl)ethane-1,2-diol (128).** Prepared according to a literature procedure.[32]

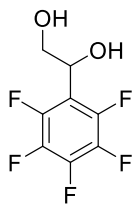

$K_3Fe(CN)_6$ (9.90 g, 30.0 mmol, 3.00 eq.), K_2CO_3 (4.15 g, 30.0 mmol, 3.00 eq.), DABCO (56 mg, 0.5 mmol, 5 mol%) and $K_2OsO_2(OH)_4$ (37 mg, 0.1 mmol, 1 mol%) were dissolved in *tert*-BuOH/ H_2O (1:1, 100 mL) and the mixture was stirred mechanically. The resulting orange solution was cooled to 0 °C and pentafluorostyrene (**127**) (1.94 g, 10.0 mmol, 1.00 eq.) was added dropwise. The mixture was stirred for a further 30 min at 0 °C and thickened to a cloudy orange mixture. The reaction was warmed to room temperature over 2

h and then stirred for a further 2 h at that temperature. The mixture was then diluted with EtOAc (25 mL), quenched with Na_2SO_3 (*ca*. 10 g) and stirred for 10 min. The phases were separated and the aqueous layer was further extracted with EtOAc (3 × 50 mL). The combined extracts were washed with 1 M HCl (50 mL), followed by sat. aq. $NaHCO_3$. They were then dried with $MgSO_4$, filtered and the solvent evaporated to afford 1-pentafluorophenylethane-1,2-diol (**128**) (2.21 g, 9.70 mmol, 97%) as a white powder which was used directly in the next step without further purification. NMR data were in agreement with those previously reported.[32] ^{1}H NMR (400 MHz, $CDCl_3$) δ (ppm) = 5.22 (dd, *J* = 8.0, 4.0 Hz, 1H), 4.02 (ddt, *J* = 10.7, 8.0, 1.3 Hz, 1H), 3.84 (dd, *J* = 10.7, 4.0 Hz, 1H), 2.94 (bs, 1H), 2.26 (bs, 1H).

***rac*-2-Amino-2-(pentafluorophenyl)ethanol (129).** Prepared according to a literature procedure.[32]

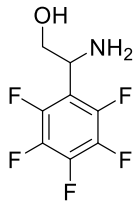

rac-1-Pentafluorophenylethane-1,2-diol (**128**) (3.00 g, 13.15 mmol, 1.00 eq.) was dissolved in dry MeCN (22 mL) under argon. Conc. H_2SO_4 (98%, 12.9 g, 131.5 mmol, 10.0 eq) was added dropwise to the mixture at room temperature before it was heated to reflux for 3 h. The mixture was then cooled to room temperature and water (33 mL) was added. The organic solvent was removed by distillation under atmospheric pressure to leave an aqueous residue that was subsequently heated to reflux for 2 h. The mixture was cooled to room temperature and DCM (10 mL) was added. The biphasic mixture was stirred for 5 min and the layers were separated. The aqueous layer was next treated with 50% NaOH solution until pH 13 and finally extracted with EtOAc (3 × 50 mL). The combined extracts were washed with water (20 mL), dried over $MgSO_4$, filtered and the solvent removed under reduced pressure to afford *rac*-2-amino-2-(pentafluorophenyl)ethanol (**129**) (2.24 g, 9.86 mmol, 75%), which was sufficiently pure for use in the next step. NMR data were in agreement with those previously published.[32] ^{1}H NMR (400 MHz, $CDCl_3$) δ (ppm) = 4.39 (dd, *J* = 8.9, 5.4 Hz, 1H), 3.83 – 3.77 (m, 1H), 3.76 – 3.69 (m, 1H), 2.10 (bs, 3H).

***rac*-4-(Pentafluorophenyl)-2-(2-hydroxy-5-trifluoromethylphenyl)oxazoline (131).** *rac*-2-Amino-2-(pentafluorophenyl)ethanol (**129**) (1.21 g, 5.33 mmol, 1.21 eq.) and 2-hydroxy-5-trifluoromethylbenzonitrile (**130**) (829 mg, 4.40 mmol, 1.00 eq.) were combined in dry toluene (12 mL). A solution of $ZnCl_2$ in THF was added (0.7 M, 0.31 mL, 0.22 mmol, 5 mol%) and the resulting mixture was heated to reflux for 20 h. The reaction mixture was cooled to room temperature and evaporated under reduced pressure. The residue was purified by flash chromatography on silica gel (eluent: gradient 1:0–1:3 *n*-hexane/ DCM with *ca*. 0.5% NEt_3 as additive) to afford *rac*-4-(pentafluorophenyl)-2-(2-hydroxy-5-trifluoromethylphenyl)oxazoline (**131**) as a white powder (730 mg, 1.80 mmol, 41%). M.pt. 117–119 °C; ^{1}H NMR (700 MHz, $CDCl_3$) δ

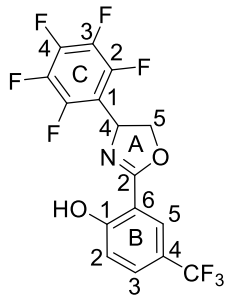

(ppm) = 11.91 (s, $1H_{OH}$), 8.02 (d, *J* = 2.3 Hz, $1H_{B5}$), 7.64 (dd, *J* = 8.8, 2.3 Hz, $1H_{B3}$), 7.09 (d, *J* = 8.8 Hz, $1H_{B2}$), 5.83 (dd, *J* = 10.7, 7.6 Hz, $1H_{A4}$), 4.81 (dd, *J* = 10.7, 8.8 Hz, $1H_{A5}$), 4.51 (dd, *J* = 8.2, 7.6 Hz, $1H_{A5}$); ^{13}C NMR (101 MHz, $CDCl_3$) δ (ppm) = 166.5 (C_{A2}), 161.3 (C_{B1}), 146.0 – 136.0 ($C_{ring\ C}$), 130.7 (C_{B3}), 126.2 (C_{B5}), 123.9 (q, *J* = 270 Hz, C_{CF3}), 121.4 (q, *J* = 32.3 Hz, C_{B4}), 117.6 (C_{B2}), 109.9 (C_{B6}), 71.2 (C_{A5}), 58.93 (C_{A4}); $^{19}F\{^1H\}$ NMR (376 MHz, $CDCl_3$) δ (ppm) = -61.7 (d, *J* = 1.1 Hz, $3F_{CF3}$), -143.3 – -143.5 (m, $2F_{C2}$), -153.1 (ddt, *J* = 23.1, 21.0, 2.2 Hz, $1F_{C4}$), -160.9 – -161.1 (m, $2F_{C3}$); HRMS (ESI): *m/z* 398.0459 [MH^+]. Calcd. for $C_{16}H_8F_8NO_2^+$: 398.0422. Due to extensive coupling to ^{19}F nuclei, the ^{13}C signals for ring C are stated as a range.

Complexes 132a and **132b.** $[Ir(dfppy)_2\mu–Cl]_2$ (315 mg, 0.26 mmol, 1.00 eq.), *rac*-4-(pentafluorophenyl)-2-(2-hydroxy-5-trifluoromethylphenyl)oxazoline (**131**) (211 mg, 0.53 mmol, 2.05 eq.) and K_2CO_3 (90 mg, 0.65 mmol, 2.50 eq.) were combined in dry diglyme (10 mL) under argon and heated in a 140 ° C heating mantle overnight. The reaction mixture was cooled to room temperature and the solvent evaporated under reduced pressure. The residue was purified by flash chromatography on silica gel (eluent: gradient 1:9–4:6 DCM sat. K_2CO_3/ *n*-hexane v/v) to elute **132a**. Increasing the solvent polarity to 6:4 DCM sat. K_2CO_3/ *n*-hexane v/v eluted **132b**. Each diastereomer was further purified through dissolving it in minimal DCM (*ca*. 10 mL), adding *n*-hexane (30 mL), and reducing the solvent volume to *ca.* 15 mL to induce precipitation. After cooling in a freezer for *ca.* 1 h the precipitates were isolated via filtration and washed with ice cold pentane before being dried under high vacuum.

132a. Isolated as a yellow microcrystalline powder (331 mg, 0.34 mmol, 66%). ^1H NMR (600 MHz, 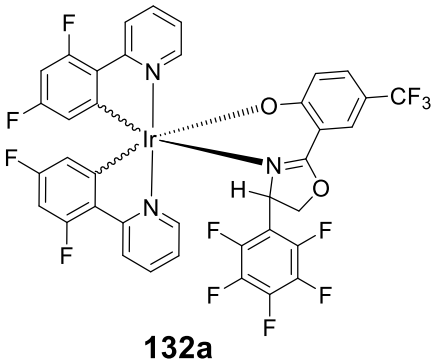
132a
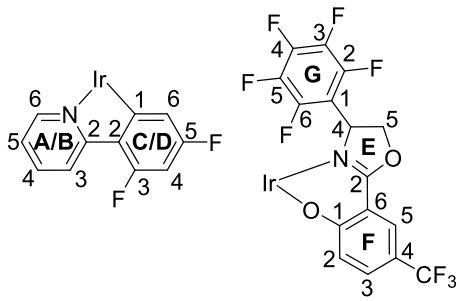
d$_2$-1,1,2,2-TCE) δ (ppm) = 8.76 (dt, *J* = 5.5, 1.3 Hz, $1H_{A6}$), 8.36 (dt, *J* = 5.5, 1.6 Hz, $1H_{B6}$), 8.26 (d, *J* = 8.5 Hz, $1H_{B3}$), 8.08 (dd, *J* = 2.7, 1.0 Hz, $1H_{F5}$), 7.89 (d, *J* = 8.4 Hz, $1H_{A3}$), 7.82 (td, *J* = 8.5, 1.6 Hz, $1H_{B4}$), 7.76 (ddd, *J* = 8.4, 7.6, 1.3 Hz, $1H_{A4}$), 7.39 (dd, *J* = 9.2, 2.7 Hz, $1H_{F3}$), 7.25 – 7.21 (m, $2H_{A5,\ B5}$), 6.74 (d, *J* = 9.2 Hz, $1H_{F2}$), 6.45 – 6.39 (m, $2H_{C4,\ D4}$), 5.80 (dd, *J* = 8.6, 2.3 Hz, $1H_{C6}$), 5.51 (dd, *J* = 10.5, 5.7 Hz, $1H_{E4}$), 5.27 (dd, *J* = 8.8, 2.4 Hz, $1H_{D6}$), 4.86 (dd, *J* = 10.5, 9.4 Hz, $1H_{E5}$), 4.29 (dd, *J* = 9.4, 5.7 Hz, $1H_{E5}$); $^{19}F\{^1H\}$ NMR (376 MHz, *d*$_2$-1,1,2,2-TCE) δ (ppm) = -60.34 (s, $3F_{CF3}$), -107.03 (d, *J* = 10.5 Hz, $1F_{dfppy}$), -107.63 (d, *J* = 9.9 Hz, $1F_{dfppy}$), -109.80 (d, *J* = 10.0 Hz, $1F_{dfppy}$), -110.36 (dd, *J* = 10.5, 2.8 Hz, $1F_{dfppy}$), -141.73 (dd, *J* = 22.6, 7.5 Hz, $1F_{G2/\ G6}$), -142.44 (dd, *J* = 22.2, 7.7 Hz, $1F_{G2/\ G6}$), -152.55 (t, *J* = 21.0 Hz, $1F_{G4}$), -

159.59 (td, *J* = 21.0, 7.5 Hz, $1F_{G3/G5}$), -160.76 (td, *J* = 21.0, 7.5 Hz, $1F_{G3/G5}$); ^{13}C NMR (151 MHz, d_2-1,1,2,2-TCE) δ (ppm) = 171.4 (C_{F1}), 165.5 (d, *J* = 9 Hz, C_{B2}), 164.4 (d, *J* = 263 Hz, C_{D5}), 165.0 – 160.0 ($C_{Ring\ G}$), 164.2 (d, J = 258 Hz, C_{C5}), 164.1 (d, *J* = 7 Hz, C_{A2}), 163.82 (C_{F6}), 161.6 (t, *J* = 273 Hz, C_{C3}), 161.6 (t, *J* = 273 Hz, C_{D3}), 155.5 (d, *J* = 6.0 Hz, C_{D1}), 150.5 (d, *J* = 7.1 Hz, C_{C1}), 148.7 (C_{A6}), 147.56 (C_{B6}), 138.30 (C_{B5}), 137.9 (C_{A4}), 130.1 (C_{F3}), 128.8 (C_{F5}), 128.4 (C_{D2}), 128.3 (C_{C2}), 125.8 (C_{F2}), 123.4 (d, *J* = 20.4 Hz, C_{B3}), 122.6 (C_{B5}), 122.2 (C_{A5}), 121.9 (d, *J* = 19.5 Hz, C_{A3}), 115.0 (d, *J* = 14.7 Hz, C_{C6}), 114.9 (C_{CF3}), 113.5 (C_{E2}), 113.3 (d, *J* = 15.9 Hz, C_{D6}), 108.7 (C_{F4}), 98.1 (t, *J* = 26.5 Hz, C_{D4}), 97.4 (t, *J* = 26.9 Hz, C_{C4}), 72.4 (C_{E5}), 61.3 (C_{E4}); HRMS (ESI): *m/z* 968.0905 [MH^+]. Calcd. for $C_{38}H_{19}F_{12}IrN_3O_2^+$: 968.0892; Anal. Calcd. for $C_{38}H_{18}F_{12}IrN_3O_2$: C, 47.11; H, 1.87; N, 4.34. Found: C, 46.98; H, 1.97; N, 4.26. Due to extensive coupling to ^{19}F nuclei, the ^{13}C signals for ring G are stated as a range.

132b. Isolated as an amorphous yellow powder (151 mg, 0.16 mmol, 30%). ^1H NMR (600 MHz, d_2-1,1,2,2-TCE) δ (ppm) = 8.96 (ddd, *J* = 5.8, 1.6, 0.7 Hz, $1H_{A6}$), 8.52 (dt, *J* = 5.6, 1.3 Hz, $1H_{B6}$), 8.36 (d, *J* = 8.5 Hz, $1H_{A3}$), 8.16 (d, *J* = 7.4 Hz, $1H_{B3}$), 7.98 – 7.93 (m, $2H_{A4,\ F5}$), 7.73 (td, *J* = 7.4, 1.3 Hz, $1H_{B4}$), 7.35 – 7.29 (m, $2H_{A5,\ F3}$), 7.04 (ddd, *J* = 7.4, 5.6, 1.4 Hz, $1H_{B5}$), 6.56 (d, *J* = 9.0 Hz, $1H_{F2}$), 6.41 (ddd, *J* = 12.0, 9.2, 2.4 Hz, $1H_{C4}$), 6.32 (ddd, *J* = 12.0, 9.3, 2.4 Hz, $1H_{D4}$), 5.47 (dd, *J* = 8.7, 2.4 Hz, $1H_{C6}$), 5.19 (dd, *J* = 8.6, 2.4 Hz, $1H_{D6}$), 4.63 – 4.54 (m, $2H_{E4,\ E5}$), 4.36 – 4.29 (m, $1H_{E5}$); $^{19}F\{^1H\}$ NMR (376 MHz, d_2-1,1,2,2-TCE) δ (ppm) = -60.36 (s, $3F_{CF3}$), -107.94 (d, *J* = 9.7 Hz, $1F_{dfppy}$), -108.78 (d, *J* = 10.2 Hz, $1F_{dfppy}$), -109.21 (d, *J* = 10.3 Hz, $1F_{dfppy}$), -109.98 (d, *J* = 9.8 Hz, $1F_{dfppy}$), -140.59 (d, *J* = 22.5 Hz, $1F_{G2/G6}$), -142.17 (d, *J* = 22.5 Hz, $1F_{G2/G6}$), -152.11 (t, *J* = 20.9 Hz, $1F_{G4}$), -159.31 (t, *J* = 19.5 Hz, $1F_{G3/G5}$), -161.08 (t, *J* = 22.1 Hz, $1F_{G3/G5}$); ^{13}C NMR (151 MHz, d_2-1,1,2,2-TCE) δ (ppm) = 172.50 (C_{F1}), 165.0 – 160.0 ($C_{Ring\ G}$), 164.9 (C_{A2}), 164.7 (C_{B2}), 164.2 (C_{F6}), 162.4 (d, J = 259 Hz, C_{D5}), 162.3 (d, *J* = 249 Hz, C_{C5}), 161.2 (d, J = 261 Hz, C_{D3}), 160.6 Hz (d, J = 259 Hz, C_{C3}), 154.2 (d, *J* = 6.2 Hz, C_{C1}), 151.4 (d, *J* = 7.5 Hz, C_{D1}), 149.6 (C_{B6}), 149.0 (C_{A6}), 138.8 (C_{A4}), 138.3 (C_{B4}), 130.4 (C_{F3}), 128.6 (C_{C2}), 128.4 (C_{D2}), 128.0 (C_{F5}), 124.9 (C_{F2}), 122.9 (C_{B3}), 122.8 (C_{A3}), 122.5 (C_{A5}), 121.8 (C_{B5}), 115.3 (C_{CF3}), 114.0 (d, *J* = 15.7 Hz, C_{D6}), 113.5 (d, *J* = 16.5 Hz, C_{C6}), 113.1 (C_{E2}), 110.7 (C_{F4}), 97.9 (t, J = 25.9 Hz, C_{C4}), 96.8 (t, *J* = 27.9 Hz, C_{D4}), 71.5 (C_{E5}), 59.7 (C_{E4}); HRMS (ESI): *m/z* 968.0919 [MH^+]. Calcd. for $C_{38}H_{19}F_{12}IrN_3O_2^+$: 968.0892; Anal. Calcd. for $C_{38}H_{18}F_{12}IrN_3O_2$: C, 47.11; H, 1.87; N, 4.34; Anal. Calcd. for $C_{38}H_{18}F_{12}IrN_3O_2 \cdot 0.6CH_2Cl_2$: C, 45.46; H, 1.90; N, 4.12; Found: C, 45.30;

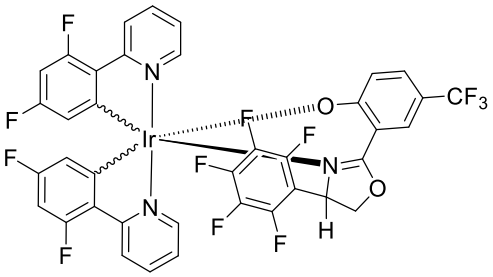

132b

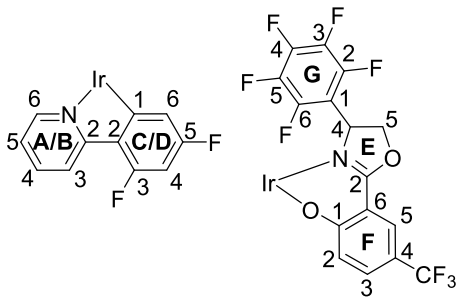

H, 1.84; N, 4.11. Due to extensive coupling to ^{19}F nuclei, the ^{13}C signals for ring C are stated as a range.

References

1 Gaussian 09, Revision A.02, M. J. Frisch, G. W. Trucks, H. B. Schlegel, G. E. Scuseria, M. A. Robb, J. R. Cheeseman, G. Scalmani, V. Barone, B. Mennucci, G. A. Petersson, H. Nakatsuji, M. Caricato, X. Li, H. P. Hratchian, A. F. Izmaylov, J. Bloino, G. Zheng, J. L. Sonnenberg, M. Hada, M. Ehara, K. Toyota, R. Fukuda, J. Hasegawa, M. Ishida, T. Nakajima, Y. Honda, O. Kitao, H. Nakai, T. Vreven, J. A. Montgomery, Jr., J. E. Peralta, F. Ogliaro, M. Bearpark, J. J. Heyd, E. Brothers, K. N. Kudin, V. N. Staroverov, R. Kobayashi, J. Normand, K. Raghavachari, A. Rendell, J. C. Burant, S. S. Iyengar, J. Tomasi, M. Cossi, N. Rega, J. M. Millam, M. Klene, J. E. Knox, J. B. Cross, V. Bakken, C. Adamo, J. Jaramillo, R. Gomperts, R. E. Stratmann, O. Yazyev, A. J. Austin, R. Cammi, C. Pomelli, J. W. Ochterski, R. L. Martin, K. Morokuma, V. G. Zakrzewski, G. A. Voth, P. Salvador, J. J. Dannenberg, S. Dapprich, A. D. Daniels, O. Farkas, J. B. Foresman, J. V. Ortiz, J. Cioslowski, D. J. Fox, Gaussian, Inc., Wallingford CT, 2009.

2 A.-R. Allouche, *J. Comput. Chem.*, 2011, **32**, 174–182.

3 N. M. O'Boyle, A. L. Tenderholt and K. M. Langner, *J. Comput. Chem.*, 2008, **29**, 839–845.

4 A. D. Becke, *J. Chem. Phys.*, 1993, **98**, 5648.

5 C. Lee, W. Yang and R. G. Parr, *Phys. Rev. B*, 1988, **37**, 785–789.

6 P. J. Hay and W. R. Wadt, *J. Chem. Phys.*, 1985, **82**, 270–283.

7 W. R. Wadt and P. J. Hay, *J. Chem. Phys.*, 1985, **82**, 284–298.

8 P. J. Hay and W. R. Wadt, *J. Chem. Phys.*, 1985, **82**, 293–310.

9 G. A. Petersson, A. Bennett, T. G. Tensfeldt, M. A. Al-Laham, W. A. Shirley and J. Mantzaris, *J. Chem. Phys.*, 1991, **94**, 6081–6090.

10 J. Melorose, R. Perroy and S. Careas, *J. Chem. Phys.*, 1988, **89**, 2193–2218.

11 L. Krause, R. Herbst-Irmer, G. M. Sheldrick and D. Stalke, *J. Appl. Crystallogr.*, 2015, **48**, 3–10.

12 G. M. Sheldrick, *Acta Crystallogr. A*, 2008, **A64**, 112–122.

13 L. J. Bourhis, O. V. Dolomanov, R. J. Gildea, J. A. K. Howard and H. Puschmann, *Acta Crystallogr.*, 2015, **A71**, 7–13.

14 G. M. Sheldrick, *Acta Crystallogr. C*, 2015, **71**, 3–8.

15 G. M. Sheldrick, *Acta Crystallogr.*, 2015, **C71**, 3–8.

16 R. Davidson, Y. Hsu, T. Batchelor and A. Beeby, *Dalton Trans.*, 2016, **45**, 11496–11507.

17 H. Benjamin, Y. Zheng, A. S. Batsanov, M. A. Fox, H. A. Al-Attar, A. P. Monkman and M. R. Bryce, *Inorg. Chem.*, 2016, **55**, 8612–8627.

18 L-O. Pålsson and A. P. Monkman, *Adv. Mater.*, 2002, **14**, 757–758.

19 J. C. de Mello, H. F. Wittmannn and R. H. Friend, *Adv. Mater.*, 1997, **9**, 230–232.

20 S. Sprouse, K. A. King, P. J. Spellane and R. J. Watts, *J. Am. Chem. Soc.*, 1984, **106**, 6647–6653.

21 I. L. Finar and D. M. Rackham, *J. Chem. Soc. B*, 1968, **0**, 211–214.

22 D. Toummini, A. Tlili, J. Berges, F. Ouazzani and M. Taillefer, *Chem. Eur. J.*, 2014, **20**, 14619–14623.

23 Y. Cudre, F. F. de Carvalho, G. R. Burgess, L. Male, S. J. A. Pope, I. Tavernelli and E. Baranoff, *Inorg. Chem.*, 2017, **56**, 11565–11576.

24 Siegrist, A. E., Patent DE1094753, 1959.

25 S. Xun, G. LeClair, J. Zhang, X. Chen, J. P. Gao and Z. Y. Wang, *Org. Lett.*, 2006, **8**, 1697–1700.

26 V. N. Kozhevnikov, Y. Zheng, M. Clough, H. A. Al-Attar, G. C. Griffiths, K. Abdullah, S. Raisys, V. Jankus, M. R. Bryce and A. P. Monkman, *Chem. Mater.*, 2013, **25**, 2352–2358.

27 Ai. et al., Patent US2005265686 (A1), 2005.

28 V. V. Il'in, O. V. Slavinskaya, Y. A. Strelenko, A. V. Ignatenko and V. A. Ponomarenko, *Bull. Acad. Sci. USSR, Div. Chem. Sci. (English Trans.)*, 1992, **40**, 2177–2180.

29 D. R. Martir, C. Momblona, A. Pertegás, D. B. Cordes, A. M. Z. Slawin, H. J. Bolink and E. Zysman-Colman, *ACS Appl. Mater. Interfaces*, 2016, **8**, 33907–33915.

30 A. Fürstner, M. Alcarazo, V. César and C. W. Lehmann, *Chem. Commun.*, 2006, 2176–2178.
31 M. Micksch, M. Tenne and T. Strassner, *Eur. J. Org. Chem.*, 2013, 6137–6145.
32 M. Bandini, P. G. Cozzi, M. Gazzano and A. Umani-Ronchi, *Eur. J. Org. Chem.*, 2001, 1937–1942.

Appendix

Chapter 2

X-ray crystallography

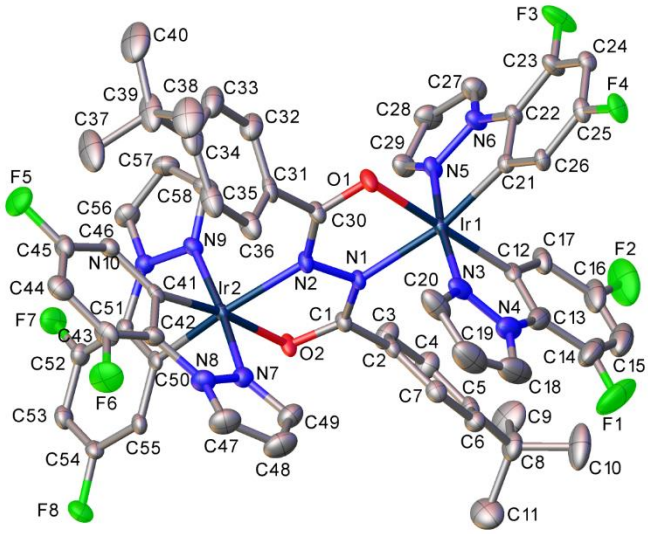

Figure A1. One of the independent molecules of **36b*** in the crystal of **36b***·DCM. DCM of crystallisation and all H atoms are omitted for clarity.

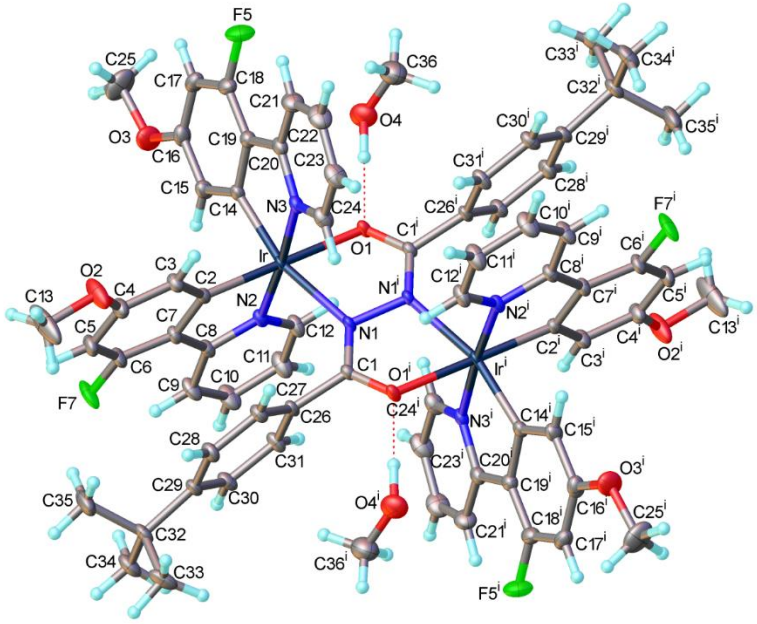

Figure A2. Molecular structure of **37a** in the crystal of **37a**·1.84MeOH·0.16DCM. DCM of crystallisation (partly substituting the shown methanol molecules) is omitted for clarity. Atoms generated by the inversion centre are primed.

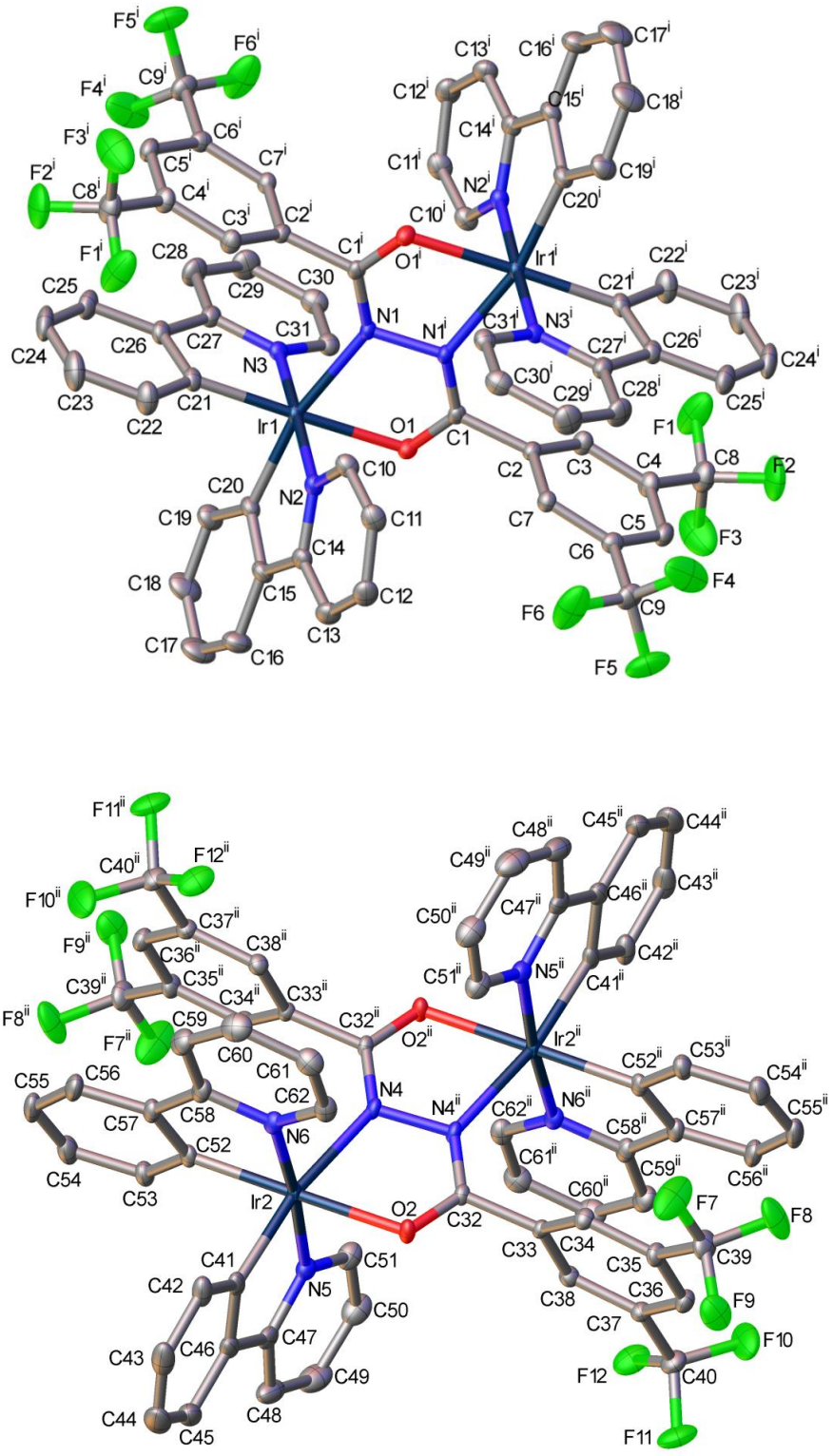

Figure A3. Two independent molecules of **38a***·in the crystal of **38a***·½CD_2Cl_2. The disordered solvent of crystallisation and all H atoms are omitted for clarity. Atoms generated by inversion centres are primed and double-primed.

Computational study

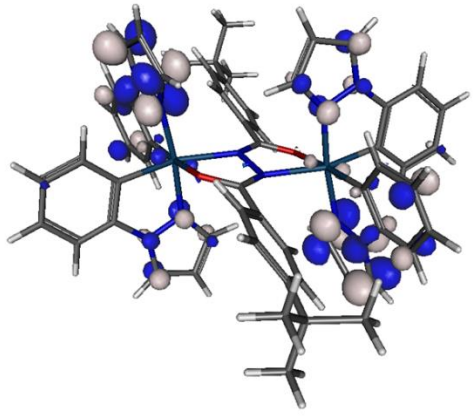

LUMO

–0.84 eV

Ir : Bridge : Ph : Pz

4 : 1 : 29 : 65

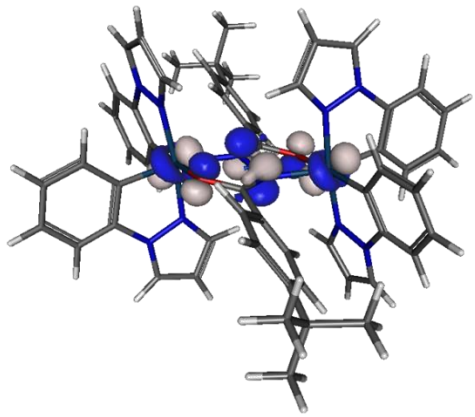

HOMO

–4.52 eV

Ir : Bridge : Ph : Pz

35 : 48 : 12 : 4

Figure A4. Frontier molecular orbitals for the most stable minimum of **35a**.

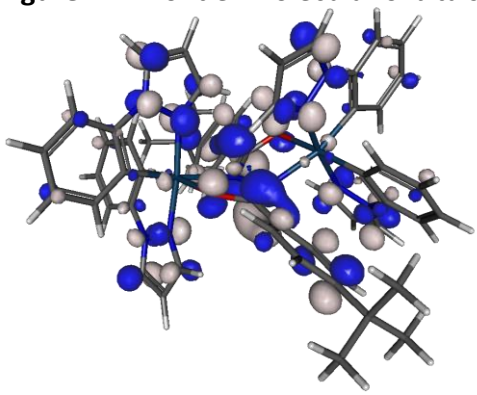

LUMO

–0.89 eV

Ir : Bridge : Ph : Pz

3 : 45 : 16 : 36

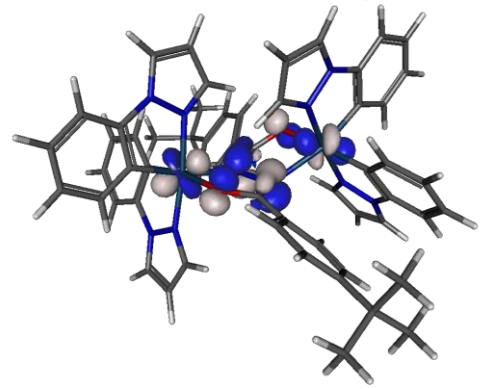

HOMO

–4.52 eV

Ir : Bridge : Ph : Pz

29 : 61 : 4 : 6

Figure A5. Frontier molecular orbitals for the most stable minimum of **35b**.

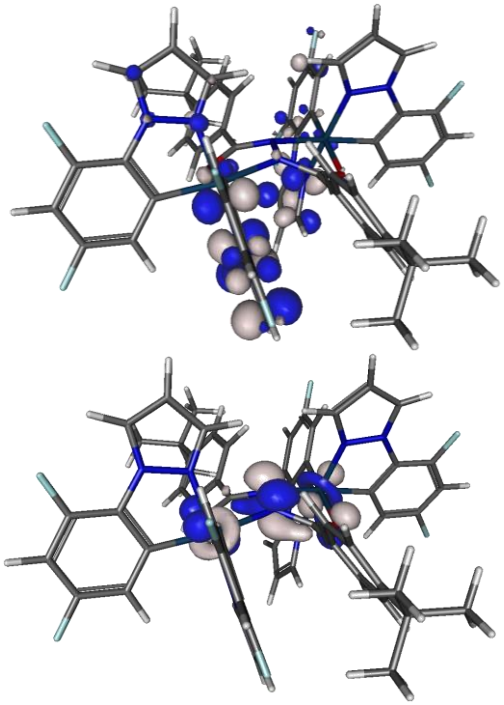

LUMO

–1.10 eV

Ir : Bridge : Ph : Pz

4 : 7 : 28 : 60

HOMO

–5.05 eV

Ir : Bridge : Ph : Pz

30 : 61 : 5 : 4

Figure A6. Frontier molecular orbitals for the most stable minimum of **36b**.

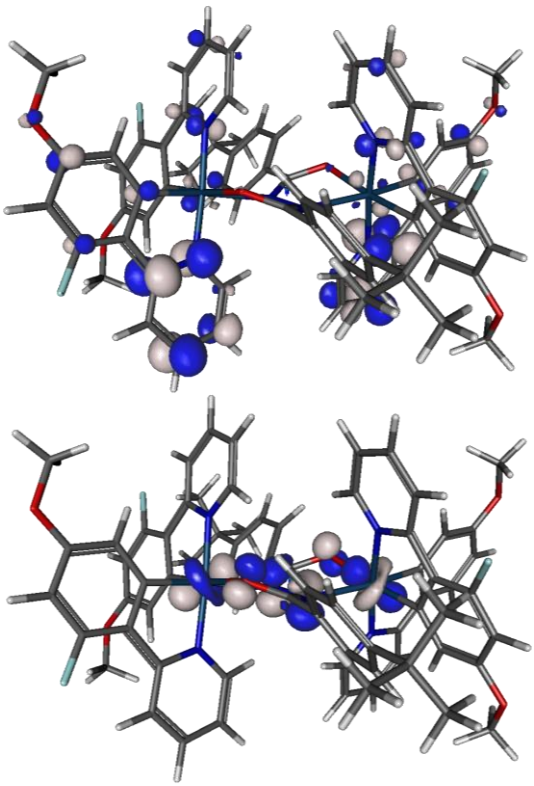

LUMO

–1.36 eV

Ir : Bridge : Ph : Py

6 : 1 : 21 : 72

HOMO

–4.82 eV

Ir : Bridge : Ph : Py

34 : 51 : 10 : 5

Figure A7. Frontier molecular orbitals for the most stable minimum of **37b**.

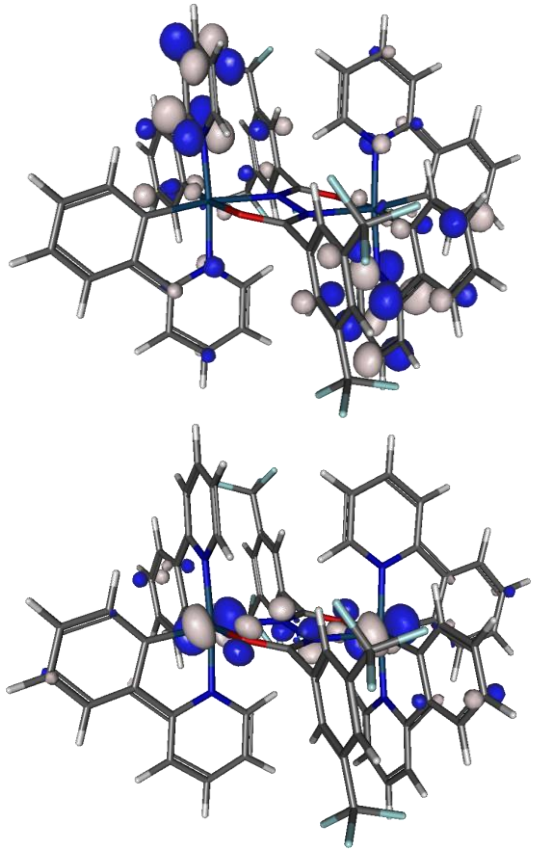

LUMO

–1.63 eV

Ir : Bridge : Ph : Py

4 : 17 : 21 : 58

HOMO

–5.01 eV

Ir : Bridge : Ph : Py

45 : 18 : 32 : 5

Figure A8. Frontier molecular orbitals for the most stable minimum of **38a**.

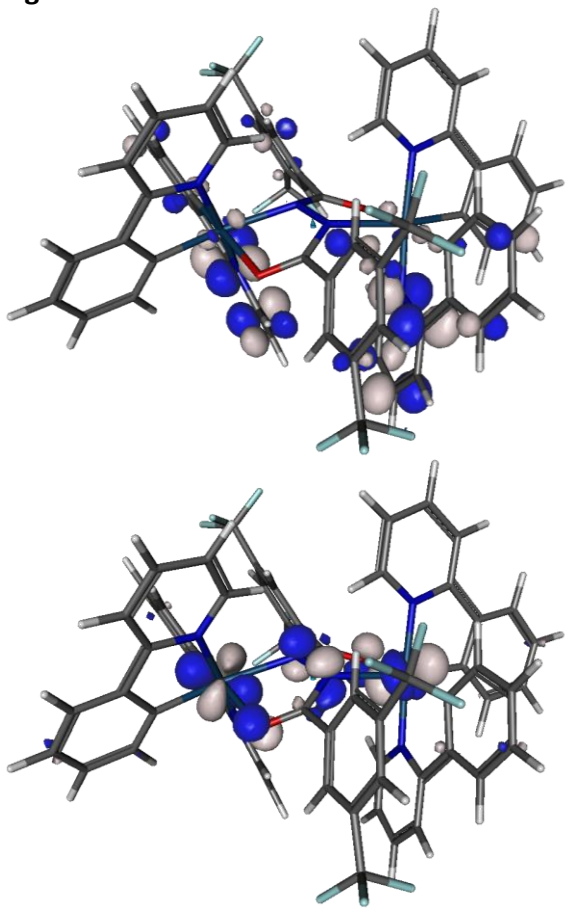

LUMO

–1.62 eV

Ir : Bridge : Ph : Py

4 : 18 : 18 : 60

HOMO

–5.04 eV

Ir : Bridge : Ph : Py

41 : 30 : 23 : 5

Figure A9. Frontier molecular orbitals for the most stable minimum of **38b**.

Chapter 3

X-ray crystallography

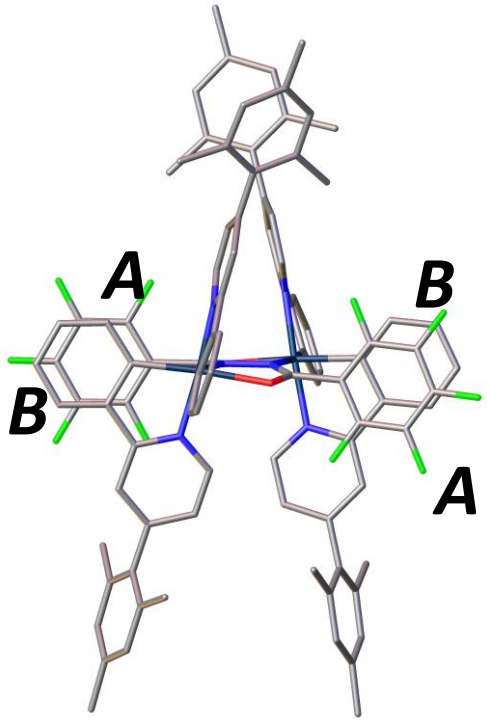

Figure A10. Molecular structure of ΔΔ **66** viewed perpendicular to the plane of the cyclometallating phenyl moieties to highlight intramolecular π–π interactions. The bridge (*A*) and cyclometallating ligand (*B*) phenyl groups that are engaged in intramolecular π–π stacking are labelled.

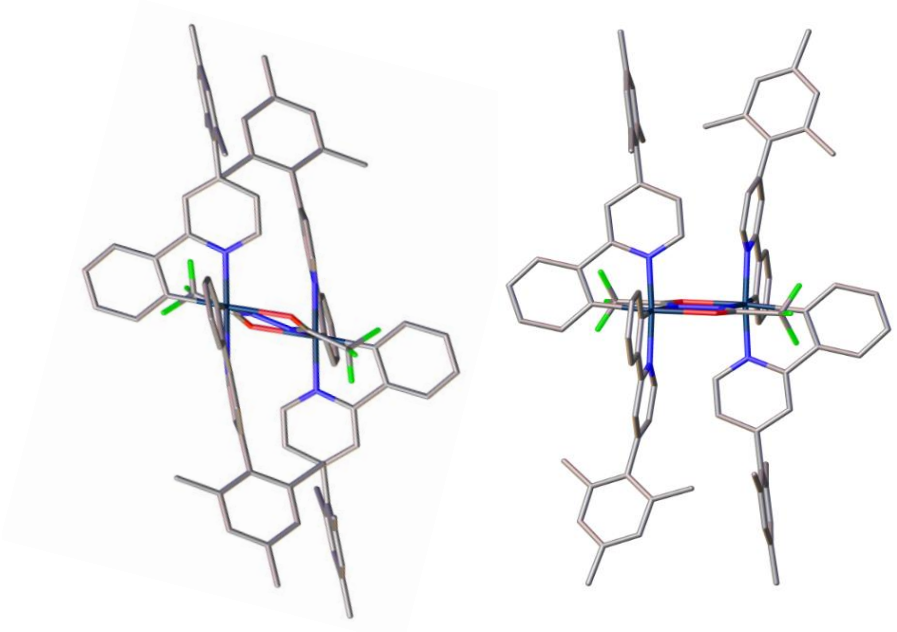

Figure A11. Molecular structures of molecule A (left) and molecule B (right) of *meso* **67** viewed perpendicular to the plane of the cyclometallating phenyl moieties.

Computational study

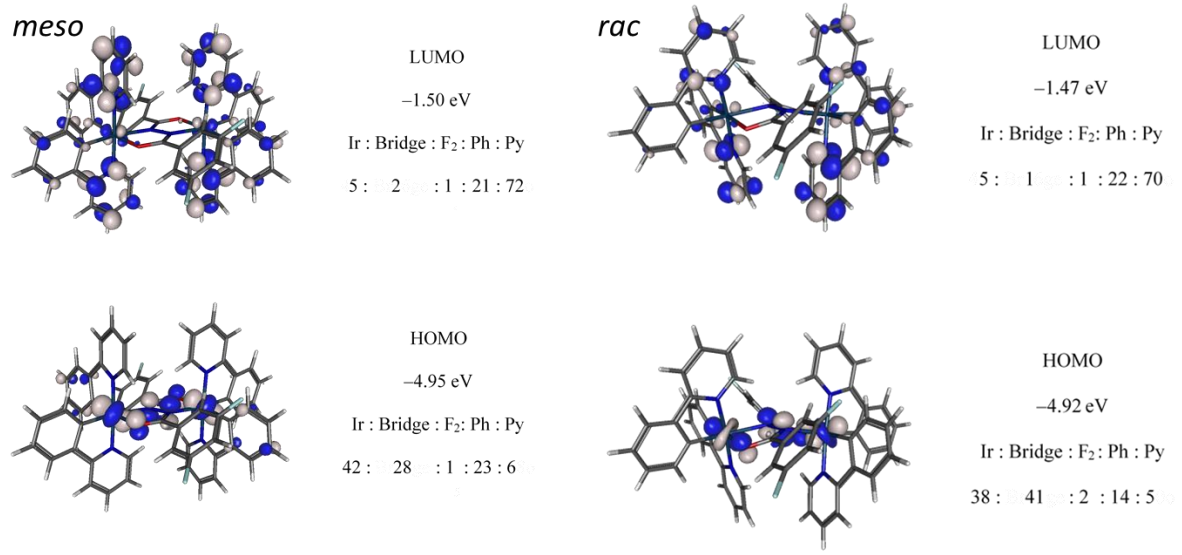

Figure A12. Frontier molecular orbitals for the most stable minima of **62**

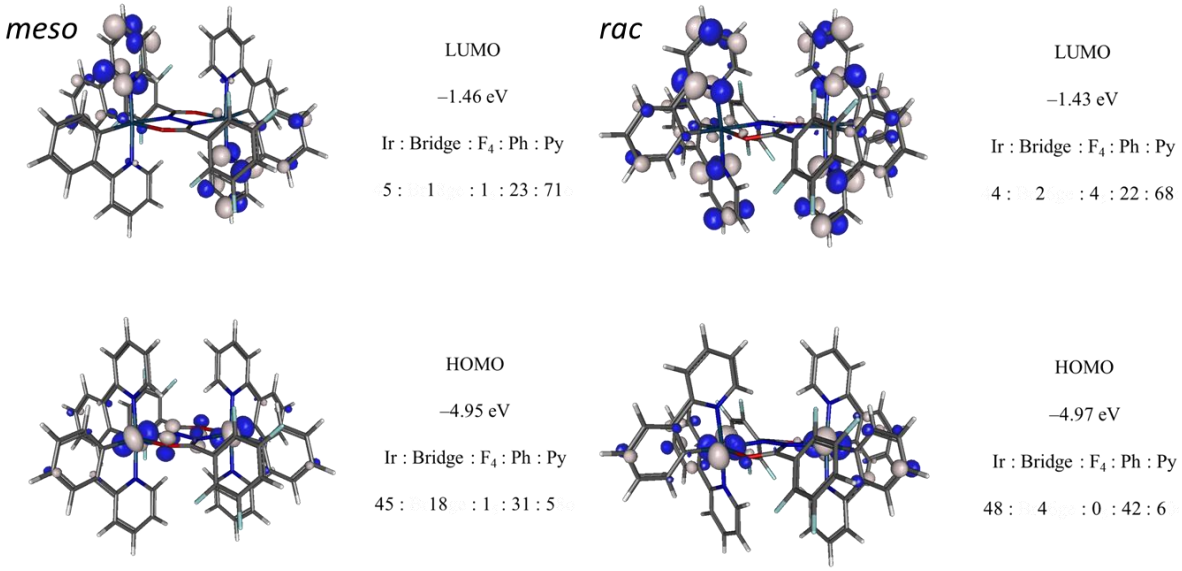

Figure A13. Frontier molecular orbitals for the most stable minima of **63**

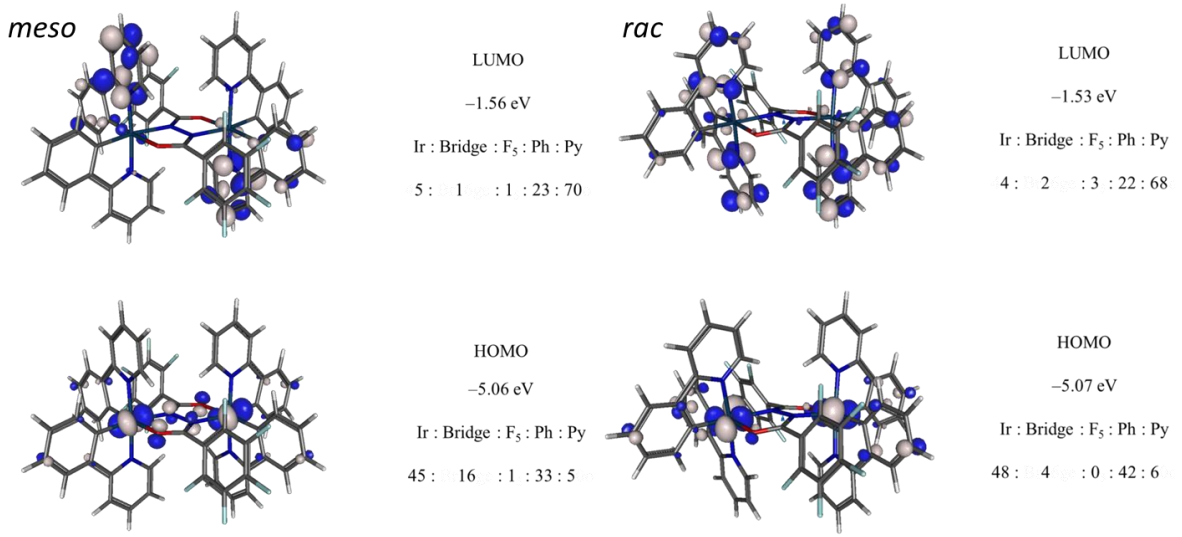

Figure A14. Frontier molecular orbitals for the most stable minima of **64**

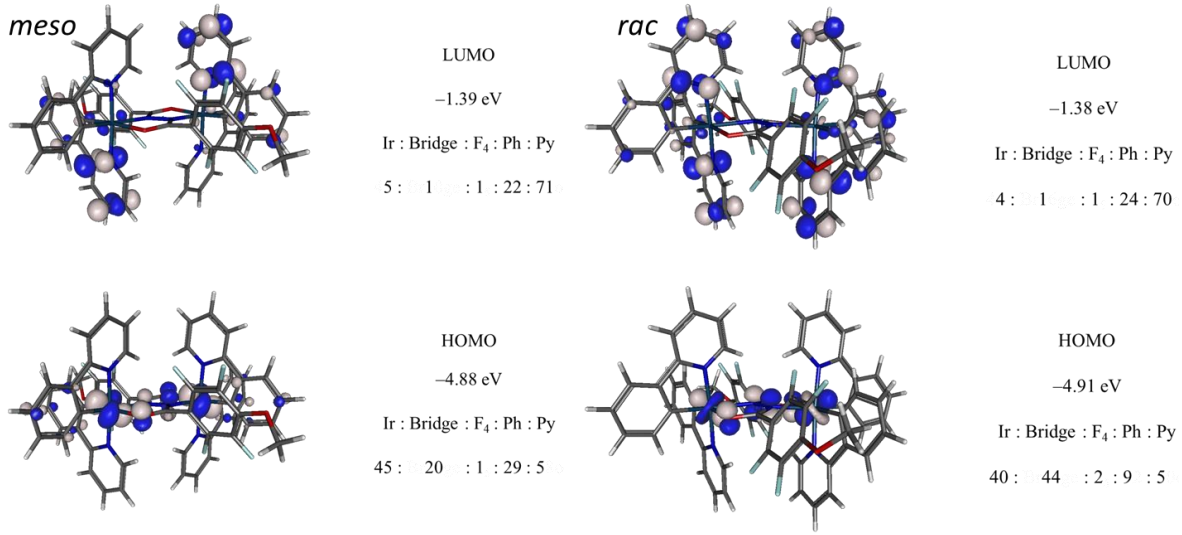

Figure A15. Frontier molecular orbitals for the most stable minima of **65**

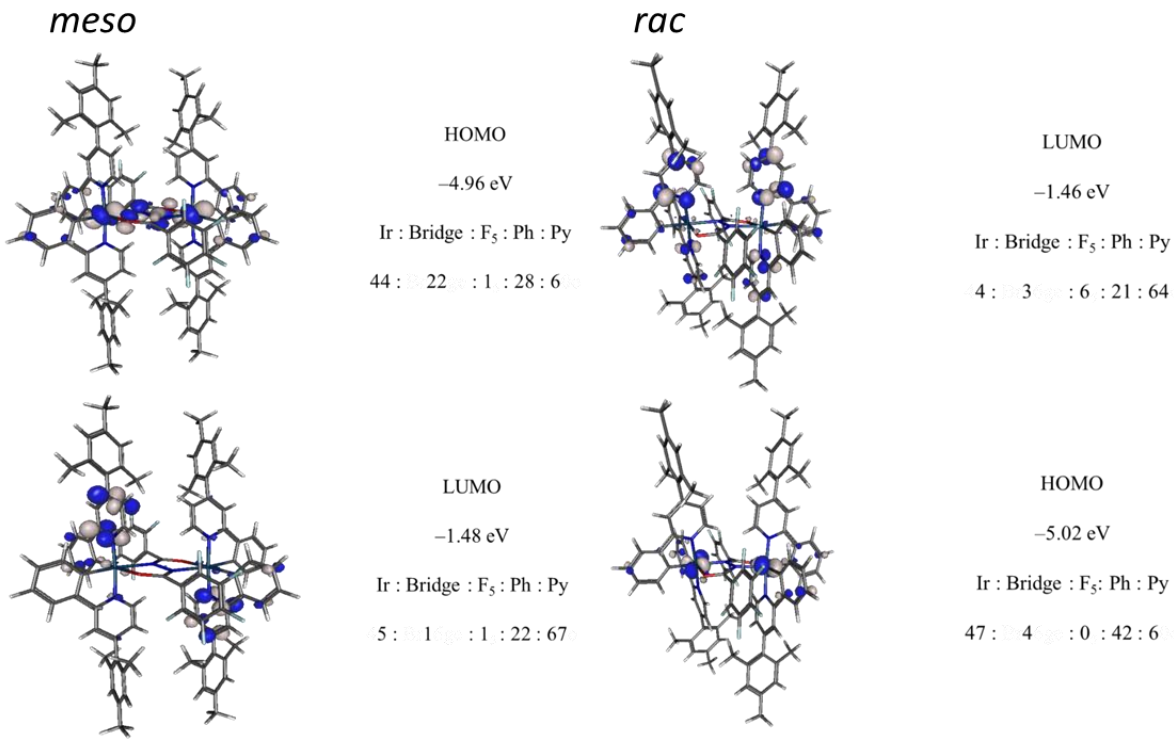

Figure A16. Frontier molecular orbitals for the most stable minima of **66**

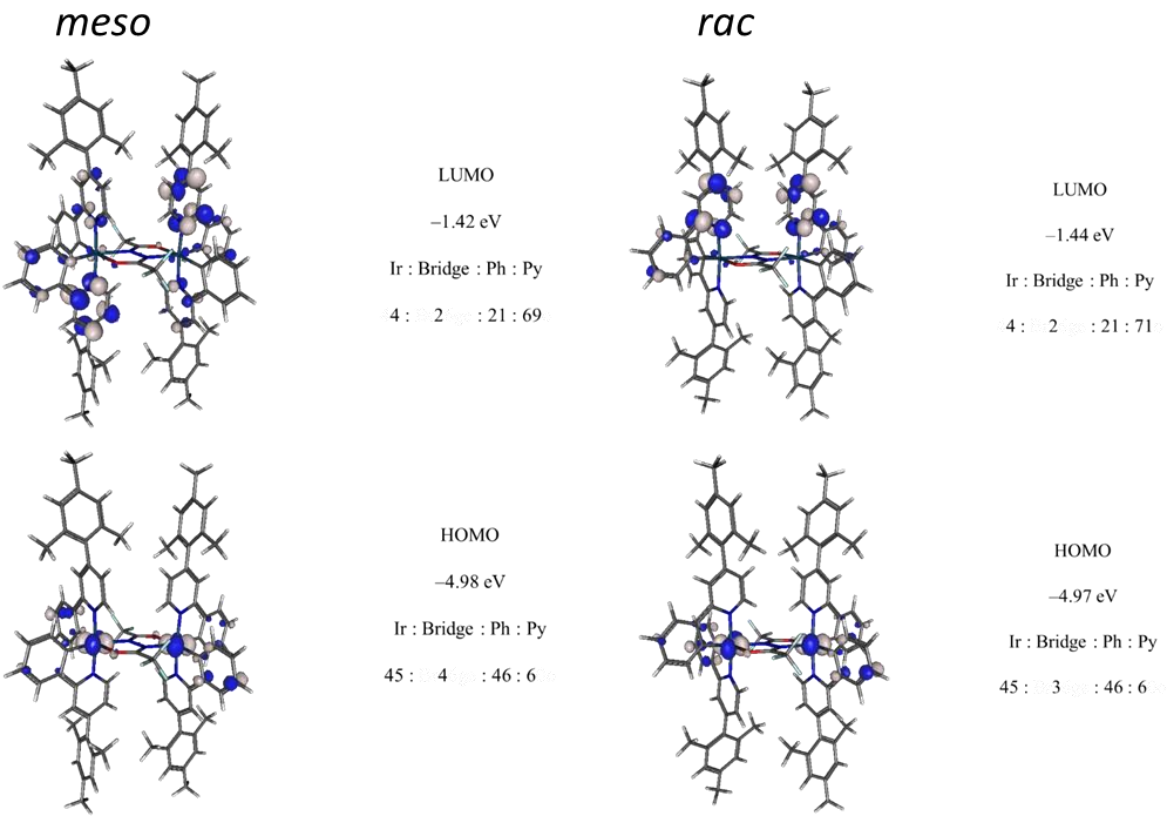

Figure A17. Frontier molecular orbitals for the most stable minima of **67**

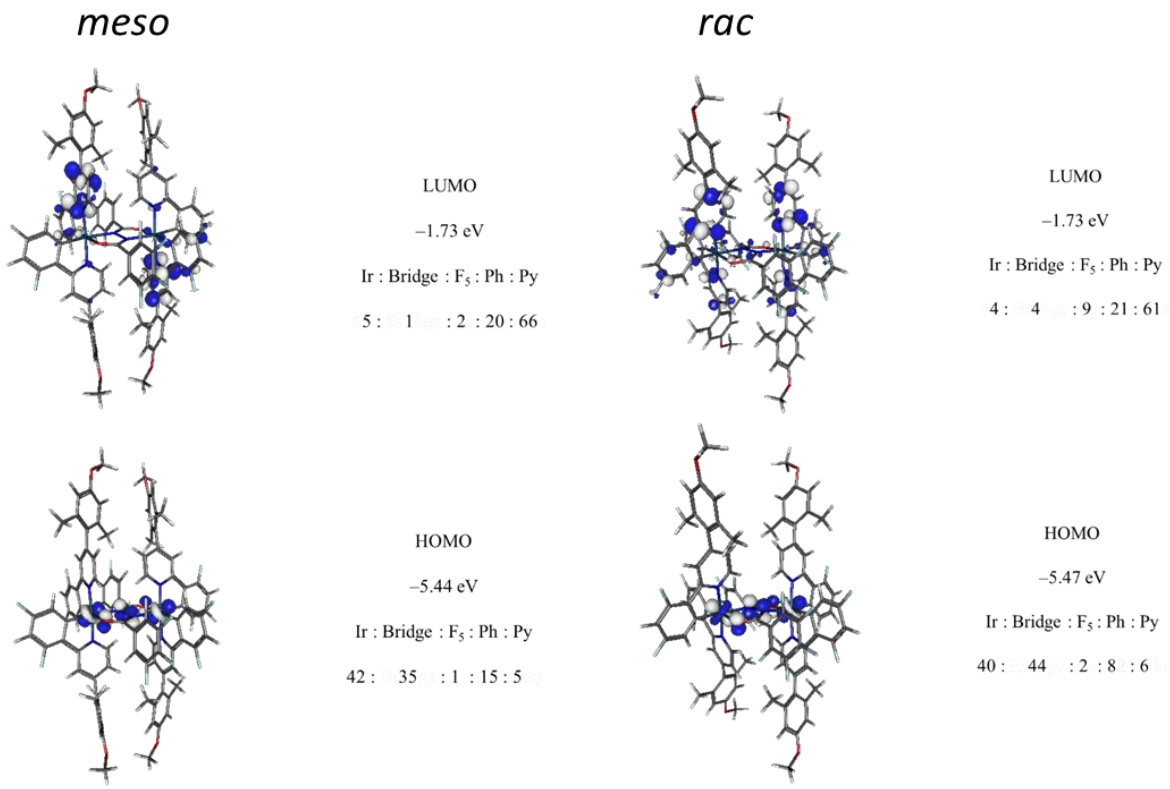

Figure A18. Frontier molecular orbitals for the most stable minima of **68**

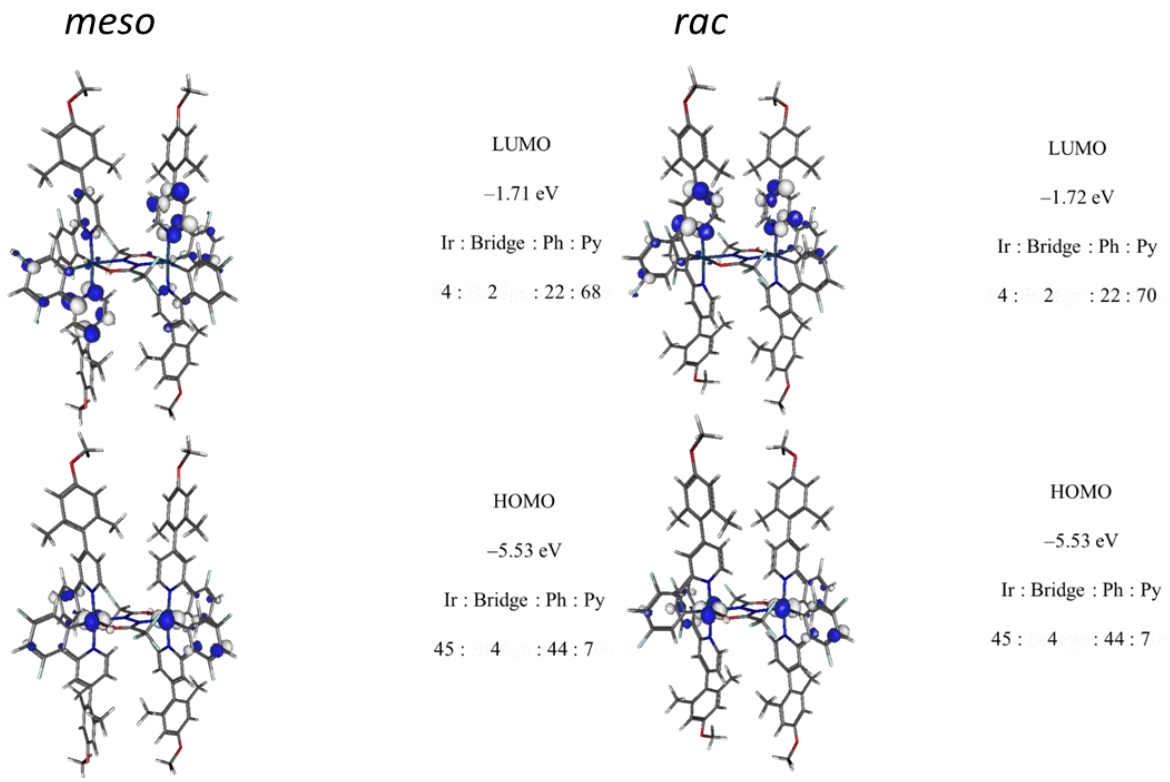

Figure A19. Frontier molecular orbitals for the most stable minima of **69**

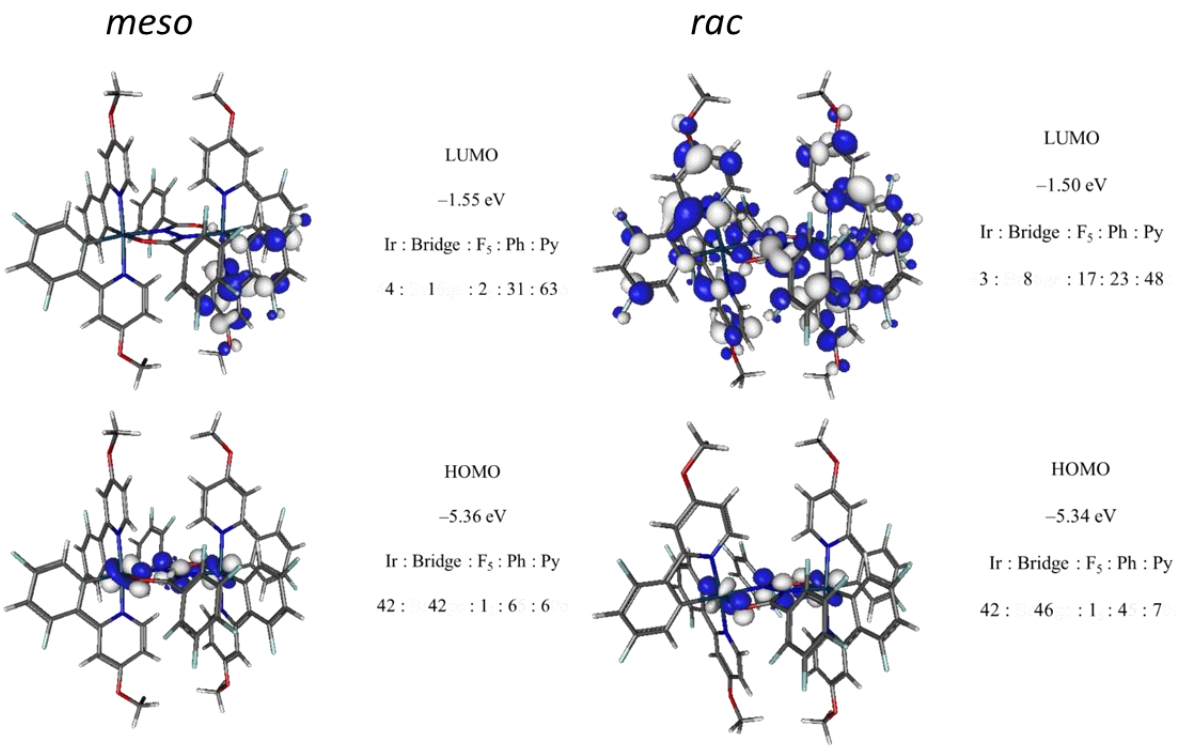

Figure A20. Frontier molecular orbitals for the most stable minima of **70**

Table A1. Summary of the orbital contributions for complex **66**.

Complex	Isomer	Orbital	Ir	Bridge centre	Bridge aryl	Ph[a]	Py[b]
66	*meso*	LUMO+5	2%	0%	4%	13%	77%
		LUMO+4	2%	0%	5%	13%	76%
		LUMO+3	4%	0%	1%	19%	69%
		LUMO+2	5%	0%	1%	19%	69%
		LUMO+1	5%	1%	3%	21%	66%
		LUMO	5%	1%	1%	22%	67%
		HOMO	44%	22%	1%	28%	6%
		HOMO-1	46%	2%	0%	45%	7%
		HOMO-2	43%	32%	1%	18%	6%
		HOMO-3	67%	7%	0%	12%	12%
		HOMO-4	32%	3%	1%	46%	17%
		HOMO-5	27%	1%	1%	49%	21%
	rac	LUMO+5	3%	6%	14%	7%	68%
		LUMO+4	2%	17%	50%	8%	23%
		LUMO+3	5%	1%	2%	23%	68%
		LUMO+2	5%	2%	1%	22%	69%
		LUMO+1	5%	1%	1%	24%	67%
		LUMO	4%	3%	6%	21%	64%
		HOMO	47%	4%	0%	42%	6%
		HOMO-1	42%	31%	1%	20%	6%
		HOMO-2	44%	18%	0%	30%	7%
		HOMO-3	68%	9%	1%	10%	12%
		HOMO-4	61%	3%	1%	20%	14%
		HOMO-5	24%	1%	1%	53%	21%

Table A2. Summary of the orbital contributions for complex **70**.

Complex	Isomer	Orbital	Ir	Bridge centre	Bridge aryl	Ph[a]	Py[b]
70	*meso*	LUMO+6	3%	12%	30%	3%	53%
		LUMO+5	2%	7%	20%	3%	67%
		LUMO+4	2%	9%	26%	4%	60%
		LUMO+3	4%	1%	1%	31%	63%
		LUMO+2	4%	1%	2%	31%	63%
		LUMO+1	3%	1%	3%	31%	62%
		LUMO	4%	1%	2%	31%	63%
		HOMO	42%	42%	1%	9%	6%
		HOMO-1	47%	10%	0%	35%	7%
		HOMO-2	47%	3%	0%	42%	8%
		HOMO-3	64%	7%	0%	10%	18%
		HOMO-4	57%	4%	0%	17%	12%
		HOMO-5	51%	3%	0%	23%	23%
	rac	LUMO+5	1%	10%	71%	2%	16%
		LUMO+4	3%	15%	34%	16%	32%
		LUMO+3	4%	0%	1%	30%	65%
		LUMO+2	4%	1%	2%	32%	61%
		LUMO+1	3%	7%	15%	25%	50%
		LUMO	3%	8%	17%	23%	48%
		HOMO	42%	46%	1%	4%	7%
		HOMO-1	49%	4%	0%	40%	6%
		HOMO-2	45%	4%	0%	43%	8%
		HOMO-3	64%	8%	1%	9%	18%
		HOMO-4	61%	3%	1%	13%	22%

Electrochemistry

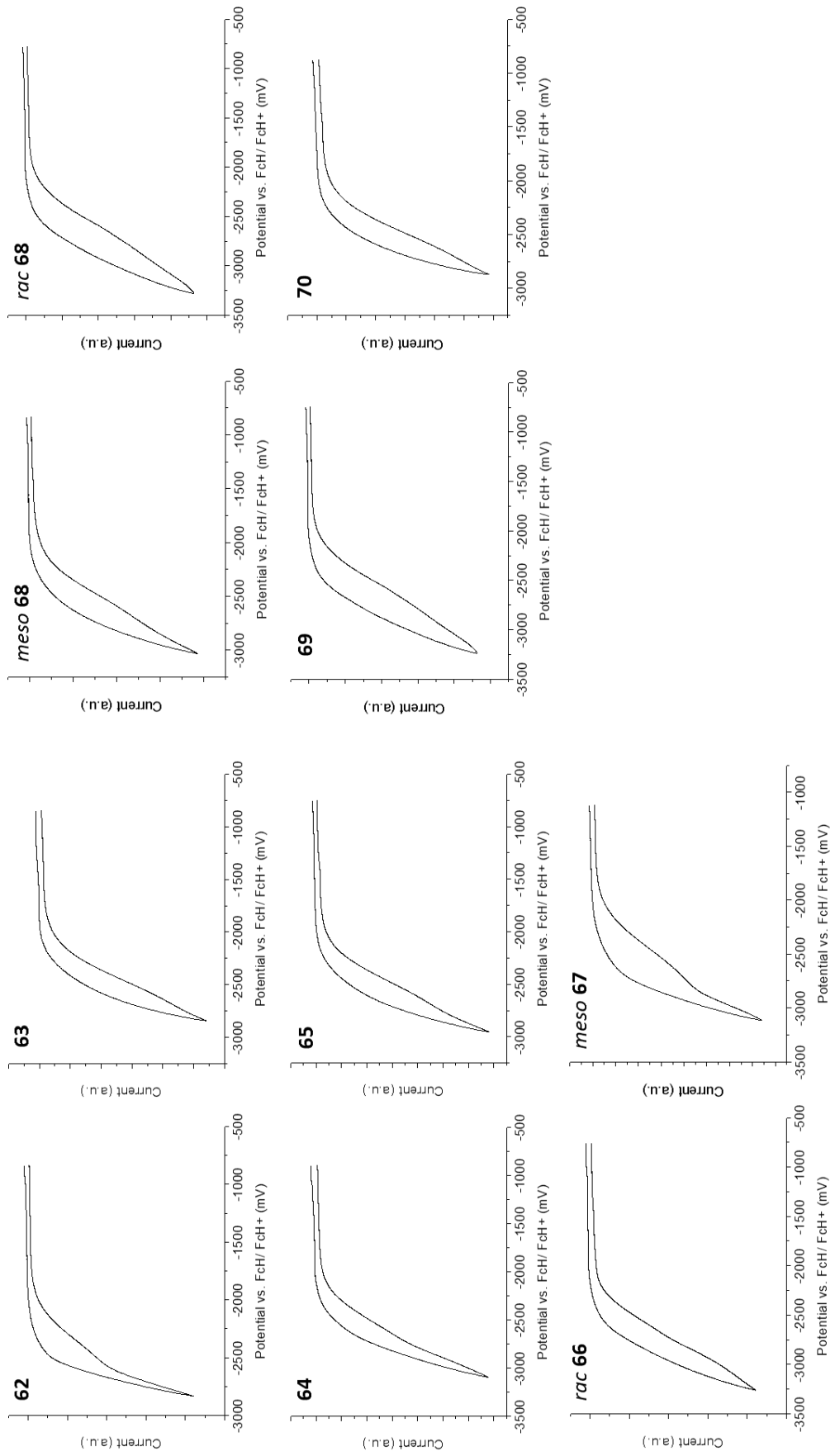

Figure A21. Cyclic voltammograms in 0.1 M *n*-Bu_4PF_6/ THF showing the reduction process for complexes **62–70**.

Infrared spectroscopy

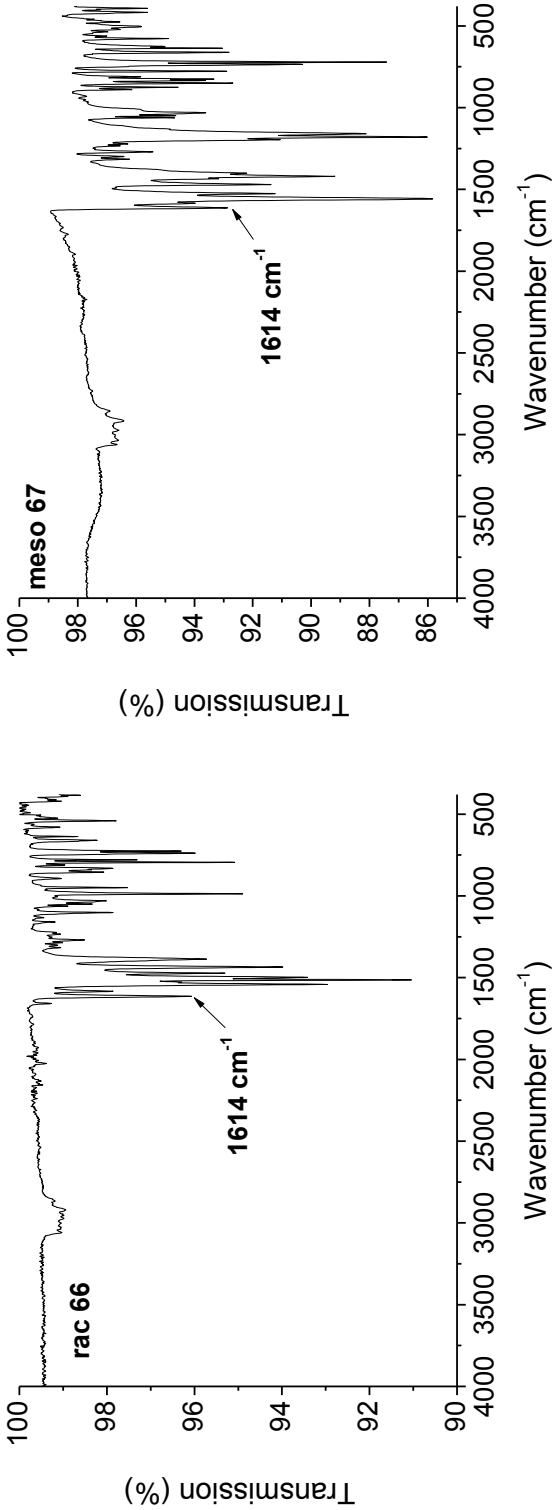

Figure A22. Infrared spectra for complexes *rac* **66** and *meso* **67**

Table A3. Summary of the orbital contributions for complex **105**–**107**.

Complex	Isomer	Orbital	Ir	Bridge centre	Ph[a]	Im[b]	Complex	Isomer	Orbital	Ir	Bridge centre	Bridge aryl	Ph[a]	Im[b]	Complex	Isomer	Orbital	Ir	Bridge centre	Bridge aryl	Ph[a]	Im[b]
105	*meso*	LUMO+5	3%	7%	35%	36%	**106**	*meso*	LUMO+5	1%	0%	10%	11%	13%	**107**	*meso*	LUMO+5	2%	1%	16%	26%	27%
		LUMO+4	0%	4%	4%	6%			LUMO+4	2%	1%	4%	29%	28%			LUMO+4	2%	1%	5%	36%	36%
		LUMO+3	1%	5%	4%	6%			LUMO+3	3%	3%	30%	34%	27%			LUMO+3	1%	1%	13%	45%	38%
		LUMO+2	3%	17%	28%	28%			LUMO+2	1%	1%	18%	42%	36%			LUMO+2	3%	2%	22%	38%	32%
		LUMO+1	3%	4%	43%	42%			LUMO+1	4%	2%	57%	19%	17%			LUMO+1	4%	3%	68%	13%	12%
		LUMO	3%	1%	49%	44%			LUMO	2%	7%	58%	17%	16%			LUMO	1%	9%	67%	11%	11%
		HOMO	45%	14%	33%	8%			HOMO	44%	41%	1%	7%	7%			HOMO	43%	43%	1%	6%	7%
		HOMO-1	47%	2%	40%	10%			HOMO-1	47%	7%	0%	37%	8%			HOMO-1	46%	5%	0%	38%	10%
		HOMO-2	48%	31%	13%	8%			HOMO-2	47%	2%	1%	40%	10%			HOMO-2	45%	2%	1%	38%	14%
		HOMO-3	63%	6%	18%	13%			HOMO-3	65%	7%	0%	14%	14%			HOMO-3	50%	4%	1%	23%	22%
		HOMO-4	45%	4%	28%	23%			HOMO-4	45%	4%	1%	25%	25%			HOMO-4	48%	5%	1%	27%	19%
		HOMO-5	43%	3%	29%	25%			HOMO-5	60%	5%	1%	16%	19%			HOMO-5	55%	5%	1%	20%	19%
	rac	LUMO+5	1%	0%	6%	94%		*rac*	LUMO+5	2%	2%	16%	25%	54%		*rac*	LUMO+5	3%	1%	5%	39%	36%
		LUMO+4	1%	1%	6%	93%			LUMO+4	2%	0%	6%	32%	59%			LUMO+4	2%	2%	9%	36%	35%
		LUMO+3	1%	0%	8%	92%			LUMO+3	2%	3%	40%	28%	26%			LUMO+3	3%	2%	24%	37%	31%
		LUMO+2	1%	1%	14%	84%			LUMO+2	3%	3%	74%	10%	11%			LUMO+2	2%	2%	4%	47%	41%
		LUMO+1	3%	1%	44%	52%			LUMO+1	2%	1%	1%	49%	46%			LUMO+1	3%	4%	78%	8%	7%
		LUMO	2%	1%	43%	53%			LUMO	2%	3%	50%	23%	22%			LUMO	1%	4%	67%	14%	13%
		HOMO	46%	34%	13%	7%			HOMO	44%	40%	1%	8%	7%			HOMO	43%	42%	1%	7%	7%
		HOMO-1	49%	4%	40%	8%			HOMO-1	50%	3%	0%	38%	8%			HOMO-1	48%	3%	0%	37%	11%
		HOMO-2	42%	13%	35%	10%			HOMO-2	44%	8%	0%	38%	10%			HOMO-2	41%	6%	0%	385	14%
		HOMO-3	64%	8%	14%	14%			HOMO-3	64%	9%	0%	13%	14%			HOMO-3	60%	8%	0%	16%	15%
		HOMO-4	40%	2%	31%	27%			HOMO-4	42%	2%	1%	28%	27%			HOMO-4	33%	2%	1%	35%	28%
		HOMO-5	61%	3%	19%	17%			HOMO-5	63%	2%	0%	17%	17%			HOMO-5	53%	2%	1%	26%	18%

[a]Phnyl moieties of the cyclometallating ligands. [b]Imidazole moieties of the cyclometallating ligands.

Table A4. Summary of the orbital contributions for complex **108**.

Complex	Isomer	Orbital	Ir	Bridge centre	Bridge aryl	Ph[a]	Im[b]
108	*meso*	LUMO+5	3%	1%	25%	36%	33%
		LUMO+4	4%	1%	1%	48%	44%
		LUMO+3	3%	3%	31%	34%	28%
		LUMO+2	1%	1%	18%	42%	36%
		LUMO+1	4%	2%	53%	21%	19%
		LUMO	2%	8%	56%	17%	17%
		HOMO	42%	45%	1%	5%	8%
		HOMO-1	47%	4%	0%	37%	11%
		HOMO-2	47%	3%	1%	35%	15%
		HOMO-3	47%	4%	1%	25%	24%
		HOMO-4	47%	5%	1%	27%	19%
		HOMO-5	49%	4%	1%	26%	20%
	rac	LUMO+5	3%	3%	22%	37%	33%
		LUMO+4	4%	1%	10%	45%	38%
		LUMO+3	4%	2%	14%	41%	37%
		LUMO+2	3%	2%	2%	48%	43%
		LUMO+1	3%	2%	70%	13%	12%
		LUMO	1%	4%	71%	12%	11%
		HOMO	43%	44%	1%	6%	6%
		HOMO-1	50%	3%	0%	35%	12%
		HOMO-2	41%	5%	1%	37%	17%
		HOMO-3	56%	8%	0%	21%	14%
		HOMO-4	33%	2%	1%	32%	32%
		HOMO-5	50%	2%	1%	31%	16%

[a]Phnyl moieties of the cyclometallating ligands.

[b]Imidazole moieties of the cyclometallating ligands.

Table A5. Summary of the TD-DFT data for complexes **105** and **107**.

Transition	105				107			
	meso		*rac*		*meso*		*rac*	
	Main orbital contribution	**λ/ nm (f)**	**Main orbital contribution**	**λ/ nm (f)**	**Main orbital contribution**	**λ/ nm (f)**	**Main orbital contribution**	**λ/ nm (f)**
$S_0 \rightarrow T_1$	HOMO-2 → LUMO+6, HOMO-2 → LUMO+8	458	HOMO → LUMO+8	460	HOMO → LUMO	424	HOMO-1 → LUMO+3, HOMO → LUMO+2	415
$S_0 \rightarrow T_2$	HOMO → LUMO+1	425	HOMO-1 → LUMO+1, HOMO → LUMO	425	HOMO → LUMO+1, HOMO-2 → LUMO+2	415	HOMO-1 → LUMO+2, HOMO → LUMO+3	415
$S_0 \rightarrow T_3$	HOMO-1 → LUMO	422	HOMO-1 → LUMO, HOMO → LUMO+1	425	HOMO-2 → LUMO+3, HOMO → LUMO+2	404	HOMO → LUMO+1, HOMO → LUMO+16	411
$S_0 \rightarrow T_4$	HOMO → LUMO+5, HOMO → LUMO+8	417	HOMO-1 → LUMO+2	416	HOMO-2 → LUMO+3, HOMO-1 → LUMO+4	406	HOMO-1 → LUMO+2, HOMO-1 → LUMO+4	407
$S_0 \rightarrow T_5$	HOMO-1 → LUMO+2	414	HOMO-2 → LUMO+2, HOMO-1 → LUMO+7	416	HOMO-2 → LUMO+4, HOMO-1 → LUMO+3	406	HOMO-2 → LUMO+2, HOMO-1 → LUMO+5	407

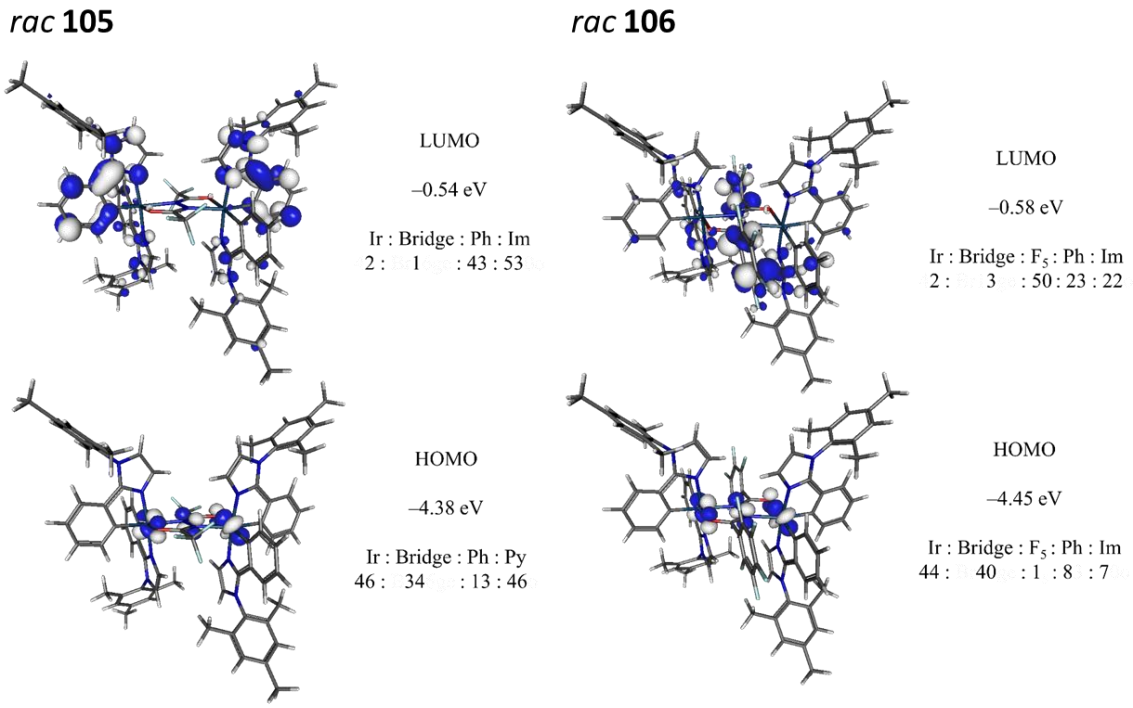

Figure A23. Frontier molecular orbitals for the most stable minima of *rac* **105** and *rac* **106**.

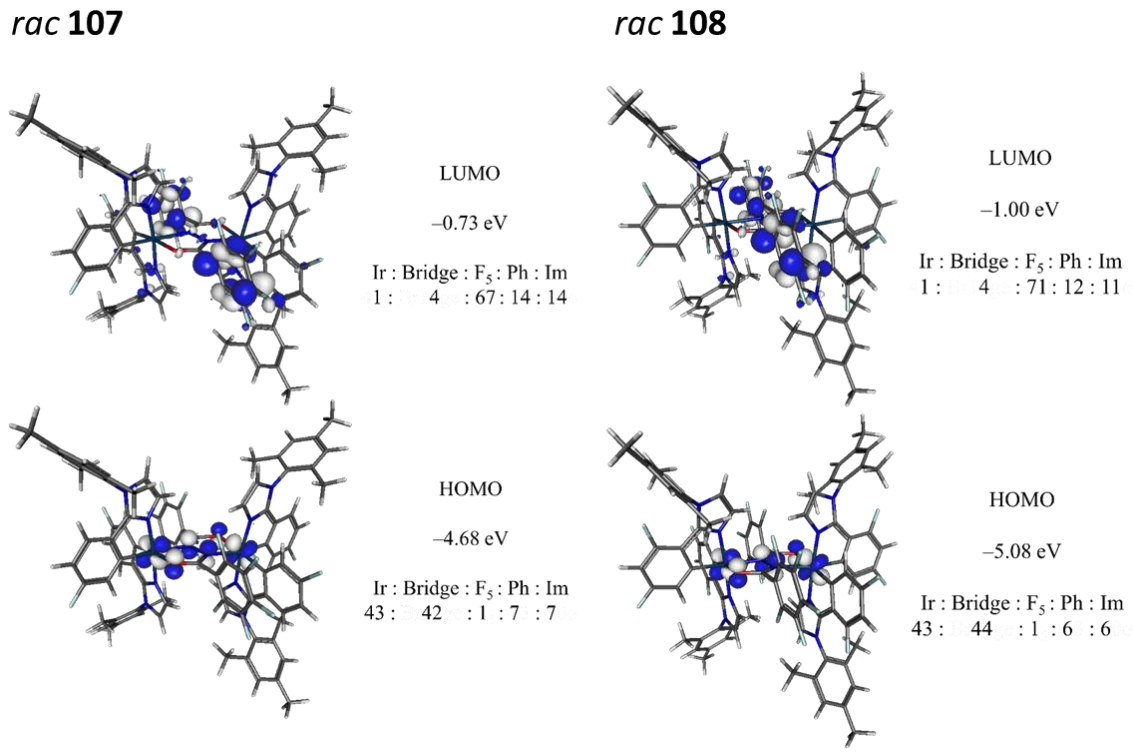

Figure A24. Frontier molecular orbitals for the most stable minima of *rac* **107** and *rac* **108**.

Electrochemical study and photophysical properties

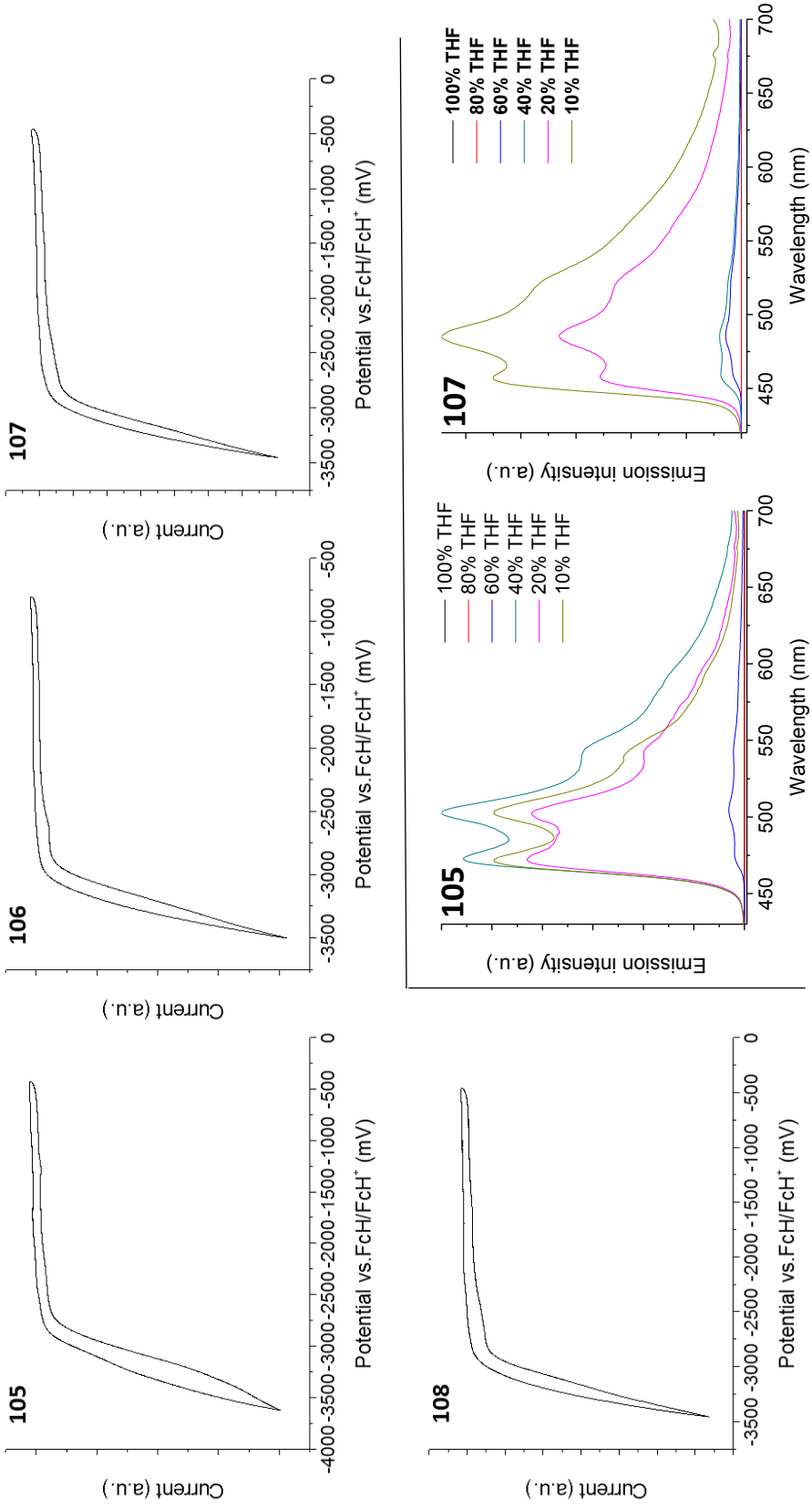

Figure A25. Cyclic voltammograms in 0.1 M *n*-Bu_4PF_6/ THF showing the reduction process for complexes **105–108.**

Figure A26. Emission spectra for THF solutions of complexes **105** and **107** upon incremental titration of water to induce precipitation (λ_{exc} 355 nm). THF fraction is percentage volume. Complex **105** has significantly poorer solubility in THF than **107–108**. Consequently, below 40% THF a dense precipitate forms, which settles and gives a perceived decrease in emission